University of California

Los Angeles

Stellar Populations, Outflows, and Morphologies of High-Redshift Galaxies

A dissertation submitted in partial satisfaction

of the requirements for the degree

Doctor of Philosophy in Astronomy

by

Katherine Anne Kornei

2012

Abstract of the Dissertation

Stellar Populations, Outflows, and Morphologies of High-Redshift Galaxies

by

Katherine Anne Kornei

Doctor of Philosophy in Astronomy

University of California, Los Angeles, 2012

Professor Alice E. Shapley, Chair

Understanding the regulation and environment of star formation across cosmic time is critical to tracing the build-up of mass in the Universe and the interplay between the stars and gas that are the constituents of galaxies. Three studies are presented in this thesis, each examining a different aspect of star formation at a specific epoch. The first study presents the results of a photometric and spectroscopic survey of 321 Lyman break galaxies (LBGs) at $z \sim 3$ to investigate systematically the relationship between Lyα emission and stellar populations. Lyα equivalent widths ($W_{\mathrm{Ly}\alpha}$) were calculated from rest-frame UV spectroscopy and optical/near-infrared/*Spitzer* photometry was used in population synthesis modeling to derive the key properties of age, dust extinction, star formation rate (SFR), and stellar mass. We directly compare the stellar populations of LBGs with and without strong Lyα emission, where we designate the former group ($W_{\mathrm{Ly}\alpha} \geq 20$ Å) as Lyα-emitters (LAEs) and the latter group ($W_{\mathrm{Ly}\alpha} < 20$ Å) as non-LAEs. This controlled method of comparing objects from the same UV luminosity distribution represents an improvement over previous studies in which the stellar populations of LBGs and narrowband-selected LAEs were contrasted,

where the latter were often intrinsically fainter in broadband filters by an order of magnitude simply due to different selection criteria. Using a variety of statistical tests, we find that Lyα equivalent width and age, SFR, and dust extinction, respectively, are significantly correlated in the sense that objects with strong Lyα emission also tend to be older, lower in star formation rate, and less dusty than objects with weak Lyα emission, or the line in absorption. We accordingly conclude that, within the LBG sample, objects with strong Lyα emission represent a later stage of galaxy evolution in which supernovae-induced outflows have reduced the dust covering fraction. We also examined the hypothesis that the attenuation of Lyα photons is lower than that of the continuum, as proposed by some, but found no evidence to support this picture.

The second study focuses specifically on galactic-scale outflowing winds in 72 star-forming galaxies at $z \sim 1$ in the Extended Groth Strip. Galaxies were selected from the DEEP2 survey and follow-up LRIS spectroscopy was obtained covering Si II, C IV, Fe II, Mg II, and Mg I lines in the rest-frame ultraviolet. Using *GALEX*, *HST*, and *Spitzer* imaging available for the Extended Groth Strip, we examine galaxies on a per-object basis in order to better understand both the prevalence of galactic outflows at $z \sim 1$ and the star-forming and structural properties of objects experiencing outflows. Gas velocities, measured from the centroids of Fe II interstellar absorption lines, are found to span the interval [–217, +155] km s^{-1}. We find that $\sim 40\%$ (10%) of the sample exhibits blueshifted Fe II lines at the 1σ (3σ) level. We also measure maximal outflow velocities using the profiles of the Fe II and Mg II lines; we find that Mg II frequently traces higher velocity gas than Fe II. Using quantitative morphological parameters derived from the *HST* imaging, we find that mergers are not a prerequisite for driving outflows. More face-on galaxies also show stronger winds than highly inclined systems, consistent with the canonical picture of winds emanating per-

pendicular to galactic disks. In light of clumpy galaxy morphologies, we develop a new physically-motivated technique for estimating areas corresponding to star formation. We use these area measurements in tandem with *GALEX*-derived star-formation rates to calculate star-formation rate surface densities. At least 70% of the sample exceeds a star-formation rate surface density of 0.1 $M_\odot$ yr^{-1} kpc^{-2}, the threshold necessary for driving an outflow in local starbursts. At the same time, the outflow detection fraction of only 40% in Fe II absorption provides further evidence for an outflow geometry that is not spherically symmetric. We see a $\sim 3\sigma$ trend between outflow velocity and star-formation rate surface density, but no significant trend between outflow velocity and star-formation rate. Higher resolution data are needed in order to test the scaling relations between outflow velocity and both star-formation rate and star-formation rate surface density predicted by theory.

Galactic winds are further explored in the third study of this thesis, where we present a study at $z \sim 1$ of the prevalence and kinematics of ultraviolet emission lines from fine-structure Fe II* transitions and resonance Mg II transitions. Utilizing a multiwavelength dataset of 212 star-forming galaxies, we investigate how the strength and kinematics of Fe II* and Mg II emission lines vary as a function of galaxy properties. We find that Fe II* emission is prevalent in the sample; composite spectra assembled on the basis of a variety of galaxy properties all show Fe II* emission, particularly in the stronger 2396 and 2626 Å lines. This prevalence of emission is in contrast to observations of local galaxies; the lack of Fe II* emission in the small star-forming regions targeted by spectroscopic observations at $z \sim 0$ may imply that Fe II* emission arises in more extended galaxy halos. The strength of Fe II* emission is most strongly modulated by star-formation rate, dust attenuation, and [O II] equivalent width, such that systems with lower star-formation rates, lower dust levels, and larger [O II] equivalent

widths show stronger Fe II* emission. Mg II emission, while not observed in a spectral stack of all the data in our sample, is seen in $\sim 30\%$ of individual objects. We find that objects showing Mg II emission have preferentially larger [O II] equivalent widths, bluer $U - B$ colors, and lower stellar masses than the sample as a whole. Active galactic nuclei are not likely responsible for the Mg II emission in our sample, since we have excluded active galaxies from our dataset. We also do not observe the Ne V emission line at 3425 Å characteristic of active galaxies in our co-added spectra. We find that the kinematics of Fe II* emission lines are consistent with the systemic velocity. This result does not necessarily imply that these lines arise from star-forming regions, however, as an optically thin galactic wind could show blueshifted and redshifted Fe II* emission lines centered around 0 km s^{-1}. We note that Fe II* emission arising from extended gas is consistent with the hypothesis that slit losses are responsible for the lack of Fe II* emission in local samples. We propose that dust is primarily responsible for the correlations between Fe II* strength and galaxy properties, as objects with lower star-formation rates and larger [O II] equivalent widths also exhibit lower dust attenuations, on average. The strong Mg II emission seen in systems with larger [O II] equivalent widths, bluer $U - B$ colors, and lower stellar masses may also be the result of low dust attenuation in these objects. Larger studies composed of high signal-to-noise observations will be critical for testing the hypothesis that dust is the primary modulator of fine-structure and resonance emission.

The dissertation of Katherine Anne Kornei is approved.

Steven R. Furlanetto

Jean L. Turner

Edward D. Young

Alice E. Shapley, Committee Chair

University of California, Los Angeles

2012

Table of Contents

List of Figures

List of Tables

Acknowledgments

There are many people whom I owe thanks to for helping me along the road of graduate school. My peers at UCLA readily shared humor, merriment, and scientific advice. Ian Crossfield was my faithful lunch buddy – thank you for your company all those days at exactly 12:00 PM. My good friend and Southern California expert Matt House was always up for museum outings, trips to the Hollywood Bowl, and French practice – *je te remerci beaucoup*. Kristine Yu, my dear roommate, introduced me to yoga, ultimate frisbee, and truffles made with Ecuadorian chocolate. Last, but most certainly not least, my classmate Chris Crockett (Goose) was my wingman in Los Angeles. Our late-night West Wing marathons, guitar and juggling sessions, and permanent encampment at Boba Loca to study for exams are some of my best memories of graduate school. I count myself lucky to have met you.

My friend Ariane Lotti played therapist on all matters, astronomy and otherwise. Thank you for your patient ear.

As I was starting my study of astronomy in high school and college, several individuals provided inspiration and encouragement: Stephen Widmark, Katie Thornburg, Rosanne di Stefano, Yvonne Pendleton, Dale Cruikshank, Meg Urry, and Pieter van Dokkum. Thank you.

I have been lucky to benefit from having two advisors in graduate school. Nate McCrady, my Master's thesis advisor, patiently taught me programming and the wonders of IDL. I now appreciate the beauty of a well-labeled figure, and I know to *always* include a scale bar. Thank you, Nate, for your mini lectures that occurred whenever I entered your office; it was truly good fortune to learn from someone with such a flair for explanation. The mai tais in Honolulu were

great and I forgive you for the unfortunate trip to Ken's House of Pancakes in Hilo.

Alice Shapley, my advisor for doctoral work, has given me the opportunity to work with incredible datasets and telescopes. With your guidance, Alice, I've been able to truly experience *doing science*. Thank you for your patience listening to my theories and intuitions, no matter how wrong they were. I am constantly amazed at your ability to juggle a small army of students and postdocs while still devoting an extraordinary amount of time to each of us individually; you always knew exactly what I was working on. I appreciate your mentorship and I know that I have become a better writer thanks to all the red ink on my paper drafts.

Finally, I thank my family – Tom, Mary, and Mark – for their unending support and love.

Vita

2004–2007	Assistant Researcher, NASA Ames Research Center
2006	B.S. (Astronomy & Physics), Yale University
2006	Chancellor's Prize, UCLA
2008	M.S. (Astronomy), UCLA
2011	Dissertation Year Fellowship, UCLA

Publications

K. A. Kornei, A. E. Shapley, C. L. Martin, A. L. Coil, and J. M. Lotz, in preparation. "Fine-Structure Fe II* Emission and Mg II Emission in $z \sim 1$ Star-Forming Galaxies"

C. L. Martin, A. E. Shapley, A. L. Coil, K. A. Kornei, K. Bundy, B. J. Weiner, K. G. Noeske, and D. Schiminovich, submitted to ApJ, astro-ph/1206.5552. "Demographics and Physical Properties of Gas Out/Inflows at $0.4 < z < 1.4$"

K. A. Kornei, A. E. Shapley, C. L. Martin, A. L. Coil, J. M. Lotz, D. Schiminovich, K. Bundy, and K. G. Noeske, submitted to ApJ, astro-ph/1205.0812. "The Properties and Prevalence of Galactic Outflows at $z \sim 1$ in the Extended Groth Strip"

K. A. Kornei, A. E. Shapley, D. K. Erb, C. C. Steidel, N. A. Reddy, M. Pettini, and M. Bogosavljević, 2010, ApJ, 711, 693. "The Relationship Between Stellar Populations and Lyα Emission in Lyman Break Galaxies"

D. P. Cruikshank, J. P. Emery, K. A. Kornei, G. Bellucci, and E. d'Aversa, 2010, Icarus, 205, 516. "Eclipse Reappearances of Io: Time-Resolved Spectroscopy (1.9–4.2 μm)"

K. N. Hainline, A. E. Shapley, K. A. Kornei, M. Pettini, E. Buckley-Geer, S. S. Allam, and D. L. Tucker, 2009, ApJ, 701, 52. "Rest Frame Optical Spectra for Three Strongly Lensed Galaxies at $z \sim 2$"

K. A. Kornei and N. McCrady, 2009, ApJ, 697, 1180. "A Young Super Star Cluster in the Nuclear Region of NGC 253"

CHAPTER 1

Introduction

The reservoirs of gas, dust, and stars within galaxies exist in constant interplay. Cold gas is the fuel from which stars are formed, gas and dust are returned to the interstellar medium when a star dies, and the energy injected from supernovae and stellar winds heats and accelerates gas. Investigating the environment and regulation of star formation over a broad range of redshifts – the aim of this thesis – therefore requires an understanding of the complexities of maintaining and replenishing a repository of cold gas subject to forces that act to disperse, heat, and remove gas from the system. Tracing the environment and regulation of star formation over billions of years is critical to investigating the cosmic history of star formation in the Universe and the relationship between local star-forming systems and high-redshift galaxies.

1.1 The H I Lyα line at $z \sim 3$

The H I Lyα line at 1216 Å is an observational signature of star formation. This prominent resonance feature arises in star-forming regions from the recombination of hydrogen ions and is a useful probe of high-redshift star formation due to its intrinsic strength and its redshifted placement in the optical wavelength regime where detector sensitivity is high. Many studies have focused on investigating how Lyα line emission is correlated with galaxy stellar populations using two classes of

galaxies selected with different observational techniques. These two classes, Lyα-emitters and Lyman break galaxies, have consequently emerged as archetypes of star-forming systems. Lyα-emitters (LAEs) are isolated using narrowband filters tuned to the wavelength of Lyα, where a Lyα rest-frame equivalent width $\geq$ 20 Å is typically required (Cowie & Hu, 1998; Rhoads et al., 2000; Gawiser et al., 2006). As these systems are targeted solely based on line emission, LAEs are often faint in broadband imaging. Population synthesis modeling, achievable only for combined observations of multiple LAEs, reveals that LAEs are low-mass systems with minimal dust attenuation (Gawiser et al., 2007). Some authors have accordingly proposed that LAEs represent the beginning of an evolutionary sequence in which galaxies increase in mass and dust content through successive mergers and star formation episodes (Gawiser et al., 2007).

Lyman break galaxies (LBGs), on the other hand, are selected using color cuts around the Lyman limit at 912 Å in the rest frame (e.g., Steidel et al., 1996a, 1999). With no explicit Lyα selection criteria, LBGs exhibit a diversity of Lyα profiles: emission, absorption, emission superimposed on absorption, and no signature at all. LBGs are brighter than LAEs ($\mathcal{R} \leq 25.5$ (Steidel et al., 2003) versus $R \sim 27$ for LAEs (Gawiser et al., 2006), where $\mathcal{R}$ and R magnitudes are comparable). This luminosity difference between LBGs and LAEs makes it difficult to accurately compare the respective stellar populations of these systems, given the potential biases of contrasting galaxies of significantly different luminosity classes. A preferable approach to understanding how stellar populations vary as a function of Lyα strength is to make measurements of Lyα within a controlled sample of objects at similar redshifts drawn from the same parent luminosity distribution. The intrinsic variation in Lyα profiles within a large sample of LBGs ensures adequate statistics for measuring how stellar populations change with Lyα strength, as discussed in this thesis.

Recent work by Lai et al. (2008) suggests that LAEs detected in the 3.6 μm band of the *Spitzer* Infrared Array Camera (IRAC; Fazio et al., 2004) are significantly older and more massive than IRAC-undetected LAEs. These authors propose that IRAC-detected LAEs may therefore be a lower-mass extension of the LBG population and that the dichotomy between LAEs and LBGs may not be as large as previously thought.

As a resonance line, Lyα's susceptibility to scattering can also be exploited to probe the geometry of the interstellar medium in high-redshift galaxies where resolved imaging of galaxy structure is difficult. By observing the relative attenuation of Lyα and (non-resonance) continuum emission, one can infer the relative distribution of ionized, neutral, and dust species in the interstellar medium based on assumptions of how these populations interact with Lyα and continuum photons. If dust in the interstellar medium is confined to clouds surrounded by largely ionized species (Neufeld, 1991; Hansen & Oh, 2006), Lyα photons will scatter off the surface of the clouds – never encountering the dust – and will escape from the galaxy. Therefore, it is entirely possible that dusty galaxies can exhibit strong Lyα emission when the conditions in the interstellar medium favor the escape of these photons. If, on the other hand, the geometry of the interstellar medium is such that ionized, neutral, and dust species are evenly mixed, then the longer path lengths of the Lyα photons (due to resonant scattering) will result in an increased probability that these photons will encounter a dust grain and be absorbed. Studying the ratio of Lyα and continuum emission yields an estimate of the Lyα "escape fraction" – the percent of Lyα photons produced in a galaxy that scatter out of the system and are observed. Authors have observed escape fractions on the order of several tens of percent (e.g., Blanc et al., 2011), consistent with a well-mixed interstellar medium in which Lyα photons are preferentially attenuated compared with continuum photons.

In the first chapter of this thesis, I use a sample of 321 LBGs at $z \sim 3$ to investigate both the relationship between Lyα strength and stellar populations and the Lyα escape fraction. I utilize an extensive data set of rest-frame ultraviolet spectroscopy from LRIS on Keck I and accompanying optical and near-infrared imaging. This chapter has been previously published in the Astrophysical Journal as Kornei et al. 2010 and is reproduced with permission of the American Astronomical Society.

1.2 Galactic winds at $z \sim 1$

The global star-formation rate density of the Universe peaked around $z \sim 2$ and has declined by nearly an order of magnitude over the intervening 10 billion years to the present epoch (e.g., Lilly et al., 1996). This precipitous drop in the star-formation rate density may be due to the heating, acceleration, and subsequent depletion of gas reservoirs by galactic winds. These winds, arising from the combined energy and radiation pressure of supernovae and massive stars, have been observed in both local and high-redshift systems (e.g., Martin, 2005; Veilleux et al., 2005; Rupke et al., 2005; Tremonti et al., 2007; Weiner et al., 2009; Steidel et al., 2010; Coil et al., 2011). Galactic winds are a candidate to explain the steep decrement in the star-formation rate density between $z \sim 2$ and today, although other factors such as the lower rate of infalling gas onto local galaxies may also be responsible for the trend in star-formation rate density. Winds are also a critical component of galaxy evolution, as outows may contribute to the limiting of black hole and spheroid growth (Ferrarese & Merritt, 2000; Robertson et al., 2006) and the enrichment of the intergalactic medium (Oppenheimer & Davé, 2006).

One technique for studying galactic winds relies on observing foreground gas absorbed against the light of a background host galaxy. By measuring the kine-

matic offsets of the foreground gas with respect to the systemic redshift of the background galaxy, the velocity of gas flows can be estimated. Absorption lines from a variety of neutral and ionized species are employed in studies of galactic winds, including C IV, Fe II, Mg II, Mg I, Na I, and H I. Outflows with extremely large velocities (> 1000 km s^{-1}) have been seen in a sample of post-starburst galaxies at $z \sim 0.6$ (Tremonti et al., 2007), although the majority of winds in star-forming galaxies have velocities ranging from 20–300 km s^{-1} (Martin, 2005).

Substantial work has been devoted to understanding both the geometry of the outflowing gas and the properties of the galaxies exhibiting galactic winds (e.g., Heckman et al., 1990; Steidel et al., 1996b; Franx et al., 1997; Martin, 1999; Pettini et al., 2000, 2001; Shapley et al., 2003; Martin, 2005; Veilleux et al., 2005; Rupke et al., 2005; Tremonti et al., 2007; Weiner et al., 2009; Steidel et al., 2010; Coil et al., 2011). Based on imaging of local starburst galaxies, a biconical outflow geometry has been suggested where outflow emerge perpendicular to the galactic disks with opening angles of tens of degrees (Heckman et al., 1990). At $0.5 < z < 0.9$, spectroscopy of foreground halo gas absorbed against the light of background galaxies reveals stronger absorption at small azimuthal angles relative to the foreground disk axis (Bordoloi et al., 2011); this result is consistent with the biconical outflow structures imaged in local samples. However, at higher redshifts ($1.5 < z < 3.6$), Law et al. (2012b) find that disk inclination and outflow velocity are not correlated, suggesting that outflows are only weakly collimated.

Determining the stellar and morphological properties of galaxies hosting galactic winds is critical to understanding the physical origin of gas flows. Star formation is the primary driver of galactic winds if the population of Active Galactic Nuclei (AGN) are neglected. The radiation pressure of young, hot stars and the kinetic energy and thermal pressure of supernovae are thought to work in tan-

dem to loft gas above, and potentially away from, the galaxy disk (e.g., Murray et al., 2011). Given the stellar origin of galactic winds, it is unsurprising that a correlation exists between the outflow velocity of gas and the star-formation rate of the host galaxy (Martin, 2005). However, this relationship between outflow velocity and star-formation rate is evident only over a large dynamic range in star-formation rate (0.1–1000 $M_\odot$ yr^{-1}). The correlation flattens in the interval 10-100 $M_\odot$ yr^{-1}, precisely the observed range of star-formation rates at $z \geq 1$ (Steidel et al., 2010). Therefore, recovering the trend between outflow velocity and star-formation rate in high-redshift samples is difficult except in the rare case of studies probing both quiescent dwarf galaxies and ultra-luminous infrared galaxies.

Other authors have suggested that a correlation between outflow velocity and star-formation rate *surface density* may be more fundamental than the relation between outflow velocity and star-formation rate. An episode of star formation occurring over a small area will produce energy concentrated enough to loft a column of gas while an equal level of star formation spread over a larger area does not produce the requisite concentration of energy to drive a gas flow (Murray et al., 2011). Accurate measurements of star-formation rate surface densities in high-redshift galaxies are difficult due to the need for spatially-resolved imaging.

The second chapter of this thesis presents a study of outflowing galactic winds at $z \sim 1$. Using ultraviolet Fe II and Mg II resonance absorption lines as probes of gas flows, we study the properties and prevalence of galactic winds as a function of host galaxy characteristics. We employ an extensive dataset of *GALEX*, *Hubble Space Telescope*, and *Spitzer* imaging to estimate dust-corrected star-formation rates, star-formation rate surface densities, galaxy areas, and disk inclinations. These data make it possible to isolate the most important factors modulating

outflows. We can also investigate the geometry of outflows using the spatially-resolved *Hubble Space Telescope* imaging. By measuring outflow velocity from both Fe II and Mg II lines, we can furthermore study how these two species probe similar (or different) properties of galactic winds. This chapter has been submitted to the Astrophysical Journal for publication as Kornei et al. 2012 and is reproduced with permission of the American Astronomical Society.

1.3 Emission-line probes of galactic winds

While studies of galactic winds commonly rely on absorption lines that unambiguously probe gas between Earth and a more distant light source, emission lines can arise from either foreground or background gas due to scattering. Observations of emission lines in systems hosting galactic winds accordingly comprise rich datasets complementing absorption-line investigations. Understanding the extent of circumgalactic gas and the morphology and kinematics of galactic winds is achievable with datasets of emission-line observations. A variety of emission lines are employed in wind studies, including resonance transitions (e.g., H I Lyα, Mg II 2796 Å) and fine-structure transitions arising from the decay of resonance transitions to excited ground states (i.e., Si II* 1265,1309,1533 Å, Fe II* 2626 Å). While spectroscopy of high-redshift star-forming galaxies frequently exhibits fine-structure emission (e.g., Giavalisco et al., 2011; Rubin et al., 2011; Coil et al., 2011; Kornei et al., 2012; Martin et al., 2012), local star-forming galaxies are strikingly bereft of fine-structure lines (Leitherer et al., 2011). Several authors have suggested that slit losses are responsible for the lack of fine-structure emission in nearby samples, where spectroscopic slits probe scales of parsecs as opposed to encompassing galactic halos where the emission may be arising (Giavalisco et al., 2011).

Determining the kinematics of emission lines requires detailed spectroscopic information. Rubin et al. (2011) investigated fine-structure Fe II* emission in a starburst galaxy at $z \sim 0.7$ and concluded that the emission was redward or within 30 km s^{-1} of the systemic velocity. On the other hand, Coil et al. (2011) reported that these same transitions are consistently *blueshifted* in a sample of post-starburst and AGN host galaxies at $0.2 < z < 0.8$. Prochaska et al. (2011) present models of galactic winds in which Fe II* emission is seen from both the backside (i.e., receding) and frontside (i.e., approaching) of the wind; these authors accordingly predict that Fe II* emission can appear at roughly the systemic velocity while still tracing gas flows.

Understanding how the prevalence, kinematics, and spatial extent of emission lines vary with galaxy properties necessitates an extensive multiwavelength dataset. Erb et al. (2012, in preparation) examined 96 star-forming galaxies at $1 \lesssim z \lesssim 2$ and found that stacks of composite spectra showed variations in fine-structure Fe II* emission strength. Specifically, low-mass objects exhibited stronger Fe II* emission than high-mass objects, and objects with strong resonance Mg II emission in the 2796, 2803 Å doublet also showed stronger Fe II* emission than objects lacking Mg II emission.

The third chapter of this thesis investigates fine-structure Fe II* emission and resonance Mg II emission in a sample of star-forming galaxies at $z \sim 1$. We utilize a large spectroscopic dataset of rest-frame ultraviolet observations from LRIS on Keck I, in addition to multiwavelength imaging from which properties such as stellar mass, color, dust attenuation, star-formation rate, and star-formation rate surface density are measured. We aim to understand the origin of fine-structure and resonance emission lines associated with galaxies hosting galactic winds. This chapter is being prepared as a submission to the Astrophysical Journal and will

appear as Kornei et al. 2012.

1.4 Adopted Conventions

We assume a standard ΛCDM cosmology throughout with $H_0 = 70$ km s^{-1} Mpc^{-1}, $\Omega_{\rm M} = 0.3$, and $\Omega_\Lambda = 0.7$.

CHAPTER 2

The Relationship between Stellar Populations and Lyα Emission in Lyman Break Galaxies

An increasing number of high-redshift galaxies have been found in the last two decades using selection techniques reliant on either color cuts around the Lyman limit at 912 Å in the rest frame (e.g., Steidel et al., 1996a, 1999) or strong Lyα line emission (e.g., Cowie & Hu, 1998; Rhoads et al., 2000; Gawiser et al., 2006). These two methods, which preferentially select Lyman break galaxies (LBGs) and Lyα-emitters (LAEs), respectively, have successfully isolated galaxies at redshifts up to $z = 7$ (Iye et al., 2006; Bouwens et al., 2008). Extensive data sets of LBGs and LAEs have afforded detailed studies of galactic clustering (e.g., Adelberger et al., 1998; Giavalisco & Dickinson, 2001), the universal star formation history (e.g., Madau et al., 1996; Steidel et al., 1999), and the galaxy luminosity function (e.g., Reddy et al., 2008; McLure et al., 2009). While the nature of LBGs and LAEs has been studied at a range of redshifts (e.g., Shapley et al., 2001; Gawiser et al., 2006; Verma et al., 2007; Pentericci et al., 2007; Nilsson et al., 2009b; Ouchi et al., 2008; Finkelstein et al., 2009), the epoch around $z \sim 3$ is particularly well-suited to investigation of these objects' detailed physical properties.

At this redshift, the prominent HI Lyα line ($\lambda_{\rm rest} = 1216$ Å), present in all LAE spectra and a significant fraction of LBG spectra, is shifted into the optical, where current imaging and spectroscopic instrumentation is optimized. Consequently,

there are large existing data sets of spectroscopically-confirmed $z \sim 3$ LBGs (e.g., Steidel et al., 2003) and LAEs (e.g., Lai et al., 2008), where extensive multiwavelength surveys often complement the former and, less frequently, the latter.

The mechanism responsible for LAEs' large Lyα equivalent widths is not fully understood, although several physical pictures have been proposed (e.g., Dayal et al., 2009; Kobayashi et al., 2010). As Lyα emission is easily quenched by dust, one explanation for LAEs is that they are young, chemically pristine galaxies experiencing their initial bursts of star formation (e.g., Hu & McMahon, 1996; Nilsson et al., 2007). Conversely, LAEs have also been proposed to be older, more evolved galaxies with interstellar media in which dust is segregated to lie in clumps of neutral hydrogen surrounded by a tenuous, ionized dust-free medium (Neufeld, 1991; Hansen & Oh, 2006; Finkelstein et al., 2009). In this picture, Lyα photons are resonantly scattered near the surface of these dusty clouds and rarely encounter dust grains. Continuum photons, on the other hand, readily penetrate through the dusty clouds and are accordingly scattered or absorbed. This scenario preferentially attenuates continuum photons and enables resonant Lyα photons to escape relatively unimpeded, producing a larger Lyα equivalent width than expected given the underlying stellar population. To date, the distribution of dust in the interstellar medium has only been investigated using relatively small samples (e.g., Verhamme et al., 2008; Atek et al., 2009; Finkelstein et al., 2009).

Given the different selection techniques used to isolate LBGs and LAEs, understanding the relationship between the stellar populations of these objects has been an important goal of extragalactic research. Recent work by Gawiser et al. (2006) has suggested that LAEs are less massive and less dusty than LBGs, prompting these authors to propose that LAEs may represent the beginning of

an evolutionary sequence in which galaxies increase in mass and dust content through successive mergers and star formation episodes (Gawiser et al., 2007). The high specific star formation rate – defined as star formation rate (SFR) per unit mass – of LAEs ($\sim 7 \times 10^{-9}$ yr^{-1}; Lai et al., 2008) relative to LBGs ($\sim 3 \times 10^{-9}$ yr^{-1}; Shapley et al., 2001) illustrates that LAEs are building up stellar mass at a rate exceeding that of continuum-selected galaxies at $z \sim 3$. This rapid growth in mass is consistent with the idea that LAEs represent the beginning of an evolutionary sequence of galaxy formation. However, results from Finkelstein et al. (2009) cast doubt on this simple picture of LAEs as primordial objects, given that these authors find a range of dust extinctions ($A_{1200} = 0.30$–4.50) in a sample of 14 LAEs at $z \sim 4.5$. Nilsson et al. (2009b) also find that $z \sim 2.25$ LAEs occupy a wide swath of color space, additional evidence that not all LAEs are young, dust-free objects. Furthermore, the assertion that LAEs are pristine galaxies undergoing their first burst of star formation is called into question by the results of Lai et al. (2008). These authors present a sample of 70 $z \sim 3.1$ LAEs, $\sim 30\%$ of which are detected in the 3.6 μm band of the *Spitzer* Infrared Array Camera (IRAC; Fazio et al., 2004). These IRAC-detected LAEs are significantly older and more massive ($\langle t_\star \rangle \sim 1.6$ Gyr, $\langle M \rangle \sim 9 \times 10^9$) than the IRAC-undetected sample ($\langle t_\star \rangle \sim 200$ Myr, $\langle M \rangle \sim 3 \times 10^8$ $M_\odot$); Lai et al. (2008) suggest that the IRAC-detected LAEs may therefore be a lower-mass extension of the LBG population. Narrowband-selected LAEs are clearly marked by heterogeneity, and the relationship between these objects and LBGs continues to motivate new studies.

When comparing the stellar populations of LBGs and LAEs, it is important to take into account the selection biases that result from isolating these objects with broadband color cuts and line flux/equivalent width requirements, respectively. By virtue of selection techniques that rely on broadband fluxes and colors, LBGs

generally have brighter continua than LAEs. Spectroscopic samples of LBGs typically have an apparent magnitude limit of $\mathcal{R} \leq 25.5$ ($0.4L^*$ at $z \sim 3$; Steidel et al., 2003) while LAEs have a median apparent magnitude of $R \sim 27$ (Gawiser et al., 2006), where $\mathcal{R}$ and R magnitudes are comparable. Even though the majority of LBGs studied to date are an order of magnitude more luminous in the continuum than typical LAEs, both populations have similar rest-frame UV colors (Gronwall et al., 2007). Therefore, LAEs fainter than $\mathcal{R} = 25.5$ are excluded from LBG spectroscopic surveys not because of their colors, but rather because of their continuum faintness. Given the significant discrepancy in absolute magnitude between LBGs and LAEs, understanding the relationship between these objects can be fraught with bias. An preferable approach to comparing these populations is to investigate how the strength of Lyα emission is correlated with galaxy parameters, for a controlled sample of objects at similar redshifts *drawn from the same parent UV luminosity distribution*.

Several authors have looked at the question of the origin of Lyα emission in UV flux-limited samples (e.g., Shapley et al., 2001; Erb et al., 2006a; Reddy et al., 2008; Pentericci et al., 2007; Verma et al., 2007). Shapley et al. (2001) analyzed 74 LBGs at $z \sim 3$ and constructed rest-frame UV composite spectra from two samples of "young" ($t_\star \leq 35$ Myr) and "old" ($t_\star \geq 1$ Gyr) galaxies, respectively. These authors found that younger objects exhibited weaker Lyα emission than older galaxies; Shapley et al. (2001) attributed the difference in emission strength to younger LBGs being significantly dustier than their more evolved counterparts. On the other hand, Erb et al. (2006a) examined a sample of 87 star-forming galaxies at $z \sim 2$ and found that objects with lower stellar mass had stronger Lyα emission features, on average, than more massive objects. In a sample of 139 UV-selected galaxies at $z \sim 2$–3, Reddy et al. (2008) isolated 14 objects with Lyα equivalent widths ≥ 20 Å and noted no significant difference in

the stellar populations of strong Lyα-emitters relative to the rest of the sample. Pentericci et al. (2007) examined 47 LBGs at $z \sim 4$ and found that younger galaxies generally showed Lyα in emission while Lyα in absorption was associated with older galaxies (in contrast to the Shapley et al. (2003) results). Probing even earlier epochs, Verma et al. (2007) examined a sample of 21 LBGs at $z \sim 5$ and found no correlation between Lyα equivalent width and age, stellar mass, or SFR. These authors noted, however, that only 6/21 of the brightest LBGs had corresponding spectroscopy from which equivalent widths were estimated. Therefore, the lack of a correlation between Lyα equivalent width and stellar populations may, in this case, have been masked by a small sample that was biased towards the brightest objects. These aforementioned investigations have shown that there does not yet exist a clear picture relating stellar populations to Lyα emission.

Here, we present a precise, systematic investigation of the relationship between Lyα emission and stellar populations using our large photometric and spectroscopic data set of $z \sim 3$ observations. As an improvement over previous studies, we approach the data analysis from multiple aspects: we compare not only the stellar population parameters derived from population synthesis modeling, but also examine the objects' best-fit SEDs and photometry. Furthermore, all analysis is conducted on objects drawn from the same parent sample of continuum-bright ($\mathcal{R} \leq 25.5$) LBGs. By controlling for continuum magnitude, we avoid the biases of comparing objects with significantly different luminosities while still retaining the ability to comment on the nature of strong Lyα-emitting galaxies within the LBG sample. Our conclusions are applicable to both LBGs and bright ($\mathcal{R} \leq 25.5$) narrowband-selected LAEs. While we are unable to make inferences about the population of faint LAEs, our study is complete with respect to bright LAEs given these objects' similar colors to LBGs in the rest-frame UV.

We are motivated by the following questions: how do the stellar populations of Lyα-emitting LBGs differ from those of other LBGs at $z \sim 3$ where the Lyα emission line is weaker (or absent altogether)? To what degree are galactic parameters such as dust extinction, SFR, age, and stellar mass correlated with Lyα line strength? What do the relative escape fractions of Lyα and continuum photons reveal about the distributions of gas and dust in these objects' interstellar media?

In §2.1, we present details of the observations and data reduction, including a description of the systematic technique used to calculate Lyα equivalent widths. Stellar population modeling is discussed in §2.2. The properties of objects with and without strong Lyα emission are presented in §2.3 and we discuss how our data can be used to address several of the outstanding questions pertaining to the physical nature of LBGs and LAEs in §2.4. A summary and our conclusions appear in §2.5.

2.1 Observations and Data Reduction

2.1.1 Imaging and Spectroscopy

The data presented here are drawn from the LBG surveys of Steidel and collaborators, with approximately half of the observations described in Steidel et al. (2003, 2004) and half from subsequent programs by the same authors. These surveys employed photometric preselection in the $U_nG\mathcal{R}$ passbands in a variety of fields (Reddy et al., 2008) to target galaxies in the redshift interval $z \sim 2$–3. Follow-up optical spectroscopy of a subset of these galaxies, paired with supplemental near and mid-infrared photometry, has yielded an extensive data set upon which multiple studies have been based (e.g., Shapley et al., 2003; Adelberger et al., 2005a;

Shapley et al., 2005; Erb et al., 2006c; Reddy et al., 2008).

Here, we introduce a spectroscopic and photometric sample of $z \sim 3$ LBGs. These data were photometrically preselected with the following standard LBG $U_n G\mathcal{R}$ flux and color cuts:

$$\mathcal{R} \leq 25.5, \quad G - \mathcal{R} \leq 1.2, \quad U_n - G \geq G - \mathcal{R} + 1 \tag{2.1}$$

where the U_n, G, and $\mathcal{R}$ passbands sample $\lambda_{\rm rest} \sim$ 900, 1200, and 1700 Å at $z \sim 3$, respectively. Object detection, color cuts, and photometry are discussed in Steidel et al. (2003). Multi-object optical spectroscopy was obtained using the Low Resolution Imaging Spectrometer (L RIS; Oke et al., 1995) on the Keck I 10m telescope. The majority of the data (93%) were taken with the blue arm of LRIS (LRIS-B; McCarthy et al., 1998; Steidel et al., 2004), and the remainder of the data were obtained with LRIS prior to its blue arm upgrade in September 2000. The LRIS-B data were collected using 300, 400, and 600 line mm^{-1} grisms, which resulted in spectral resolutions of $\lambda/\Delta\lambda = 1000$, 1200, and 2000, respectively. The 400 (600) line mm^{-1} grism was used for 55% (39%) of the observations, and the remaining $\sim$ 6% of the LRIS-B spectra were obtained with the 300 line mm^{-1} grism. LRIS-B rest-frame wavelength coverage extended from $\sim$ 900–1500 Å and a typical integration time was 3 $\times$ 1800 s. The data were reduced (flat-fielded, cosmic ray rejected, background subtracted, extracted, wavelength and flux calibrated, and transformed to the vacuum wavelength frame) using `IRAF` scripts. Details of the data collection and reduction of both the preselection and spectroscopic samples are presented in Steidel et al. (2003).

Approximately 3% of the spectroscopically-confirmed $z \sim 3$ LBGs were classified as either active galactic nuclei (AGN) or quasi-stellar objects (QSOs) on the basis of broad lines and high-ionization emission features, respectively (Reddy et al., 2008). These objects were excluded from the spectroscopic sample, as

were galaxies at redshifts $z \leq 2.7$. The final sample, spanning 13 photometric preselection fields totaling 1700 arcmin^2, includes 321 objects with an average redshift of $\langle z \rangle = 2.99 \pm 0.19$ (Table 2.1.1, Figure 2.1). We note that this sample is distinct from previous studies of $z \sim 3$ LBGs (e.g., Shapley et al., 2001, 2003) in that the majority of these objects have corresponding near- and mid-infrared photometry.

Near-infrared photometry in the J ($\lambda_c = 1.25$ μm) and K_s ($\lambda_c = 2.15$ μm) bands was obtained for a subset of the sample (8/13 fields) using the Wide Field Infrared Camera (Wilson et al., 2003) on the Palomar 5m telescope. 102/321 objects (32%) were detected in K_s imaging and an additional 69 objects fell on the K_s images and were not detected. We assigned K_s upper limits corresponding to 3σ image depths ($K_s \sim 22.2$ (Vega); Erb et al., 2006c) to these 69 galaxies. J band photometry was also obtained for 57/102 objects (56%) detected in the K_s sample. Details of the data collection and reduction of the near-infrared sample are presented in Shapley et al. (2005) and Erb et al. (2006c).

Mid-infrared imaging was obtained for 5/13 fields with IRAC on *Spitzer*. Observations at 3.6, 4.5, 5.8, and 8.0 μm were obtained for the GOODS-N (Dickinson et al., 2003; Giavalisco et al., 2004; Reddy et al., 2006a), Q1700 (Shapley et al., 2005), and Q1549, Q1623, and Q2343 (Erb et al. in preparation) fields, where 3σ IRAC detection limits ranged from 25.1–24.8 (AB). The mid-infrared data were reduced according to procedures described in Shapley et al. (2005). 112/321 objects (35%) have detections in at least one IRAC passband, and 34/321 objects (11%) have both K_s and IRAC detections.

Table 2.1. Spectroscopic Survey Fields

Field Name	α[a] (J2000.0)	δ[b] (J2000.0)	Field Size (arcmin^2)	N_{LBG}[c]
Q0100*	01 03 11	13 16 18	42.9	22
Q0142	01 45 17	–09 45 09	40.1	20
Q0449	04 52 14	–16 40 12	32.1	13
Q1009*	10 11 54	29 41 34	38.3	30
Q1217	12 19 31	49 40 50	35.3	13
GOODS-N[d]†	12 36 51	62 13 14	155.3	54
Q1307	13 07 45	29 12 51	258.7	8
Q1549*†	15 51 52	19 11 03	37.3	48
Q1623*†	16 25 45	26 47 23	290.0	24
Q1700*†	17 01 01	06 11 58	235.3	39
Q2206*	22 08 53	–19 44 10	40.5	23
Q2343*†	23 46 05	12 49 12	212.8	26
Q2346	23 48 23	00 27 15	280.3	1
TOTAL	**...**	**...**	**1698.9**	**321**

[a]Right ascension in hours, minutes, and seconds.

[b]Declination in degrees, arcminutes, and arcseconds.

[c]Number of spectroscopically-confirmed LBGs with redshifts $z \geq 2.7$, excluding QSOs and AGN.

[d]This field is also referred to as "HDF".

*Denotes a field with near-infrared imaging.

†Denotes a field with mid-infrared *Spitzer* IRAC imaging.

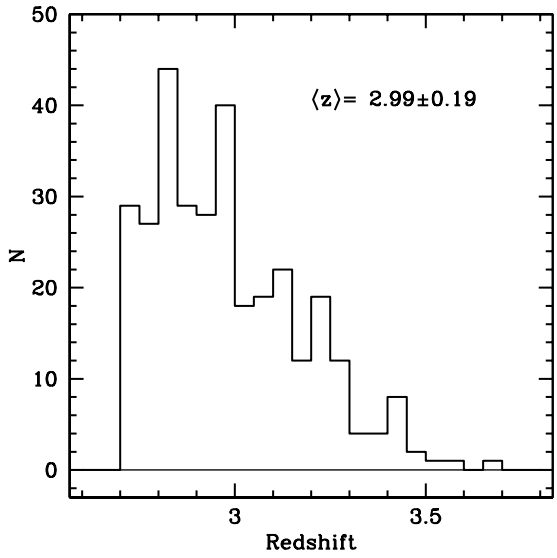

Figure 2.1 Redshift distribution of the sample, where $\langle z \rangle = 2.99 \pm 0.19$.

2.1.2 Galaxy Systemic Redshifts

In order to prepare the spectra for subsequent measurement and analysis, we transformed each spectrum into the stellar systemic frame where the galaxy's center of mass was at rest. To do so, we employed the procedure of Adelberger et al. (2003) to infer the galaxy's systemic redshift from measurements of its redshifts of both Lyα in emission and interstellar lines in absorption. For the spectra that clearly exhibited a double-peaked Lyα emission feature (12/321 objects), we adopted the convention of setting the Lyα emission redshift equal to the average redshift of the two emission peaks. This technique of inferring a zero-velocity center-of-mass redshift, as opposed to measuring it directly, was necessary due to the fact that stellar lines arising from OB stars (assumed to be at rest with respect to the galaxy) are too weak to measure in individual spectra at $z \sim 3$. Furthermore, a systemic redshift could not be measured from prominent LBG spectral signposts (e.g., Lyα or interstellar absorption lines) as these features

trace outflowing gas which is offset from the galaxy's center-of-mass frame by several hundred km s^{-1} (Shapley et al., 2003).

2.1.3 Lyα Equivalent Width

HI Lyα, typically the strongest feature in LBG spectra, is characterized by its equivalent width, $W_{\mathrm{Ly}\alpha}$, where we use a negative equivalent width to correspond to the feature in absorption. We present here a systematic method for estimating $W_{\mathrm{Ly}\alpha}$, taking into account the various Lyα spectroscopic morphologies that were observed in the sample. In particular, this method employs a more robust technique than used previously to determine the wavelength extent over which the Lyα feature should be integrated to extract a line flux.

We first binned the 321 systemic-frame spectra into one of four categories based on the morphology of Lyα: "emission", "absorption", "combination", and "noise". The spectra in the "emission" bin were clearly dominated by a Lyα emission feature, and a small subset of this sample exhibited two peaks in emission. The spectra in the "absorption" bin were dominated by a trough around Lyα, typically extending for tens of angstroms bluewards of line center. The spectra deemed to be "combination" contained a Lyα emission feature superimposed on a larger Lyα absorption trough and the "noise" spectra were generally featureless around Lyα, save for a possible absorption signature whose secure identification was hindered by low signal-to-noise. Four example spectra, characterized as falling into each of these four bins, are shown in Figure 2.2.

Each spectrum, regardless of its category classification, was fit with two average continuum levels, one bluewards (1120–1180 Å; c_{blue}) and one redwards (1225–1255 Å; c_{red}) of Lyα; these wavelength ranges were chosen to avoid the prominent Si III and Si II absorption features at 1206 and 1260 Å, respectively.

We worked with both the spectra and the adopted continua in f_λ units (erg s^{-1} cm^{-2} Å^{-1}). Below, we briefly describe the procedure for calculating $W_{\mathrm{Ly}\alpha}$ for each of the four morphological classification bins.

Emission: 189/321 objects (59%): The wavelength of the maximum flux value between 1213–1221 Å was calculated, as well as the wavelengths on either side of the maximum where the flux level intersected c_{red} and c_{blue}, respectively. These latter two wavelengths were adopted as the extremes of the emission feature. In a limited number of cases (12/188 objects), double-peaked spectra were individually examined to ensure that this methodology counted both peaks as contained within the Lyα feature. The `IRAF` routine `SPLOT` was next used to calculate the enclosed flux between the two wavelength bounds. The enclosed flux was then divided by the level of c_{red} to yield a measurement of $W_{\mathrm{Ly}\alpha}$ in Å. The level of c_{blue} was not used in the calculation of $W_{\mathrm{Ly}\alpha}$ due to its substantial diminution by the intergalactic medium (IGM).

Absorption: 50/321 objects (16%): The boundaries of the Lyα absorption feature were calculated in the same manner as those of the "emission" spectra described above, with the exception that the flux value between 1213 and 1221 Å was isolated as a minimum and the "absorption" spectra were initially smoothed with a boxcar function of width six pixels ($\sim$ 2.5 Å) in order to minimize the possibility of noise spikes affecting the derived wavelength boundaries of the Lyα feature. These smoothed spectra were only used to define the extent of the Lyα line; the original unsmoothed spectra were used for the flux integration in `IRAF` and the enclosed flux was divided by c_{red} to yield $W_{\mathrm{Ly}\alpha}$.

Combination: 31/321 objects (10%): Objects in the "combination" bin were characterized by a Lyα emission feature superposed on a larger absorption trough. The boundaries of the Lyα feature were computed by beginning at the base of the

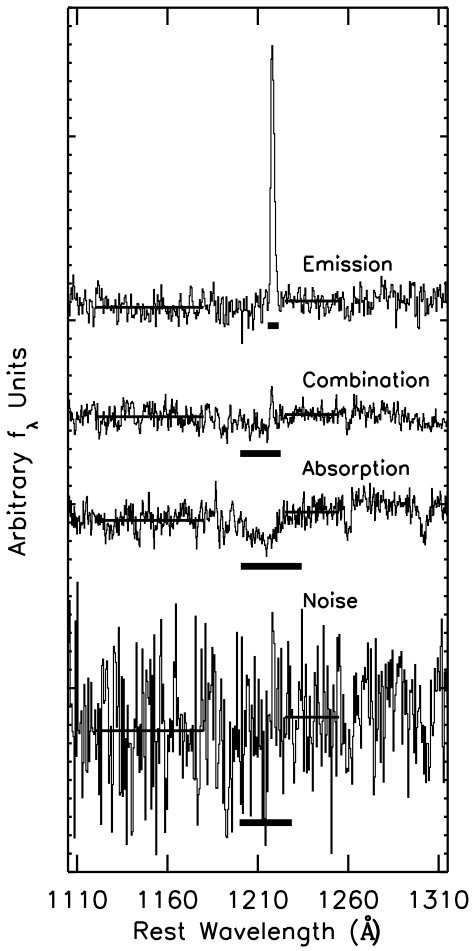

Figure 2.2 The Lyα feature varies widely in its morphology. Four spectra are plotted to show representative examples of objects classified in the "emission," "combination," "absorption," and "noise" bins, respectively. In order to systematically calculate Lyα equivalent width, we adopted red- and blue-side continua (horizontal lines from 1120–1180 Å and from 1225–1255 Å, respectively) and inferred the extent of the Lyα feature (thick line below each spectrum) using the methodology described in §2.1.3. Note that in the case of the "absorption" spectrum shown here, the extent of the Lyα feature appears to extend redwards of the adopted red-side continuum – this difference arises because the plotted spectrum is unsmoothed while a smoothed spectrum was employed to calculate the wavelength bounds of the Lyα feature.

Lyα emission peak and moving toward larger fluxes until the smoothed spectrum (see above) intersected c_{red} and c_{blue}, respectively (the same technique used for the "absorption" spectra). Flux integration and division by c_{red} were furthermore identical to those objects discussed above.

Noise: 51/321 objects (16%): For these spectra dominated by noise, we adopted set values for the endpoints of the Lyα feature based on the average boundary values of the absorption and combination spectra – 1199.9 and 1228.8 Å. (The boundaries of the "emission" spectra were not included in this calculation, as the spectral morphologies of the "emission" galaxies differed greatly from those of the "noise" galaxies). As above, the integrated flux was divided by the level of c_{red} to yield $W_{Ly\alpha}$.

Rest frame equivalent widths ranged from -40 Å $\lesssim W_{Ly\alpha} \lesssim 160$ Å, although one object (HDF–C41) had an equivalent width of ~ 740 Å; we attributed this outlier to a continuum level in the spectrum comparable with zero and omitted this object from further analysis. The median equivalent width of the sample was ~ 4 Å (Figure 2.3), consistent with values reported by Shapley et al. (2001, 2003) for $z \sim 3$ LBGs.

2.1.4 Composite Spectra

A composite spectrum offers the distinct advantage of higher signal-to-noise over individual observations. We accordingly constructed several composite spectra from our sample, using, in each case, the same basic steps discussed below.

The one-dimensional, flux-calibrated, rest-frame input spectra of interest were stacked (mean-combined) using the `IRAF scombine` routine. Each input spectrum was scaled to a common mode over the wavelength range 1250–1380 Å and a small number of positive and negative outliers ($< 10\%$ of the data) were rejected

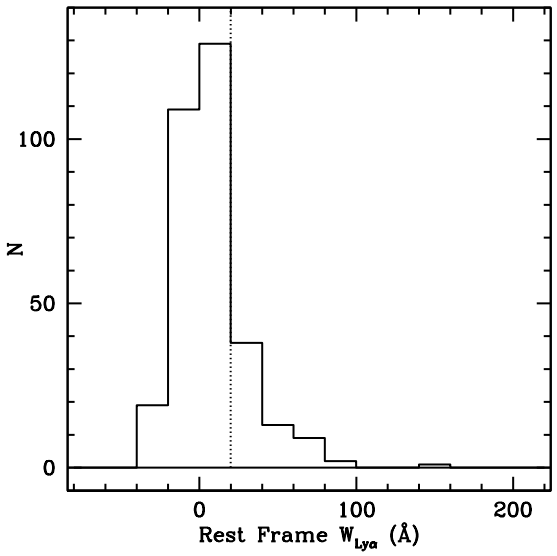

Figure 2.3 The distribution of Lyα rest-frame equivalent widths, where objects with $W_{\mathrm{Ly}\alpha} \geq 20$ Å (dashed line) were classified as LAEs. The median equivalent width of the sample is $\sim$ 4 Å, and an outlier at $\sim$ 740 Å (attributed to an uncertain continuum level) is not shown for visual clarity.

at each pixel position to prevent poor sky-subtraction or cosmic ray residuals from affecting the composite spectrum. The final composite spectrum was then rebinned to a dispersion of 1 Å pixel^{-1}. A composite spectrum[1] of the entire sample is shown in Figure 2.4, where several photospheric and low- and high-ionization interstellar features are visible in addition to Lyα.

2.2 Stellar Population Modeling

As the majority of the spectroscopic sample had extensive accompanying photometric wavelength coverage, we conducted population synthesis modeling to derive the key properties of age, extinction, star formation rate, and stellar mass. We required at least one photometric measurement redwards of the Balmer break ($\lambda_{\rm rest} = 3646$ Å) for robust population synthesis modeling. 248/320 objects satisfied this criterion of photometry in at least one near-infrared or IRAC passband, including 69 objects with K_s upper limits (and no IRAC data). We modeled galaxies using Bruzual & Charlot (2003a) SEDs (assuming a Salpeter (1955) initial mass function (IMF) over the mass range 0.1–125 $M_\odot$) and the Calzetti (2000) extinction law derived from local starbursts, where dust extinction, parameterized by E(B–V), was estimated from the latter. While the Calzetti et al. (2000) law appears valid on average for $z \sim 3$ LBGs, we discuss in §2.3.2 some caveats associated with adopting this law; we also present in that same section a brief discussion of our adoption of the Bruzual & Charlot (2003a) population synthesis models. We furthermore assumed a constant star formation history and

[1]This composite spectrum is meant to represent only the average of the objects in our sample, not the average of the entire $z \sim 3$ LBG population. There are a variety of observational biases that affect that relative proportions of Lyα-emitters and Lyα-absorbers selected: large Lyα emission lines contaminating the G band result in redder $U_n - G$ colors, scattering objects into the color section window (Equation 2.1), while Lyα absorption limits the dynamic range in continuum magnitude over which objects are selected. We refer the reader to Steidel et al. (2003) for a detailed discussion of these biases.

solar metallicity. Recent work has suggested that the Salpeter (1955) IMF has too steep a slope below 1 $M_{\odot}$ and consequently overpredicts the mass-to-light ratio and stellar mass by a factor ~ 2 (Bell et al., 2003; Renzini, 2006). We accordingly converted stellar masses and SFRs to the Chabrier (2003) IMF by dividing the model output values by 1.8. The modeling procedure is described in detail in Shapley et al. (2001); we briefly present a summary below.

Firstly, for the subset of the sample where Lyα fell in the G bandpass ($2.48 \lesssim z \lesssim 3.38$; 238/248 objects), we corrected the G band photometry to account for the discrepancy between the equivalent widths of the sample (-40 Å $\lesssim W_{\mathrm{Ly}\alpha} \lesssim 160$ Å) and those of the Bruzual & Charlot (2003a) model SEDs ($W_{\mathrm{Ly}\alpha} \sim -10$ Å). According to the formula in Papovich et al. (2001), we applied a correction in the cases where the incremental change in G magnitude, ΔG, was larger than the uncertainty on the original photometric measurement. This procedure affected 51/238 objects (21%), for which $\langle \Delta G \rangle_{\mathrm{median}} = 0.15$ magnitudes. We did not correct for possible contamination in the K_s band from nebular line emission ([OIII] $\lambda\lambda$5007,4959, Hβ λ4861), although we tested that our reported correlations (§2.3) were still robust when all objects at $z \geq 2.974$ (such that [OIII] λ5007, the strongest of these nebular lines, is shifted into the K_s band) were excluded from the analysis.

Next, for each galaxy modeled, a grid of SEDs was attenuated by dust and shifted to match the redshift of the galaxy. These redshifted SEDs were further attenuated by IGM absorption (Madau, 1995) and were multiplied by the $G, \mathcal{R}, J, K_s$, and four IRAC channel filter transmission curves to extract model colors. A model $U_n - G$ color was not calculated, as many of the objects had only upper limits in U_n due to the significant flux diminution in that passband from both galactic and intergalactic HI absorption. These predicted colors were then

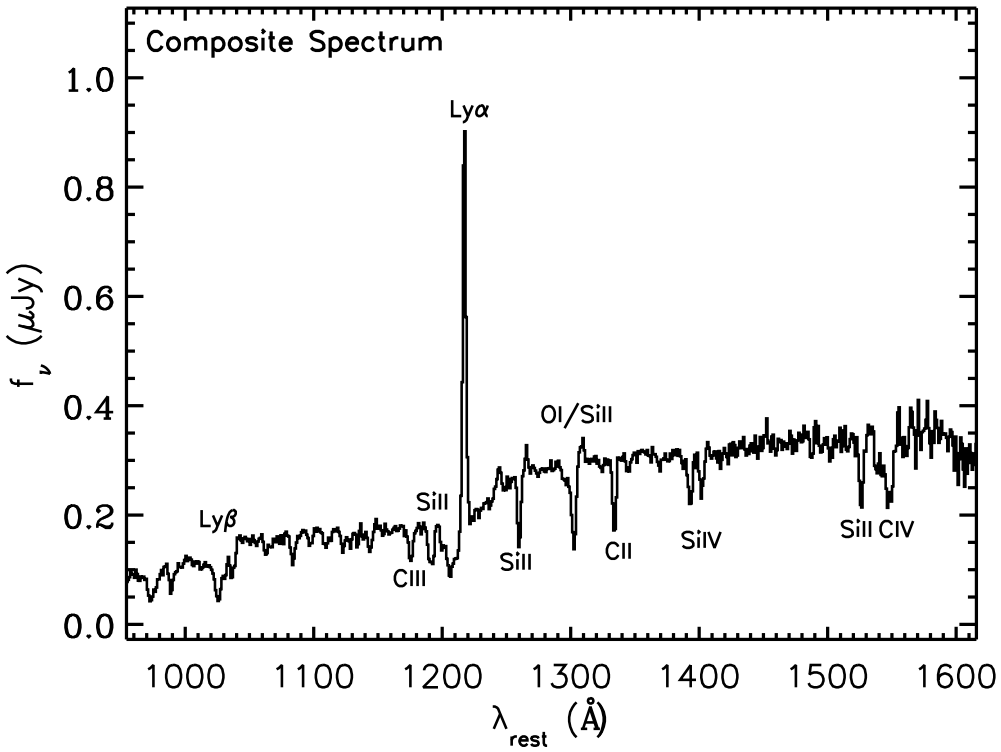

Figure 2.4 Composite rest-frame spectrum assembled from one-dimensional, flux-calibrated spectra (§2.1.4). Lyα appears in strong emission and Lyβ is prominent at 1026 Å. Photospheric features (e.g., CIII λ1176) and both low- (e.g., SiII $\lambda\lambda$1190,1193, SiII λ1260, OI+SiII λ1303, CII λ1334, and SiII λ1527) and high- (e.g., SiIV $\lambda\lambda$1393,1402 and CIV λ1549) ionization absorption lines are visible in this high signal-to-noise composite.

compared with the observed colors by means of the χ^2 statistic and a best-fit E(B–V) and age ($t_\star$) were extracted based on the lowest value of χ^2. We also applied the constraint that $t_\star$ had to be less than the age of the Universe at the redshift of each object. A best-fit dust-corrected SFR was inferred from the normalization of a galaxy forming stars at a rate of 1 $M_\odot$ yr^{-1}. Stellar mass, $m_{\rm star}$, was defined as the integral of the SFR and the age of the galaxy. We did not correct stellar masses for interstellar medium (ISM) recycling, whereby a mass fraction of stellar material is returned to the ISM via winds and supernovae (Cole et al., 2000). Given that we are concerned with the relative stellar populations of objects modeled in an identical fashion, the constant mass factor introduced by assuming ISM recycling is unimportant.

Best-fit SFR, stellar mass, E(B–V), and age values were extracted for the 179 galaxies without photometric upper limits. The additional 69 galaxies undetected in K_s imaging were modeled by adopting 3σ upper limits in $\mathcal{R}$ – K_s color as photometric data points. We tested that an upper limit in $\mathcal{R} - K_s$ color was a robust proxy for an upper limit in both age and stellar mass by perturbing the $\mathcal{R} - K_s$ colors in several increments, both redwards and blue wards, and remodeling the perturbed SEDs (holding all other colors constant). The expected trend that a redder galaxy would be best fit with an older age and a larger stellar mass was borne out for the entire sample. We additionally found that E(B–V) and SFR were generally insensitive to perturbations in $\mathcal{R} - K_s$ color. Therefore, given a galaxy with an upper limit in $\mathcal{R}$ – K_s color, its model age and stellar mass were adopted as upper limits and its model E(B–V) and SFR were assumed to be best-fit values.

Considering the entire sample of 248 objects, we found median best-fit SFR, stellar mass, E(B–V), and age values of 37 $M_\odot$ yr^{-1}, 7.2 $\times$ 10^9 $M_\odot$, 0.170, and 320

Myr, respectively. When objects with K_s upper limits (and corresponding upper limits in stellar age and mass) were removed from the analysis, the medians were 51 $M_\odot$ yr^{-1}, 8.3 $\times$ 10^9 $M_\odot$, 0.180, and 320 Myr, respectively. A dust attenuation described by E(B–V) = 0.170 corresponds to $A_V \sim 0.7$ magnitudes, using the Calzetti et al. (2000) starburst attenuation law with $R'_V = 4.05$. Histograms of the best-fit values are shown in Figure 2.5.

For each galaxy, confidence intervals of the best-fit stellar parameters were estimated with Monte Carlo simulations. First, each object's photometry was perturbed by an amount drawn from a Gaussian distribution described by the photometric error. Then, the galaxy was remodeled with these new "observed" colors, and this process was repeated 1000 times. These simulations resulted in estimates of the distributions of best-fit stellar parameters allowed by the uncertainties in the photometry. In some instances, these confidence intervals were not centered on the best-fit stellar population parameters derived from fitting the photometry. In all cases, we proceeded to adopt the best-fit values as representative of each galaxy's properties, and we furthermore assumed that the error on each parameter was described by the standard deviation of that parameter's confidence interval. We used the quantity $\sigma_x/\langle x \rangle$ to express the ratio of the standard deviation of each parameter's confidence interval, σ_x, to the mean of that parameter's confidence interval, $\langle x \rangle$. On average, using 3σ rejection to suppress the effect of outliers, we found that the median values of $\sigma_x/\langle x \rangle$ for each of the four best-fit stellar population parameters (E(B–V), age, SFR, and stellar mass) were $\sim$ 0.4, 1.0, 0.8, and 0.6, respectively.

2.3 Stellar Populations & Lyα Line Strength

With Lyα equivalent widths and best-fit stellar population parameters in hand, we now turn to examining the relationship between Lyα emission and stellar populations in LBGs. The aim of this analysis is to investigate the physical nature of $z \sim 3$ LBGs by studying how objects with and without strong Lyα emission differ in the fundamental parameters of age, stellar mass, extinction, and star formation rate. Our full complement of data are used in this analysis, including rest-frame UV spectroscopy, broadband photometry, and best-fit stellar population parameters and SEDs. We also make comparisons between our LBG data and narrowband-selected LAEs from Nilsson et al. (2007) and Gawiser et al. (2007), although we caution that the relationship between LBGs and narrowband-selected LAEs is a field of extragalactic research unto itself; we refer the reader to §2.4.1 for a summary of the salient points of this topic.

2.3.1 Statistical Tests

We employed several statistical methods central to our investigation, including survival analysis techniques that were capable of analyzing data with limits ("censored data"). It was important to include limits in the statistical analysis as a non-negligible fraction of the sample (28%) was undetected in K_s imaging. We used ASURV ("*A*stronomy *SURV*ival *A*nalysis") Rev 1.2 (Isobe & Feigelson, 1990; Lavalley et al., 1992), which implements the methods presented in Feigelson & Nelson (1985) and Isobe et al. (1986). The bivariate correlation tests Kendall τ and Spearman ρ were utilized, where, for each test, the degree of correlation is expressed in two variables: $\tau_{\rm K}$ ($r_{\rm SR}$) and $P_{\rm K}$ ($P_{\rm SR}$). The first variable represents the test statistic and the second variable represents the probability of a null hypothesis (i.e., the probability that the data are uncorrelated). We

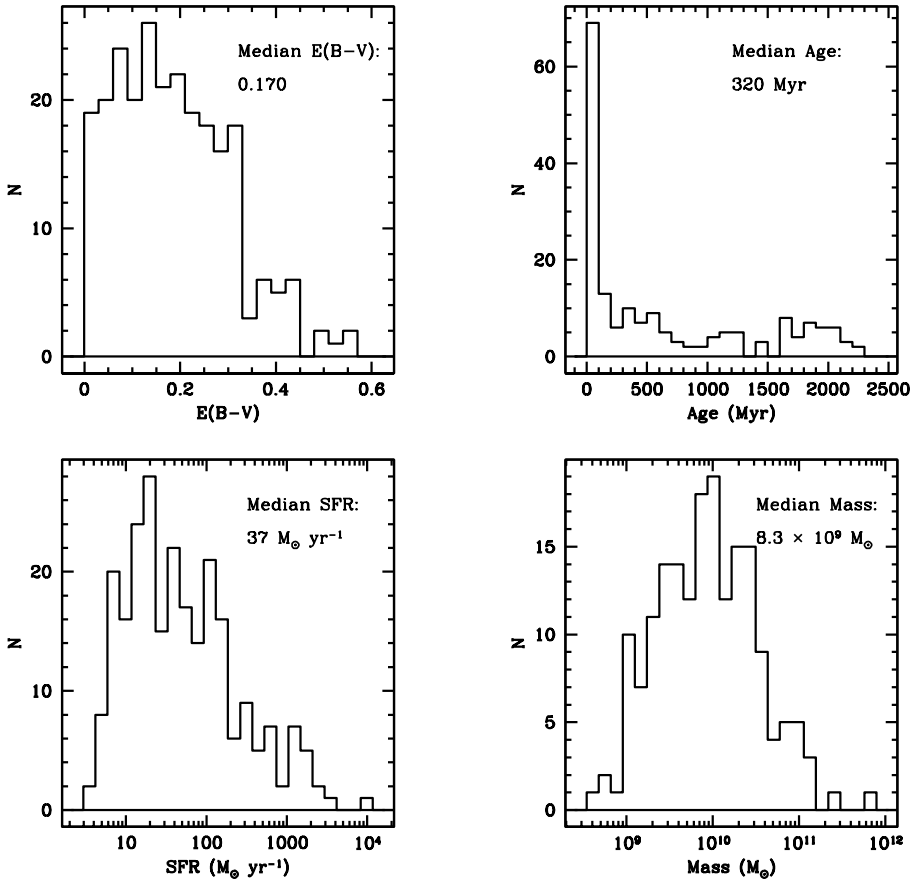

Figure 2.5 Histograms of best-fit stellar population parameters, with median values indicated. K_s-undetected galaxies were omitted when making the age and stellar mass distributions, as these parameters represent upper limits in the presence of a K_s non-detection. Dust attenuations span the range E(B–V) = 0.0–0.6, where the median extinction level corresponds to A_{1600} (A_V) $\sim$ 1.7 (0.7) magnitudes. While LBGs are fit with a variety of ages, note the large number of objects in the youngest age bin, $t_\star < 100$ Myr. The SFRs of LBGs fall between those of quiescent, Milky Way-type galaxies (SFR $\sim 4\ M_\odot\ \mathrm{yr}^{-1}$; e.g., Diehl et al., 2006) and vigorously star-forming submillimeter galaxies (SFR $\sim 1000\ M_\odot\ \mathrm{yr}^{-1}$; e.g., Chapman et al., 2005). Stellar masses range from $\sim 10^9$ to $10^{11}\ M_\odot$, where the highest mass object, $6 \times 10^{11}\ M_\odot$, is extremely red ($\mathcal{R} - K_s = 4.48$).

also used routines from Numerical Recipes (Press et al., 1992), specifically the Kolmogorov-Smirnov (K–S) test between two data sets (`kstwo`), the Spearman's rank correlation (`spear`), and the Kendall's τ correlation (`kendl1`). The K–S test produces two outputs: D and P, where the former is the test statistic and the latter is the probability that the two samples are drawn from the same underlying population. `spear` and `kendl1` are duplicates of the Spearman ρ and Kendall τ tests available in ASURV; we employed the ASURV routines when it was necessary to include data with limits.

2.3.2 Equivalent Width Versus Stellar Parameters

Firstly, we investigated the correlation between Lyα equivalent width and extinction, age, star formation rate, and stellar mass, respectively, using the Spearman ρ and Kendall τ bivariate correlation tests. For this analysis, we used the entire sample with population modeling, including galaxies with upper limits in the K_s passband (248 objects). We note that while the correlations shown in Figure 2.6 are not without scatter, we have employed a variety of quantitative statistical analyses that have yielded a consistent picture of how stellar populations are correlated with Lyα emission in $z \sim 3$ LBGs. Below, we introduce these results.

E(B–V), age, and SFR all exhibited very strong correlations with $W_{\mathrm{Ly}\alpha}$ ($P_{\mathrm{SR}} \leq 0.0002$ in each case)[2], whereas stellar mass was uncorrelated ($P_{\mathrm{SR}} = 0.8630$). These results did not change when the 69 galaxies with K_s upper limits (and corresponding upper limits in mass and age) were excluded from the analysis (Table 2.3.2). In order to test the robustness of these results while taking into account the uncertainty on the best-fit parameters, we used the bootstrapping method. We created 100 bootstrap samples by randomly extracting one line from

[2]We note, however, that SFR and E(B–V) are not independent; the probability that these two parameters are uncorrelated is $P_{\mathrm{SR}} = 0.0000$.

each object's 1000-entry confidence interval of stellar parameters (generated by perturbing the initial photometry according to its errors and then re-modeling the galaxy; §2.2) and then re-ran the Spearman ρ test on each of these 100 artificial samples. A null hypothesis was consistently ruled out at between the 3 and 5σ levels for the SFR and E(B–V) bootstrap samples and at the 3σ level for the age sample. In the case of the stellar mass sample, where the null hypothesis was ruled out at only the 1σ level, the data do not support a correlation between $W_{\mathrm{Ly}\alpha}$ and stellar mass. These bootstrap samples show that even when accounting for the uncertainty in best-fit parameters, a strong correlation exists between equivalent width and age, E(B–V), and SFR, respectively, such that objects with strong Lyα emission tend to be older, less dusty, and lower in star formation rate (more quiescent) than objects with weak or no Lyα emission.

As an independent test of the above results, we next used the rest-frame UV spectra to investigate how the morphology of the Lyα feature was, qualitatively, correlated with best-fit stellar population parameters. For this analysis, we limited our study to objects satisfying two criteria: *1)* population synthesis modeling had been completed and *2)* K_s photometry consisted of detections, not upper limits[3]. Together, these criteria isolated 179 objects. For each stellar population parameter, we divided the objects into three groups ("tertiles") based on their best-fit value. A composite rest-frame UV spectrum was then constructed from each tertile according to the methodology presented in §2.1.4, for a total of 12 composite spectra (3 tertiles $\times$ 4 parameters; Figure 2.7). A strong correlation of equivalent width with age, E(B–V), and SFR was observed, such that stronger Lyα emission was more prevalent in older, less dusty, and more quiescent galaxies. At the same time, the strength of low-ionization interstellar absorption lines

[3]Objects with K_s upper limits were excluded due to their corresponding upper limits in best-fit ages and masses; such limits led to uncertainty as to the age and mass bin in which these objects should be grouped.

Table 2.2. Correlation Coefficients

Parameter	Parameter	Kendall τ $\tau_{\rm K}{}^{\rm a}(P_{\rm K})^{\rm b}$	Spearman ρ $r_{\rm SR}{}^{\rm a}(P_{\rm SR})^{\rm b}$
Entire Sample (248 objects)			
$W_{\rm Ly\alpha}$	E(B–V)	6.585 (0.0000)	–0.413 (0.0000)
.....	Age	3.655 (0.0003)	0.238 (0.0002)
.....	SFR	6.515 (0.0000)	–0.410 (0.0000)
.....	Stellar Mass	0.358 (0.7205)	0.011 (0.8630)
Omitting K_s non-detections (179 objects)			
$W_{\rm Ly\alpha}$	E(B–V)	5.163 (0.0000)	–0.385 (0.0000)
.....	Age	4.122 (0.0000)	0.319 (0.0000)
.....	SFR	5.299 (0.0000)	–0.394 (0.0000)
.....	Stellar Mass	0.917 (0.3592)	0.068 (0.3641)

[a]Test statistic.

[b]Probability of a null hypothesis (i.e., the probability that a correlation is not present).

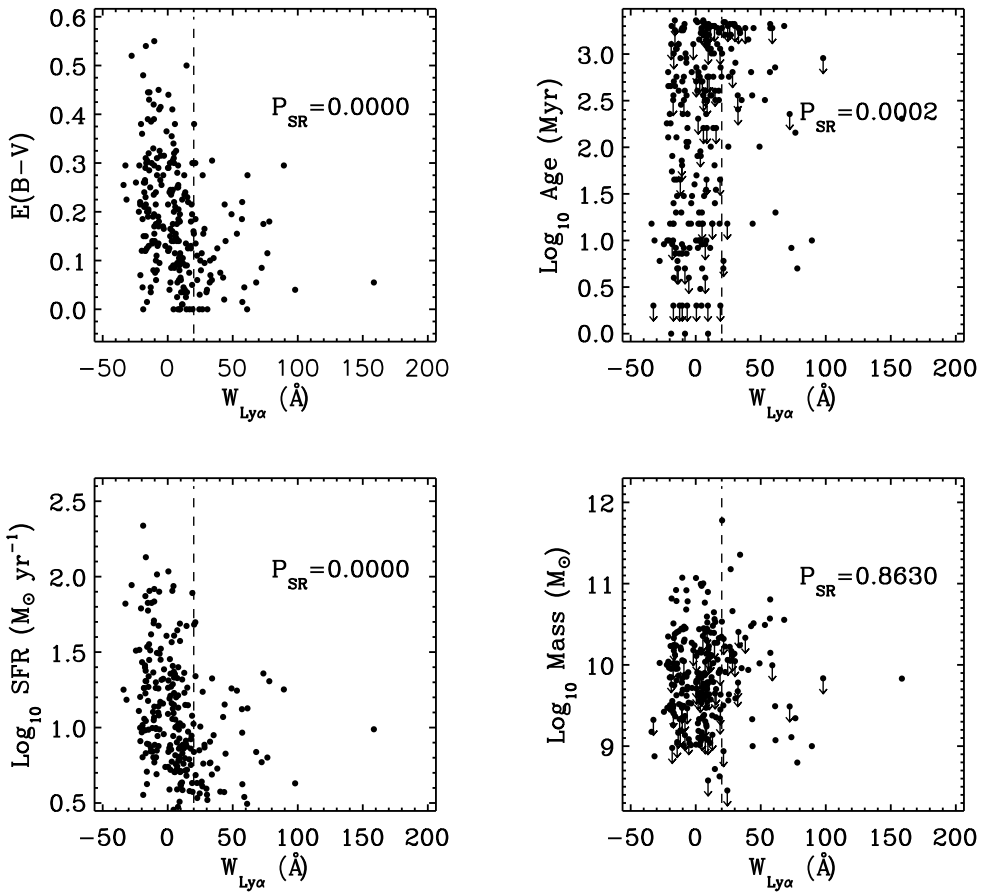

Figure 2.6 Plots indicating the correlation between $W_{\mathrm{Ly}\alpha}$ and each of the four best-fit stellar population parameters. Upper limits in age and mass are indicated by downward-facing arrows and the vertical dashed line in each panel delineates $W_{\mathrm{Ly}\alpha} = 20$ Å, the adopted lower bound in Lyα equivalent width for LAEs. The probability of a null hypothesis (i.e., no correlation) from the Spearman ρ test is shown in each plot. Note the significant correlation between equivalent width and E(B–V), age, and SFR, respectively, in the sense that galaxies with strong Lyα emission also tend to be less dusty, older, and more quiescently forming stars. $W_{\mathrm{Ly}\alpha}$ and stellar mass are not significantly correlated, as evidenced by the high probability of the null hypothesis.

decreased with increasing Lyα emission strength (Shapley et al., 2003). We note that these trends were still present when the spectra were median-combined to make to the composites (as opposed to mean-combined).

Next, we reversed the independent and dependent variables from the previous investigation and, this time, divided the sample into tertiles according to Lyα equivalent width. The mean equivalent widths of each tertile were –15.5, 2.8, and 33.1 Å, respectively. We then calculated the average stellar parameters of each tertile, in addition to the error on the mean (Figure 2.8). Consistent with the results of the bivariate correlation tests and the composite spectra divided by stellar population parameters discussed above, we found that as the average equivalent width varied from -15.5 Å to 33.1 Å, $\langle t_\star \rangle$ increased from 440 Myr to 850 Myr, $\langle$E(B–V)$\rangle$ decreased from 0.24 to 0.14, and $\langle$SFR$\rangle$ decreased from 300 $M_\odot$ yr^{-1} to 70 $M_\odot$ yr^{-1}. A weak positive correlation between best-fit stellar mass and equivalent width was observed, although, given the errors on the average masses, we chose to adopt the stance that stellar mass was generally insensitive to changes in equivalent width.

From the three aforementioned investigations, a consistent picture has emerged: strong Lyα emission is associated with galaxies that are older, less dusty, and more quiescent than their counterparts with weaker Lyα emission or the line in absorption. We note that the trend of increasing Lyα strength with decreasing E(B–V) is a well-known result (e.g., Shapley et al., 2003; Reddy et al., 2006b; Pentericci et al., 2007). Deharveng et al. (2008), however, found no apparent correlation between Lyα equivalent width and UV color in a sample of 96 LAEs at $z \sim 0.3$, although we caution that the transformation from UV color to E(B–V) is sensitive to the geometry of the emitting stars and absorbing dust and may therefore not be constant for a heterogeneous population such as LAEs (e.g.,

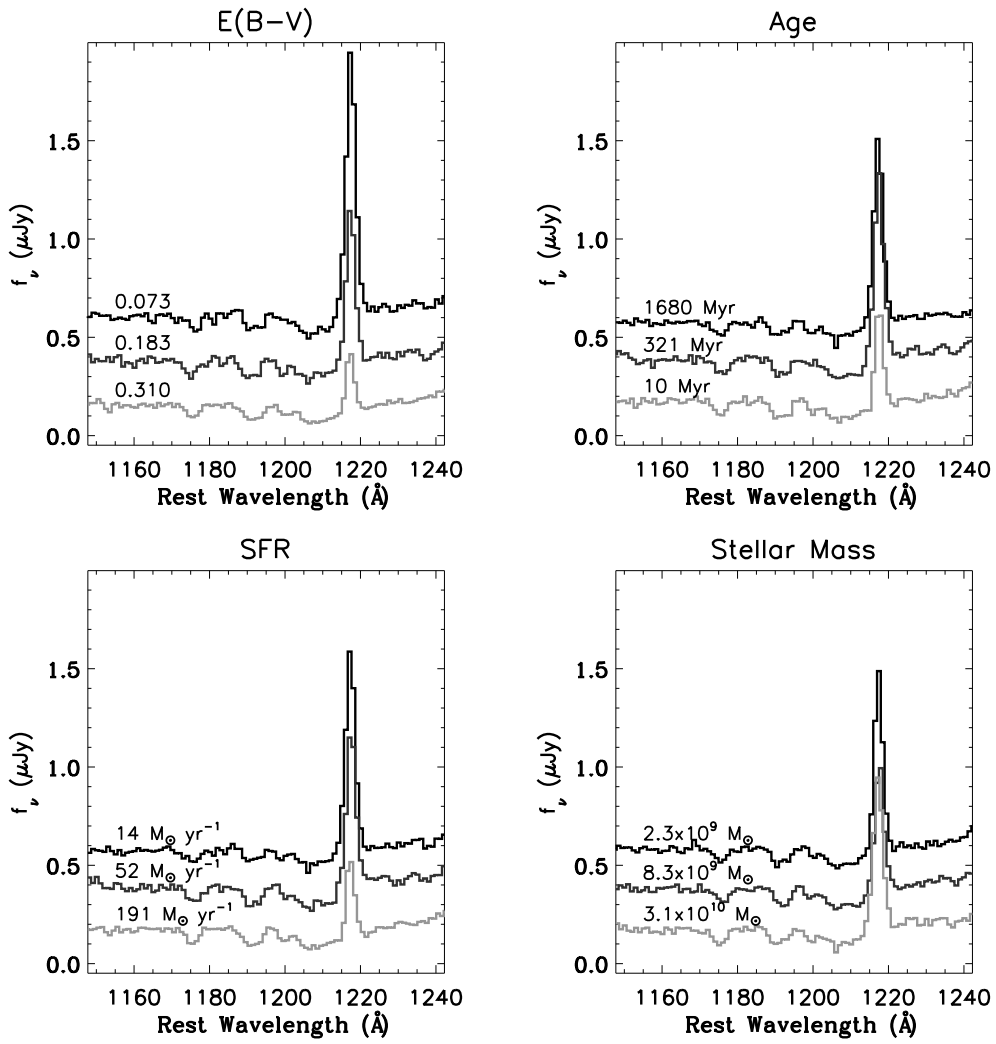

Figure 2.7 Composite spectra assembled from objects ordered by E(B–V), age, SFR, and stellar mass, respectively, where objects with K_s upper limits were omitted. The medium and dark gray spectra are offset by +0.2 and +0.4 μJy, respectively, from the light gray spectrum and the median value in each tertile is printed next to its composite. Notice how strong Lyα emission is associated with older, less dusty, and more quiescent galaxies. There does not appear to be a significant correlation between Lyα emission strength and best-fit stellar mass.

Witt & Gordon, 2000; Granato et al., 2000). The relationship between age and $W_{\mathrm{Ly}\alpha}$ observed in our data – older objects exhibiting stronger Lyα emission than younger objects – is in agreement with the results of Shapley et al. (2003). The inverse correlation between dust-corrected SFR and $W_{\mathrm{Ly}\alpha}$ that we observe has been noted by several authors as well (e.g., Ando et al., 2004; Reddy et al., 2006b; Tapken et al., 2007), although Nilsson et al. (2007) report a $\sim 2\sigma$ direct correlation between SFR and $W_{\mathrm{Ly}\alpha}$ in a sample of 24 LAEs at $z \sim 3.15$. In contrast with the results presented here, however, Erb et al. (2006a) reported a correlation between stellar mass and Lyα strength in a sample of 87 star-forming galaxies at $z \sim 2$. These authors found that composite spectra constructed from the 30 least massive galaxies ($\langle M \rangle = 5 \times 10^9\ M_\odot$) and the 28 most massive galaxies ($\langle M \rangle = 7 \times 10^{10}\ M_\odot$) in their sample differed widely in nebular line strength, with the former sample exhibiting a pronounced Lyα emission feature and the latter sample showing a smaller Lyα feature superimposed on a larger absorption trough. Erb et al. (2006a) attributed these results to the lower velocity dispersion of the interstellar medium in the less massive galaxies, where, following the arguments of Mas-Hesse et al. (2003), velocity dispersion and Lyα escape fraction are anti-correlated. We therefore conclude here that the observed correlations we find between $W_{\mathrm{Ly}\alpha}$ and E(B–V), SFR, and age are supported by the work of others, whereas the lack of correlation between stellar mass and $W_{\mathrm{Ly}\alpha}$ may either be a tenable result (and evidence of LBG evolution during the 1.1 Gyr intervening $z = 2$ and $z = 3$) or otherwise an indication that further studies of the relationship between $W_{\mathrm{Ly}\alpha}$ and stellar mass at $z \sim 3$ are necessary.

The correlations discussed above were derived assuming the Calzetti et al. (2000) dust attenuation law. While this relation has routinely been applied to samples of high-redshift galaxies (e.g., Erb et al., 2006c; Gawiser et al., 2006; Gronwall et al., 2007), recent work by Reddy et al. (2006b), based on *Spitzer*

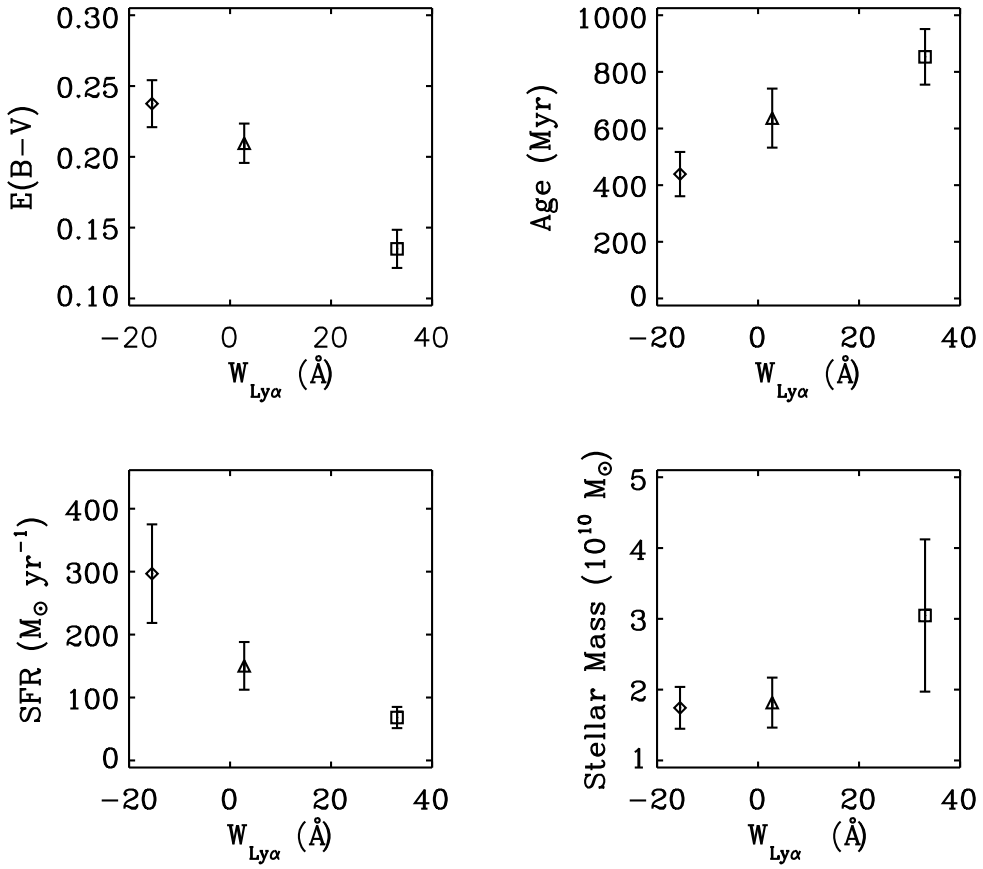

Figure 2.8 Best-fit stellar population parameters versus rest-frame Lyα equivalent width. Omitting galaxies with K_s upper limits, the remaining 179 objects with stellar population modeling were ordered by equivalent width and divided into three groups. The average stellar population parameters of each group were extracted, along with the error on the mean ($\sigma/\sqrt{n}$, where n was the number of objects in each group). With increasing Lyα strength, galaxies are, on average, older, less dusty, and more quiescent. A weak trend of increasing stellar mass with increasing Lyα strength is observed, although this is likely not a significant correlation.

MIPS observations, has suggested that dust extinction in young ($t_\star \leq 100$ Myr), UV-selected galaxies at $z \sim 2$ is often overestimated by modeling a given rest-frame UV color with the Calzetti et al. (2000) attenuation law. At $z \sim 3$, there have been no corresponding statistical studies, but Siana et al. (2008, 2009) have presented preliminary evidence for a similar trend based on two strongly lensed objects. On the other hand, for a single unlensed LBG at $z \sim 2.8$, Chapman & Casey (2009) find good agreement between the dust extinction inferred from the Calzetti et al. (2000) law and that estimated from the ratio of SCUBA 850 μm and rest-frame UV fluxes. Based on their findings, Reddy et al. (2006b) and Siana et al. (2008) accordingly proposed that a steeper, SMC-like extinction relation (e.g., Prévot et al., 1984) may be more appropriate for young objects.

With these results in mind, we assessed the uncertainties inherent in the choice of attenuation law. Limiting our analysis to the 179 objects without K_s upper limits, we re-modeled the 70 galaxies with $t_\star \leq 100$ Myr with a SMC-like extinction law (and retained the original fits assuming the Calzetti et al. (2000) law for the remaining 109 objects). In this mixed sample with some objects modeled with a SMC-like law and others modeled with the Calzetti et al. (2000) relation, we found no significant correlations between $W_{\rm Ly\alpha}$ and stellar populations. We also investigated the effect of re-modeling all 179 galaxies, regardless of age, with a SMC-like attenuation law. In this case, we observed correlations between $W_{\rm Ly\alpha}$ and E(B–V) and between $W_{\rm Ly\alpha}$ and SFR. Given the uncertainties in adopting the SMC law for part or all of our sample, another approach consists of restricting our analysis to objects for which the validity of the Calzetti et al. (2000) law has not been questioned. When we omitted objects younger than $t_\star = 100$ Myr from our original analysis assuming the Calzetti et al. (2000) dust attenuation law, the trends between $W_{\rm Ly\alpha}$ and E(B–V), age, and SFR, respectively, were still present (but only at a 2σ level of significance).

Given the lack of systematic studies of the dust attenuation law in $z \sim 3$ objects, and the uncertainty regarding the age at which a galaxy may transition from being fit with a SMC-like law to the Calzetti et al. (2000) law, we choose to present all analysis on results derived from assuming the Calzetti et al. (2000) attenuation law. We acknowledge that the choice of an extinction law is a systematic uncertainty in our analysis, yet the persistence of trends between Lyα and stellar populations in the sample limited to objects with $t_\star \geq 100$ Myr supports the analysis with the Calzetti law applied to the full sample.

We now turn to discussing our adoption of the Bruzual & Charlot (2003a) population synthesis models. While other models more fully take into account the Thermally-Pulsing Asymptotic Giant Branch (TP-AGB) stellar phase (e.g., Maraston, 2005), a study of young star-forming "BzK" galaxies at $z \sim 2$ by Daddi et al. (2007) found that the Maraston (2005) and Bruzual & Charlot (2003a) models yielded consistent M/L ratios; the LBGs in our sample are as least as dominated by the young stellar component as the Daddi et al. (2007) BzK objects. Furthermore, a significant fraction ($\sim 40\%$) of our sample does not have IRAC coverage, and therefore our SED fitting only includes photometry out to the rest-frame V band (observed K_s band) where the effects of TP-AGB stars on the derived parameters are less pronounced. Additionally, and perhaps most importantly, we are concerned with trends in the data (rather than specific stellar population values). It is these trends that are preserved regard less of model choice; Lai et al. (2008) find that even though the Maraston (2005) models yield lower stellar masses and younger ages than Bruzual & Charlot (2003a) models for two samples of objects, the distinction between the two samples is significant irrespective of which population synthesis model is adopted. Finally, we note that our population synthesis results are supported by empirical color differences (§2.3.4). In this sense, the choice of synthesis code is rendered less important –

there are clearly intrinsic differences between objects.

In the next section, we divide the LBGs into two groups according to Lyα strength and compare the stellar populations of these subgroups in order to more generally comment on the differences between objects with and without strong Lyα emission.

2.3.3 The Distinct Properties of Strong Lyα Emitters in the LBG Sample

From the perspective of examining Lyα emission, the simplest division of our data is according to Lyα equivalent width. We turn here to comparing the properties of objects with strong ($W_{\mathrm{Ly}\alpha} \geq 20$ Å) Lyα emission and with weak Lyα emission, or the line in absorption ($W_{\mathrm{Ly}\alpha} < 20$ Å). Given our large sample size, these two groups each have sufficient membership to ensure robust statistics even when we restrict our analysis to only those objects with both stellar population modeling and no K_s upper limits (34 and 145 objects, respectively). We call these two groups LAEs and non-LAEs, respectively, where we differentiate these objects from LAEs isolated with narrowband filters by explicitly referring to the latter as narrowband-selected objects. The motivation for choosing 20 Å as the delineating equivalent width stems from the adoption of this value as a typical limit in narrowband LAE studies (e.g., Gawiser et al., 2007; Nilsson et al., 2009b; Pentericci et al., 2009). In order to investigate how stellar populations vary between LAEs and non-LAEs, we examined the age, E(B–V), stellar mass, and SFR distributions of both samples (Figure 2.9). We discuss below the striking differences between the properties of UV continuum-bright LAEs and non-LAEs.

There is a remarkable dissimilarity between the age histograms of LAEs and non-LAEs: LAEs are generally fit with older best-fit ages than non-LAEs: LAEs

have a median age more than four times that of the non-LAEs (763 Myr versus 181 Myr). LAEs furthermore lack the conspicuous overdensity of young objects ($t_\star < 100$ Myr) that characterizes the non-LAE sample. The disparity in ages between LAEs and non-LAEs is reflected in the K–S test probability of $\sim 2\%$ that the two age samples are drawn from the same underlying population.

The distributions of dust attenuations for the LAE and non-LAE samples differ significantly, with a median E(B–V) of 0.13 for the LAEs and 0.20 for the non-LAEs. While both populations have roughly the same distribution of E(B–V) values below 0.30, the non-LAE distribution is characterized by a tail of high extinction values. No LAEs have E(B–V) > 0.40, whereas 12/145 (8%) of non-LAEs do. The K–S test probability that the LAE and non-LAE extinction distributions derive from the same parent population is $\sim 2\%$.

The star formation rates of LAEs and non-LAEs are markedly different, as the LAEs have a median rate of 25 $M_\odot$ yr^{-1} and the non-LAEs are characterized by a median rate of 59 $M_\odot$ yr^{-1}. The relative quiescence of strong Lyα-emitters is in contrast to the high SFR tail observed in non-LAEs, where star formation rates in excess of 500 $M_\odot$ yr^{-1} are recorded for 22 objects[4]. There is a $\sim 1\%$ probability of these LAE and non-LAE star formation rate distributions are drawn from the same underlying population.

Unlike age, E(B–V), and SFR, the stellar mass distributions of LAEs and non-LAEs are not strongly dissimilar. The median value of the LAEs (1.1×10^{10} $M_\odot$) is only 40% larger than that of the non-LAEs (7.9×10^9 $M_\odot$) and a K–S test predicts that the two distributions have a $\sim 27\%$ chance of being drawn from the same parent distribution.

[4]15/22 of these objects, however, are younger than 10 Myr. While these objects have unphysically young ages (given that the dynamical timescale of LBGs is ≥ 10 Myr; Giavalisco et al., 1996; Pettini et al., 1998, 2001), re-modeling these galaxies with the constraint that $t_\star \geq 10$ Myr still results in best-fit star formation rates of several hundred $M_\odot$ yr^{-1}.

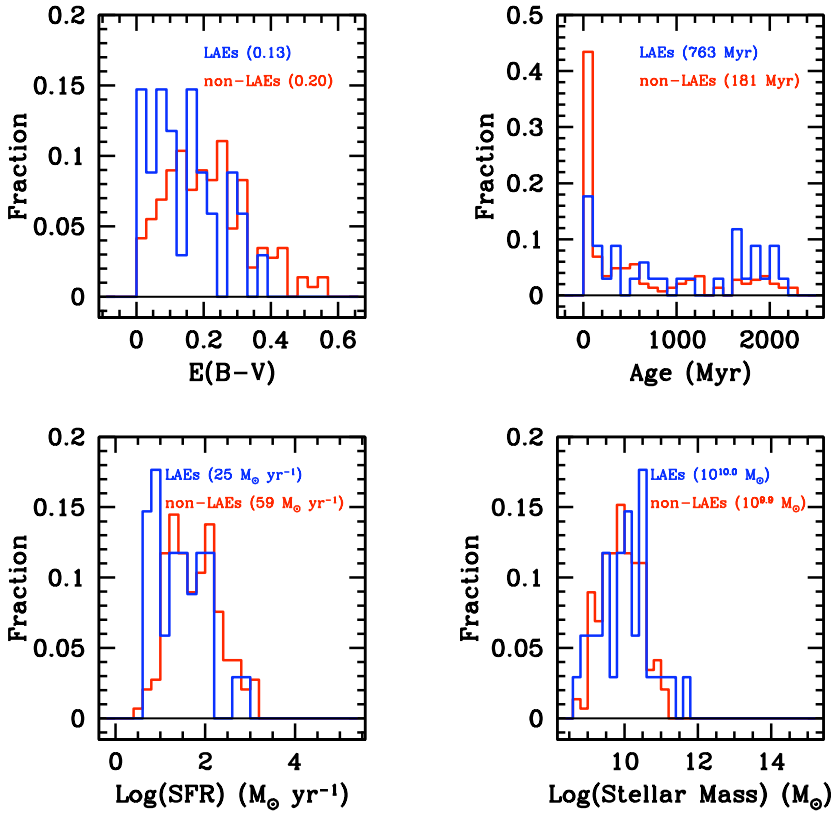

Figure 2.9 Histograms of best-fit dust attenuations, ages, star formation rates, and stellar masses for the 34 LAEs (blue line) and 145 non-LAEs (red line), non-inclusive of objects with K_s upper limits. The ordinate is the fractional percentage of the sample and the median value of each sample is indicated. The LAE sample is characterized by lower dust attenuation levels than the non-LAE sample; all objects with E(B-V) ≥ 0.40 are non-LAEs. The median age (763 Myr) of LAEs is significantly older than that of the non-LAEs (181 Myr). Furthermore, the LAEs lack the conspicuous overdensity of objects in the youngest ($t_\star < 100$ Myr) age bin that characterizes the non-LAE distribution. While the fraction of LAEs and non-LAEs with star formation rates between $\sim$ 80–120 $M_\odot$ yr^{-1} is roughly the same, LAEs show a larger fraction of objects with small SFRs and non-LAEs exhibit a tail of high star formation rate objects. LAEs are marginally more massive than non-LAEs, on average, although the distributions are similar.

Table 2.3. Average Photometry

Sample ($\langle z \rangle$)	$\langle \mathcal{R} \rangle$ (σ)	$\langle G \rangle^{a}$(σ)	$\langle G_{\rm IGM\ corr.} \rangle$ (σ)	$\langle K_s \rangle^{b}$
LAEs (2.99)	24.31 (0.02)	24.85 (0.03)	24.67 (0.03)	21.24
non-LAEs (2.97)	24.34 (0.01)	24.99 (0.01)	24.81 (0.01)	21.36

*Galaxies with K_s upper limits were omitted from this analysis, as were objects lacking stellar population modeling.

[a]G magnitudes have been corrected to account for contributions from Lyα.

[b]Photometry calculated from best-fit SED, for objects lacking K_s imaging.

*

We have shown that three of the best-fit stellar population parameters – age, E(B–V), and SFR – have markedly different distributions in the LAE and non-LAE samples. LAEs are typically older, less dusty, and less vigorously forming stars than non-LAEs. We tested the robustness of these results by constructing bootstrap samples from the confidence intervals of best-fit stellar parameters (§2.3.2). The mean and the error on the mean ($\sigma/\sqrt{n}$, where n is the sample size) were calculated for each best-fit stellar population parameter in the LAE and non-LAE samples. This process was repeated for 100 bootstrap samples. For E(B–V), age, and SFR, we found that the means of the LAE and non-LAE samples were consistently offset by at least their errors. In terms of stellar mass, the LAEs samples had consistently larger values; we note, however, that the

masses of the LAE and non-LAE samples were comparable within their errors. These results, in agreement with the histograms discussed above, support the observed correlation that galaxies with strong Lyα emission tend to be older, less dusty, and more quiescent than objects with weak Lyα emission, or the line in absorption.

2.3.4 Spectral Energy Distributions

In order to place the results of the previous section on a more empirical footing, we transition here from focusing on stellar parameters and instead examine more broadly the relative colors of objects with and without strong Lyα emission. We also contrast our data with SEDs of narrowband-selected LAEs from Gawiser et al. (2007) and Nilsson et al. (2007) with the aim of investigating the color differences, if any, between objects isolated with color cuts and narrowband filters. Our analysis is focused on the 179 objects in the LBG sample satisfying the criteria of population synthesis modeling and no K_s upper limits. This empirical approach is complementary to the stellar population modeling discussed previously, and is furthermore a non-parametric probe of the differences between objects with and without strong Lyα emission. Such a study is necessary given the well-known degeneracies among physical properties (e.g., dust extinction and age) derived from stellar population modeling (Shapley et al., 2003).

We find stark differences between the colors of LAEs and non-LAEs (Table 2.3.3), where all G magnitudes have been corrected for the contribution of Lyα (§2.2). Strong Lyα-emitters have bluer G – $\mathcal{R}$ colors than non-LAEs ($\langle G-\mathcal{R}\rangle_{\rm LAE} = 0.54$; $\langle G-\mathcal{R}\rangle_{\rm non-LAE} = 0.65$) and this trend is consistent when a correction for IGM absorption (Madau, 1995) is applied to the objects' G magnitudes ($\langle G_{\rm IGM\ corr.}-\mathcal{R}\rangle_{\rm LAE} = 0.36$; $\langle G_{\rm IGM\ corr.}-\mathcal{R}\rangle_{\rm non-LAE} = 0.47$). Given

that non-LAEs have younger best-fit stellar ages than LAEs (§2.3.2), we expect that non-LAEs should have intrinsically bluer stellar continua than objects with strong Lyα emission. The fact that we instead observe redder G – $\mathcal{R}$ colors in these objects is evidence that non-LAEs are more strongly attenuated by dust than LAEs. This result is consistent with the larger E(B–V) values derived for the non-LAEs than the LAEs (§2.3.2).

LAEs and non-LAEs also differ in their $\mathcal{R}$ – K_s colors, where K_s magnitudes were inferred from best-fit SEDs for the 78 objects lacking near-infrared photometry. We find that LAEs are characterized by $\langle \mathcal{R} - K_s \rangle = 3.07$, whereas non-LAEs are bluer by 0.1 magnitudes with $\langle \mathcal{R} - K_s \rangle = 2.98$. Given that the $\mathcal{R}$ and K_s passbands bracket the Balmer break for objects at $z \sim 3$, a redder $\mathcal{R}$ – K_s color is indicative of a larger Balmer break. A more pronounced Balmer break, in turn, is correlated with an older stellar population (e.g., Bruzual & Charlot, 2003a). Therefore, the result that LAEs have redder $\mathcal{R}$ – K_s colors than non-LAEs is empirical, non-parametric evidence that strong Lyα-emitters are older on average. We have accordingly shown that the different colors of LAEs and non-LAEs are reflective of the trends discerned using stellar population modeling.

Composite best-fit SEDs of the LAE and non-LAE samples were assembled by directly summing the individual best-fit SEDs over the rest frame range 912 Å–1.0 μm and normalizing by the number of constituent spectra (34 and 145, respectively). In Figure 2.10, we compare the composite LAE and non-LAE spectra with best-fit average SEDs from two studies of narrowband-selected LAEs. Data from Nilsson et al. (2007) and Gawiser et al. (2007), where the former include LAEs at $z \sim 3.1$ in the GOODS South Field and the latter encompass LAEs at $z \sim 3.1$ in the Extended Chandra Deep Field South, are shown both normalized and un-normalized with our LAE and non-LAE composite spectra. It is imme-

diately apparent that the LBG-selected LAEs and non-LAEs are significantly brighter than the narrowband-selected LAEs ($\sim$ 2.3 magnitudes in the $\mathcal{R}$ band). The LBG-selected objects also have redder $G - \mathcal{R}$ and redder $\mathcal{R} - K_s$ colors than both the Nilsson et al. (2007) and Gawiser et al. (2007) data. These differences in color are consistent with LBG-selected objects being both dustier and older than objects isolated with narrowband filters, as has been suggested by some authors (e.g., Gawiser et al., 2007; Nilsson et al., 2009b). The relationship between LBGs and narrowband-selected LAEs is far from clear, though; some authors hypothesize a continuity between at least portions of the two populations based on similarities in stellar mass, color, and clustering (e.g., Adelberger et al., 2005b; Gronwall et al., 2007; Gawiser et al., 2007; Lai et al., 2008; Verhamme et al., 2008) whereas others maintain that the large luminosity and $W_{\mathrm{Ly}\alpha}$ discrepancies between LBGs and objects isolated with narrowband filters dictate separate evolutionary paths (e.g., Malhotra & Rhoads, 2002).

2.4 Discussion

Our large data set of both spectroscopically-determined Lyα equivalent widths and stellar population parameters constitutes a unique sample with which to investigate some of the current trends reported for continuum- and narrowband-selected objects. We turn here to examining several of the outstanding questions pertaining to LBGs and narrowband-isolated LAEs, with the constant aim of physically motivating our work. We begin below with a discussion of the necessity of comparing objects drawn from the same parent luminosity distribution.

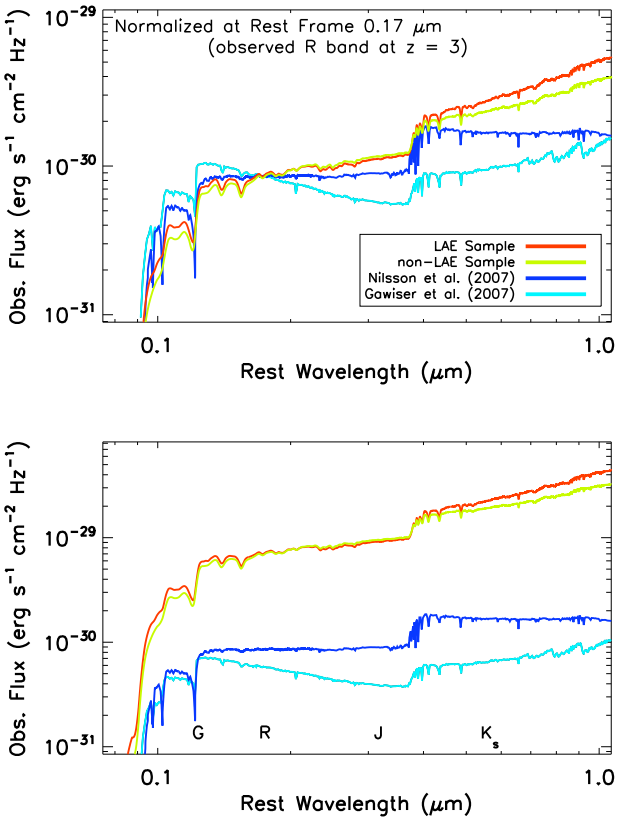

Figure 2.10 *Top panel:* Composite rest-frame UV to near-infrared SEDs of the LAE and non-LAE samples, assembled from best-fit SEDs from population synthesis modeling (omitting galaxies with K_s upper limits). Data from $z \sim 3.1$ narrowband-selected LAEs (Nilsson et al., 2007; Gawiser et al., 2007) are overplotted and all spectra have been normalized to the Nilsson et al. (2007) flux value at 0.17 μm (observed $\mathcal{R}$ band at $z \sim 3$). Note that the LBG-selected objects have significantly redder $G - \mathcal{R}$ and $\mathcal{R} - K_s$ colors than the narrowband-selected LAEs, consistent with the older ages and higher dust attenuations derived for LBGs in the literature. *Bottom panel:* Un-normalized spectra; note the significant flux discrepancy ($\sim$ 2.3 magnitudes) between the color-selected LBGs and the narrowband-selected LAEs.

2.4.1 A Caveat: Differing Rest-Frame Luminosities

By virtue of broadband selection techniques, LBGs have characteristically brighter optical continua than narrowband-selected LAEs ($\mathcal{R} \leq 25.5$ versus $R \sim 27$). As it is critical to disentangle how luminosity and stellar populations are related before attributing galaxy differences purely to the same mechanisms that modulate Lyα emission, it is of interest to investigate how, if at all, the derived properties of narrowband-selected LAEs are a natural result of preferentially isolating continuum-faint, line-bright objects. We compare our data with the work of several authors to explore the dependencies of Lyα emission, stellar populations, and spatial clustering on broadband luminosity and we discuss the applications of such investigations to both LBGs and narrowband-selected LAEs.

Luminosity and Equivalent Width: Recent work has suggested a correlation between luminosity and Lyα equivalent width, in the sense that few luminous LBGs have been observed with large equivalent widths (e.g., Shapley et al., 2003; Erb et al., 2006a; Ando et al., 2006; Ouchi et al., 2008; Vanzella et al., 2009; Pentericci et al., 2009). Several physical pictures have been suggested to explain this correlation, which has been noted in samples at redshifts $z \sim 3$–6. Verhamme et al. (2008) and Vanzella et al. (2009) hypothesized that different dust attenuations (from a luminosity-dependent chemical evolution history) could be responsible while Ando et al. (2006) suggested that an enhanced presence of HI gas around luminous LBGs could explain the lack of large Lyα equivalent widths in bright galaxies (consistent with the prediction of more massive galaxies residing in larger dark matter halos that are presumably richer in HI gas). Some authors, however, have conversely reported that the correlation between luminosity and Lyα equivalent width is tenuous, at best (e.g., Steidel et al., 2000; Verma et al., 2007; Stanway et al., 2007; Nilsson et al., 2009a). Given the ongoing debate about

such a correlation, we examined our extensive data set to test for a deficiency of luminous objects with large Lyα equivalent widths.

We restricted our analysis to the 64 objects with $W_{\mathrm{Ly}\alpha} \geq 20$ Å in order to ensure completeness as a function of $\mathcal{R}$ magnitude, given that spectroscopic follow-up is biased toward objects with large, positive Lyα equivalent widths. These objects have $W_{\mathrm{Ly}\alpha} < 160$ Å and M_{UV} ranging from –20.0 to –22.4 (neglecting corrections for dust attenuation). This parameter space is comparable to that of Ando et al. (2006), where these authors suggest a threshold luminosity of $M_{1400} = -21.5$ to –21.0 above which objects are deficient in large $W_{\mathrm{Ly}\alpha}$ values. We find that M_{UV} and $W_{\mathrm{Ly}\alpha}$ are not correlated in our sample, where the Spearman ρ test statistic, r_{SR}, is –0.104 and the probability of a null hypothesis, P_{SR}, is 0.4076. Furthermore, we see no evidence for any such threshold luminosity in our data; when the sample is divided into bright ($M_{\mathrm{UV}} < -21.0$) and faint ($M_{\mathrm{UV}} > -21.0$) groups, the median $W_{\mathrm{Ly}\alpha}$ of each group are identical (~ 32 Å).

These results are contradictory to those presented by Shapley et al. (2003) who also examined a sample of $z \sim 3$ LBGs. The Shapley et al. sample, when limited to objects with $W_{\mathrm{Ly}\alpha} \geq 20$ Å, consisted of objects with absolute UV luminosities between –19.5 and –22.4 (neglecting corrections for dust attenuation). In those data, there is a significant correlation between M_{UV} and $W_{\mathrm{Ly}\alpha}$ ($r_{\mathrm{SR}} = 0.274$; $P_{\mathrm{SR}} = 0.0002$). Dividing this sample into bright and faint subgroups, where the boundary luminosity is $M_{\mathrm{UV}} = -21.0$, also yielded a pronounced difference in the median $W_{\mathrm{Ly}\alpha}$ values of each group: M_{UV}(bright) = 35 Å and M_{UV}(faint) = 44 Å. Given that both our present sample and the Shapley et al. sample are composed of $z \sim 3$ LBGs, we hypothesize that one of reasons our data may not exhibit a correlation between M_{UV} and $W_{\mathrm{Ly}\alpha}$ is that our sample includes only a limited number of high equivalent width objects. Nine objects have $W_{\mathrm{Ly}\alpha} \geq 70$

Å and just one has $W_{\mathrm{Ly}\alpha} \geq 100$ Å in our data set whereas, in the Shapley et al. sample, 45 objects have $W_{\mathrm{Ly}\alpha} \geq 70$ Å and 20 have $W_{\mathrm{Ly}\alpha} \geq 100$ Å. After testing that our systematic approach to calculating Lyα equivalent width returned values consistent with those reported by Shapley et al., we combined our data with the 189 objects[5] from Shapley et al. with $W_{\mathrm{Ly}\alpha} \geq 20$ Å. This combined sample of 243 objects, with equivalent widths measured in a uniform manner, was then tested for a correlation between M_{UV} and $W_{\mathrm{Ly}\alpha}$. We found only a moderate correlation ($r_{\mathrm{SR}} = 0.149$; $P_{\mathrm{SR}} = 0.0202$), where we hypothesize that the trend between M_{UV} and $W_{\mathrm{Ly}\alpha}$ is simply not strong enough to be unequivocally detected in all samples. Furthermore, the correlation between M_{UV} and $W_{\mathrm{Ly}\alpha}$ in these data may be masked by the relatively small range of M_{UV} probed by LBGs. Narrowband-selected LAEs exhibit a wider range of absolute luminosities ($23.0 \lesssim R \lesssim 27.0$) than LBGs do ($23.0 \lesssim \mathcal{R} \lesssim 25.5$); any trend between M_{UV} and $W_{\mathrm{Ly}\alpha}$ will consequently be more pronounced in a sample of LAEs. In order to test this statement, we analyzed a sample of LAEs from Gronwall et al. (2007). We divided the data into two samples, where the first subsample included only objects brighter than the LBG spectroscopic limit and the second subsample was inclusive of all the data. The first subsample showed no correlation between M_{UV} and $W_{\mathrm{Ly}\alpha}$ ($r_{\mathrm{SR}} = -0.015$; $P_{\mathrm{SR}} = 0.9185$) whereas the second subsample exhibited a strong correlation ($r_{\mathrm{SR}} = 0.585$; $P_{\mathrm{SR}} = 0.0000$). These results support our hypothesis that the trend between M_{UV} and $W_{\mathrm{Ly}\alpha}$ at $z \sim 3$ is apparent only when considering data encompassing a large range in absolute luminosity. In Figure 2.11, we present a plot of M_{UV} versus $W_{\mathrm{Ly}\alpha}$ for $\mathcal{R} \leq 25.5$, $W_{\mathrm{Ly}\alpha} \geq 20$ Å LBGs and the Gronwall et al. (2007) sample of narrowband-selected LAEs. Even

[5]We limit our analysis to the 179/189 galaxies satisfying the criterion $W_{\mathrm{Ly}\alpha} \geq 20$ Å, measured according to our methodology described in §2.1.3; 10 objects classified as LAEs in the Shapley et al. sample do not have equivalent widths above 20 Å when measured using our systematic technique.

if one assumes incompleteness in the Gronwall et al. (2007) sample at the faint end, the lack of large equivalent widths among bright objects is striking (but see Nilsson et al., 2009a). Ando et al. (2006) report a deficiency of bright objects with large equivalent widths in their sample of $z = 5 - 6$ objects; that fact that we observe several such objects here while those authors do not can be attributed to the small sample size of Ando et al. (2006).

Luminosity and Stellar Populations: Understanding how luminosity and stellar populations are correlated is critical to commenting on the nature of LBGs and LAEs, given that the latter are commonly an order of magnitude fainter in optical broadband filters. Lai et al. (2008) examined a sample of 70 $z \sim 3.1$ LAEs, $\sim 30\%$ of which were detected in the *Spitzer* IRAC 3.6 μm band. These authors found that the IRAC-detected LAEs were significantly older and more massive ($\langle t_\star \rangle \sim 1.6$ Gyr, $\langle M \rangle \sim 9 \times 10^9\ M_\odot$) than the IRAC undetected sample ($\langle t_\star \rangle \sim 200$ Myr, $\langle M \rangle \sim 3 \times 10^8\ M_\odot$). In addition to having redder colors, the IRAC-detected sample was also approximately three times brighter in the R band. This correlation between luminosity and redness, age, and mass prompted Lai et al. (2008) to suggest that the IRAC-detected LAEs may be a low-mass extension of the LBG population. The relationship between luminosity and average dust attenuation was examined by Reddy et al. (2008), where these authors studied a sample of UV-selected objects at $1.9 \leq z < 3.4$ and found no correlation between $M_{\rm UV}$ and E(B–V) over the absolute magnitude range $22.0 \leq \mathcal{R} \leq 25.5$. While bright objects do not appear to exhibit a correlation between dust attenuation and luminosity, Reddy et al. (2008) postulate that objects fainter than the LBG spectroscopic limit of $\mathcal{R} = 25.5$ may have lower average dust attenuations than brighter objects. This has been confirmed by Bouwens et al. (2009), who examined a sample of objects at $z \sim 2$–6 over a larger dynamic range ($0.1 L^*_{z=3}$ to $2 L^*_{z=3}$) than had been previously studied. These authors reported a correlation

between UV luminosity and dust attenuation such that fainter objects are bluer. Given the correlation we find between E(B–V) and $W_{\mathrm{Ly}\alpha}$, the evolution of dust attenuation with UV luminosity may have implications for the fraction of LAEs as a function of UV luminosity (Reddy & Steidel, 2009). These results have highlighted that examining objects over only a limited range of absolute magnitudes may mask an underlying correlation.

Luminosity and Clustering: Several authors have noted the different clustering properties of LBGs and LAEs, where the former exhibit a mean halo occupation of $\sim 100\%$ (e.g., Conroy et al., 2008) in dark matter halos with minimum masses of $\sim 10^{11.3}\ h^{-1}\ M_{\odot}$ (e.g., Adelberger et al., 2005b; Conroy et al., 2008) and the latter cluster more weakly and appear to occupy only 1/100 – 1/10 of similarly-clustered dark matter halos with lower limit masses of $\sim 10^{10.6}\ h^{-1}\ M_{\odot}$ (e.g., Gawiser et al., 2007). Given the direct dependence of clustering strength on UV luminosity (e.g., Ouchi et al., 2004; Adelberger et al., 2005b; Lee et al., 2006), the spatial differences between LBGs and LAEs may simply reflect the discrepancy in typical UV luminosity between the two samples. It is therefore of interest to investigate how the clustering strength of LAEs correlates with Lyα luminosity or Lyα equivalent width, given that these quantities govern the selection of LAEs. Discerning the relative clustering properties of objects with and without strong Lyα emission *within the same UV luminosity range* is critical to understanding the correlation between Lyα and galactic properties.

These results – that objects more luminous in the rest-frame UV may *1)* be deficient in large Lyα equivalent widths and *2)* be generally redder, older, and more massive relative to less luminous objects – may be the driving factors responsible for (faint, high equivalent width) narrowband-selected LAEs being typically younger, bluer, and less massive than (bright, lower equivalent width)

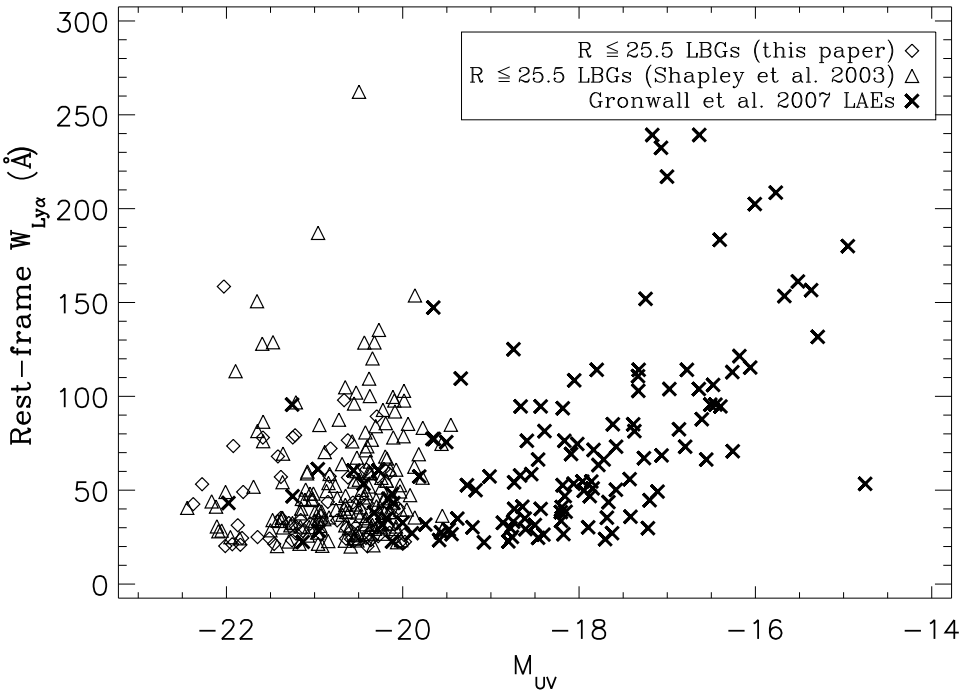

Figure 2.11 Absolute UV magnitude versus rest-frame $W_{\mathrm{Ly}\alpha}$ for $\mathcal{R} \leq 25.5$, $W_{\mathrm{Ly}\alpha}$ $\geq$ 20 Å LBGs (diamonds and triangles) and the Gronwall et al. (2007) sample of $z = 3.1$ LAEs (crosses). Note that the LBG data include objects from Shapley et al. (2003) and therefore span a larger range of $W_{\mathrm{Ly}\alpha}$ than that presented in this paper. A strong correlation between M_{UV} and $W_{\mathrm{Ly}\alpha}$ is observed in the Gronwall et al. (2007) sample while weaker correlations are seen in the sample of $z \sim 3$ LBGs. We attribute this discrepancy to the larger range of M_{UV} probed by LAEs. Object Q1009-C9 is both anomalously bright ($M_{\mathrm{UV}} = -22.0$) and the strongest Lyα emitter in our sample ($W_{\mathrm{Ly}\alpha} = 158.5$ Å), yet this galaxy does not exhibit any spectral signatures indicative of an AGN.

LBGs.

As the LBG spectroscopic limit of $\mathcal{R} \leq 25.5$ necessarily limits our sample to a smaller absolute magnitude range than probed by narrowband-selected LAEs ($23.0 \lesssim R \lesssim 27.0$), the luminosity-dependent trends reported above for Lyα equivalent width, stellar populations, and clustering (e.g., Ando et al., 2006; Lai et al., 2008; Adelberger et al., 2005b) may only become apparent in narrowband-selected samples where the absolute luminosity range is significantly larger than it is in samples of LBGs. We remind the reader that while our conclusions are applicable to both LBGs and bright ($\mathcal{R} \leq 25.5$) narrowband-selected LAEs, we are unable to make inferences about the population of faint LAEs. We refer the reader to Lai et al. (2008) for a discussion of these objects.

2.4.2 LBG and LAE Equivalent Width Distributions

The equivalent width of the Lyα feature is a common benchmark that can be used to make comparisons between studies of LBGs and LAEs. Observing programs of flux-selected Lyα-emitters typically employ a narrowband ($\sim$ 50–100 Å) filter centered on the redshifted Lyα line, paired with a broadband filter used to characterize the local continuum. Samples are defined according to a minimum Lyα equivalent width – typically $\sim$ 20 Å in the rest frame – where $W_{\mathrm{Ly}\alpha}$ is calculated photometrically by ratioing the flux in the narrowband filter to the flux density in the broadband filter. LBGs, on the other hand, are selected according to broadband flux and color cuts, with no implicit requirement on $W_{\mathrm{Ly}\alpha}$. Equivalent widths of LBGs are most commonly calculated spectroscopically, as these objects are characterized by relatively bright continua ($\mathcal{R} \leq 25.5$). Given these different selection techniques and methods of calculating $W_{\mathrm{Ly}\alpha}$, it is of interest to compare the equivalent width distributions of LBG-selected LAEs and

narrowband-selected LAEs. A difference in the $W_{\mathrm{Ly}\alpha}$ distributions of these two populations would be indicative of an underlying dissimilarity between LBG-selected LAEs and narrowband-selected LAEs, even though both classes of objects can be broadly classified as strong Lyα-emitters[6].

For this analysis, we combined our present sample of 64 LBG-selected LAEs with the 179 objects from Shapley et al. (2003) satisfying the criterion of $W_{\mathrm{Ly}\alpha} \geq 20$ (measured using our methodology described in §2.1.3). Integrating these two data sets yields a large sample of $z \sim 3$ objects for which equivalent widths were measured in an identical manner. We find that these data are characterized by a median equivalent width of 42 Å and mean of 57 Å. In contrast, a sample of 160 LAEs at $z = 3.1$ in the Extended Chandra Deep Field South observed by Gronwall et al. (2007) had a median of $\sim$ 60 Å and a mean of $\sim$ 80 Å. We used the K–S test to quantify the likelihood that the LBG-selected LAEs and the narrowband-selected LAEs derived from the same parent equivalent width distribution. When the entire sample of objects from Gronwall et al. (2007) was considered, we found a probability of 3.5×10^{-4} that the objects shared a common equivalent width distribution. Alternatively, when we limited the Gronwall et al. (2007) data to include only objects satisfying the LBG spectroscopic limit of $\mathcal{R} \leq 25.5$, we obtained a probability of $\sim$ 0.95 that the equivalent widths of the LBG- and narrowband-selected LAE samples could be described as originating from the same population. This result, consistent with Verhamme et al. (2008), is indicative of the similarity in equivalent width of objects spanning comparable UV luminosities. Conversely, the probability that the equivalent widths of our

[6]Reddy et al. (2008) found that the standard LBG color selection criteria (Equation 2.1) do little to bias the intrinsic distribution of $W_{\mathrm{Ly}\alpha}$ for $z \sim 3$ LBGs, given the low probability of an object having a strong enough Lyα feature to perturb its colors out of the LBG selection window. We therefore attribute any differences in the $W_{\mathrm{Ly}\alpha}$ distributions of LBGs and narrowband-selected LAEs to intrinsic dissimilarities between the two populations.

sample of LBG-selected LAEs and the faint ($R \geq 25.5$) Gronwall et al. (2007) LAEs derive from the same parent population is 8×10^{-8}. Similarly, when the Gronwall et al. (2007) data are divided using the boundary $R = 25.5$, a K–S test yields a probability of 7.9×10^{-6} that the two equivalent width populations derive from the same parent distribution.

In other words, while the equivalent width distributions of LBG- and narrowband-selected LAEs are quite disparate when considered at face value, it appears that the bulk of this disparity can be attributed to the different luminosities probed by the respective samples. When narrowband-selected LAEs are restricted to objects more luminous than $R = 25.5$, a K–S test reveals a high probability that the equivalent width distributions of strong Lyα-emitting LBGs and bright LAEs derive from the same parent population. This similarity in equivalent width, when a standard continuum magnitude range is adopted, is consistent with the picture that bright LAEs represent the same population as Lyα-emitting LBGs (e.g., Verhamme et al., 2008).

2.4.3 Escape of Lyα Photons

As Lyα is susceptible to a variety of complex radiation transport effects including resonant scattering (e.g., Neufeld, 1990) and the velocity field of the ISM (e.g., Verhamme et al., 2008), the escape of Lyα emission is a probe of the physical conditions of galaxies' interstellar media. In the simplest case of a single-phase ISM in which gas and dust are well mixed, Lyα photons experience more attenuation than continuum photons due to the longer dust absorption path lengths expected for resonantly scattered radiation. To explain the large Lyα equivalent widths observed in some apparently dusty LAEs, the presence of a multi-phase ISM – in which dust is segregated in neutral clouds – has been proposed (Neufeld, 1991;

Hansen & Oh, 2006; Finkelstein et al., 2009). In such a geometry, Lyα photons are scattered at the surface of dusty clumps while continuum photons penetrate the clumps and are preferentially scattered or absorbed. Galaxies in which the dust is segregated in neutral clouds are consequently predicted to exhibit larger Lyα equivalent widths than would be expected given their stellar populations.

We considered the likelihood of the above dust geometry in our sample of LBGs. Our methodology relied on comparing observed and predicted Lyα luminosities, where the former, $L_{\mathrm{Ly}\alpha(\mathrm{flux})}$, was calculated simply from the Lyα line flux and the latter, $L_{\mathrm{Ly}\alpha(\mathrm{SFR})}$, was derived from the conversion between SFR (from population synthesis modeling) and Lyα luminosity, assuming the conventions (Case B recombination; T_{e} = 10,000 K) of Kennicutt (1998) and Brocklehurst (1971):

$$L_{\mathrm{Ly}\alpha(\mathrm{SFR})} = \frac{\mathrm{SFR}\ [M_{\odot}\ \mathrm{yr}^{-1}]}{9.1 \times 10^{-43}} \tag{2.2}$$

where SFR was calculated assuming a Salpeter (1955) IMF. Two similar parameters incorporating observed and predicted Lyα luminosities were of interest: the escape fraction, f_{esc}, and the relative escape fraction, $f_{esc,rel}$. The escape fraction is the ratio of observed to predicted Lyα luminosities, whereas the relative escape fraction is this same ratio with an extra term corresponding to a dust correction at the rest wavelength of Lyα. $f_{esc,rel}$ is a probe of the degree to which Lyα and continuum photons experience the same level of dust attenuation. In the case that $f_{esc,rel} = 1$, Lyα and continuum photons are attenuated by the same E(B–V). On the other hand, a relative escape fraction less than unity is indicative of a dust geometry in which Lyα photons are attenuated more than continuum photons. Conversely, a galaxy in which dust is segregated in neutral clouds and where the Lyα flux is consequently enhanced relative to the continuum flux would have

$f_{esc,rel} > 1$. We present the equations for f_{esc} and $f_{esc,rel}$ below, where $k'(1216)$ parameterizes the Calzetti et al. (2000) starburst attenuation law at 1216 Å:

$$f_{esc} = \frac{L_{\mathrm{Ly}\alpha(\mathrm{flux})}}{L_{\mathrm{Ly}\alpha(\mathrm{SFR})}}, \tag{2.3}$$

$$f_{esc,rel} = f_{esc} \times 10^{0.4\mathrm{E(B-V)}k'(1216)}. \tag{2.4}$$

When calculating f_{esc} and $f_{esc,rel}$, we limited our analysis to only those objects with $W_{\mathrm{Ly}\alpha} > 0$ Å due to the unphysical nature of inferring a Lyα luminosity from a negative Lyα flux. We also required objects to have best-fit stellar ages older than 100 Myr in order to ensure the validity of Equation 2.2, which assumes continuous star formation for at least that duration (Kennicutt, 1998). These criteria isolated a sample of 105 objects. We note that the questions raised about the nature of the dust extinction law for young objects (§2.3.2) are not of concern given this older sample. To correct for slit losses, we normalized the G magnitudes determined from photometry and spectroscopy; the latter were calculated by multiplying the G filter transmission curve (4780/1100 Å) over the optical spectra. The Lyα line fluxes were adjusted accordingly, where the median flux correction was an increase by a factor of ~ 1.7 (0.6 magnitudes). This procedure relies on the assumption that Lyα emission has the same spatial extent as broadband 940–1470 Å emission. While some recent work (e.g., Steidel et al., 2000; Matsuda et al., 2004; Hayashino et al., 2004) has suggested that Lyα and UV continuum emission may be spatially decoupled with Lyα more extended than continuum emission, in the absence of simultaneous high-resolution Lyα and UV continuum imaging for our entire sample we assume for simplicity that the line and continuum emission are coincident.

The calculated values of f_{esc} vary from 0.00–0.85. In Figure 2.12, we plot

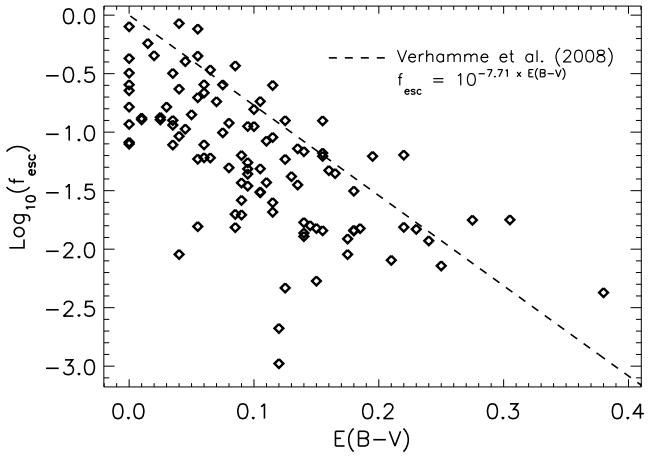

Figure 2.12 Lyα escape fraction as a function of dust extinction, for objects with best-fit stellar ages $t_\star > 100$ Myr. A significant correlation is observed, in the sense that objects with lower dust attenuations have larger escape fractions. The best-fit line from Verhamme et al. (2008) is overplotted as a dashed line.

E(B–V) versus f_{esc}; we find a strong correlation in the sense that objects with large dust attenuations tend to have small Lyα escape fractions ($r_{\rm SR}$= –0.712, $P_{\rm SR}$ = 0.0000). We note that this trend is consistent with the existence of LBGs in our sample exhibiting both Lyα in absorption and red UV continua, where these particular objects were not included in this analysis due to their negative Lyα fluxes. Other authors have derived similar results, although with significantly smaller sample sizes (e.g., Verhamme et al., 2008; Atek et al., 2009). The scatter present in our larger data set – some of which may be due to systematics in estimating f_{esc} – is a useful probe of the nature of Lyα radiative transfer in LBGs. We further discuss a physical picture of LBGs consistent with these f_{esc} results in §2.5.

In order to investigate the nature of the gas and dust distributions for the

objects in our sample, we derived the relative escape fraction of the 105 LBGs with $W_{\mathrm{Ly}\alpha} > 0$ Å and $t_\star > 100$ Myr. We found that 103 objects had $f_{esc,rel} < 1$ and the sample as a whole was characterized by $\langle f_{esc}(\mathrm{rel})\rangle = 0.27$ (Figure 2.13). For comparison, Gronwall et al. (2007) and Nilsson et al. (2009b) report typical $f_{esc,rel}$ values of ~ 0.30 and ~ 0.60 in LAE samples at $z \sim 3.1$ and $z \sim 2.25$, respectively. Even if we conservatively assume Lyα slit losses for our sample approaching a factor of two (Hayashino et al., 2004), these low relative escape fractions, well below unity, do not support the hypothesis in which dust is primarily segregated to neutral clouds in Lyα-emitting LBGs. We note that the absorption of Lyα photons by the IGM is not a plausible explanation for these low relative escape fractions; at $z \sim 3$, Lyα line fluxes are predicted to experience an IGM-induced decrement of only $\sim 20\%$ (Madau, 1995; Shapley et al., 2006). Furthermore, the observed symmetry of the Lyα lines in our sample (Figures 2.1 and 2.7) are indicative of minimal IGM absorption. Additionally, if one adopts a sub-solar metallicity (in contrast to $Z_\odot$ used in this paper), the calculated values of $f_{esc,rel}$ will be *lower* than those presented here due to the fact that the ratio of the ionizing photon luminosity to the observed UV luminosity increases with decreasing metallicity (e.g., Leitherer et al., 1999). This result of relative escape fractions below unity indicates that Lyα appears to experience more attenuation than continuum photons, consistent with the physical picture of a homogeneous distribution of gas and dust in which resonantly scattered Lyα photons have longer dust absorption path lengths than continuum photons. Such a simple picture is likely not an accurate representation of the ISM of $z \sim 3$ LBGs; indeed, the ISM of our own Milky Way is known to be highly inhomogeneous (Dickey & Garwood, 1989). However, our results suggest a scenario in which dust and gas are well mixed among the different phases of an inhomogeneous ISM.

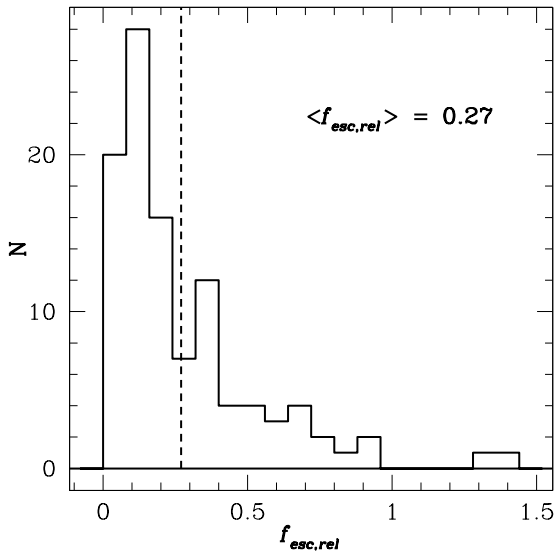

Figure 2.13 Histogram of $f_{esc,rel}$ values, for objects with $t_\star > 100$ Myr. Note that the majority of objects (103/105) have $f_{esc,rel} < 1$, where the sample as a whole is characterized by $\langle f_{esc,rel} \rangle = 0.27$. These low relative escape fractions are indicative of Lyα photons experiencing more attenuation than non-resonance continuum photons. These results are not consistent with the hypothesis of a clumpy interstellar medium, as has been suggested to exist in some LAEs (e.g., Finkelstein et al., 2009).

2.5 Summary and Conclusions

We have analyzed a sample of 321 optically-selected $z \sim 3$ Lyman break galaxies in order to investigate the relationship between stellar populations and Lyα emission. The equivalent width of the Lyα feature was robustly estimated from rest-frame UV spectroscopy and broadband $G\mathcal{R}JK_s$ + *Spitzer* IRAC photometry was used to conduct stellar population modeling to derive the key properties of age, extinction, star formation rate, and stellar mass for all objects with photometric coverage in at least one near- or mid-infrared passband ($\sim$ 80% of the sample). The limited luminosity range of LBGs enabled a controlled investigation of the nature of Lyα emission *within a sample of objects spanning similar luminosities.* Given the luminosity-dependent trends in Lyα equivalent width, stellar populations, and clustering (e.g., Gronwall et al., 2007; Lai et al., 2008; Adelberger et al., 2005b), this controlled study represents an improvement over previous work. We used a variety of statistical tests to analyze the correlation between Lyα emission and stellar populations in LBGs from the standpoint of comparing spectroscopic observations, photometric data, and best-fit stellar population parameters. The relative Lyα escape fraction was used to probe the relative distributions of gas and dust in the objects' interstellar media. Below, we summarize our results.

- Lyα equivalent width is correlated with age, SFR, and E(B–V), respectively, in the sense that galaxies with strong Lyα emission are older, more quiescent, and less dusty than their counterparts with weak or absent Lyα emission. Taking into account the uncertainties on the best-fit population parameters, the probability of a null hypothesis (i.e., no correlation) was excluded at the 3–5σ level for these relationships. We found that stellar mass was not significantly correlated with $W_{\mathrm{Ly}\alpha}$ – the null hypothesis could

be excluded at only the $\sim 1\sigma$ level. These results were consistently derived from several different analyses of the data, including correlation tests, composite spectra, and the binary division of the sample into LAEs ($W_{\mathrm{Ly}\alpha} \geq$ 20 Å) and non-LAEs ($W_{\mathrm{Ly}\alpha} <$ 20 Å).

- Analysis of the relative escape fraction of Lyα is consistent with Lyα photons experiencing more attenuation than non-resonance continuum photons. We also find that the Lyα escape fraction is strongly correlated with E(B–V), where galaxies with more dust attenuation also have lower escape fractions.

The observed correlations between Lyα emission and stellar populations are consistent with the physical picture proposed by Shapley et al. (2001), in which young, dusty LBGs experience vigorous outflows from supernovae and massive star winds. Shapley et al. (2003) reported evidence that both gas and dust are entrained in the outflows, evidence that these "superwinds" could tenably decrease a galaxy's dust and gas covering fraction over several tens of Myr. While the more mature LBGs may have as much or more overall dust content than younger galaxies, the fact that these older objects ($t_\star \gtrsim 100$ Myr) are also more likely to exhibit Lyα emission is an important point: this trend demonstrates that it is the dust covering fraction – not the total amount of dust – that modulates Lyα emission. Independent evidence for a lower covering fraction of dusty gas in older objects is provided by a trend toward weaker low-ionization interstellar absorption lines with increasing age in the composite spectra presented in §2.3.2.

While this physical picture has been put forth previously, our current results are more strongly supported due to the wide range of statistical tests and analysis methods that we employed. We compared our larger sample of data in different forms – spectroscopic, photometric, and best-fit parameters – using a battery of

statistical methods including correlation and K–S tests. Lyα emission strength was furthermore treated as both an independent and dependent variable. These analyses represent a systematic, powerful approach to elucidating trends.

Results of both the escape fraction and the relative escape fraction can be used to further constrain the physical picture of LBGs and bright narrowband-selected LAEs. While the observed inverse relationship between E(B–V) and f_{esc} is consistent with earlier results (e.g., Verhamme et al., 2008; Atek et al., 2009), the scatter present in our larger sample highlights the myriad factors modulating the Lyα escape fraction (e.g., galaxy kinematics, dust, and outflow geometry). Further analysis of this scatter will be instrumental in constraining how the Lyα escape fraction varies. The observed relative escape fraction of Lyα emission – where the majority of LBGs have $f_{esc,rel}$ below unity – is indicative of a physical picture in which LBGs contain gas and dust that is well mixed. In this geometry, Lyα photons experience more attenuation than continuum photons do because of the former's increased path lengths from resonant scattering. This is in contrast to the scenario proposed by Finkelstein et al. (2009), in which dust is segregated in neutral gas clumps surrounded by an ionized, dust-free medium. We caution, however, that the relative escape fraction of Lyα is likely modified by a variety of factors including galaxy kinematics, dust, and outflow geometry. As such, additional observations are necessary in order to more fully understand the distribution (and evolution) of gas and dust in LBGs.

While we hope that this work has illuminated the relationship between Lyα emission and stellar populations in $z \sim 3$ LBGs, future systematic studies at other redshifts – ideally over larger dynamic ranges in UV luminosity – are necessary in order to address the discrepancies between trends reported here and those at $z \sim 2$ or $z \sim 4$ (e.g., Erb et al., 2006a; Pentericci et al., 2007). The nature of

complex Lyα emission morphologies – such as the double-peaked objects that comprise $\sim 4\%$ of the sample discussed here – has also yet to be explored in light of understanding if these objects' stellar populations and gas distributions differ from those of more typical Lyα-emitters or absorbers. Similarly, an analysis of the geometry of dust and gas in the interstellar media of $z \sim 3$ LBGs is vital to understanding what kind of dust attenuation law – the Calzetti et al. (2000) relation, a SMC-like law, or another relation completely – most accurately describes these objects. Furthermore, a basic property critical to placing galaxies in an evolutionary context – metallicity – remains poorly constrained for the $z \sim 3$ LBG population (but see Maiolino et al., 2008). While metallicity has been investigated in the rare cases of gravitationally lensed objects (e.g., Teplitz et al., 2000; Pettini et al., 2002; Hainline et al., 2009; Quider et al., 2009), a systematic study of elemental abundances in a larger sample of $z \sim 3$ LBGs would be illuminating (akin to the $z \sim 2$ sample discussed in Erb et al., 2006a). Given anticipated advances in both telescopes and instrumentation, we hope that these questions are illustrative of many others that will help to guide future LBG research.

CHAPTER 3

The Properties and Prevalence of Galactic Outflows at $z \sim 1$ in the Extended Groth Strip

Far from being closed boxes, galaxies are known to affect their environment by expelling gas and metals into the intergalactic medium (IGM) via "superwinds" (e.g., Heckman et al., 1990; Steidel et al., 1996b; Franx et al., 1997; Martin, 1999; Pettini et al., 2000, 2001; Shapley et al., 2003; Martin, 2005; Veilleux et al., 2005; Rupke et al., 2005; Tremonti et al., 2007; Weiner et al., 2009; Steidel et al., 2010; Coil et al., 2011). These outflows may contribute to the limiting of black hole and spheroid growth (possibly resulting in the correlation between black hole and bulge mass; e.g., Ferrarese & Merritt, 2000; Robertson et al., 2006), the enrichment of the IGM (Oppenheimer & Davé, 2006), and the regulation of star formation through the ejection of cold gas (Scannapieco et al., 2005; Croton et al., 2006). At high redshifts, winds may have played a critical role in reionization by clearing paths for ionizing radiation to escape from galaxies (Dove et al., 2000; Steidel et al., 2001; Heckman et al., 2001a; Gnedin et al., 2008).

The kinematics of interstellar absorption lines provide one of the key probes of outflowing gas in galaxies. Observations of blueshifted interstellar absorption lines at a variety of rest wavelengths and ionization states have been observed in both local and high-redshift samples (e.g., Heckman et al., 2000; Martin, 2005; Pettini et al., 2002; Shapley et al., 2003; Steidel et al., 2010; Coil et al., 2011;

Kulas et al., 2012; Law et al., 2012b). The presence of outflows with blueshifted velocities relative to stars and H II regions appears to be associated with objects undergoing starburst episodes: UV-selected star-forming galaxies at $z = 2$–3 with large star-formation rates (SFRs) (Pettini et al., 2002; Shapley et al., 2003; Steidel et al., 2010), local ULIRGs (Heckman et al., 2000; Rupke et al., 2002; Martin, 2005; Rupke et al., 2005), and local dwarf starbursts (Lequeux et al., 1995; Heckman & Leitherer, 1997; Heckman et al., 2001b; Schwartz & Martin, 2004). Studies of X-ray and Hα emission in local samples have focused on correlating outflows with spatially-resolved properties such as star-formation rate surface density ($\Sigma_{\rm SFR}$), morphology, and galaxy inclination (e.g., Lehnert & Heckman, 1996; Heckman, 2002; Strickland et al., 2004). Only recently, however, have absorption-line studies of winds at higher redshifts begun similar investigations (Sato et al., 2009; Weiner et al., 2009; Rubin et al., 2010b; Steidel et al., 2010; Talia et al., 2012; Law et al., 2012b). Studies of spatially-resolved properties necessitate high-resolution imaging and careful measurement of the galactic regions in which stars are forming. These studies are particularly relevant around $z \sim 1$; examining the processes regulating star formation is critical to understanding why the global star-formation rate density declines between $z \sim 1$ and $z \sim 0$ (Reddy et al., 2008).

The study of outflows in $z \sim 1$ objects to date has relied primarily on composite spectra and visual classification of galaxy morphology (e.g., Weiner et al., 2009; Rubin et al., 2010b). Here, we use a sample of galaxies drawn from the $z \sim 1$ DEEP2 redshift survey (Newman et al., 2012) to examine the relationship between outflows and host galaxy properties. For these objects, we obtain observations with the Low Resolution Imaging Spectrometer (LRIS; Oke et al., 1995; Steidel et al., 2004) on Keck I. These LRIS spectra cover a bluer wavelength range than the DEIMOS discovery spectra from the DEEP2 survey and

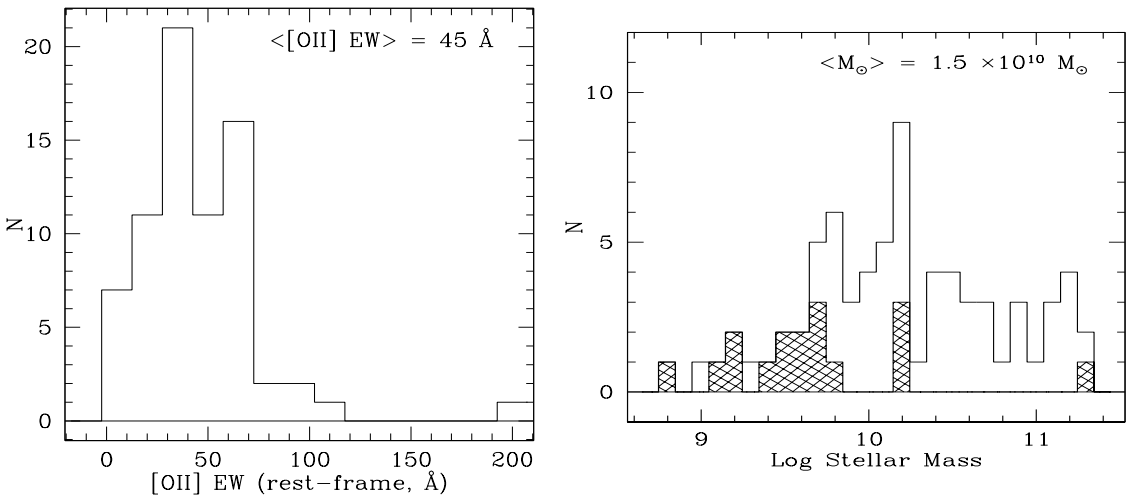

Figure 3.1 Distributions of rest-frame [O II] equivalent widths (*left*) and stellar masses (*right*) for our sample of 72 EGS objects at $0.7 < z < 1.3$. The hatched histogram in the stellar mass panel denotes galaxies without K-band detections (17 objects). Stellar masses were estimated from SED fitting using BRI (and K, when available) photometry (Bundy et al., 2006), assuming a Chabrier (2003) IMF.

are inclusive of a variety of rest-frame UV features from which wind kinematics can be measured (Si II λ1526, C IV λ1549, Fe II λ1608, Al II λ1670, Fe II λ2344, Fe II $\lambda\lambda$2374/2382, Fe II $\lambda\lambda$2587/2600, Mg II $\lambda\lambda$2796/2803, and Mg I λ2852). In this paper, we focus specifically on objects in the Extended Groth Strip (EGS) field, where an extensive multiwavelength dataset enables SFR, $\Sigma_{\rm SFR}$, morphology, inclination, and dust attenuation to be estimated and in turn correlated with outflow properties on a per-object basis. We aim to determine which, if any, of these properties most strongly drives outflows at $z \sim 1$. Furthermore, with our unique data set we can statistically probe the geometry of galactic winds.

In Section 3.1, we present the imaging and spectroscopic data used in our anal-

ysis, including extensive datasets of EGS observations. We discuss SFR, a new technique for estimating galaxy areas, and $\Sigma_{\rm SFR}$ in Section 3.2. Absorption-line modeling is reviewed in Section 3.3, while Section 3.4 is devoted to results. In Section 4.4, we present a discussion of the results. Our conclusions are summarized in Section 3.6. Throughout the paper, we assume a standard ΛCDM cosmology with $H_0 = 70$ km s^{-1} Mpc^{-1}, $\Omega_{\rm M} = 0.3$, and $\Omega_\Lambda = 0.7$. All wavelengths are measured in vacuum. At $z = 0.7$ (1.3), an angular size of $1''$ corresponds to 7.1 (8.4) kpc.

3.1 Sample and Observations

3.1.1 DEEP2 Survey

The objects presented here were drawn from the DEEP2 survey conducted from 2002–2005 using the DEep Imaging Multi-Object Spectrograph (DEIMOS) on Keck II (Newman et al., 2012). With four fields totaling three square degrees, the DEEP2 survey obtained high-quality redshifts for $\sim$ 30,000 galaxies at $0.7 \leq z \leq 1.5$ brighter than $R_{\rm AB} = 24.1$ to study clustering and evolution in galactic properties out to $z \sim 1$.

The DEIMOS spectra were obtained with a 1200 lines mm^{-1} grating and a $1.''0$ slit and have a resolution of $R \approx 5000$ (Newman et al., 2012). Wavelength coverage extends from $\sim$ 6500–9100 Å inclusive of the [O II] λλ3727/3729 doublet, which is typically resolved. Galaxy properties, including luminosities, colors, stellar masses (M_*), and [O II] equivalent widths, have been measured (Figure 3.1; Bundy et al., 2006; Willmer et al., 2006). Stellar masses were calculated from SED modeling with *BRIK* photometry, assuming Bruzual & Charlot (2003b) spectral templates and a Chabrier (2003) initial mass function (IMF).

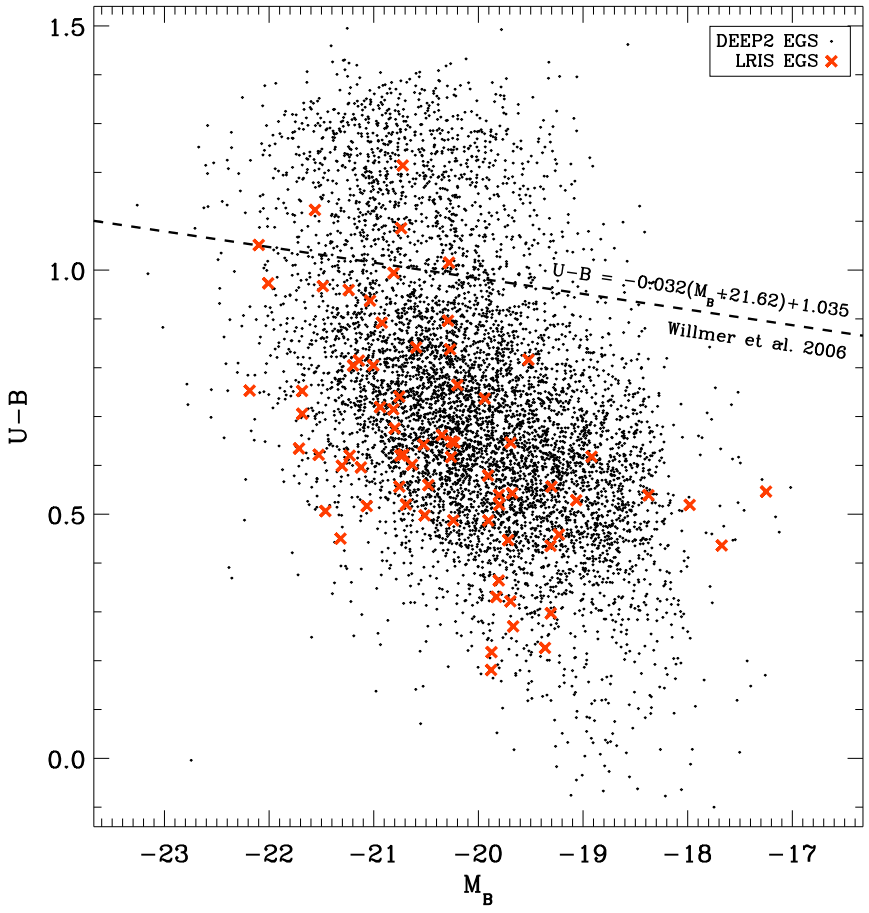

Figure 3.2 Rest-frame color-magnitude diagram with photometry corrected for Galactic extinction, assuming $H_0 = 100$ km s^{-1} Mpc^{-1} (Willmer et al., 2006). Small dots show objects at $0.70 < z < 1.35$ in the EGS field of the DEEP2 survey and red crosses mark the 72 EGS objects with LRIS follow-up discussed in this paper. The red sequence and blue cloud are delineated by the dashed line (Willmer et al., 2006); we emphasize that the majority of the objects presented in this work are brighter, blue cloud galaxies.

For our study, modeling was done with *BRI* photometry alone if objects lacked K-band detections (24% of the sample).

Photometric preselection based on *BRI* colors was applied in three out of the four DEEP2 fields in order to isolate galaxies at $z \geq 0.7$. In the fourth field, the EGS, no color cuts were applied and galaxies at lower redshifts were accordingly targeted for spectroscopy. The EGS dataset is unique not only for its inclusion of more local galaxies, but also for its extensive multi-wavelength coverage from the All-Wavelength Extended Groth Strip International Survey (AEGIS; Davis et al., 2007). The objects presented in this paper are all in the EGS and consequently have, in addition to the original DEIMOS spectra, a variety of complementary data spanning from the X-ray to the radio regimes (Section 3.1.3).

3.1.2 LRIS Observations

While the DEIMOS spectra are generally dominated by nebular emission features ([O II], [Ne III], Hγ, Hδ, Hβ, [O III]), the majority of low- and high-ionization interstellar absorption features tracing outflows are in the rest-frame UV and are observed at shorter wavelengths than the blue edge of the typical DEIMOS spectra in the DEEP2 survey ($\sim$ 6500 Å in the observed frame). In order to probe these outflow features (e.g., Fe II λ2344, Fe II $\lambda\lambda$2374/2382, Fe II $\lambda\lambda$2587/2600, Mg II $\lambda\lambda$2796/2803), we obtained complementary spectroscopic data for 212 objects using the LRIS spectrograph on Keck I. These observations, covering all four DEEP2 survey fields, are described in further detail in Martin et al. (2012).

In this paper, we discuss 72 objects in the EGS, which are drawn from our larger sample of 212 spectroscopically-confirmed DEEP2 objects with LRIS follow-up (Martin et al., 2012). In Figure 3.2, we show the color-magnitude diagram for both the present sample of 72 objects and also the parent sample of

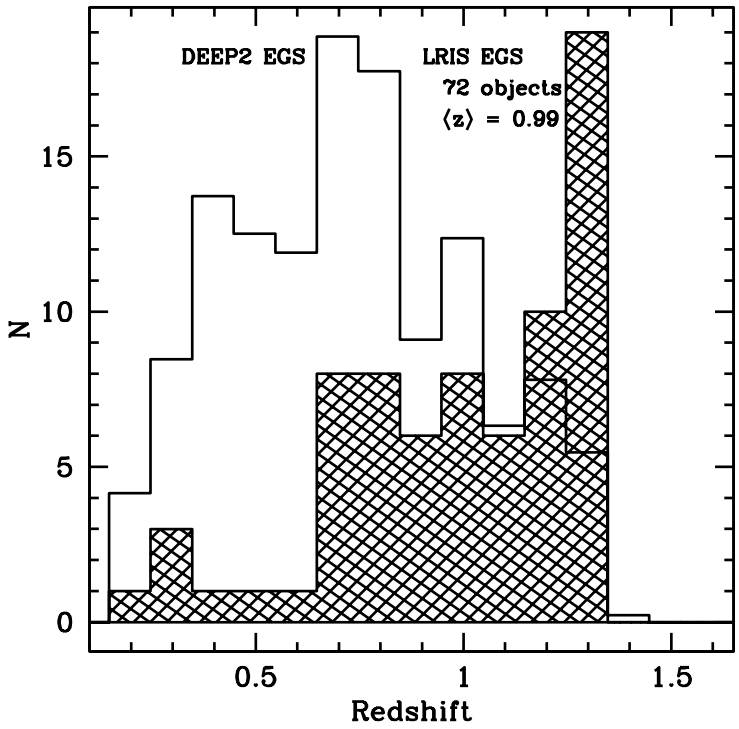

Figure 3.3 The redshift distribution of the LRIS EGS sample (hatched histogram), compared with a normalized histogram of redshifts of EGS objects in the parent DEEP2 survey. Objects at $z > 0.7$ were prioritized for LRIS follow-up, given the target wavelength coverage of 1500–2800 Å in the rest-frame. The significant fraction of objects at larger redshifts reflects our heightened prioritization of galaxies at $1.19 \leq z \leq 1.35$. Observations of galaxies in this redshift interval yield simultaneous coverage of the C IV λ1549 and Mg I λ2852 features for the typical LRIS set-up, enabling a comparison of the kinematics of neutral, low-, and high-ionization species (Shapley et al., in prep.).

$\sim$ 7,000 spectroscopically-confirmed DEEP2 EGS objects at $0.70 < z < 1.35$. Objects with $B < 24.5$ were targeted for LRIS observations, resulting in a sample dominated by brighter, bluer galaxies. The redshift distribution of our EGS sample is presented in Figure 3.3, where $\langle z \rangle = 0.99 \pm 0.29$.

The LRIS data, collected in October 2007, June 2008, September 2008, and June 2009, were obtained using 1.″2 slits on nine multi-object slitmasks targeting 20–28 objects each. The dichroic capability of LRIS was employed with the grism on the blue side and the grating on the red side. We used two set-up configurations, both with the Atmospheric Dispersion Corrector: the d680 dichroic with the 400 line mm^{-1} grism and the 800 line mm^{-1} grating (145 objects; 47 in the EGS) and the d560 dichroic with the 600 line mm^{-1} grism and the 600 line mm^{-1} grating (67 objects; 25 in the EGS). The resolutions of the 800, 600 and 400 line mm^{-1} grisms/gratings are $R = 2000$, 1100, and 700, respectively. Features bluer than Mg II $\lambda\lambda$2796/2803 generally fell on the blue side while Mg II $\lambda\lambda$2796/2803 and longer wavelength lines (e.g., [O II]) were recorded on the red side.

Continuum signal-to-noise (S/N) ratios ranged from $\sim$ 1–20 per pixel over the rest wavelength interval 2400–2500 Å. In Figure 3.4, we show several individual LRIS spectra with a range of measured S/N ratios. Integration times varied from 3–9 hours per slitmask, where objects observed with the d560 dichroic had typically shorter exposures (3–5 hours) than objects observed with the d680 dichroic (5–9 hours). The reduction procedure – flat-fielding, cosmic ray rejection, background subtraction, extraction, wavelength and flux calibration, and transformation to the vacuum wavelength frame – was completed using `IRAF` scripts. The spectra were continuum-normalized and composite spectra were assembled from stacks of mean-combined rest-frame spectra scaled to a common mode over the wavelength range 2080–2150 Å. In assembling the composite spectra discussed in

later sections, we smoothed the objects obtained with the 600 line mm^{-1} grism or grating in order to account for the difference in resolution between the objects observed with the 600 line mm^{-1} and 400 line mm^{-1} setups.

3.1.3 AEGIS Multiwavelength Data

The 72 EGS objects presented in this paper have extensive multi-wavelength coverage from the AEGIS dataset. These data products cover observations over nine decades in wavelength, including *Chandra* X-ray, *GALEX* FUV and NUV imaging, *HST* ACS F606W (V) and F814W (I) imaging, optical CFHT and MMT observations, Palomar/WIRC J and K_s imaging, *Spitzer* IRAC and MIPS pointings, and VLA radio observations. This wealth of data permits many analyses, including the estimation of SFR, specific star-formation rate (sSFR = SFR/M_*), $\Sigma_{\rm SFR}$, morphology, inclination, and dust attenuation. Here, we discuss the diffraction-limited *HST* Advanced Camera for Surveys (ACS; Ford et al., 2003) imaging that forms the backbone of our spatially-resolved analyses. In the sample of 72 EGS objects presented here, 56 galaxies have *HST* coverage.

Reduced *HST* images (Cycle 13, Program 10134, PI Marc Davis) were drizzled from four exposures to produce final 8000 × 8000 pixel images with a sampling of 0.″03 pixel^{-1} and a point spread function (PSF) FWHM of $\sim$ 0.″1. These deep (V = 28.75 AB [5σ]; I = 28.10 AB [5σ]) images were used for several estimates of galaxy extent and light distribution, including the Petrosian radius, the Gini coefficient, and M_{20}. The Gini coefficient originated from the field of economics to describe the distribution of wealth in a society; the term is used in astronomy to parameterize how a galaxy's light is distributed. Gini coefficients close to 1 indicate that a galaxy's flux is concentrated in a few bright pixels while values closer to 0 mean that the flux is more evenly distributed over many

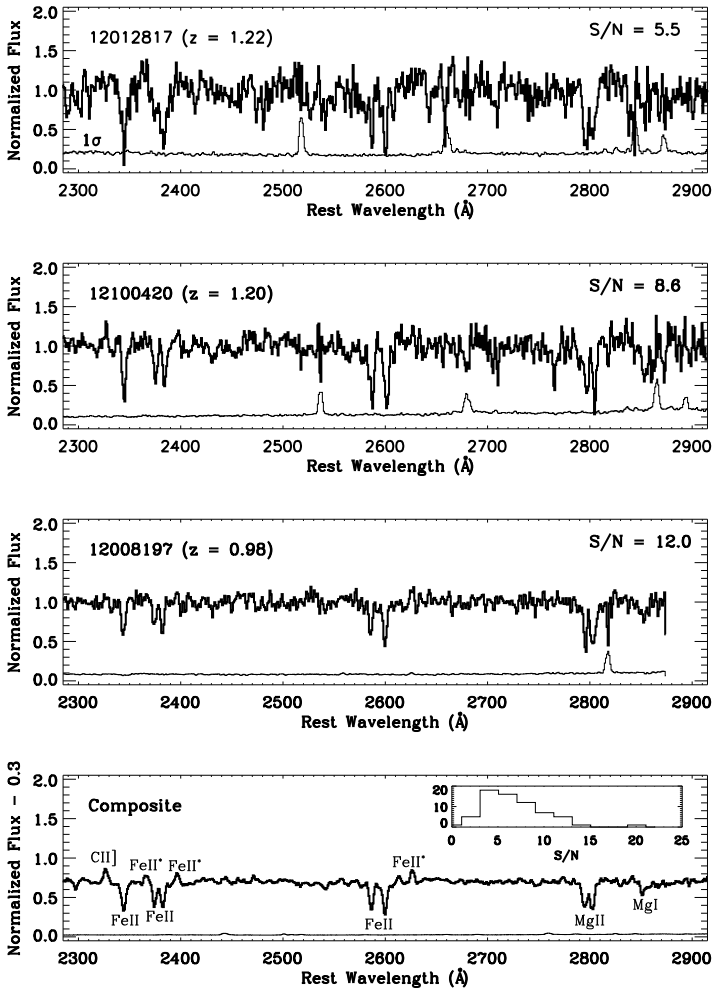

Figure 3.4 *Top three panels*: Individual LRIS spectra exhibiting a range in continuum S/N. The 1σ error spectrum is plotted for each object on the same scale. In each panel, the S/N per pixel measured over 2400–2500 Å is indicated in the upper right-hand corner. We note that Fe II and Mg II absorption lines are detected in objects with a variety of S/N values. *Bottom:* A composite spectrum assembled from all EGS spectra (S/N = 39.1 pixel^{-1}), with emission and absorption lines of interest labeled. The inset shows a histogram of continuum S/N ratios, where $\langle \mathrm{S/N} \rangle \sim 6.7$ pixel^{-1}.

pixels. M_{20} refers to the normalized second-order moment of the brightest 20% of a galaxy's flux; larger M_{20} values are associated with merging systems while smaller M_{20} values describe more compact galaxies. We direct the reader to Lotz et al. (2004) for a more complete description of the Gini coefficient and M_{20}.

3.2 Star-Formation Rates, Galaxy Areas, and Star-Formation Rate Surface Densities

The multi-wavelength observations of the AEGIS dataset enable detailed measurements of the star-forming properties of the sample. Based on *HST* imaging, we note that the majority of objects appear to have clumpy morphologies (Figure 3.5). The UV-bright clumps may be star-forming regions embedded in lower surface brightness disks (Förster Schreiber et al., 2006). We consequently derive a new estimate of galaxy size inclusive of only the brightest regions likely associated with star formation and use these areas in tandem with SFR estimates in order to calculate $\Sigma_{\rm SFR}$. We also use standard Petrosian size measurements to calculate $\Sigma_{\rm SFR}$ as well.

3.2.1 Star-Formation Rates

We used *Galaxy Evolution Explorer* (*GALEX*; Martin et al., 2005) and *Spitzer Space Telescope* imaging from the AEGIS dataset to estimate the SFRs of the sample. Given the significant attenuation experienced by UV radiation, SFRs inferred from *GALEX* measurements must be corrected for dust absorption. Data from *GALEX*'s FUV and NUV detectors, along with B-band observations (for the higher-redshift objects in the sample), were used to calculate a spectral slope, β, where the flux level over the rest-frame interval 1250–2500 Å is parametrized

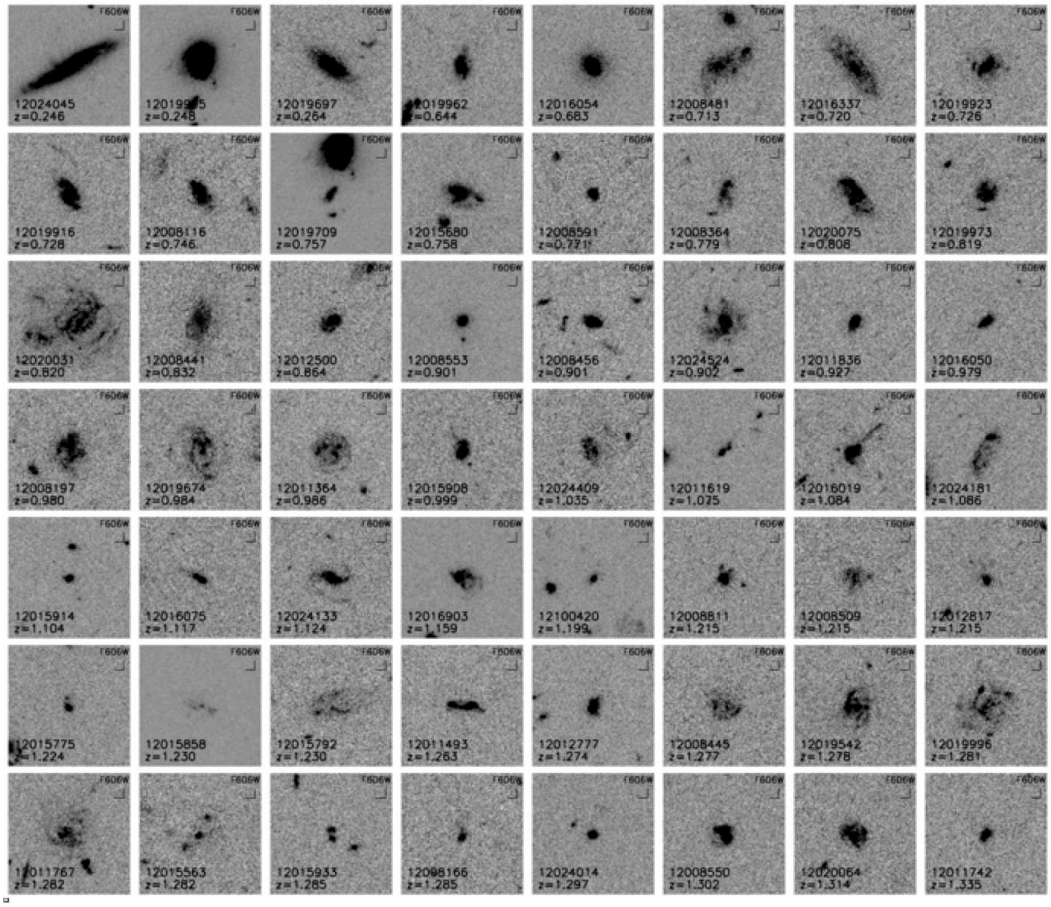

Figure 3.5 V-band thumbnails of the 56 objects with HST imaging, ordered by ascending redshift. Each postage stamp is 6″ on a side and oriented with North up and East to the left. Note the clumpy morphologies and discrete star-forming clumps of many objects. At the mean redshift of the sample, $\langle z \rangle = 0.99$, the V-band traces ~ 3000 Å in the rest-frame.

as $f_\lambda \propto \lambda^\beta$. Following Meurer et al. (1999), Seibert et al. (2005) derived a relationship between β and the UV attenuation, A_{UV}, based on a sample of several hundred nearby galaxies with both *GALEX* and *Infrared Astronomical Satellite* (Neugebauer et al., 1984) imaging. For the sample presented here, Schiminovich et al. (2007) used the β/A_{UV} relationship from Seibert et al. (2005) to correct *GALEX* luminosities for attenuation. The median A_{UV} value in the sample is 1.8, which corresponds to a factor of ~ 5 correction. UV SFRs corrected for dust – $SFR_{UV,corr}$ – were then calculated for a Salpeter (1955) IMF over 0.1–100 $M_\odot$, according to Salim et al. (2007). We converted all values to the Chabrier (2003) IMF by dividing the Salpeter (1955) values by 1.8. 54/72 objects ($\sim 75\%$) have $SFR_{UV,corr}$ measurements, where the 18 objects lacking β measurements were observed by *GALEX* but were either not significantly detected or suffered from confusion with neighboring objects[1]. The $SFR_{UV,corr}$ measurements of the sample are characterized by a median value of 12 $M_\odot$ yr^{-1} and extrema of [1, 97] $M_\odot$ yr^{-1} (Figure 3.6).

These $SFR_{UV,corr}$ values are consistent with SFRs inferred from longer wavelength measurements. Robust *Spitzer* 24μm detections ($f_{24\mu m} \geq 60$ μJy) were used to calculate a total infrared luminosity, L_{IR}, based on templates relating L_{IR} and $f_{24\mu m}$ (Chary & Elbaz, 2001). While these templates are representative only of quiescent and starbursting galaxies – not Active Galactic Nuclei (AGN) – we note that AGN are likely a minimal contaminant in the sample given that a cross-correlation with *Chandra* X-ray catalogs yielded only 1 match for our sample above the limiting fluxes of 5.3×10^{-17} (3.8×10^{-16}) erg s^{-1} cm^{-2} in the soft (hard) bands (Laird et al., 2009). At the mean redshift of our sample, $\langle z \rangle = 0.99$, these flux limits correspond to AGN luminosities of 2.7×10^{41} (1.9×10^{42})

[1] *GALEX* has a PSF of $\sim 5''$–$6''$ for FUV and NUV observations (Martin et al., 2005).

erg s^{-1} in the soft (hard) bands[2]. A SFR was then estimated from the addition of SFRs derived from L_{IR} (Kennicutt, 1998) and L_{UV} (Schiminovich et al., 2007), where the latter term is a UV luminosity uncorrected for dust. While only 17/72 objects presented here ($\sim$ 25%) have both UV detections and $f_{24\mu m} \geq 60$ μJy, a larger sample of objects with these measurements shows a correlation between the two SFRs with a scatter of $\sim$ 0.4 dex (Figure 3.7). In light of this consistency and the relative scarcity of objects with $f_{24\mu m}$ detections, we use $SFR_{UV,corr}$ ("SFR") in all of the following analyses.

It is useful to compare the SFRs of the present sample with the SFRs of other recent outflow studies at $z \sim 1$. Weiner et al. (2009) presented an outflow survey of DEEP2 objects at $z \sim 1.4$ with 25th and 75th percentile values of SFR of 14 and 28 $M_\odot$ yr^{-1}, respectively, derived from UV measurements assuming a Kroupa (2001) IMF. Work by Rubin et al. (2010b) utilized objects with smaller SFRs: 25th and 75th percentile values of SFR of 4 and 9 $M_\odot$ yr^{-1}, respectively. The Rubin et al. (2010b) SFRs were also derived assuming a Kroupa (2001) IMF using UV measurements. The objects in this paper have 25th and 75th percentile values of 6 and 25 $M_\odot$ yr^{-1}, respectively, assuming a Chabrier (2003) IMF. For direct comparison with the Weiner et al. (2009) and Rubin et al. (2010b) samples, these values correspond to 8 and 31 $M_\odot$ yr^{-1}, respectively, for a Kroupa (2001) IMF.

In Figure 3.8, we plot SFR versus stellar mass and sSFR versus stellar mass. We find a pronounced correlation between SFR and stellar mass. As this relationship is consistent with the correlation observed in the larger DEEP2 sample,

[2]As we do not include the one X-ray detected object (12015320) in our analyses, we believe that the winds we observe are driven by star formation as opposed to AGN activity. Based on rest-frame UV spectra, the objects in our sample do not exhibit signatures of AGN activity although we acknowledge possible contributions from obscured AGN. Krug et al. (2010) note that starburst and Seyfert 2 systems show similar outflow kinematics.

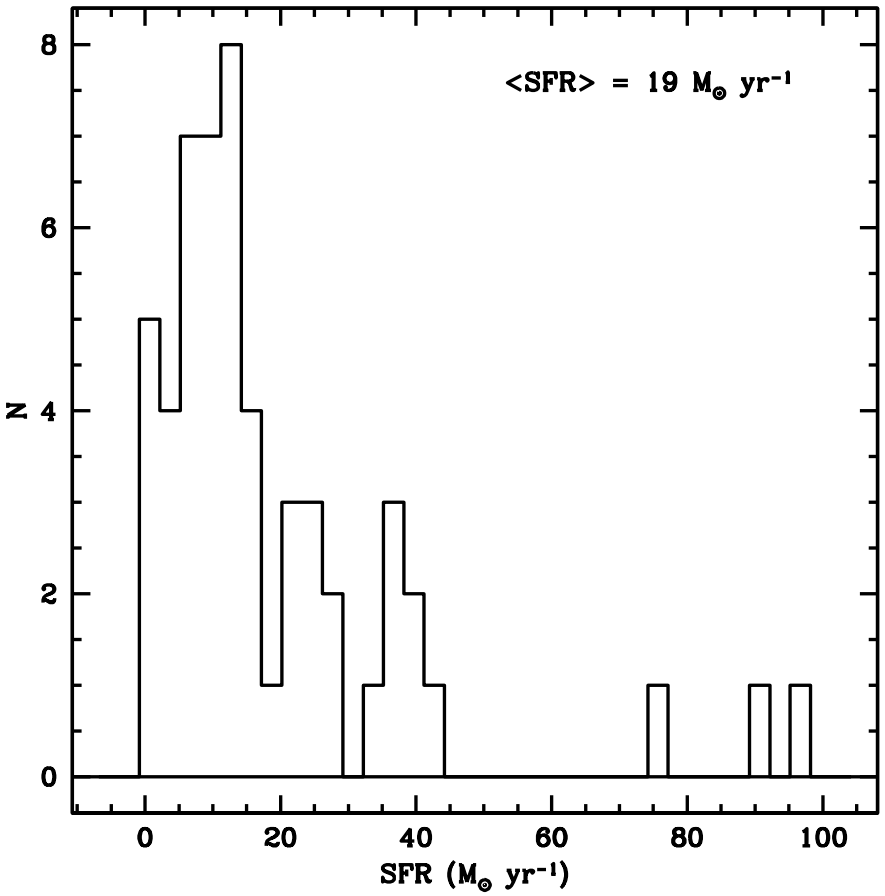

Figure 3.6 Histogram of SFRs, assuming a Chabrier (2003) IMF. The sample is characterized by a mean value of $\langle \mathrm{SFR} \rangle = 19\ M_{\odot}\ \mathrm{yr}^{-1}$.

the subsample of objects discussed here do not appear to have star-formation histories grossly inconsistent with other datasets.

3.2.2 Calculating a "Clump Area"

It has been suggested that there exists a threshold star-formation rate surface density of $\Sigma_{\rm SFR} = 0.1$ $M_{\odot}$ yr^{-1} kpc^{-2} for driving an outflow in local starbursts (Heckman, 2002). As estimating $\Sigma_{\rm SFR}$ requires areal information, it is important to characterize properly the extent over which star formation is occuring. While values in the literature often refer to r = half-light radius or Petrosian radius (Rubin et al., 2010b; Steidel et al., 2010), the clumpy morphologies of high-redshift galaxies observed in the rest-frame UV necessitate a different treatment. Rubin et al. (2010b) noted that the simple approximation of πr^2 for the area of a galaxy may result in an overestimate; these authors proposed that the inclusion of only star-forming knots above a specified luminosity threshold may be the most physically motivated method for calculating a galaxy area associated with outflowing material.

As the majority of objects in our EGS sample appear to have irregular knots of star formation instead of being clearly disk-dominated (Figure 3.5), we used diffraction-limited *HST* V-band imaging to investigate appropriate areal measurements. V-band imaging traces rest-frame $\sim$ 2970 Å at $z = 0.99$, the mean redshift of the sample. We began by estimating the total non-contiguous area of each galaxy above a certain surface brightness limit. The motivation behind this technique stemmed from flagging pixels that corresponded to some measurable physical quantity (in this case, surface brightness or, equivalently, $\Sigma_{\rm SFR}$). Schematically, the conversion from counts per pixel in the images to $\Sigma_{\rm SFR}$ can be illustrated as follows:

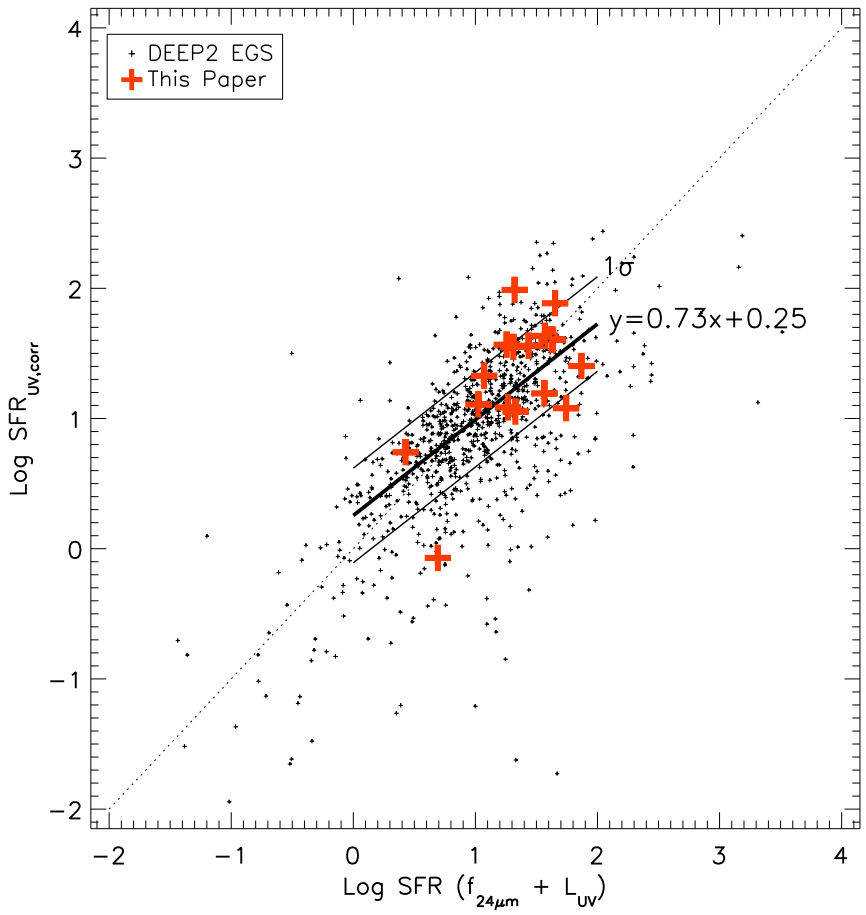

Figure 3.7 Comparison of two SFR indicators: a UV-corrected SFR ($SFR_{UV,corr}$, where the dust correction is inferred from UV colors) and a SFR inferred from the sum of 24μm data and uncorrected UV observations: SFR ($f_{24\mu m}$ + L_{UV}). The units of SFR are $M_{\odot}$ yr^{-1}. The bold crosses indicate the 17 EGS objects in this paper with robust 24μm data and the smaller crosses mark objects in the larger DEEP2 EGS parent sample. Data in the interval 1 < SFR ($f_{24\mu m}$ + L_{UV}) < 100, the approximate range of SFRs measured in this paper, have been used to calculate the best-fit line (y = 0.73x + 0.25). The dotted line indicates the 1:1 relation. The good agreement between $SFR_{UV,corr}$ and SFR ($f_{24\mu m}$ + L_{UV}), $\sigma \sim 0.4$ dex, supports adopting $SFR_{UV,corr}$ given the relatively small number of objects with 24μm data.

$$\frac{\textbf{counts}}{\textbf{pixel}} \xrightarrow{\text{via zpt}} \frac{\textbf{f}_\nu}{\textbf{pixel}} \xrightarrow{\text{via } z} \frac{\textbf{L}_\nu}{\textbf{kpc}^2} \xrightarrow{\text{via K98}} \frac{\textbf{SFR}}{\textbf{kpc}^2} \tag{3.1}$$

where zpt is the *HST* V-band zeropoint (26.5 AB) and K98 refers to the conversion between rest-frame UV luminosity over 1500–2800 Å ($L_{\rm UV}$) and SFR assuming a Salpeter (1955) IMF over 0.1–100 $M_\odot$ (SFR $= 1.4 \times 10^{-28}$ $L_{\rm UV}$; Kennicutt, 1998). With images now in units of $\Sigma_{\rm SFR}$, a simple $\Sigma_{\rm SFR}$ threshold can be implemented. In light of local work by Heckman (2002)[3], we adopted the criterion $\Sigma_{\rm SFR} = 0.1$ M$_\odot$ yr^{-1} kpc^{-2}. While imposing this threshold produces areas that visually trace luminous galaxy clumps, we note two limitations to this methodology: 1) no correction for dust attenuation is applied, as estimates of the UV slope β are available for only a subset of the sample and 2) we do not account for effects of galaxy inclination i, given the uncertainties of estimating i for clumpy objects with angular sizes $\sim 0.''5$. Increased dust and higher i will both act to reduce the measured luminosity.

While the unknowns of dust attention and inclination translate into uncertainties in the derived galaxy area (and consequently in $\Sigma_{\rm SFR}$), there is a more fundamental limitation to adopting the aforementioned methodology: the available V-band imaging ceases to trace below rest-frame 2800 Å – the edge of the window over which the Kennicutt (1998) conversion is valid – for galaxies at lower redshifts ($z < 1.10$; 32 objects). For these comparably closer objects – comprising $\sim 60\%$ of the sample – the Kennicutt (1998) relation between $L_{\rm UV}$ and SFR cannot be applied.

It was accordingly necessary to develop a new technique for estimating areas of the entire sample, irrespective of redshift. To this end, we focused on character-

[3]As the Heckman (2002) threshold is only approximate, and was calculated assuming a Salpeter (1955) IMF, we adopt the same IMF in converting from luminosity to SFR.

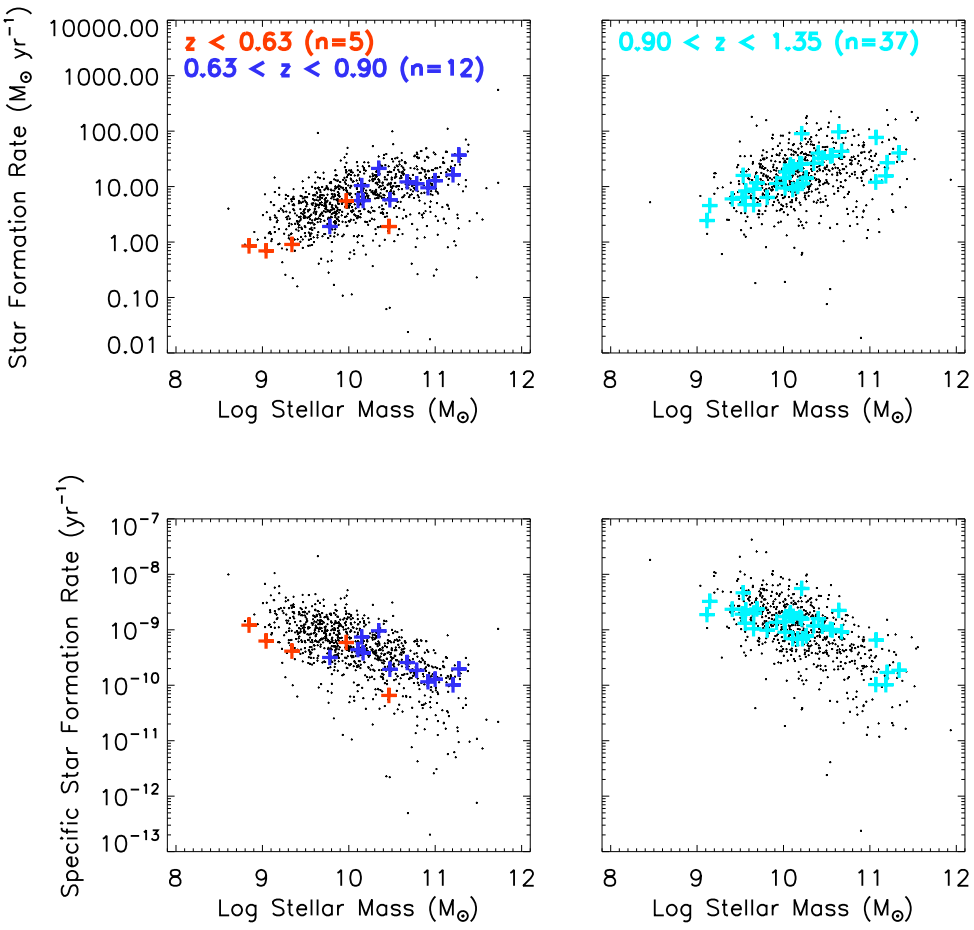

Figure 3.8 *Top left:* SFR versus stellar mass, where the small background points indicate EGS galaxies at $0.63 < z < 0.90$ without LRIS follow-up and colored crosses mark galaxies observed with LRIS, divided into two redshift bins. *Top right:* Same as the plot on the left, for the redshift interval $0.90 < z < 1.35$. We note that the data presented in this paper have stellar masses and SFRs consistent with the parent DEEP2 sample. *Bottom:* Stellar mass versus sSFR, where symbols are as above.

izing the areas of the higher redshift galaxies in the sample ($z > 1.10$; 24 objects) for which the V-band imaging *does* trace rest-frame 1500–2800 Å. For each of these objects, we noted the area calculated using the methodology described above and the threshold 0.1 $M_\odot$ yr^{-1} kpc^{-2}. We then sought to parametrize these physically-motivated areas as containing a simple percentage (N) of the total flux within the Petrosian radius, R_P. This technique enabled us to estimate an average value for N and then apply this value uniformly to both the higher and lower redshift galaxies.

We found that, with the exception of several diffuse disks and extremely compact spheroids, the majority of objects required N = [40–80]. The median of the sample was N = 74; we adopted this value as representative of the fractional flux within R_P that traced regions of intense star formation. For each galaxy with *HST* imaging, we calculated the area derived by adding flux-ordered pixels, brightest first, until the enclosed flux was 74% of the total flux within R_P[4]. This method permits a single, systematic area calculation (A_{74}) for each galaxy independent of redshift while still being based on the physical grounding of a surface brightness threshold. We make the implicit assumption that N does not vary significantly over the range of look-back times probed by our sample.

We find that areas calculated using this new technique are, on average, a factor of 3.7 smaller than the areas inferred from the V-band Petrosian radii: $A_{74} \sim \pi R_P^2/3.7$. As seen in Figure 3.9, A_{74} appears to closely trace luminous clumpy regions[5] while the Petrosian area consistently overestimates the area likely associated with star formation. We consequently favor the adoption of A_{74} over πR_P^2, although we use both area estimates below in tandem with derived SFRs in

[4]Two objects were excluded from this analysis (12008364 and 12015792), given that their surface brightness levels were too low to measure R_P.

[5]The *HST* resolution, while excellent, is finite, so these areas represent upper limits.

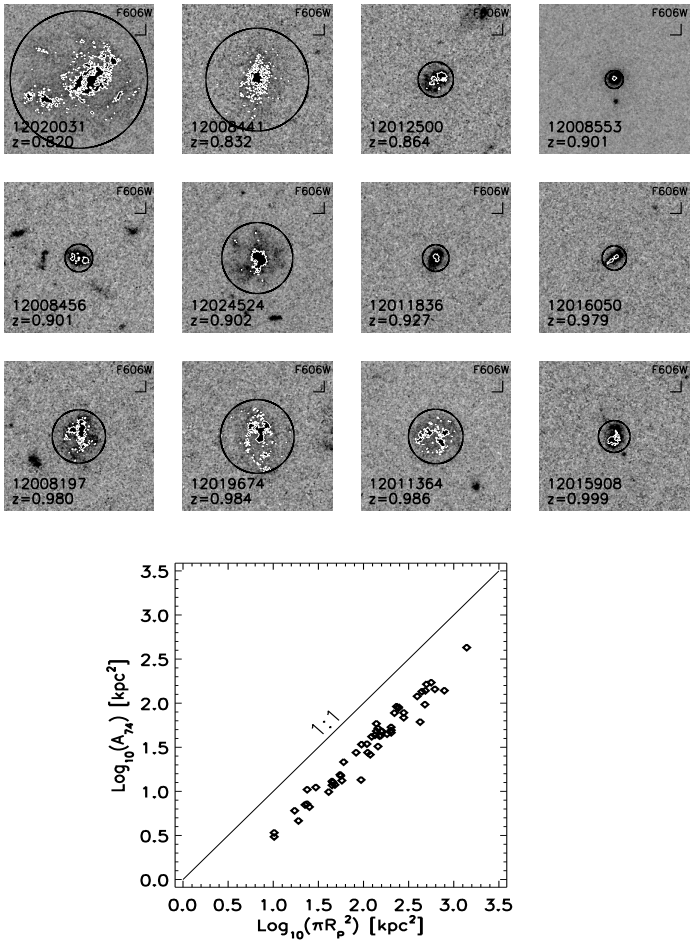

Figure 3.9 V-band *HST* thumbnails, 6″ on a side, are shown for a subset of 12 objects to illustrate the A_{74} clump areas derived in Section 3.2. These 12 objects were chosen as representing a diversity of clump areas, from compact, contiguous areas to more diffuse, segmented areas. Petrosian radii are plotted as black circles while the clump areas are shown as white contours. The ratio between the areas – $\pi R_P^2/A_{74}$ – is indicated in the lower right of each thumbnail. The lower plot compares the πR_P^2 and A_{74} areas for the sample, where $\langle \pi R_P^2/A_{74} \rangle \sim 3.7$. We note that the strong correlation between the Petrosian area and the clump area explains the similar results obtained with the two Σ_{SFR} measurements (Section 3.4).

order to calculate Σ_{SFR}. Given the strong correlation between A_{74} and πR_P^2, we note that our primary results remain unchanged regardless of which area estimate is adopted (Section 3.4). While the initial motivation for calculating A_{74} was to isolate an area measurement distinct from, and uncorrelated with, πR_P^2, our finding that these two area estimates are in fact strongly linked is evidence that the structural morphologies of the galaxies in the sample are rather similar. If the light distributions of the galaxies were widely disparate, we would not expect that galaxies with larger Petrosian areas would also have larger A_{74} areas while galaxies with smaller πR_P^2 would likewise have smaller clump areas. We verified that the correlation between πR_P^2 and clump area holds for a variety of N values.

3.2.3 Star-Formation Rate Surface Densities

With two estimates of galaxy area (A_{74} and πR_P^2) and one estimate of SFR, we calculated the star-formation rate surface densities of the sample. We define two Σ_{SFR} quantities, depending on which area measurement we adopt:

$$\Sigma_{SFR}(A_{74}) = SFR/A_{74} \tag{3.2}$$

$$\Sigma_{SFR}(R_P) = SFR/\pi R_P^2 \tag{3.3}$$

Figure 3.10 shows the distributions of $\Sigma_{SFR}(A_{74})$ and $\Sigma_{SFR}(R_P)$. Irrespective of the area measurement assumed, most objects have star-formation rate surface densities above the local threshold of 0.1 $M_\odot$ yr^{-1} kpc^{-2} thought to be necessary for driving an outflow (Heckman, 2002). While this is by construction for $\Sigma_{SFR}(A_{74})$, the fact that greater than 70% of objects also have $\Sigma_{SFR}(R_P) > 0.1$ $M_\odot$ yr^{-1} kpc^{-2} leads to the prediction that if a threshold Σ_{SFR} is the sole requirement for driving an outflow, the majority of objects ought to exhibit blueshifted Fe II features. Of course, other factors such as local environment, halo mass,

galaxy escape speed, and viewing angle, as well as the S/N of the data, may strongly influence the observed fraction of galaxies hosting winds. As discussed above, we do not correct A_{74} areas for either dust or inclination effects. We find kinematic evidence for 1σ significant outflows based on Fe II absorption lines in 40% of the sample (Section 3.3.2), although we note that the Mg II features often exhibit strong blueshifts of their centroids and blue wings even when the Fe II lines do not (Section 4.4).

3.3 Modeling Absorption Lines

3.3.1 Systemic Redshift

Spectral analysis of outflowing gas requires an accurate determination of systemic redshift, $z_{\rm sys}$. Nebular emission lines such as [O II] $\lambda\lambda$3726/3729, [O III] $\lambda\lambda$4959/5007, and the Balmer series trace star forming regions and are consequently assumed to be at rest with respect to a galaxy's center of mass. While both the DEIMOS and LRIS spectral datasets are inclusive of nebular features, it is preferable to calculate $z_{\rm sys}$ from the LRIS spectra in order to ensure constancy in both slit position angle and spatial sampling for the $z_{\rm sys}$ and outflow measurements. We constructed a linear, S/N-weighted sum of three template spectra – post-starburst, old stellar population absorption line, and emission line – and used the DEEP2 `IDL` pipeline to compare the template spectrum with each science spectrum. In the estimation of systemic redshifts, only lines with rest wavelengths longer than 3000 Å were fit in order to exclude bluer features tracing winds. The χ^2 of the fit was minimized according to redshift, and a best-fit $z_{\rm sys}$ was extracted. For 63/72 objects ($\sim$ 90%), it was possible to extract $z_{\rm sys}$ from the LRIS spectra. For the nine objects in the sample without [O II] spec-

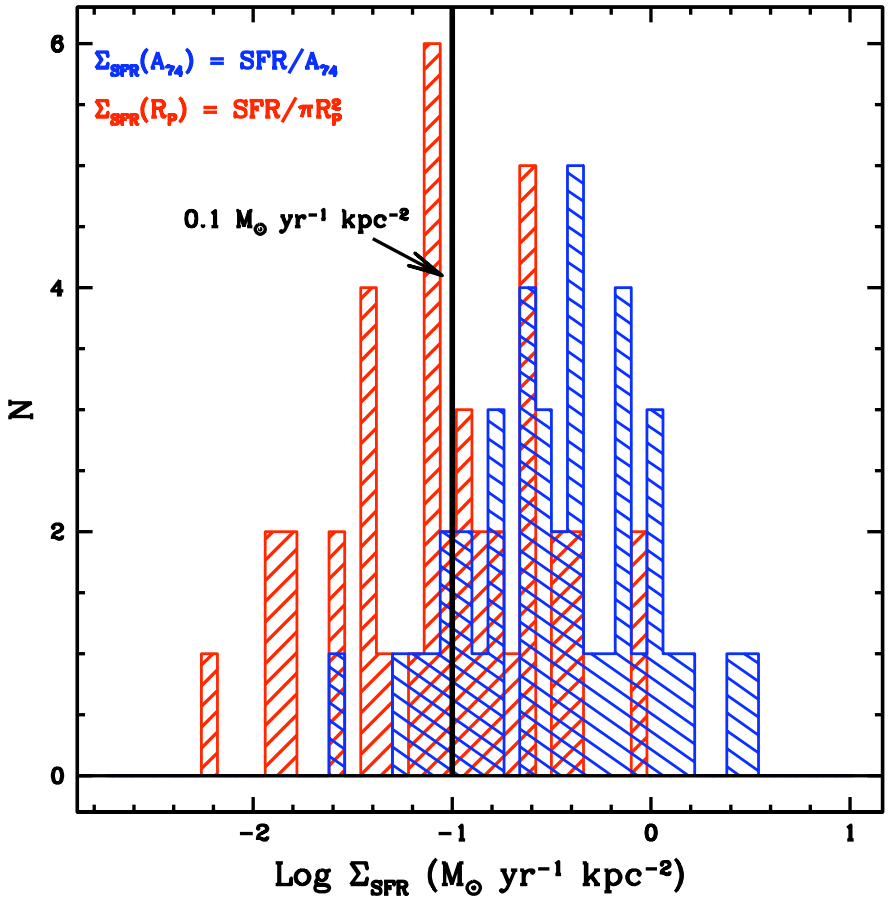

Figure 3.10 Distributions of star-formation rate surface densities $\Sigma_{SFR}(A_{74})$ and $\Sigma_{SFR}(R_P)$, where these quantities are calculated using SFR and either A_{74} or πR_P^2. Greater than 70% of objects have $\Sigma_{SFR}(R_P) > 0.1$ $M_\odot$ yr^{-1} kpc^{-2}, the local threshold for driving an outflow (Heckman, 2002). The two objects with the highest $\Sigma_{SFR}(A_{74})$ and $\Sigma_{SFR}(R_P)$ – 12015914 and 12100420 – are both extremely compact galaxies with A_{74} (πR_P^2) areas of ~ 3 (10) kpc^2.

tral coverage in the LRIS data, $z_{\rm sys}$ was calculated from the DEIMOS spectra using the same technique. In comparing measurements of $z_{\rm sys}$ with those given for the DEIMOS data in the DEEP2 catalogs, we find a mean discrepancy and standard deviation of $\langle \delta z \rangle = 9 \times 10^{-5}$ (16 km s^{-1}) and $\sigma_{\delta z} = 2.6 \times 10^{-4}$ (42 km s^{-1}), respectively. These results are consistent with the values obtained when considering the entire LRIS sample (Martin et al., 2012).

3.3.2 Fitting Lines – Fe II Centroids

Simulations of galactic winds suggest that multiple fronts of outflowing material are present along any one sightline (e.g., Fujita et al., 2009). While fitting several outflow components simultaneously would in principle provide the best diagnostic of these superimposed winds, the finite spectral resolution and S/N of observations typically limit fitting to a single wind component that is assumed to trace the integrated bulk motion of the outflow. The measurements we present here, which derive from and are discussed more fully in Martin et al. (2012), make the approximation of a single outflow velocity. Furthermore, we do not decompose the observed absorption profile into both a wind component and an absorption trough at the systemic velocity, where the latter may arise from stationary material present in stellar atmospheres or in the surrounding interstellar medium. Several recent outflow studies have modeled absorption lines as arising from the sum of wind and systemic components (Weiner et al., 2009; Chen et al., 2010; Coil et al., 2011), although the implementation of such a technique is strongly dependent on the quality of the spectroscopic data. Steidel et al. (2010) note that the limited resolution and finite S/N of typical spectroscopic observations at $z = 1$–3 often preclude fitting a more complex model than a single absorption profile. In light of the S/N of our data, we do not apply a correction for material

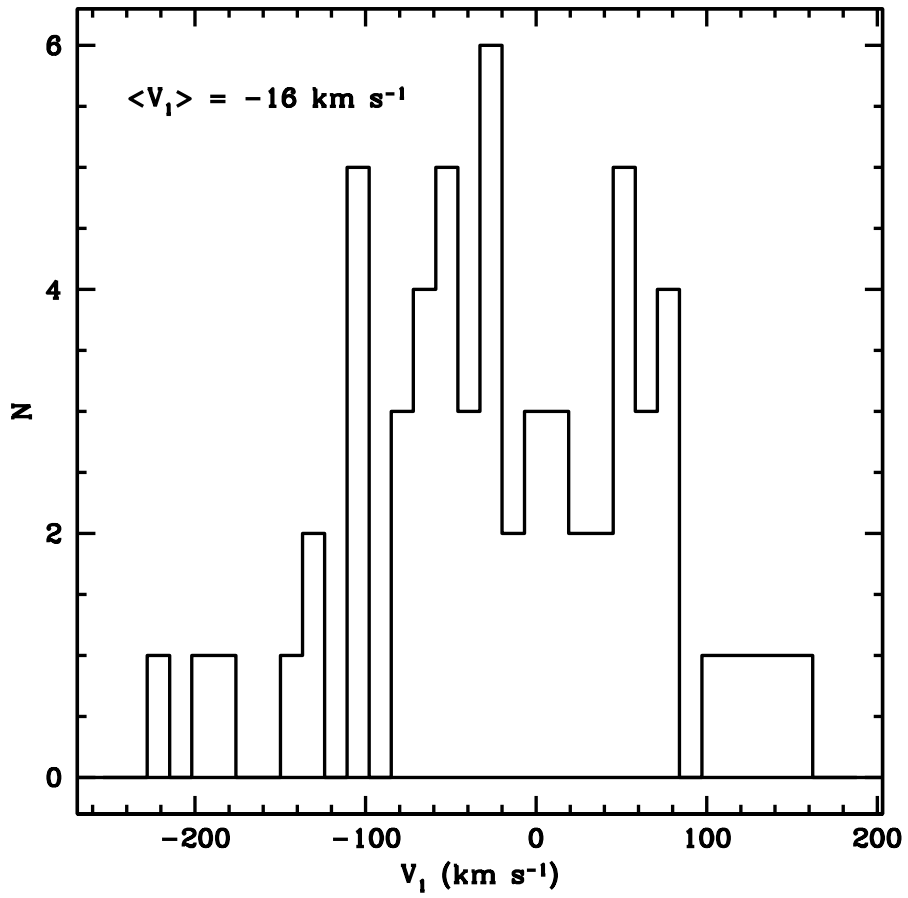

Figure 3.11 Histogram of outflow velocities measured from fitting Fe II interstellar absorption lines. Outflows (negative V_1 values) are seen at the 1σ level in $\sim 40\%$ of the sample. A non-negligible fraction of objects ($\sim 25\%$) show positive Fe II velocities at the 1σ level. The sample as a whole is characterized by $\langle V_1 \rangle \sim -16$ km s^{-1}, with a 1σ scatter of 82 km s^{-1}.

at the systemic velocity[6]. The outflow velocities presented here are accordingly conservative lower limits (Martin et al., 2012).

In Martin et al. (2012), we fit a single-component model simultaneously to five resonance Fe II lines at 2249.88, 2260.78, 2344.21, 2374.46, and 2586.65 Å in the LRIS spectra. These lines trace cool ($T < 10^4$ K) gas. Upon absorbing a resonance photon at one of these five wavelengths, the Fe II ion can decay by either emitting a photon of equal wavelength as the one it just absorbed (scattering) or emitting a photon to intermediate fine-structure levels (fluorescence). The presence of these fine-structure levels ensures that the resonance absorption lines are not simply filled in with scattered re-emitted resonance photons ("emission filling"; Prochaska et al., 2011). The Fe II features at 2382.76 and 2600.17 Å are more susceptible to emission filling due to their dearth of alternate decay paths (Prochaska et al., 2011, Martin et al. 2012b, in prep.) and we purposefully omit these lines from fitting as emission filling can shift the measured centroid of absorption lines to bluer wavelengths (e.g., Prochaska et al., 2011). The Mg II features at $\lambda\lambda$2796/2803 are particularly affected by emission filling as these transitions have no fine-structure levels; in the absence of dust extinction, all absorbed resonance photons are re-emitted to the ground state. We accordingly do not measure the centroids of Mg II absorption but instead develop a method to parameterize the blue wing of the absorption profile (Section 3.3.3).

The model fit to the Fe II lines has four free parameters: Doppler shift, column density, Doppler width (b, where $b = \sqrt{2}\sigma = \mathrm{FWHM}/2\sqrt{\ln 2}$), and covering fraction. Due to the low spectral resolution and finite S/N of the observations,

[6]As the majority of the sample is composed of actively star-forming galaxies, stellar absorption in the Fe II and Mg II lines is assumed to be minimal (e.g., Bruzual & Charlot, 2003b). While objects with $U-B$ colors between the red sequence and the blue cloud (i.e., "Green Valley" galaxies) may experience substantial stellar Mg II absorption, we have verified that our results are qualitatively unchanged when the ten Green Valley galaxies in our sample are omitted from analyses.

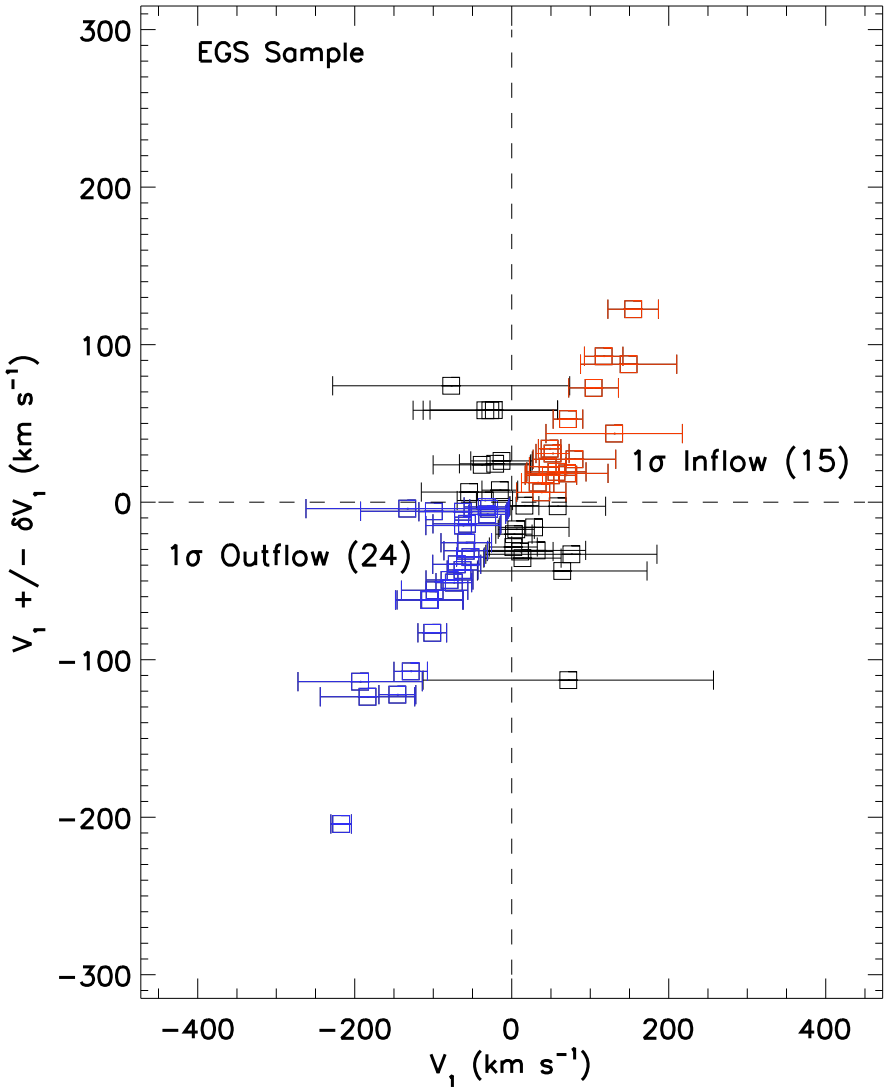

Figure 3.12 A graphical representation of outflows and inflows, for the 61 objects with measured velocities. The y-axis is the measured Fe II outflow velocity modulated by its 1σ uncertainty, where the uncertainty was added to the velocity for objects showing outflows ($V_1 < 0$ km s^{-1}) and subtracted from objects exhibiting inflows ($V_1 > 0$ km s^{-1}). With the Fe II outflow velocity as the x-axis, the plot divides into quadrants: objects with significantly detected outflows cluster in the lower left (blue points) and galaxies with significantly detected inflows appear in the upper right (red points).

the Doppler shift fit to the five Fe II lines is the primary quantity of interest; the other three parameters of the model will not be discussed in this paper. We measured velocities for 61/72 objects, where 11 objects had no significant absorption lines and therefore could not be modeled, and find velocities ranging from –217 km s^{-1} to +155 km s^{-1} with a mean of –16 km s^{-1} and a 1σ dispersion of 82 km s^{-1} (Figure 3.11). This range and mean are similar to the values measured for the entire LRIS sample (Martin et al., 2012). We define here the convention of employing "V_1" to refer to the measured velocity shift of the deepest part of the Fe II absorption line fit, relative to a systemic reference frame defined by [O II] and Balmer emission lines. Negative V_1 values refer to blueshifts ("outflows") while positive V_1 values correspond to redshifts ("inflows"). Fe II velocity shifts significant at the 1σ (3σ) level are observed in $\sim$ 40% (10%) of the sample (Figure 3.12). Within the sample of objects with 1σ (3σ) outflows, $\langle V_1 \rangle$ = –93 km s^{-1} (–130 km s^{-1}). We can also parameterize the sample by stating what percentage of objects exhibit outflows at a certain threshold velocity (Martin et al., 2012). The 1σ error associated with the each object's velocity can be taken as the standard deviation of a Gaussian probability distribution for the outflow velocity of the object. Using these probability distributions, we calculated the fraction of objects in the sample having blueshifts of at least –40 km s^{-1} (i.e., the systemic redshift uncertainty; Section 3.3.1). We estimated errors on the outflow fraction via bootstrap resampling. We find that 40 $\pm$ 5% of objects show outflows with blueshifts of at least –40 km s^{-1}. The outflow characteristics of the EGS objects presented in this paper are consistent with the properties of the parent sample discussed in Martin et al. (2012).

While the blueshifted signature of outflowing gas has been observed at a range of look-back times and in a variety of galaxy types (e.g., Steidel et al., 1996b; Franx et al., 1997; Pettini et al., 2000, 2001; Shapley et al., 2003; Martin, 2005;

Veilleux et al., 2005; Rupke et al., 2005; Tremonti et al., 2007; Weiner et al., 2009; Steidel et al., 2010; Coil et al., 2011), detections of redshifted interstellar absorption lines – i.e., gas inflows – are much more elusive (Coil et al., 2011; Giavalisco et al., 2011; Rubin et al., 2012). We defer a discussion of individual objects in our sample showing redshifted absorption lines to our accompanying demographics paper (Martin et al., 2012).

In objects with blueshifted Fe II profiles, we still observe significant absorption at the systemic velocity of the galaxy. These absorption profiles are similar to those presented in Weiner et al. (2009) and Rubin et al. (2010b) and are distinctly different from those appearing in Tremonti et al. (2007). The massive post-starburst galaxies at $z \sim 0.6$ in the Tremonti et al. (2007) sample exhibit Mg II velocities ranging from 500-2000 km s^{-1}, where the profiles of Mg II are blueshifted enough as to nearly eliminate any residual absorption at $z_{\rm sys}$. It is evident that the systems presented in this work represent a more typical star-forming population than the galaxies discussed in Tremonti et al. (2007).

3.3.3 Maximal Outflow Velocity

While outflow velocities can be measured from the centroids of Fe II absorption lines, as discussed above, another complementary technique widely used for parameterizing outflow velocities utilizes the Mg II doublet features at 2796.35 and 2803.53 Å (Weiner et al., 2009; Giavalisco et al., 2011; Rubin et al., 2012). As the Mg II transitions are resonantly trapped – such that no decay paths exist other than the re-emission of resonance photons – these absorption lines are highly susceptible to filling from resonance emission lines. In the presence of a net outflow of gas, this filling shifts the centroid of Mg II absorption to bluer wavelengths due to the sum of blueshifted and redshifted emission preferentially

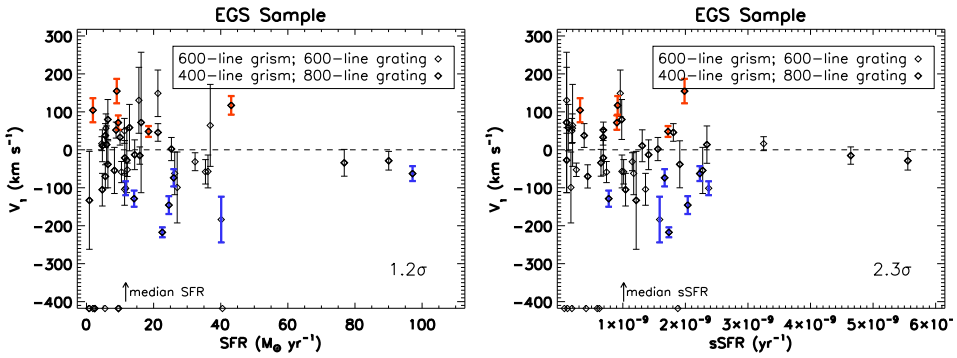

Figure 3.13 *Left:* V_1 outflow velocity versus SFR. Objects with 3σ detected outflows and inflows are indicated in blue and red, respectively. The grism and grating pair used in the LRIS observations is noted and the SFRs of objects without measured velocities (due to poor spectral signal-to-noise) appear along the x-axis. In the lower right, we indicate the significance level of the correlation. There is not a strong trend between SFR and outflow velocity in our sample, possibly due to the limited range in SFR probed by the data ($\sim$ 1–100 $M_\odot$ yr^{-1}; Rupke et al., 2005; Steidel et al., 2010; Law et al., 2012b). *Right:* V_1 outflow velocity versus sSFR, where a correlation is observed between V_1 and sSFR at the 2.3σ ($r_S = -0.33$) level. Symbols are the same as in the V_1 versus SFR plot.

filling in the absorption around the systemic velocity. The most meaningful velocity measurements of Mg II are therefore those made largely independently of the Mg II centroid. We quantify shifts in Mg II using a technique reliant on the profile of the blue side of the 2796 Å feature; we do not use the 2803 Å feature as it may be contaminated by emission from the 2796 Å line. We adopt a methodology similar to the $V_{10\%}$ measurement of Weiner et al. (2009), as described in Martin et al. (2012). Firstly, we isolate the minimum of the 2796 Å trough and proceed to shorter wavelengths until the sum of one pixel and its uncertainty, σ, is greater than a threshold value defined by the data's continuum S/N: 1.0 - $\frac{1.0}{\mathrm{S/N}}$. We record the wavelength value at which this threshold is first met, perturb the science spectrum by a value drawn from a Gaussian distribution of width σ, and repeat the same procedure a total of 1000 times. We iteratively compute the average of these 1000 wavelengths excluding outliers and adopt this value as the maximal outflow velocity of Mg II, V_{max}(Mg II). We measure an analogous maximal outflow velocity for the Fe II 2374 Å feature using the same technique, V_{max}(Fe II). We choose to utilize the 2374 Å feature over other Fe II lines given that the blue wings of other Fe II features are often contaminated by neighboring absorption lines; the only feature close to the blue side of the 2374 Å line is a fine-structure Fe II* emission line at 2365 Å (–1124 km s^{-1}).

We report maximal outflow velocities only for composite spectra, in light of the following limitations of the maximal outflow velocity technique. Firstly, only resolved absorption lines will yield meaningful maximal outflow velocities, given that unresolved absorption lines simply reflect the instrumental profile as opposed to the intrinsic distribution of gas kinematics. Secondly, as discussed above, maximal outflow velocities are strongly dependent on the S/N of the spectroscopic data, with higher S/N data showing more blueshifted values. The uniformly high S/N of the composite spectra (27–39 pixel^{-1}) ensure that the effects of

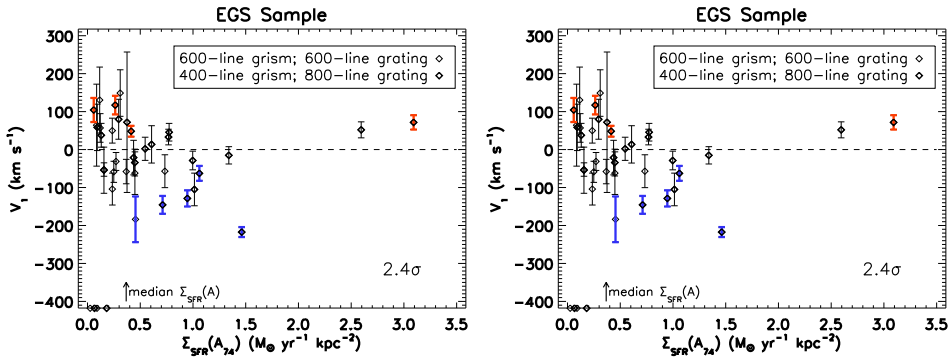

Figure 3.14 *Left:* V_1 outflow velocity versus $\Sigma_{\rm SFR}(\rm A_{74})$, where symbols are as in Figure 3.13. A correlation at the 2.4σ level (r_S = –0.40) is observed between V_1 and $\Sigma_{\rm SFR}(\rm A_{74})$, where objects with larger $\Sigma_{\rm SFR}$ show larger blueshifts in their Fe II lines. *Right:* V_1 outflow velocity versus $\Sigma_{\rm SFR}(\rm R_P)$. All objects with 3$\sigma$ detections of outflows have $\Sigma_{\rm SFR}(\rm R_P) > 0.1$ $\rm M_\odot$ $\rm yr^{-1}$ $\rm kpc^{-2}$, in agreement with the $\Sigma_{\rm SFR}$ threshold proposed by Heckman (2002). A 2.4σ correlation (r_S = –0.40) is observed between V_1 and $\Sigma_{\rm SFR}(\rm R_P)$. When the two outliers at the highest $\Sigma_{\rm SFR}$ are removed from the sample – objects 12015914 and 12100420 with extremely compact morphologies – trends at the 3.1σ level (r_S = –0.54) are observed for both $\Sigma_{\rm SFR}$ estimates. Law et al. (2012b) observed a 2.1σ correlation between outflow velocity and $\Sigma_{\rm SFR}$ in a sample of 35 star-forming galaxies at $z \sim 2$, although other authors have noted weaker correlations (Rubin et al., 2010b; Steidel et al., 2010).

differential S/N are largely mitigated. We measure V_{max}(Mg II) ranging from [–605, –855] km s^{-1} while V_{max}(Fe II) varies from [–444, –614] km s^{-1}. As these V_{max}(Mg II) and V_{max}(Fe II) values are generally more blueshifted than –435 km s^{-1}, the absorption lines are resolved and therefore yield meaningful velocity measurements.

3.4 Results

With measurements of the star-forming and structural properties of the sample, we now turn to examining the correlations between these parameters and outflow velocity. We focus here on galaxy properties inferred from the ancillary data of the EGS (morphology, inclination, SFR, sSFR, $\Sigma_{\rm SFR}$, etc.). A discussion of how outflows relate to galaxy parameters such as stellar mass, color, redshift, and luminosity measured for all objects in the parent DEEP2 sample appears in Martin et al. (2012). A comparison of the kinematics of lines tracing high- and low-ionization interstellar features will also be presented in an upcoming paper (Shapley et al., in prep.).

We adopt two complementary techniques when presenting the data: 1) direct comparison of individual outflow velocities with galaxy properties and 2) the construction of composite spectra based on subsamples of objects exhibiting similar star-forming or structural characteristics. These methods are both useful in that the former enables ones to draw conclusions about specific objects while the latter produces high S/N spectra from which global, averaged trends can be inferred across the sample as a function of a single property. In Table 3.1, we present a summary of the data including redshift, luminosity, color, stellar mass, SFR, dust attenuation, areal measurements, and outflow velocity. Summaries of outflow velocities and correlation coefficients appear in Tables 3.2 and 3.3.

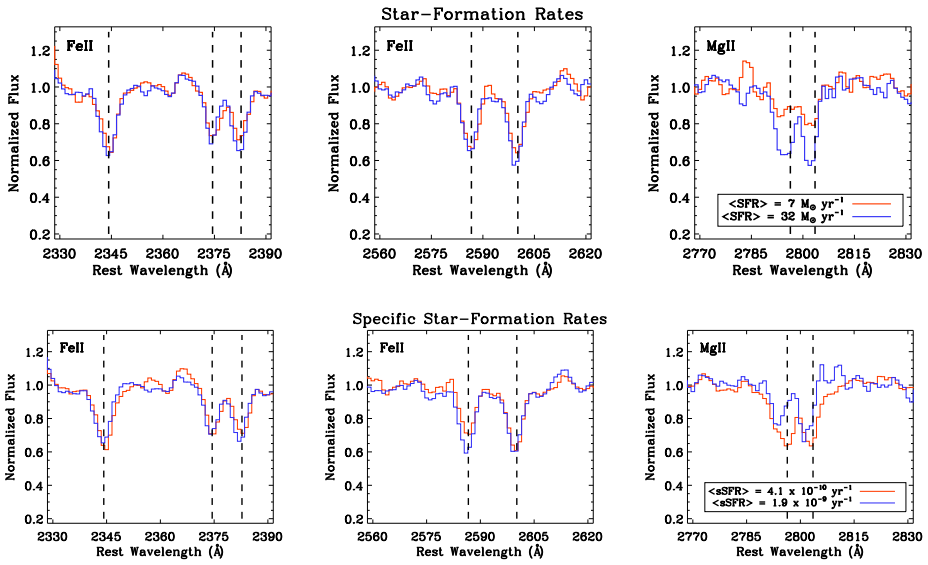

Figure 3.15 *Top:* Composites of high and low SFR objects, where the dashed vertical lines indicate the rest-frame wavelengths of resonance Fe II and Mg II features. We measure V_1 outflow velocities of –24 ± 9 km s^{-1} for the high-SFR composite (blue line) and 29 ± 11 km s^{-1} for the low-SFR composite (red line). The trend of higher SFR objects exhibiting stronger outflows is consistent with the weak correlation between SFR and V_1 observed on a per-object basis (Figure 3.13). The most pronounced spectral differences between the composites are observed around the Mg II feature at $\sim$ 2800 Å, where higher SFR objects exhibit deeper Mg II absorption troughs on average. *Bottom:* Same as above, for composite spectra assembled from high and low sSFR objects. We measure an outflow velocity of –34 ± 9 km s^{-1} for the high sSFR composite (blue line) and 27 ± 11 km s^{-1} for the low sSFR composite (red line). As with the SFR composites, the largest spectral differences are seen around Mg II. Objects with high sSFR have bluer Mg II centroids and less Mg II absorption than low sSFR objects. A full discussion of Mg II will appear in forthcoming papers (Kornei et al. 2012b, in prep. and Martin et al. 2012b, in prep.).

We focus on results from the resonance Fe II and Mg II absorption features, using outflow velocities measured from both the centroids and blue wings of these lines. At the end of this section, we present basic analyses of the strength of Mg II absorption. Forthcoming papers will include a more thorough discussion of both Mg II and fine-structure Fe II* emission (Kornei et al. 2012b, in prep. and Martin et al. 2012b, in prep.).

3.4.1 Star Formation and Outflows

The relationship between SFR and outflow velocity is one of the most commonly investigated correlations in the study of outflows (e.g., Martin, 2005; Sato et al., 2009; Weiner et al., 2009; Rubin et al., 2010b). Martin (2005) compiled data from a variety of local ULIRGs, LIRGs, and starburst dwarfs spanning four decades in SFR and showed that outflow velocity is related to SFR as $V \propto SFR^{0.35}$. While this trend is consistent with the canonical picture of galactic-scale outflows arising from the combined effects of stellar and supernovae winds (Leitherer & Heckman, 1995; Veilleux et al., 2005), recent studies probing more limited ranges in SFR have often failed to reproduce the Martin (2005) correlation (Rupke et al., 2005; Steidel et al., 2010; Law et al., 2012b). As the $V \propto SFR^{0.35}$ relation flattens for galaxies with SFRs $\gtrsim$ 10–100 $M_{\odot}$ yr^{-1} (Martin, 2005) – the very interval probed by most investigations – Rupke et al. (2005) propose that the bulk of studies simply do not span a large enough SFR interval to unambiguously detect a trend. The inclusion of low-SFR dwarf galaxies with low outflow velocities may be necessary for detecting a correlation between outflow velocity and SFR (Heckman et al., 2011). Weiner et al. (2009) examined the Mg II doublet in a sample of DEEP2 galaxies at $z = 1.4$ and found a dependence of outflow velocity on SFR consistent with the result from Martin (2005). This result is surprising given that

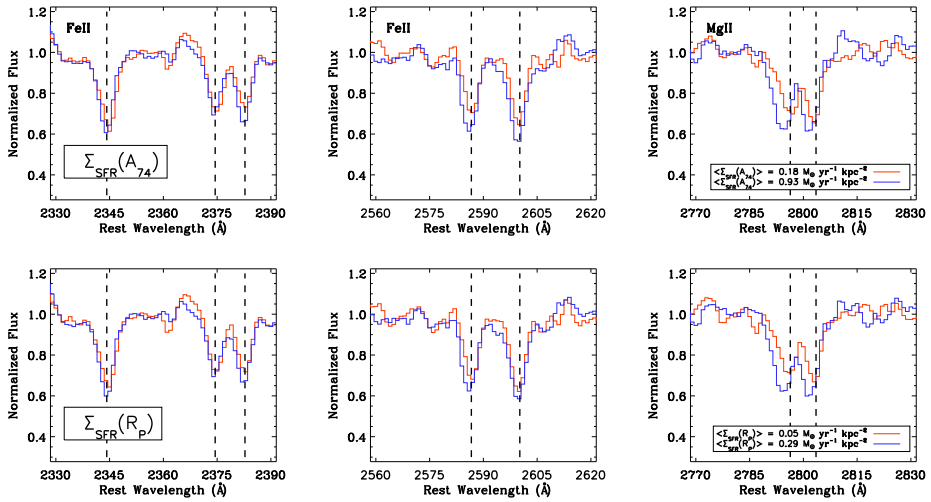

Figure 3.16 *Top:* Composite spectra assembled on the basis of $\Sigma_{\rm SFR}(A_{74})$. Kinematic shifts between the two composites in the Fe II resonance lines are evident visually; we find a V_1 outflow velocity of –31 ± 7 km s^{-1} for the high-$\Sigma_{\rm SFR}(A_{74})$ composite (blue line) and 44 ± 15 km s^{-1} for the low-$\Sigma_{\rm SFR}(A_{74})$ composite (red line). These pronounced differences are consistent with the strong trend observed between $\Sigma_{\rm SFR}(A_{74})$ and V_1 on a per-object basis (Figure 3.14). The Mg II features show a strong kinematic shift between the composites, with objects characterized by larger $\Sigma_{\rm SFR}$ exhibiting more blueshifted Mg II absorption. *Bottom:* Same as above, for $\Sigma_{\rm SFR}(R_P)$ composites. The high-$\Sigma_{\rm SFR}(R_P)$ composite is best-fit with a V_1 outflow velocity of –25 ± 6 km s^{-1} while the low-$\Sigma_{\rm SFR}(R_P)$ composite yields an outflow velocity of 33 ± 13 km s^{-1}. Objects with higher $\Sigma_{\rm SFR}(R_P)$ also show more strongly blueshifted Mg II features. These results are in the same sense as the trends seen in the $\Sigma_{\rm SFR}(A_{74})$ composites, unsurprising given the multiplicative offset between the A_{74} and πR_P^2 areas (Figure 3.9).

the Weiner et al. (2009) sample spans a much more limited SFR interval ($\sim$ 7–180 $M_{\odot}$ yr^{-1}) than the 0.1–1000 $M_{\odot}$ yr^{-1} range of Martin (2005). Weiner et al. (2009) employed two different techniques to parametrize the velocity of outflowing Mg II: a "median velocity" containing 50% of the absorption and a "maximal velocity" where the outflow crosses 10% or 25% absorption. The median velocity method is most akin to the centroid technique used in this paper and in other recent studies of outflows (Rubin et al., 2010b; Steidel et al., 2010; Krug et al., 2010; Law et al., 2012b) while the maximal velocity is similar to our V_{max}(Mg II) measurement. Relying on composite spectra, Weiner et al. (2009) found that SFR was correlated with the 10% maximal velocity of Mg II such that V $\propto$ SFR$^{0.38}$. These authors did not find a significant trend between SFR and the Mg II median velocity. In the analyses below, we employ the Spearman ρ correlation test to examine how well variables are correlated. We report the Spearman rank-order correlation coefficient, r_S, and the number of standard deviations from the null hypothesis that the quantities are uncorrelated.

3.4.1.1 Individual Measurements

In the left panel of Figure 3.13, we plot V_1 versus SFR. We find only a weak (r_S = –0.17; 1.2σ from the null hypothesis) correlation between SFR and V_1 across the sample, although this is not unexpected given the limited range in SFR probed by the data ($\sim$ 1–97 $M_{\odot}$ yr^{-1}; Rupke et al., 2005; Steidel et al., 2010; Law et al., 2012b), the small sample size, the S/N of the data, and the fitting method used for measuring outflow velocities (centroid fitting of Fe II). The three objects with the highest SFRs ($>$ 75 M$_{\odot}$ yr^{-1}) show small Fe II blueshifts ($V_1 >$ –65 km s^{-1}); we propose that the sample's small dynamic range in SFR, the limited number of objects considered, the lack of high-resolution spectroscopy, and the methodology

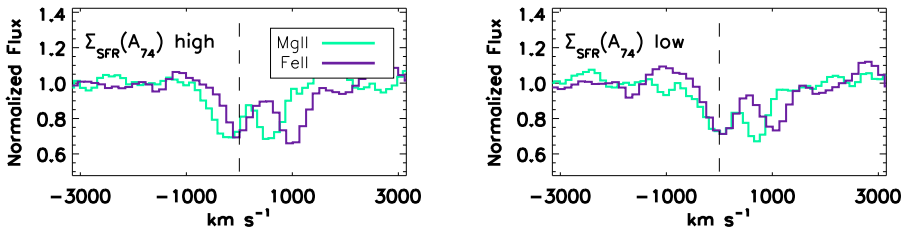

Figure 3.17 Comparison of Fe II 2374 and Mg II 2796 profiles in velocity space, for the high and low $\Sigma_{\rm SFR}(\rm A_{74})$ composite spectra. Note the pronounced variation between the blue wings of the features in the high $\Sigma_{\rm SFR}(\rm A_{74})$ composite; V_{max}(Mg II) is –855 ± 66 km s^{-1} while V_{max}(Fe II) is –611 ± 103 km s^{-1}. High$\Sigma_{\rm SFR}(\rm A_{74})$ systems show gas at high velocity, and this gas is better traced by Mg II than by Fe II (Section 4.4). The absorption features at $\sim$ +770 and $\sim$ +1000 km s^{-1} are Mg II 2803 and Fe II 2382, respectively.

of employing centroid measurements of Fe II may all contribute to this result.

We observe a stronger correlation between sSFR and V_1 outflow velocity (Figure 3.13, *right*): r_S = –0.33; 2.3σ from the null hypothesis. As sSFR is a ratio between SFR (where higher values should produce stronger winds) and stellar mass (where larger values should hinder winds, assuming that the gravitational potential energy of a system increases with increasing stellar mass), one would expect that sSFR is a tracer of both the energetics and gravitational potential of a galaxy and should therefore correlate with the observed velocity of winds. While Chen et al. (2010) do not find a trend between sSFR and either outflow velocity or the equivalent width of the outflow component in a large sample of Sloan Digital Sky Survey (SDSS; York et al., 2000) galaxies at $z \sim 0.1$, these authors hypothesize that the lack of correlation with the strength of the outflow component may be due to the effects of dust shielding on the particular atomic

species used to trace winds at low redshift[7]. Rubin et al. (2010b) also fail to find a trend between sSFR and outflow velocity at $z \sim 1.4$, although these authors draw their conclusions solely based on co-added spectra[8]. While Prochaska et al. (2011) caution that stacked spectra show only a smeared version of the original emission and absorption features present in the component spectra, we find that the composite spectra discussed below reflect the trends of the individual measurements. Therefore, the fact that Rubin et al. (2010b) do not observe a trend between sSFR and outflow velocity is more likely a result of the low S/N of their data rather than a direct consequence of relying on co-added spectra.

We find the strongest trend with V_1 outflow velocity when SFR is normalized by a representative galaxy area. Star-formation rate surface densities – both $\Sigma_{\rm SFR}(\rm A_{74})$ and $\Sigma_{\rm SFR}(\rm R_P)$ – exhibit pronounced trends with V_1 outflow velocity (Figure 3.14). Both $\Sigma_{\rm SFR}(\rm A_{74})$ and V_1 and $\Sigma_{\rm SFR}(\rm R_P)$ and V_1 are correlated at the 2.4σ level with $r_S = -0.40$. Omitting two extremely compact galaxies with uncertain area measurements yields 3.1σ measurements from the null hypothesis and correlation coefficients of $r_S = -0.54$ for both $\Sigma_{\rm SFR}(\rm A_{74})$ and $\Sigma_{\rm SFR}(\rm R_P)$. Such strong trends have not yet been reported in the literature at high redshift; Rubin et al. (2010b) noted only a 1σ correlation in a sample of 468 galaxies at $0.7 < z < 1.5$, Steidel et al. (2010) also found a 1σ correlation for 81 galaxies at $z \simeq 2$, and Law et al. (2012b) reported a 2.1σ correlation for 35 optically-selected star-forming galaxies at $z = 1.5$–3.6. However, the galaxy areas employed in the $\Sigma_{\rm SFR}$

[7]The tracer of wind kinematics used by Chen et al. (2010), Na I $\lambda\lambda$ 5892,5898 (Na D), can be ionized by photons with energies > 5.1 eV. In the presence of dust, Na I is effectively shielded and remains neutral. However, in environments with minimal attenuation – such as those found in both high and low sSFR objects (Chen et al., 2010) – ionizing photons are not destroyed by dust and Na I is stripped of an electron. As the tracer species is depleted in such scenarios (Murray et al., 2007), it follows that no correlation would be expected between sSFR and outflows.

[8]These stacked spectra have typical S/N values of 6.0 per pixel, comparable to our individual spectra (Figure 3.4).

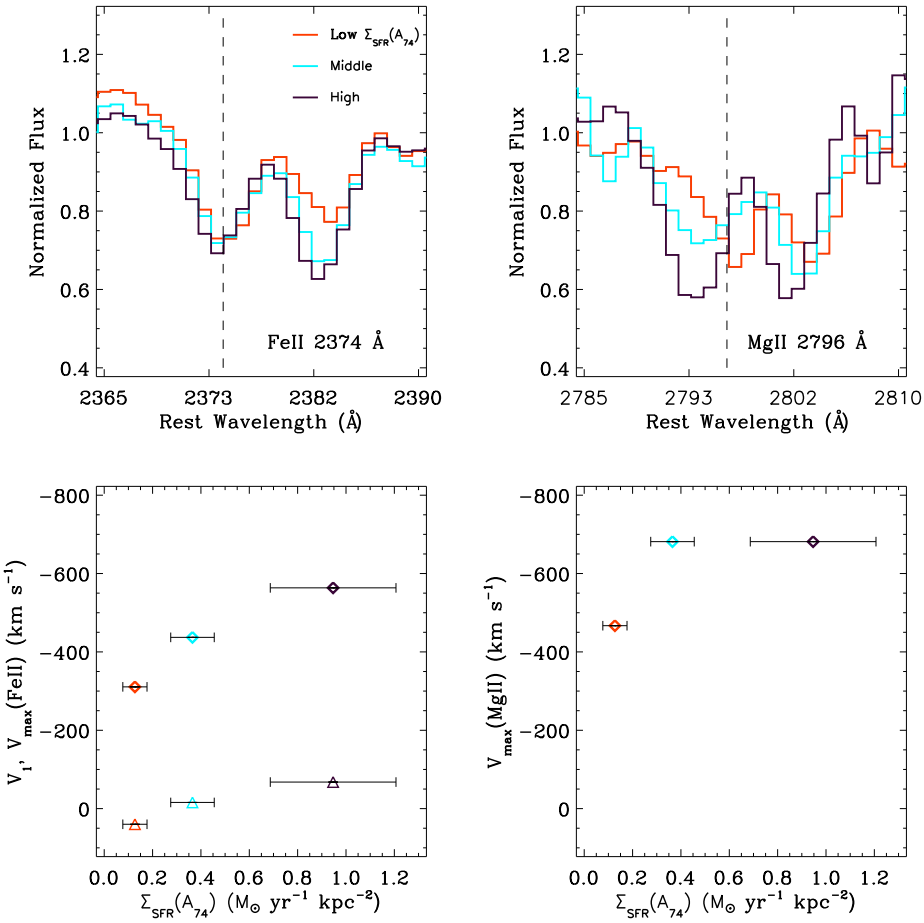

Figure 3.18 *Top:* The regions around Fe II 2374 Å and Mg II 2796 Å are shown for three composite spectra assembled from data ordered by $\Sigma_{\rm SFR}(A_{74})$. With increasing $\Sigma_{\rm SFR}$, the blue wings of both the Fe II and Mg II features extend to larger velocities. This is evidence of the increasing prevalence of high velocity gas with larger $\Sigma_{\rm SFR}$. *Bottom:* We quantify the blue wings of Fe II and Mg II with V_{max}(Fe II) and V_{max}(Mg II) measurements. The left panel shows V_{max}(Fe II)(diamonds) and V_1 (triangles) versus $\Sigma_{\rm SFR}(A_{74})$, where the errors bars on $\Sigma_{\rm SFR}(A_{74})$ indicate the 1σ dispersion in each bin. The right panel shows the relationship between V_{max}(Mg II) and $\Sigma_{\rm SFR}(A_{74})$. In all cases, more extended wing profiles tracing higher velocity gas are seen in systems with larger star-formation rate surface densities.

calculations of Rubin et al. (2010b), Steidel et al. (2010), and Law et al. (2012b) correspond to half-light radii at rest-frame $\sim$ 2200 Å, the extent of Hα emission, and circularized effective radii, respectively. Given the clumpy distribution of star formation in distant galaxies (Lotz et al., 2008; Law et al., 2012b), these areas may be overestimates of the regions corresponding to star-formation (Rubin et al., 2010b)[9]. Furthermore, the Steidel et al. (2010) measurements are from ground-based data which are seeing-limited. The Law et al. (2012b) observations, while probing the bulk of the stellar mass with H-band (rest-frame optical) *HST* imaging, approximated the areas of clumpy galaxies by adopting the circularized effective radius of the brightest clump as representative of the size of the entire galaxy. This technique results in overestimates of $\Sigma_{\rm SFR}$, given that the areas of fainter clumps are neglected. In a more local sample of SDSS galaxies at $z \sim 0.1$, Chen et al. (2010) found no correlation between outflow velocity and $\Sigma_{\rm SFR}$. These authors note that the small dynamic range of their data (outflow speed = [120–160] km s^{-1}) may obscure trends. When we limit our sample to only objects showing outflows ($V_1 < 0$ km s^{-1}), we find that star-formation rate surface density and V_1 are correlated at the $\sim 1\sigma$ level (for both area measurements). We propose that inflows and outflows represent a continuum of gas cycling and therefore correlations with galaxy properties should be investigated inclusive of both redshifted and blueshifted gas. While SFR and $\Sigma_{\rm SFR}(\rm A_{74})$ are weakly correlated, at the $\sim 2.3\sigma$ level ($r_S = 0.37$), we suggest that the scatter in the V_1 versus $\Sigma_{\rm SFR}(\rm A_{74})$ relation prevents a similar correlation from being seen in the plot of V_1 versus SFR. All objects with 3σ detections of outflows have $\Sigma_{\rm SFR}(\rm R_P) > 0.1$ M$_\odot$ yr^{-1} kpc^{-2}, in agreement with the $\Sigma_{\rm SFR}$ threshold proposed by Heckman (2002). These objects with secure detections of outflows furthermore all have SFR > 10

[9]Simply overestimating galaxy areas is not sufficient to negate a trend with outflow velocity, however, since we find equally strong correlations with outflow velocity utilizing both $\Sigma_{\rm SFR}(\rm A_{74})$ and $\Sigma_{\rm SFR}(\rm R_P)$.

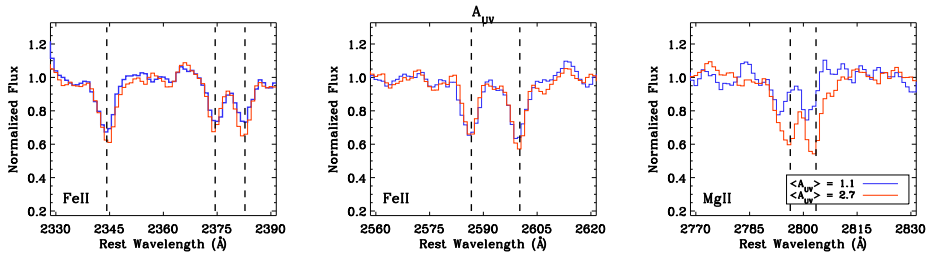

Figure 3.19 Composite spectra assembled on the basis of A_{UV}. Fitting the Fe II resonance absorption lines yields a V_1 outflow velocity of –3 ± 10 km s^{-1} for the high-A_{UV} composite (red line) and –10 ± 9 km s^{-1} for the low-A_{UV} composite (blue line). Mg II strength and kinematics are clearly correlated with A_{UV}, where less attenuated objects show shallower Mg II absorption troughs and more blueshifted features. In dusty objects, the lack of emission filling in the Mg II features likely contributes to the observed absorption depth. These results are consistent with the trends observed for individual objects (Figure 3.24).

$M_\odot$ yr^{-1}, although we hypothesize that the Σ_{SFR} threshold is more fundamental given the stronger correlation of outflow velocity with Σ_{SFR} than with SFR. The trend between outflow velocity and star-formation rate surface density supports the theory that the shifts of absorption lines are due to gas flows as opposed to galactic rotation.

Using the outflow fraction methodology discussed in Section 3.3.2, we find that 26 ± 8% of the low-$\Sigma_{SFR}(A_{74})$ sample shows outflows with blueshifts of at least –40 km s^{-1}. In contrast, 48 ± 9% of the high-$\Sigma_{SFR}(A_{74})$ shows outflows at the same level. When the two galaxies with uncertain area measurements are removed from the high-$\Sigma_{SFR}(A_{74})$ sample, the outflow fraction increases to 54 ± 9%. The significant difference in outflow fraction between the low- and high-$\Sigma_{SFR}(A_{74})$ samples is consistent both with the measurements from individual objects presented above and our findings based on composite spectra, discussed

below.

3.4.1.2 Composite Spectra

We constructed composite spectra from the binary division of data sorted according to SFR, sSFR, $\Sigma_{\rm SFR}(A_{74})$, $\Sigma_{\rm SFR}(R_P)$, A_{UV}, and i. We measured the shifts of the Fe II interstellar absorption lines in the composites using the same techniques employed for the individual spectra (Section 3.3.2). We also measured maximal outflow velocities in both Mg II and Fe II for these composites. While the robustness of the velocity measurements benefit from the increased S/N of the stacked composites, it is important to remember that relying on composite spectra only reveals the global, averaged trends across the sample.

Below, we discuss three measurements for each composite spectrum: V_1, V_{max}(Mg II), and V_{max}(Fe II). While the magnitudes of the V_1 shifts are not large, we emphasize that it is the *difference* in V_1 between composite spectra that is primary interest; the apparent detections of inflows and outflows in individual composites may be spurious given the velocity uncertainties of the LRIS data. The results implied by V_1 and V_{max}(Fe II) are corroborated by V_{max}(Mg II), where shifts in the Mg II lines are often visually obvious in the data.

In the top row of Figure 3.15, we compare high- and low-SFR composites and focus on the wavelength intervals around Fe II and Mg II (2370–2400, 2570–2650, and 2760–2840 Å). The strengths of the Fe II features are similar in both composites, although we find that the high-SFR composite ($\langle$SFR$\rangle$ = 32 $M_\odot$ yr^{-1}; extrema of [12, 97] $M_\odot$ yr^{-1}) exhibits a V_1 blueshift of –24 ± 9 km s^{-1} while the low-SFR composite ($\langle$SFR$\rangle$ = 7 $M_\odot$ yr^{-1}; extrema of [1,11] $M_\odot$ yr^{-1}) is best-fit with a model of redshifted gas with positive velocity 29 ± 11 km s^{-1}. These results are in the same sense as the trend of vigorously star-forming objects

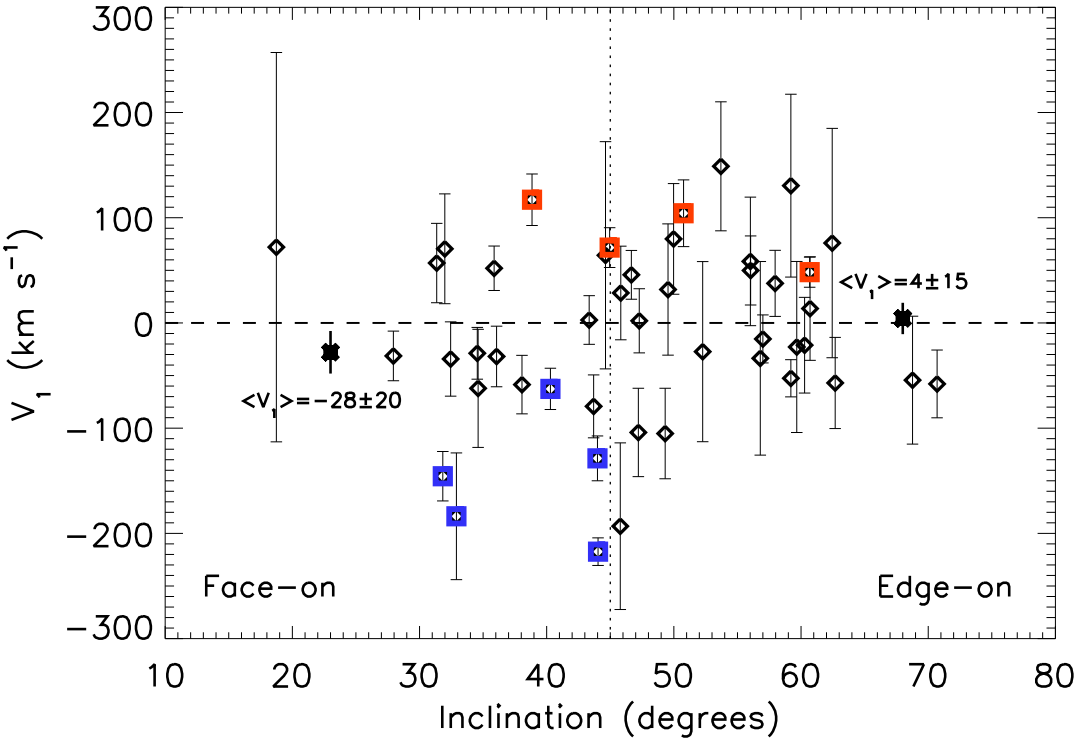

Figure 3.20 V_1 outflow velocity versus galaxy inclination, where inclination was estimated from axial ratios: $i = \cos^{-1}[b/a]$ (Tully & Fisher, 1977). Significant detections of outflows or inflows at the 3σ level are highlighted in blue and red, respectively. While individual inclination measurements are likely uncertain by $\sim 10°$ due to measurement error in the rest-frame UV, we note that a simple division of the sample at $i = 45°$ yields a subgroup of more face-on galaxies with $\langle V_1 \rangle = -28 \pm 20$ km s^{-1} and a set of more inclined galaxies with $\langle V_1 \rangle = 4 \pm 15$ km s^{-1}. These findings are in the same sense as the results of Chen et al. (2010), who observed a correlation between outflow velocity and inclination in a sample of $\sim$ 150,000 local SDSS (York et al., 2000) galaxies such that more face-on systems showed a stronger outflow component.

showing more pronounced outflows than lower SFR systems (Martin, 2005). The SFR composites differ significantly in Mg II strength, with larger SFR objects showing deeper absorption on average. The centroids of the Mg II features are blueshifted in both the high- and low-SFR composites, so systemic absorption is not likely responsible for the difference in Mg II strength. Furthermore, the red wings of the 2803 Å features are remarkably similar between the two composites, so it is not immediately apparent that emission filling is affecting one spectrum more than the other. Since SFR and stellar mass are correlated (Figure 3.8), Mg II strength may depend on stellar mass. We investigate the correlation between Mg II and stellar mass in Section 3.4.3. Higher metallicities are expected for more vigorously star-forming objects (Tremonti et al., 2004; Noeske et al., 2007; Elbaz et al., 2007), although we note that because the Fe II and Mg II lines are saturated in our study (based on the differences between the observed lines ratios and those expected according to atomic theory) it is difficult to determine if metallicity is the driving factor behind absorption line strength. The kinematics of Mg II are similar in both composites; the high (low) SFR composite has V_{max}(Mg II) = –748 ± 94 (–614 ± 83) km s^{-1}. The composites have V_{max}(Fe II) measurements of –514 ± 84 (–453 ± 104) km s^{-1}.

We compare sSFR composite spectra in the bottom row of Figure 3.15. As with the SFR composites, there is minimal variation in the strength of the Fe II resonance features between the high- and low-sSFR composites. Likewise, we find differences in the Fe II kinematics between the two composites that are similar to the shifts seen in the SFR composites: objects with high sSFR ($\langle$sSFR$\rangle$ = 1.9 × 10^{-9} yr^{-1}; extrema of [1.0 × 10^{-9}, 5.6 × 10^{-9}] yr^{-1}) exhibit an average blueshift of –34 ± 9 km s^{-1} while low sSFR objects ($\langle$sSFR$\rangle$ = 4.1 × 10^{-10} yr^{-1}; extrema of [6.5 × 10^{-11}, 9.6 × 10^{-10}] yr^{-1}) are globally characterized by a Fe II shift of 27 ± 11 km s^{-1}. The larger blueshifts seen in higher sSFR

objects supports the correlation observed in individual galaxies (Figure 3.13). The sSFR composites are comparable in Mg II strength but not in kinematics: the high (low) sSFR composite has V_{max}(Mg II) = –605 ± 80 (–834 ± 148) km s^{-1}. The composites are characterized by V_{max}(Fe II) measurements of –556 ± 94 (–456 ± 86) km s^{-1}. While the sense of the V_{max}(Mg II) measurements is contrary to both the V_1 and V_{max}(Fe II) results – i.e., objects with larger sSFRs show smaller V_{max}(Mg II) blueshifts than objects with lower sSFRs – we note that the V_{max}(Mg II) measurements of the high- and low-sSFR composites are consistent at roughly the 1σ level. The large blueshift of V_{max}(Mg II) for the low-sSFR composite may be explained by high-mass objects preferentially populating the low-sSFR composite. High-mass objects exhibit deeper and broader Mg II absorption profiles than low-mass objects (Martin et al. 2012b, in prep.). Stellar Mg II absorption and emission filling may also affect the observed profiles; the large differences in the red wings of the 2803 Å features and the blueshift seen in the Mg II centroids of the high-sSFR composite argue that emission filling may be present in the high-sSFR composite.

In Figure 3.16, we plot composite spectra assembled according to $\Sigma_{\rm SFR}$. Kinematic shifts between the high- and low-$\Sigma_{\rm SFR}$ composites are visually evident and persist irrespective of which galaxy area measurement is employed. Quantitatively, we find V_1 shifts of –31 ± 7 and –25 ± 6 km s^{-1} for the high $\Sigma_{\rm SFR}(A_{74})$ and $\Sigma_{\rm SFR}(R_P)$ composites, respectively. In contrast, the low-$\Sigma_{\rm SFR}$ composites are best-fit with models having shifts of 44 ± 15 and 33 ± 13 km s^{-1}. These results, consistent with the $\sim 3\sigma$ trends observed between outflow velocity and [$\Sigma_{\rm SFR}(A_{74})$, $\Sigma_{\rm SFR}(R_P)$] on a per-object basis (Figure 3.14), are in agreement with theoretical predictions that a higher density of star formation should lead to stronger outflows (Leitherer & Heckman, 1995; Veilleux et al., 2005; Murray et al., 2011). However, the most striking difference between the $\Sigma_{\rm SFR}$ composites are

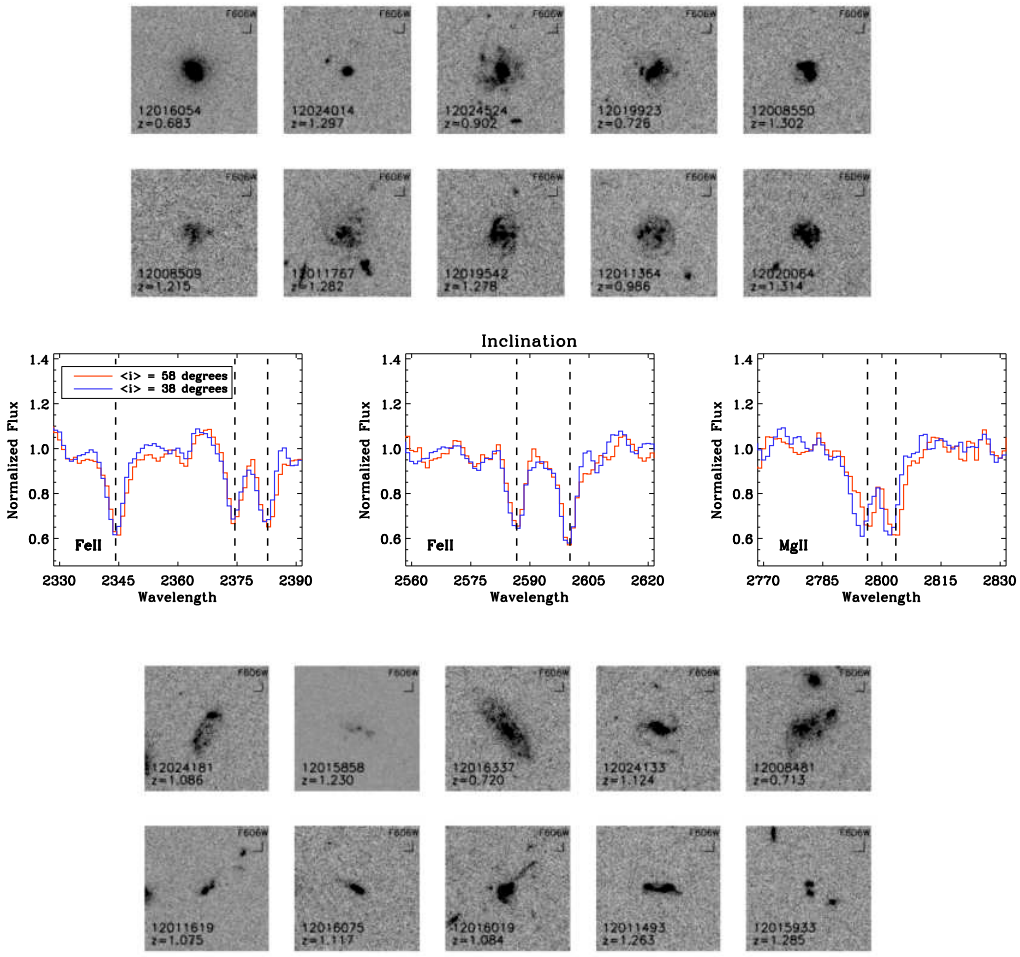

Figure 3.21 Composite spectra assembled from objects with high and low inclinations, respectively, where inclinations were estimated from *HST* $V+I$ band imaging assuming intrinsic circular disks: $i = \cos^{-1}[b/a]$ (Tully & Fisher, 1977). We find that the composite spectrum composed of high inclination objects (red line) is best-fit with $V_1 = 28 \pm 11$ km s^{-1} while the composite spectrum assembled from low inclination galaxies (blue line) has a V_1 outflow velocity of –19 ± 9 km s^{-1}. Even though the overall shifts of each composite from 0 km s^{-1} are small in magnitude, the kinematic difference between the two composites is significant. These results are consistent with the trend of stronger blueshifts with decreasing inclination, as noted by Chen et al. (2010) for a local sample of SDSS galaxies. V-band thumbnails of the ten lowest and highest inclination objects are shown above and below the composite spectra, respectively.

the blue wings of the Mg II 2796 Å features. We find visually-obvious shifts in the Mg II doublet between the high- and low-$\Sigma_{\rm SFR}$ composites, where objects with larger star-formation rate surface densities show more blueshifted Mg II absorption. Furthermore, the entire blue wing of the 2796 Å feature is offset in the composites, suggestive of actual kinematic differences as opposed to centroid shifting from emission filling. The composites of high-$\Sigma_{\rm SFR}$ objects are characterized by V_{max}(Mg II) = –855 ± 66 km s^{-1} and –862 ± 69 km s^{-1}, respectively. Conversely, the low-$\Sigma_{\rm SFR}$ composites have measured V_{max}(Mg II) values of –640 ± 117 km s^{-1} and –668 ± 105 km s^{-1}, respectively. The corresponding V_{max}(Fe II) measurements for the high-$\Sigma_{\rm SFR}$ composites are –611 ± 103 km s^{-1} and –614 ± 97 km s^{-1}, respectively. The low-$\Sigma_{\rm SFR}$ composites have V_{max}(Fe II) values of –451 ± 86 km s^{-1} and –444 ± 87 km s^{-1}, respectively. The kinematic differences between the high- and low-$\Sigma_{\rm SFR}$ composites are among the largest observed for any pair of composites (ΔV_{max}(Mg II) = 215 ± 134 km s^{-1} and 194 ± 126 km s^{-1}; ΔV_{max}(Fe II) = 160 ± 134 km s^{-1} and 170 ± 130 km s^{-1}).

The kinematic differences between Fe II and Mg II in the $\Sigma_{\rm SFR}(A_{74})$ composites are highlighted in Figure 3.17. On the left, the Fe II 2374 Å and Mg II 2796 Å lines of the high-$\Sigma_{\rm SFR}(A_{74})$ composite are overplotted in velocity space. The profiles of Fe II and Mg II absorption are clearly disparate, with the extended blue wing of Mg II indicative of high-velocity gas not traced by Fe II. On the right side of Figure 3.17, the same Fe II and Mg II transitions are shown for the low-$\Sigma_{\rm SFR}(A_{74})$ composite. In the regime of low-intensity star formation, the profiles of Fe II and Mg II are much more similar and Mg II does not exhibit an extended blue wing. These results support the association of high star-formation rate surface densities with high-velocity gas, and Mg II is observed to be better tracer of high-velocity gas than Fe II. In order to better study the trend between

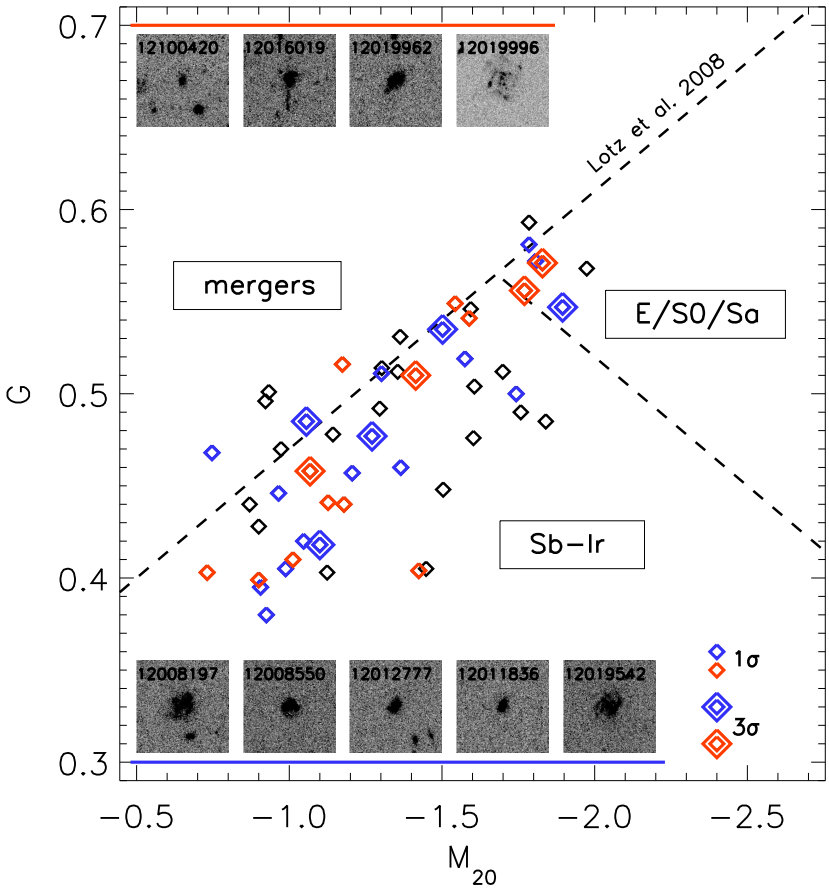

Figure 3.22 Outflow demographics as a function of the quantitative morphological parameters G and M_{20}, where parameter space can be partitioned into regions encompassing the classical morphological groups – mergers, ellipticals, and spirals/irregulars (Lotz et al., 2008). We highlight in blue (red) objects showing blueshifted (redshifted) Fe II resonance absorption lines, reserving small diamonds for 1σ significant V_1 velocities and larger diamonds for 3σ significant V_1 measurements. *HST* V-band thumbnails are shown for the nine objects with 3σ velocity dectections. Both inflows and outflows occur in galaxies spanning a variety of morphologies; merging systems do not preferentially host winds. These results are consistent with the findings of Law et al. (2012b) at higher redshift, although Sato et al. (2009) noted that outflows were preferentially seen in merger candidates at $0.11 < z < 0.54$.

outflow velocity and $\Sigma_{\rm SFR}$, we constructed composite spectra from three bins of $\Sigma_{\rm SFR}(A_{74})$. We find that the V_1, V_{max}(Fe II), and V_{max}(Mg II) measurements are all correlated with $\Sigma_{\rm SFR}(A_{74})$, where objects characterized by higher intensities of star formation have larger centroid and maximal outflow velocities (Figure 3.18). We observe that V_{max}(Fe II) is a smooth function of $\Sigma_{\rm SFR}(A_{74})$, while V_{max}(Mg II) appears to reach a maximum at $\Sigma_{\rm SFR}(A_{74}) = 0.4$ $M_\odot$ yr^{-1} kpc^{-2}. The relatively coarse pixel sampling of the composite spectra – ~ 100 km s^{-1} – is likely responsible for the plateau of V_{max}(Mg II) values. From the composite spectra, it is evident that the equivalent width of blueshifted Mg II absorption steadily increases with increasing $\Sigma_{\rm SFR}(A_{74})$.

As previous observations have shown stronger interstellar absorption lines with increasing dust attenuation (Shapley et al., 2003), indicative of an association between absorbing outflow material and dust, we investigated the relationship between $A_{\rm UV}$ and outflow velocity. In composite spectra assembled on the basis of $A_{\rm UV}$ (Figure 3.19), we find that objects with higher dust attenuation exhibit marginally stronger Fe II absorption lines (especially in the 2344 Å feature) and significantly stronger Mg II absorption. These results support the correlation found by Shapley et al. (2003), where these authors observed that more attenuated Lyman Break Galaxies (LBGs) at $z \sim 3$ showed deeper interstellar absorption lines. We find that objects with a variety of attenuation levels exhibit similar Fe II kinematics (Figure 3.19); the centroids of the Fe II lines in the high-$A_{\rm UV}$ composite ($\langle A_{\rm UV} \rangle = 2.7$; extrema = [1.7, 4.2]) are best-fit with a velocity shift of –3 ± 10 km s^{-1} while the low-$A_{\rm UV}$ composite ($\langle A_{\rm UV} \rangle = 1.1$; extrema = [0.0, 1.7]) shows a shift of –10 ± 9 km s^{-1}. These measurements are both consistent with no velocity shift. The V_{max}(Fe II) measurements of the composites are consistent with each other within their 1σ errors (–497 ± 88 km s^{-1} for the high-$A_{\rm UV}$ composite and –522 ± 91 km s^{-1} for the low-$A_{\rm UV}$ composite). Law

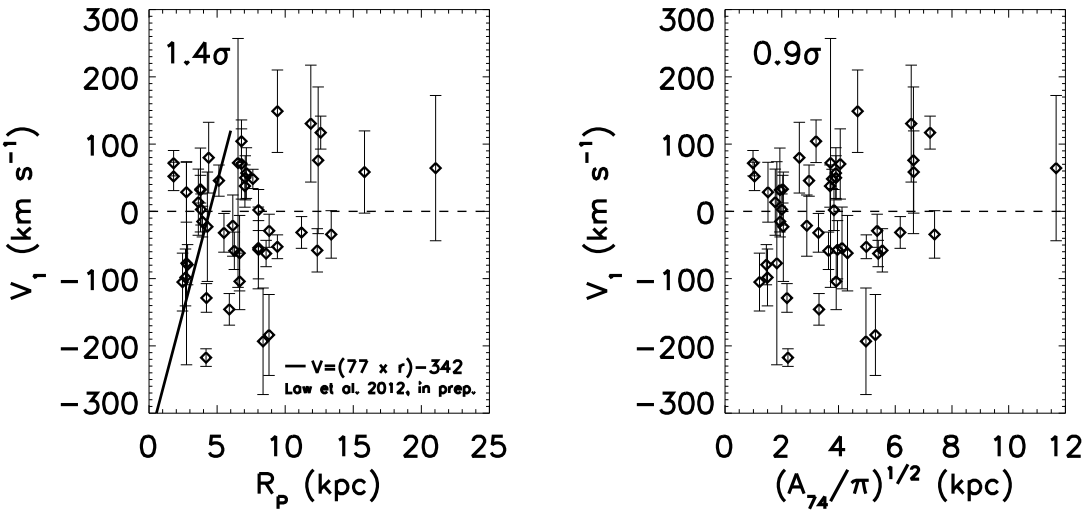

Figure 3.23 *Left:* Outflow velocity versus Petrosian radius. We overplot the relation from Law et al. (2012b), where these authors found a strong correlation between outflow velocity and size in a sample of galaxies at $z = 1.5$–3.6. The Law et al. (2012b) objects have semi-major axes $r < 6$ kpc, while our sample is characterized by $\langle \mathrm{R_P} \rangle = 7.1$ kpc. We find no statistical evidence in our sample that Petrosian radius and outflow velocity are correlated. *Right:* Outflow velocity versus the "radius" of the $\mathrm{A_{74}}$ area: $(\mathrm{A_{74}}/\pi)^{1/2}$. As with the Petrosian radius, we find no evidence indicating a relation between outflow velocity and $(\mathrm{A_{74}}/\pi)^{1/2}$.

et al. (2012b) find only a 0.7σ correlation between outflow velocity and E(B–V) in a sample of 35 star-forming galaxies at $z \sim 2$. Within a sample of local SDSS galaxies, Chen et al. (2010) also find no evidence that attenuation level is linked to outflow velocity.

While the Fe II features of the two A_{UV} composites show only minimal variation in strength and kinematics, the Mg II features are strikingly different between the high- and low-A_{UV} composites. We find that more attenuated objects have deeper Mg II absorption troughs (consistent with a relative lack of emission filling or stronger absorption in dusty galaxies), Mg II centroids roughly consistent with the systemic velocity, and V_{max}(Mg II) = –732 ± 71 km s^{-1} while objects with lower A_{UV} have weaker absorption profiles, more strongly blueshifted centroids, and V_{max}(Mg II) = –652 ± 89 km s^{-1}. Prochaska et al. (2011) proposed outflow models in which dust has a pronounced effect on observed wind profiles: resonantly trapped photons (i.e., those arising from the Mg II transitions at 2796 and 2803 Å) have an increased probability of being absorbed by dust given their longer path lengths. Our observations support this hypothesis that Mg II should show more variation with changing A_{UV} levels than the Fe II transitions that are not resonantly trapped. However, Prochaska et al. (2011) note that extreme levels of extinction ($\tau_{dust} \sim 10$) are necessary in order to measure qualitative changes in line profiles, although we see this effect at significantly lower attenuation levels ($\tau_{dust} \sim 2$).

3.4.2 Trends with Inclination and Morphology

Observations of local starbursts have shown extraplanar outflows emanating perpendicular to galaxy disks (e.g., Heckman et al., 1990; Lehnert & Heckman, 1996; Cecil et al., 2001; Strickland & Heckman, 2009). If this geometry persists

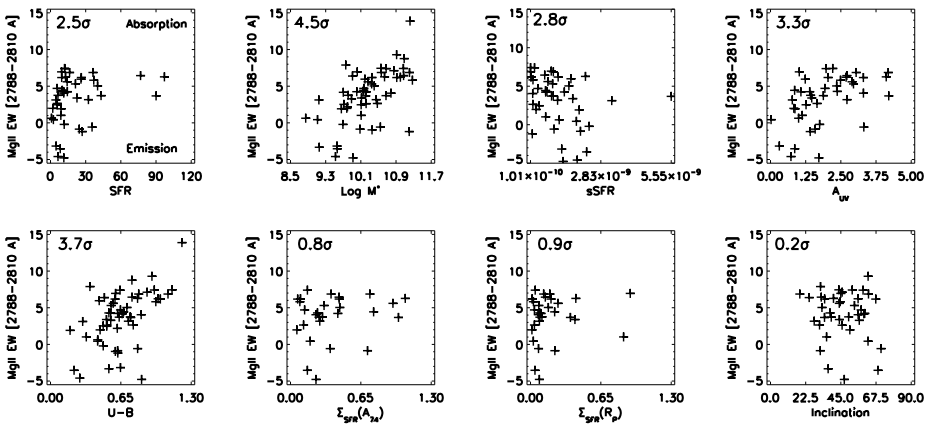

Figure 3.24 Scatter plots of various galaxy properties versus Mg II equivalent width, for galaxies in the EGS. The strength of Mg II was estimated from a simple summation of flux over the interval 2788–2810 Å encompassing both features of the doublet. We find that the strongest correlation, at 4.5σ ($r_S = 0.61$), is observed between Mg II equivalent width and stellar mass. A thorough discussion of Mg II will appear in Kornei et al. 2012b, in prep. and Martin et al. 2012b, in prep.

at higher redshifts, one would expect the measured outflow velocities in the sample to depend strongly on inclination as the wind becomes increasingly oriented toward the observer. Studies to date have primarily focused on testing this hypothesis in local samples, given the advantages of apparent magnitude and spatial resolution. Chen et al. (2010) used a sample of $\sim$ 150,000 SDSS galaxies and assembled stacks of the Na D absorption lines on the basis of galaxy inclination measured from two dimensional de Vaucouleurs (1948) fits to *ugriz* data. These authors found a striking correlation of increasing outflow velocity with decreasing inclination, consistent with the physical picture of winds escaping perpendicular to galaxy disks. Similarly, Heckman et al. (2000) observed 18 local starbursts in the Na D lines and measured an increase in the fraction of objects exhibiting outflows when the sample was restricted to objects with $i \leq 60°$. In the high-redshift regime, Weiner et al. (2009) examined 118 galaxies at $z = 1.4$ with *HST* I-band imaging and extracted minor-to-major axis ratios (b/a) using SExtractor (Bertin & Arnouts, 1996). These authors did not find a correlation between axis ratio and wind strength or outflow velocity; Weiner et al. (2009) propose that the uncertainties on the axis ratios of small, irregular galaxies imaged in the rest-frame U-band may be substantial. Law et al. (2012b) looked at 35 optically-selected star-forming galaxies at $z = 1.5$–3.6 with b/a estimated from GALFIT (Peng et al., 2002, 2010) modeling of *HST* F160W imaging and also found no correlation between outflow velocity and b/a. It is important to note that these results at high redshift are much more uncertain than the Chen et al. (2010) and Heckman et al. (2000) findings, given the very different spatial resolutions achievable at $z = 0$ and $z \sim 2$. Furthermore, while b/a and inclination are often presumed to be related by $i = \cos^{-1}[b/a]$ (Tully & Fisher, 1977), Law et al. (2012b) caution that this conversion relies on the thin-disk approximation which may not be valid for star-forming galaxies with significant vertical velocity dispersions (Law et al.,

2009; Förster Schreiber et al., 2009). However, in the absence of a significant sample of high-redshift galaxies for which spatially-resolved velocity dispersions have been measured, this simple conversion continues to be employed. As some of the objects in our sample furthermore resemble local star-forming disks more closely than the clumpy, irregular galaxies at $z \sim 2$ with large vertical velocity dispersions, the thin-disk approximation may not be a gross assumption here.

We investigate the relationship between galaxy inclination and outflow velocity using inclinations estimated from SExtractor (Bertin & Arnouts, 1996) axial measurements of summed *HST* $V+I$ detection images. In Figure 3.20, we plot outflow velocity versus inclination. While inclination estimates for individual objects are likely uncertain by $\sim 10^{\circ}$ due to measurement error in the rest-frame UV, highlighting the objects showing $\geq 3\sigma$ V_1 outflows reveals that all such five objects have $i < 45^{\circ}$. When we make a simple division of the data at $i = 45^{\circ}$, we additionally find that the sample of more edge-on systems has $\langle V_1 \rangle = 4 \pm 15$ km s^{-1} while the sample of predominantly face-on systems is characterized by $\langle V_1 \rangle = -28 \pm 20$ km s^{-1}. These results are consistent with the physical picture of a biconical wind profile where outflowing material preferentially emanates perpendicular to the galactic disk. Weiner et al. (2009) investigated the relationship between outflow velocity and galaxy inclination at $z \sim 1.4$ using *HST* imaging, although these authors relied on observations in a single band (I). The Weiner et al. (2009) imaging data are accordingly shallower than ours by a factor $\sim \sqrt{2}$, although we propose that the main reason we find a correlation between inclination and outflow velocity while Weiner et al. (2009) do not lies in the relative S/N ratios of our respective spectroscopic data. The individual spectra used by Weiner et al. (2009) have a S/N of ~ 1 per resolution element near 2820 Å. Conversely, the spectra presented in this paper have a S/N of ~ 11 per resolution element in the vicinity of the Fe II lines. The co-added spectra employed by

Weiner et al. (2009) for the majority of their analyses (although not inclination) have S/N of 16–28 per resolution element, while the spectral stacks used in this paper have S/N of 49–68 per resolution element.

We also utilized the statistical power of our sample in assembling composite spectra of high- and low-inclination objects, where $\langle i \rangle = 58°$ and 38°, respectively. In Figure 3.21, we compare these composite spectra and show thumbnails of the ten highest (lowest) inclination objects below (above) the composite spectra for visual reference. While the magnitude of the shifts with respect to systemic velocity are small in both cases, we do find that galaxies with lower inclinations exhibit bluer Fe II absorption troughs ($V_1 = -19 \pm 9$ km s^{-1}) than more inclined galaxies ($V_1 = 28 \pm 11$ km s^{-1}), qualitatively consistent with the results of Chen et al. (2010). Similarly, objects with lower inclinations show more blueshifted Mg II lines (V_{max}(Mg II) = –811 ± 140 km s^{-1}) than more edge-on systems (–692 ± 95 km s^{-1}). Likewise, the composite of lower (higher) inclination systems are characterized by V_{max}(Fe II) = –557 ± 101 (–464 ± 77) km s^{-1}.

The morphology of galaxies hosting outflows has only recently been investigated (Martin, 2005; Sato et al., 2009; Weiner et al., 2009; Rubin et al., 2010b; Law et al., 2012b). In the local universe, there is an implicit bias toward concluding that outflows are preferentially hosted by mergers. As systems with large SFRs are more likely to exhibit outflows (Martin, 2005; Rupke et al., 2005) and local galaxies with vigorous star formation are often characterized by disrupted morphologies indicative of either major or minor mergers (e.g., Sanders & Mirabel, 1996), an association between mergers and outflows naturally develops. In a study by Martin (2005) of 18 ULIRGs at $0.04 < z < 0.16$ characterized by merger signatures, these authors found evidence for neutral gas outflows in 15 systems (> 80%), consistent with Rupke et al. (2005). At larger redshifts, where

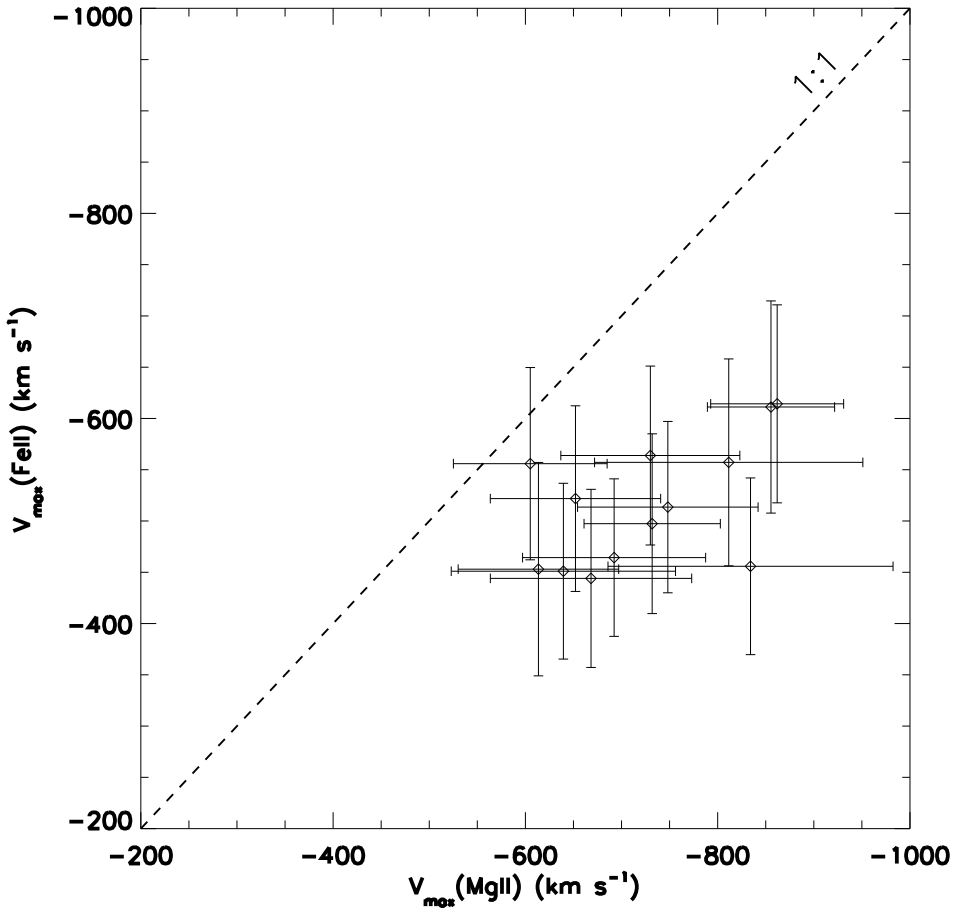

Figure 3.25 V_{max}(Mg II) versus V_{max}(Fe II), for the 13 composite spectra discussed in this paper. V_{max}(Mg II) is systematically more blueshifted than V_{max}(Fe II), as discussed in Section 4.4.

vigorous star formation and merger morphology appear to be decoupled (Law et al., 2007; Swinbank et al., 2010), Sato et al. (2009) still found that outflows traced by Na D were preferentially hosted by galaxies undergoing mergers.

We use our sample of $z \sim 1$ objects to study the prevalence of outflows in systems with large star-formation rates but a wide range of morphologies. We use quantitative morphological parameters from Lotz et al. (2004) to investigate the light distributions of galaxies hosting outflows. We employ the Gini coefficient (G) and the second order moment of the brightest 20% of each galaxy's flux, M_{20}. Figure 3.22 shows how objects in (G, M_{20}) space divide into classical early-type (E/S0/Sa), late-type (Sb–Irr), and merger candidates (Lotz et al., 2008). We find that objects exhibiting outflows and inflows span (G, M_{20}) morphological parameter space; systems classified as mergers do not appear to drive winds any more frequently than galaxies classified as E/S0/Sa or Sb–Irr. Objects with G, M_{20} values indicative of mergers, in fact, qualitatively host a relative dearth of outflows and inflows compared with other morphological classes. Both Weiner et al. (2009) and Rubin et al. (2010b) also found no trend between morphology and outflows in populations of star-forming galaxies.

Law et al. (2012b) studied the prevalence of outflows with galaxy size. These authors parameterized size using both the half-light radius along the semi-major axis (r) and the circularized effective radius ($r_e = r\sqrt{b/a}$). Law et al. (2012b) found a significant ($> 2\sigma$) correlation with both size estimates, where the smallest galaxies exhibited the largest interstellar blueshifts with respect to the systemic frame defined by Hα. In Figure 3.23, we use our data to plot outflow velocity versus two size estimates: Petrosian radius and $(A_{74}/\pi)^{1/2}$ (the "radius" of the A_{74} area). We show the best-fit line derived by Law et al. (2012b), V = 77r – 342 km s^{-1}, for reference, but note that only $\sim$ 40% of our sample has Petrosian radii

falling in the same range as the Law et al. (2012b) data. We find no evidence for a correlation between outflow velocity and either Petrosian radius or $(A_{74}/\pi)^{1/2}$.

3.4.3 Mg II Equivalent Width & Kinematics

Motivated by the range of Mg II absorption strengths observed in the sample, we investigated the primary driver of Mg II equivalent width. We estimated the equivalent width of Mg II by summing flux over the interval 2788–2810 Å, thereby encompassing both features of the Mg II doublet. We tested the correlation between Mg II equivalent width and SFR, stellar mass, sSFR, A_{UV}, U–B color, $\Sigma_{SFR}(A_{74})$, $\Sigma_{SFR}(R_P)$, and inclination, respectively (Figure 3.24). Consistent with Martin et al. (2012), we find that stellar mass and Mg II equivalent width are the most strongly correlated, at the 4.5σ level ($r_S = 0.61$). Bordoloi et al. (2011) also note the correlation between Mg II equivalent width and stellar mass in a sample of COSMOS galaxies at $0.5 < z < 0.9$. Stellar Mg II absorption may be present in objects with large stellar masses; population modeling is necessary in order to definitively address the contribution of stellar absorption.

Among the SFR, sSFR, and A_{UV} composite spectra, we find two families based on the strength and kinematics of Mg II. The low-SFR, high-sSFR, and low-A_{UV} composite spectra exhibit weaker, blueshifted Mg II features with little absorption in the red wings of the lines. On the other hand, the low-sSFR and high-A_{UV} composite spectra show stronger Mg II absorption at roughly the systemic velocity, with substantial absorption in the lines' red wings. The high-SFR composite spectrum, with its strong, blueshifted Mg II absorption, is anomalous in that appears to be included in both families. We note that the differences in the Mg II profiles of these SFR, sSFR, and A_{UV} composite spectra are mainly limited to the red wings of the lines and are distinct from the shifting of the blue

wings and centroids observed in the $\Sigma_{\rm SFR}(A_{74})$ and $\Sigma_{\rm SFR}(R_P)$ composite spectra. We propose that objects in the low-SFR, high-sSFR, and low-A_{UV} composite spectra are dominated by emission filling while the galaxies populating the low-sSFR and high-A_{UV} composite spectra experience significant systemic absorption. Furthermore, since stellar mass is correlated with SFR, sSFR, and A_{UV}, the variation in Mg II properties seen in the SFR, sSFR, and A_{UV} composite spectra may reflect the primary correlation between stellar mass and Mg II equivalent width. Accordingly, the low-SFR, high-sSFR, and low-A_{UV} composite spectra are preferentially populated with low-mass objects with weaker Mg II absorption (Martin et al., 2012). Higher mass objects may have more absorption and also less emission filling since emission is attenuated by dust. Future work involving modeling of the stellar component of Mg II absorption will help illuminate the connection between Mg II and stellar populations.

3.5 Discussion

In this section, we present a discussion and interpretation of our results. We observe the strongest trend between outflow velocity and $\Sigma_{\rm SFR}$, a finding that is supported both by theoretical work and also by observations at lower redshifts. We discuss the prevalence of outflows in the sample and consider the uncertainties of using different tracer species and measurement diagnostics to parameterize a single characteristic outflow velocity.

3.5.1 Outflow Velocity and the Star-Formation Rate Surface Density

Our finding of a strong correlation between outflow velocity and the *concentration* of star formation – as opposed to the global SFR – is consistent with previous

observations. In a sample of star-forming galaxies at $z = 1.5$–3.6, Law et al. (2012b) reported a 2.1σ correlation between outflow velocity and $\Sigma_{\rm SFR}$. At a comparable redshift, Genzel et al. (2011) used SINFONI observations of five galaxies to measure a higher incidence of broad Hα profiles in star-forming clumps with larger Hα surface brightnesses. Since broad wings are indicative of gas moving at high velocities and larger Hα surface brightnesses can be directly linked to larger star-formation rate surface densities, these authors posit that their results may be evidence for galactic winds being modulated by the intensity of star formation. The lack of broad Hα components in fainter interclump regions of the Genzel et al. (2011) sample furthermore suggests that winds may require some threshold $\Sigma_{\rm SFR}$. Similarly, in a sample of ~ 50 galaxies at $z = 1.2$–2.6 with high Hα surface brightnesses, Le Tiran et al. (2011) found that systems with the highest star-formation rate surface densities were more likely to exhibit a broad Hα component. In searching for a physical explanation for the incidence of broad Hα kinematics, which are interpreted as arising in outflowing gas, Le Tiran et al. (2011) used the ratio of [S II] 6716 / [S II] 6731 to infer electron densities (Osterbrock, 1989). Based on conversions between electron density and thermal pressure, these authors found that the systems with the highest star-formation intensities were characterized by pressures similar to the values found in local starbursts exhibiting galactic winds (e.g., Lehnert & Heckman, 1996). Le Tiran et al. (2011) accordingly proposed that thermal pressure may modulate the incidence of galactic winds.

In addition to thermal pressure arising from the hot gas expelled by supernovae, radiation pressure on dust grains is also commonly invoked as a mechanism for driving galactic winds (e.g., Socrates et al., 2008; Murray et al., 2011). When dust grains experience a force from impinging photons, the cool gas that is coupled to the dust is also accelerated. Several authors have examined the relative

contributions of thermal and radiation pressure in driving galactic winds. Murray et al. (2011) propose that radiation pressure is the primary driver lofting gas clouds above the galactic disk in the first $\sim$ 4 Myr before supernovae explode. These authors hypothesize that a critical gas surface density is required to provide the initial radiation pressure to accelerate the gas cloud above the galactic disk. Once a bubble of gas is sufficiently separated from the galactic plane, ram pressure from the hot winds of later generations of supernovae accelerates the gas (with a force comparable to the force from radiation pressure; Murray et al., 2005) above the galactic disk. The predicted scaling relation between outflow velocity and the SFR due to ram pressure alone is shallow: $V \propto SFR^{1/5}$ (Ferrara & Ricotti, 2006) or $V \propto SFR^{1/4}$ (Heckman et al., 2000). On the other hand, for a purely radiatively driven wind, the outflow velocity is expected to scale roughly linearly with the SFR (Sharma & Nath, 2012). Using data from the z $\sim$ 3 LBG study of Shapley et al. (2003), Ferrara & Ricotti (2006) find a scaling relation between SFR and outflow velocity of the form $V \propto SFR^{2/3}$. However, these authors make the assumption that outflow velocity can be calculated from the velocity difference between interstellar absorption lines and Lyα emission. As Lyα is resonantly scattered and often observed to be redshifted by several hundred km s^{-1} relative to the systemic velocity frame defined by Hα emission (Steidel et al., 2010), the outflow velocities employed by Ferrara & Ricotti (2006) may very well be overestimates. Indeed, analysis of the Shapley et al. (2003) data reveals that composite spectra differing in SFR have nearly identical gas kinematics as traced by interstellar absorption lines alone. The Ferrara & Ricotti (2006) conclusion that outflow velocity and SFR are related via the form $V \propto SFR^{2/3}$ is primarily driven by kinematic changes in Lyα as opposed to true variation in the interstellar species tracing the wind. The Shapley et al. (2003) data suggest that outflow velocity varies much more weakly, if at all, with SFR. Observations by

Martin (2005) ($V \propto SFR^{0.35}$) are not grossly inconsistent with the $SFR^{1/5}$ scaling predicted by Ferrara & Ricotti (2006) for acceleration by ram pressure alone, although various authors have suggested that galactic winds are likely accelerated by a combination of radiative and ram pressures (Sharma & Nath, 2012; Murray et al., 2011). We do not find a significant trend of outflow velocity with SFR, although we note that the relatively low resolution of our data paired with the limited range of SFRs probed may preclude a robust measurement of a trend, particularly if the scaling is shallow.

As discussed in Genzel et al. (2011), the efficiency of radiation pressure in driving galactic winds can be linked to the surface density of star formation (i.e., $\Sigma_{\rm SFR}$) via simple heuristic arguments. Environments with higher star-formation rate surface densities have higher gas surface densities (Kennicutt, 1998). Gas surface density, in turn, is correlated with the dust surface density and, analogously, the dust opacity. The radiation force on dust grains, $\dot{p}_{\rm rad}$, is more efficient in dustier environments ($\dot{p}_{\rm rad} \propto \tau L/c$, where τ is the optical depth to radiation, L is the bolometric luminosity, and c is the speed of light; Veilleux et al., 2005). As systems with higher star-formation rate surface densities will produce more radiation to begin with (having a larger concentration of star formation), it is expected that the combination of higher radiation levels and the efficient radiative coupling found in high $\Sigma_{\rm SFR}$ environments – due to larger concentrations of dust – will translate into effective driving of galactic winds. In the sample discussed here, however, we do not find that dustier systems show stronger outflows; the high- and low-$A_{\rm UV}$ composite spectra have V_1, V_{max}(Fe II), and V_{max}(Mg II) values consistent at the 1σ level. This null result may indicate that radiation pressure does not dominate the acceleration of galactic winds, or that our dataset is simply too limited in size and S/N to unambiguously detect a trend between $A_{\rm UV}$ and

outflow velocity.

Several authors have estimated the form of the scaling relation between $\Sigma_{\rm SFR}$ and outflow velocity. In the context of outflows being driven from disrupted giant molecular clouds, Murray et al. (2011) parameterize the ejection velocity of gas due to radiation pressure as proportional to the square of the gas surface density, Σ_g:

$$v_{ej} \propto \frac{R_d^2 \Sigma_g^2}{v_c^2} \tag{3.4}$$

where v_{ej} is the ejection velocity (assumed to be analogous to the outflow velocity), R_d is the galaxy disk radius, and v_c is the galaxy circular velocity. Assuming the Kennicutt-Schmidt (1998) star-formation law has the form $\Sigma_{\rm SFR} \propto \frac{\Sigma_g}{\tau_{\rm dyn}}$, where $\tau_{\rm dyn}$ is the dynamical timescale (R_d/v_c), Murray et al. (2011) alternatively express v_{ej} as proportional to the square of the star-formation rate surface density:

$$v_{ej} \propto \frac{R_d^4 \Sigma_{\rm SFR}^2}{v_c^4}. \tag{3.5}$$

The additional terms corresponding to R_d and v_c may translate into scatter in the v_{ej} – $\Sigma_{\rm SFR}$ relation; using our estimates of the Petrosian radius and the width of the [OII] emission feature as proxies for R_d and v_c, respectively, we find that $\tau_{\rm dyn}$ spans a factor of ~ 30 in our sample. Murray et al. (2011) also derive a critical surface density of star formation required to launch a galactic wind by imposing the criterion that $v_{ej} > v_c$. These authors find that this critical density is dependent on both R_d and v_c; a local L_* galaxy has $\Sigma_{\rm SFR}^{\rm crit} \approx 0.06\ M_\odot$ yr^{-1} kpc^{-2}. This result is consistent with the observationally-motivated $\Sigma_{\rm SFR}$ threshold derived by Heckman (2002): $\Sigma_{\rm SFR}^{\rm crit} \approx 0.1\ M_\odot$ yr^{-1} kpc^{-2}.

Strickland et al. (2004) suggest an alternative scaling relation between outflow

velocity and $\Sigma_{\rm SFR}$ assuming winds are driven by thermal pressure and that hot gas blows out of the galaxy three scale heights above the disk:

$$v_{ej} \propto \left(\frac{\Sigma_{\rm SFR}}{\rho_0}\right)^{1/3} \tag{3.6}$$

where ρ_0 is the gas density. Following Chen et al. (2010), the above relation can be equivalently expressed using the Kennicutt-Schmidt (1998) law and the approximation that the gas density is proportional to the gas surface density divided by the scale height of the disk, H_z:

$$v_{ej} \propto \Sigma_{\rm SFR}^{2/21} H_z^{1/3} \tag{3.7}$$

Strickland et al. (2004) adopt $\Sigma_{\rm SFR} \propto \Sigma_g^{1.4}$ as the form of the Kennicutt-Schmidt (1998) law. If one instead uses the same functional form of the Kennicutt-Schmidt (1998) law employed by Murray et al. (2011), one finds that v_{ej} is independent of $\Sigma_{\rm SFR}$. Equation 3.7 is consistent with the shallow scaling between outflow velocity and $\Sigma_{\rm SFR}$ recorded by Chen et al. (2010), although it is important to note that the small dynamic range of the Chen et al. (2010) data (120 km s^{-1} $< v_{ej} <$ 160 km s^{-1}) may obscure trends. However, as mentioned above, Chen et al. (2010) do find a significant correlation between $\Sigma_{\rm SFR}$ and the equivalent width of the Na D outflow component. The equivalent width of the outflow component is dependent on the velocity spread, covering fraction, and optical depth of the absorbing gas.

The power-law relations discussed above can be generalized as being of the form $v_{ej} \propto \Sigma_{\rm SFR}^{\alpha}$, where $\alpha = 2.0$ or 0.1. We use our V_1 and $\Sigma_{\rm SFR}(\rm A_{74})$ data with the `IDL` routine `MPFITFUN` (Markwardt, 2009) to fit a power law of the form $V_1 = \rm A\Sigma_{SFR}(A_{74})^{\alpha} + B$, where A, α, and B are free parameters. We choose to include

only objects exhibiting outflows ($V_1 < 0$ km s^{-1}) and we furthermore impose the prior that the additive term of the power law, B, is 0 (i.e., V_1 converges to 0 as $\Sigma_{\rm SFR}(A_{74})$ goes to 0). When we fit a power law with $\alpha = 2.0$ or 0.1 to our data, we find a better fit with $\alpha = 2.0$ (although the χ^2 values per degree of freedom are large in both cases: 6.3, 7.5). Removing any priors on the slope, we recover a best-fit α of 0.8. However, we caution that the relatively large errors on our outflow velocities prevent a robust discrimination of α.

We can also bin the data in order to reduce the uncertainties on the velocity measurements. We divided the individual data points into three groups according to $\Sigma_{\rm SFR}(A_{74})$ and fit a power law of the same form as discussed above to the average V_1 and $\Sigma_{\rm SFR}(A_{74})$ values in each bin. We recover a best-fit slope of 0.3. When we bin all the data, including the objects showing apparent inflows but still excluding the two outliers at $\Sigma_{\rm SFR}(A_{74}) > 2.0$, we find a best-fit slope of 1.6. As these various fits do not converge on a slope, it is clear that a larger sample of measurements is needed, ideally over a wider dynamic range in $\Sigma_{\rm SFR}(A_{74})$. Outflow velocities derived from higher resolution data will be furthermore beneficial for drawing meaningful conclusions about the slope of the power law relating outflow velocity and star-formation rate surface density.

3.5.2 Prevalence of Winds

In the sample discussed here – 72 objects in the EGS, representing a subset of the data discussed in Martin et al. (2012), – we find 1σ significant detections of blueshifted Fe II absorption in $\sim$ 40% of the sample. Likewise, 40 $\pm$ 5% of objects show outflows with blueshifts of at least –40 km s^{-1}. This 40% detection rate is a lower limit due to the incompleteness of measuring winds in low S/N spectra (Martin et al., 2012). In stating that blueshifts are seen in $\sim$ 40% of the

sample, it is important to remember that the detection rate can be explained by degenerate assumptions about the Fe II gas covering fraction and the percentage of galaxies hosting winds. If one assumes that the winds are isotropic with a covering fraction of 100%, we can conclude that $\sim$ 40% of galaxies host winds. On the other hand, 100% of the sample could in fact host outflows if the Fe II absorbing gas covers only $\sim$ 40% of each galaxy. We favor the latter scenario – in which winds are present in a majority of galaxies and yet observable only in a fraction of sources due to an average covering fraction less than unity – as our work supports the collimation of winds: $\sim$ 70% of the sample has star-formation rate surface densities above the threshold level predicted for driving outflows while only $\sim$ 40% of objects show blueshifted Fe II absorption lines. Other authors have also suggested that winds are collimated (Rupke et al., 2005; Chen et al., 2010; Bordoloi et al., 2011). Imaging observations of winds in local starburst galaxies also reveal that outflows preferentially escape perpendicular to galactic disks (e.g., Heckman et al., 1990; De Young & Heckman, 1994; Shopbell & Bland-Hawthorn, 1998) and therefore do not cover the entirety of galaxies. We caution, however, that as high-redshift galaxies look less and less disk-dominated (Lotz et al., 2004; Law et al., 2007, 2012a), the interpretation of outflows emanating particular to a presumed disk is complicated. Galactic winds appear to be ubiquitous in samples of clumpy, unresolved galaxies at $z = 2$–3 (e.g., Shapley et al., 2003). The galaxies in our $z \sim 1$ sample, while generally not grand-design spirals, do not show the preponderance of disturbed morphologies characteristic of $z \geq 2$ samples (e.g., Law et al., 2007).

Our outflow detection frequency of 40% is similar to the detection frequency reported for the parent sample of objects observed with LRIS (Martin et al., 2012), indicative that the EGS and parent samples do not differ significantly in outflow properties. We also find that our outflow detection frequency is consistent

with observations based on absorption lines in both local samples (Rupke et al., 2005) and at $z \sim 1.4$ (Weiner et al., 2009). Based on the absorption depth of Mg II in a co-added spectrum of galaxies, these authors inferred that at least half of the galaxies in their sample exhibit outflows of cool, low-ionization gas. We note that the kinematics and absorption strength of the Mg II lines in the Weiner et al. (2009) composite spectrum are similar to those seen in our composite spectrum after accounting for the different spectral resolutions of our respective data (Martin et al., 2012). This similarity is suggestive that the galactic winds probed by Mg II are fundamentally alike in both our sample and the Weiner et al. (2009) sample.

While the kinematics of Mg II in our composite spectrum are similar to those of the Weiner et al. (2009) composite (i.e., offset from the systemic velocity by several hundred km s^{-1}), we find no blueshift in the Fe II lines in our composite spectrum ($V_1 = -5 \pm 6$ km s^{-1}). The spread of both positive and negative V_1 velocities observed for individual objects (Figure 3.11) is consistent with a global average velocity close to 0 km s^{-1}, but the negligible blueshift of Fe II lines in the composite spectrum may also be due to the smaller dynamic range of gas velocities probed by Fe II than Mg II (Rubin et al., 2010b; Prochaska et al., 2011). We discuss potential explanations for this decreased dynamic range below.

3.5.3 Diagnostics of Winds

Outflowing galactic winds can be measured using a variety of samples: background quasars probing galactic halos along the line-of-sight, galaxy-galaxy pairs, and isolated galaxies in which the stellar disk provides a continuum for absorption by foreground interstellar gas. Even considering only the last technique – which we employ in this paper – a range of outflow velocity measurements will

be obtained for a galaxy depending on which interstellar tracer species are used and which parameterizations of absorption line kinematics are adopted.

From the extensive literature of galactic winds published to date, it is evident that a range of tracer elements are used in tandem with a variety of measurement techniques to parametrize the velocity of outflowing gas. Before we discuss how the choices of tracer elements and line-fitting methods may strongly affect the derived outflow velocity and its scaling with galaxy properties, it is important to acknowledge the intrinsic uncertainty of extracting a single representative outflow velocity from a physical system characterized by many interacting clouds and shells of gas at a range of radii accelerated by a population of supernovae and massive stars injecting energy and momentum over a long timescale (> 100 Myr). In the absence of extremely high resolution and high S/N spectroscopy, the kinematics extracted from the centroids of absorption lines must be thought of as tracing only the gross average of multiple fronts of outflowing gas. With this limitation in mind, we now turn to a discussion of how the choice of tracer species may impact the measured properties of the outflows.

Absorption line studies are necessarily affected by the choice of absorption line probe. Authors often rely on relatively abundant species whose transitions are redshifted into the optical window of optimized detector sensitivity. Local studies typically employ Na D while investigations of higher redshift populations may use transitions of Si II, C II, Al II, Fe II, Mg II, or Mg I in the rest-frame UV. As these species differ in abundance, ionization potential, susceptibility to emission filling, and (perhaps) spatial distribution, it is unsurprising that their associated outflow velocities differ as well. For instance, Na D stellar absorption is known to be stronger in older stellar populations; if the outflow and stellar components are not separated by means of modeling, the outflow velocity can be

significantly underestimated and trends between galaxy properties and winds can become skewed or lost (e.g., Chen et al., 2010; Coil et al., 2011). The different ionization energies of Na I, Fe II, Mg II, and Mg I (5.1, 16.1, 15.0, and 7.6 eV, respectively) result in these species tracing different populations of gas: Na I and Mg I, with low ionization potentials, require dense, shielded gas in order to survive while Fe II and Mg II are less easily ionized and therefore survive in more widespread environments. Emission filling affects particular transitions of species to a differing degree depending on the relative availability and oscillator strengths of transitions decaying to excited ground states. The Mg II doublet presents a particularly extreme case of emission filling. The doublet energy levels are such that these transitions are trapped; the absorption of a resonance photon necessarily results in the re-emission of another resonance photon. The Mg II doublet is therefore strongly susceptible to emission filling and measurements of the centroids of these transitions may yield different kinematic information (i.e., larger blueshifts) relative to that derived from features less affected by emission filling (Martin et al., 2012). The coincidental presence of additional spectral features adjacent to absorption lines of interest may also contaminate outflow signatures (e.g., He I λ5876 $\sim$ 15 Å blueward of Na D).

Differences in oscillator strengths also likely impact derived outflow velocities. In the case of comparing velocities measured from Fe II and Mg II transitions, the larger oscillator strength of the Mg II line at 2796 Å ($f_{12} = 0.60$) compared with the oscillator strengths of the Fe II lines at 2344, 2374, and 2587 Å used in our analyses ($f_{12} = 0.04$–0.11) means that Mg II is optically thick at lower column densities than Fe II. Mg II is a better probe of rarefied gas than Fe II simply due to its larger cross-section for absorption. Bordoloi et al. (2011) found that Mg II equivalent widths decrease with increasing distance from galaxies. If equivalent width is a proxy for gas column density (neglecting the effects of

saturation) then one can conclude that Mg II gas column density decreases with increasing distance from galaxies. Given that Mg II is an effective tracer of low-density gas, and presuming that low-density gas is found far from galaxies, the larger outflow velocities inferred for Mg II compared with Fe II (Figure 3.25; Rubin et al., 2010b; Prochaska et al., 2011) are suggestive that the speed of galactic winds increases with increasing galactocentric radius. This inference that galactic winds are accelerating is consistent with recent work by Martin & Bouché (2009) and Steidel et al. (2010). Martin & Bouché (2009) studied a sample of ULIRGs at $z \sim 0.25$ and concluded that winds are accelerating based on the assumption of a spherical outflow and measurements of how gas covering fractions vary with velocity. These authors found that gas covering fractions decreased with increasing outflow velocity. Pairing this observation with the prediction that a spherical outflow will suffer geometrical dilution (i.e., reduction of its covering fraction) as it breaks up and expands to larger galactocentric radii, Martin & Bouché (2009) concluded that outflowing gas is accelerating. Steidel et al. (2010) showed that models of an accelerating wind provided the best match to observations at $z \sim 2$–3 of interstellar absorption lines arising from a range galaxy impact parameters ($b \sim 0$–200 kpc). Simulations also suggest that higher velocity gas may be located at larger galactocentric radii simply due to differences in travel time (e.g., Dalla Vecchia & Schaye, 2012). Observations of decreasing gas column densities with increasing outflow velocity seen in the gravitationally-lensed Lyman Break Galaxy cB58 (Pettini et al., 2002) provide further evidence of the connection between low-density gas, large galactocentric distances, and large outflow velocities.

The effects discussed above are all dependent on the choice of tracer species. We now examine a more tangible aspect of the data analysis: how do different measurements of outflow velocity impact the derived velocities and subsequent

scaling relations with galaxy properties? Two techniques feature prominently in the literature for quantifying the blueshift of an absorption line tracing an outflow. Some authors rely on fitting the centroid of an absorption line; i.e., measuring the wavelength at which the bulk of the absorption occurs and assuming that this velocity characterizes the outflowing gas (Shapley et al., 2003; Martin, 2005; Rubin et al., 2012; Coil et al., 2011; Law et al., 2012b). Other authors parameterize a maximal outflow velocity by measuring the blue shoulder of an absorption line at some fractional level of the continuum (e.g., 90%, Weiner et al., 2009; Coil et al., 2011).

These two techniques, measuring different characteristics of the outflow, are complementary and both methods have associated uncertainties. In the case of the centroid measurement, one is susceptible to mistakenly attributing the entire absorption profile to an outflow when in fact the profile should be decomposed into both an outflow signature and a stellar absorption (or stationary ISM) component. Failing to correct for the gas not entrained in the outflow will yield an underestimate of the derived outflow velocity (Weiner et al., 2009; Coil et al., 2011), although such a correction is difficult and highly uncertain for low-resolution, low-S/N data (Steidel et al., 2010). In our sample, the Fe II absorption centroid that we measure is unlikely to be significantly contaminated by stellar absorption due to the young, star-forming nature of the majority of our galaxies; stellar Fe II absorption is more prevalent in older populations (e.g., Bruzual & Charlot, 2003b). The maximal outflow velocity method is dependent on resolved absorption lines; low spectral resolution data of unresolved absorption lines will merely reflect the instrumental profile and therefore measurements of a supposed wing profile will be meaningless. Furthermore, maximal outflow velocity measurements are strongly dependent on spectroscopic S/N (Section 3.3.3). We mitigate this effect in our present work by limiting our analyses of maximal

outflow velocities to measurements from the composite spectra which have largely uniform S/N.

3.6 Summary and Conclusions

We utilized spectroscopic and imaging observations to investigate the properties and prevalence of outflowing galactic winds in a sample of 72 objects at $0.7 < z < 1.3$ in the Extended Groth Strip. These data are part of a larger study discussed in Martin et al. (2012). We used LRIS spectroscopy to study interstellar absorption lines in the rest-frame UV, including transitions of Fe II and Mg II. With *GALEX*, *HST*, and *Spitzer* imaging from the AEGIS dataset, we employed two complementary analysis techniques to investigate how galaxy properties are correlated with the prevalence and strength of winds: 1) direct comparison of individual outflow velocities with galaxy properties and 2) construction of composite spectra based on subsamples of objects exhibiting similar star-forming or structural characteristics. We provide below a numbered list of our main conclusions in summary and expand on these points in the following paragraphs.

1. Approximately 40% of the sample exhibits $> 1\sigma$ outflows in Fe II.

2. We find a 3.1σ trend between outflow velocity and $\Sigma_{\rm SFR}$.

3. Outflow velocity and SFR are only weakly correlated.

4. There is no apparent link between outflowing gas and host galaxy morphological type.

5. Face-on galaxies exhibit more blueshifted Fe II centroids than edge-on galaxies.

6. The kinematics of Fe II and Mg II gas are often discrepant, with Mg II preferentially tracing higher velocity gas.

The sample includes objects exhibiting Fe II Doppler shifts ranging from –217 km s^{-1} to +155 km s^{-1}, where approximately 40% of the sample exhibits $> 1\sigma$ outflows in Fe II. We find that $40 \pm 5\%$ of the sample is characterized by Fe II bllueshifts of at least –40 km s^{-1}; this outflow fraction is consistent with that of the parent sample discussed in Martin et al. (2012). We used SFRs inferred from *GALEX* imaging in tandem with galaxy area estimates to measure $\Sigma_{\rm SFR}$. Given the clumpy morphologies of star-forming galaxies at $z \sim 1$, we developed a new technique to estimate the area of only UV-bright clumps. Using these new "clump areas" and also galaxy areas corresponding to Petrosian radii, we measured $\Sigma_{\rm SFR}$. The majority of objects have $\Sigma_{\rm SFR} > 0.1$ $M_\odot$ yr^{-1} kpc^{-2}, yet we observe significant Fe II blueshifts in only a minority of the sample. The lower fraction of objects showing outflows relative to that meeting the $\Sigma_{\rm SFR}$ threshold for driving a wind is evidence that winds are collimated and therefore observable only over a limited range of inclinations. We find a strong ($\sim 3\sigma$) trend between outflow velocity and $\Sigma_{\rm SFR}$ such that objects with higher star-formation rate surface densities show more blueshifted Fe II absorption. Composite spectra assembled on the basis of $\Sigma_{\rm SFR}$ also support this correlation, with V_1, V_{max}(Fe II), and V_{max}(Mg II) all varying toward more blueshifted values with increasing $\Sigma_{\rm SFR}$. At the same time, outflow veflocity and SFR are only weakly correlated. We propose that the data span too narrow a range in SFR (roughly two orders of magnitude) to show a trend. While the range of $\Sigma_{\rm SFR}$ is similarly limited ($0.03 \lesssim \Sigma_{\rm SFR}(A_{74}) \lesssim 3.0$), the trend between outflow velocity and $\Sigma_{\rm SFR}$ may be more fundamental and therefore recoverable over a smaller dynamic range.

Based on quantitative morphological analyses of $V+I$ *HST* imaging, we do not find any link between outflowing gas and galaxy structure. Rather, galaxies experiencing winds appear to span the classical morphological regimes from disks to spheroidals to mergers. We estimated galaxy inclinations from axis ratios in the

HST imaging and found that face-on systems exhibit stronger Fe II blueshifts than edge-on galaxies. This result lends credence to the canonical picture of outflowing winds emanating perpendicular to galactic disks. Motivated by recent results of faster outflows in smaller galaxies, we investigated the relationship between outflow velocity and size, but found no evidence for a trend.

Quantifying the prevalence of outflows requires an understanding of the physical processes affecting the absorption lines tracing winds. Different elemental tracer species often yield discrepant outflow velocities, for reasons including emission filling, differences in oscillator strengths, and perhaps simply intrinsic variations in gas cloud kinematics. Furthermore, the variety of techniques available for quantifying the speed of galactic winds (centroid fitting, maximal velocity measurements from a blue wing, etc.) complicate the parameterization of a single outflow velocity. Future studies utilizing higher resolution spectroscopic data and complementary spatially-resolved imaging to determine galaxy morphologies and the spatial extent of winds will be crucial for better understanding the link between galactic outflows and their host galaxies at a range of redshifts.

Table 3.1. Sample Parameters[a]

ID	RA[b] (J2000)	Dec[c] (J2000)	z_{sys}	M_B	$U-B$	M_* (log $M_\odot$)	SFR[d] ($M_\odot$ yr^{-1})	A_{UV}[e]	A_{74}[f] (kpc^2)	πR_P^2[g] (kpc^2)	$V_1 \pm \delta V_1$[h] (km s^{-1})
12008116	14 17 25.67	52 30 25.19	0.74664	–19.69	0.64	10.1	5	1.9	43	155	37 ± 31
12008166	14 17 21.59	52 28 03.62	1.28545	–19.69	0.32	9.7	···	0	11	44	31 ± 62
12008197	14 17 21.84	52 29 19.62	0.98022	–21.19	0.80	10.6	97	4.1	91	232	–62 ± 19
12008364[i]	14 17 09.44	52 29 08.95	0.77957	–19.30	0.55	9.8	···	0	0	0	–33 ± 92
12008441	14 17 16.76	52 28 39.59	0.83273	–20.81	0.99	10.9	12	2.6	138	786	58 ± 61
12008445	14 17 04.91	52 27 48.85	1.27739	–20.69	0.51	10.2	···	0	77	220	–193 ± 79
12008456	14 17 10.67	52 30 11.63	0.90230	–19.93	0.73	9.8	6	1.4	21	60	79 ± 52
12008481	14 17 10.04	52 28 39.45	0.71341	–21.03	0.93	10.9	···	0	138	484	75 ± 109
12008509	14 17 03.23	52 30 33.13	1.21577	–19.80	0.36	9.7	···	0	51	144	70 ± 52
12008550	14 16 56.74	52 29 52.48	1.30249	–21.22	0.62	10.0	24	1.5	34	109	–145 ± 23
12008553	14 17 02.57	52 29 38.86	0.90156	–21.56	1.12	10.5	···	0	6	25	–79 ± 29
12008591	14 17 14.74	52 27 57.13	0.77192	–18.37	0.53	9.1	···	0	11	29	···
12008811	14 16 55.32	52 30 24.91	1.21556	–20.79	0.67	10.1	9	0.8	13	44	33 ± 20

Table 3.1 (cont'd)

ID	RA[b] (J2000)	Dec[c] (J2000)	z_{sys}	M_B	$U-B$	M_* (log $M_\odot$)	SFR[d] ($M_\odot$ yr^{-1})	A_{UV}[e]	A_{74}[f] (kpc^2)	πR_P^2[g] (kpc^2)	$V_1 \pm \delta V_1$[h] (km s^{-1})
12011364	14 18 28.46	52 33 16.22	0.98642	–20.75	0.74	10.2	90	4.2	90	244	–28 ± 24
12011428	14 18 28.35	52 31 47.76	1.28408	–19.87	0.18	9.6	9	0.8	···	···	154 ± 32
12011493	14 18 27.94	52 33 39.53	1.26377	–20.74	0.62	10.2	11	1	26	118	–21 ± 45
12011600	14 18 25.03	52 31 08.95	0.43665	–17.67	0.43	8.8	0	0.9	···	···	–133 ± 129
12011619	14 18 24.68	52 32 48.66	1.07449	–19.30	0.43	9.1	2	0	13	93	···
12011742	14 18 16.19	52 32 16.77	1.33578	–20.81	0.71	10.2	···	0	12	45	2 ± 23
12011767	14 18 24.75	52 32 55.43	1.28170	–22.18	0.75	11.0	76	2.7	171	562	–34 ± 35
12011836	14 18 16.05	52 31 48.06	0.92707	–19.90	0.57	10.2	14	2.8	14	55	–128 ± 21
12012500	14 17 21.28	52 34 01.05	0.86494	–20.28	0.89	10.6	···	0	34	95	–31 ± 28
12012764	14 17 03.83	52 33 00.36	1.23532	–20.26	0.61	9.7	···	0	···	···	–62 ± 47
12012777	14 17 03.22	52 31 42.52	1.27426	–21.06	0.51	10.1	22	1.4	15	55	–217 ± 13
12012817	14 16 59.78	52 31 09.48	1.21583	–20.92	0.89	10.8	···	0	7	23	28 ± 44
12012842	14 16 56.45	52 33 13.77	1.31484	–21.68	0.75	11.0	···	0	···	···	5 ± 23

Table 3.1 (cont'd)

ID	RA[b] (J2000)	Dec[c] (J2000)	z_{sys}	M_B	$U-B$	M_* (log $M_\odot$)	SFR[d] ($M_\odot$ yr^{-1})	A_{UV}[e]	A_{74}[f] (kpc^2)	πR_P^2[g] (kpc^2)	$V_1 \pm \delta V_1$[h] (km s^{-1})
12012871	14 17 00.37	52 33 38.53	1.34433	–20.75	0.55	10.0	14	1.3	···	···	–13 ± 39
12013002	14 16 50.03	52 33 46.59	1.21841	–20.22	0.64	9.5	4	0.3	···	···	10 ± 42
12013145	14 16 55.46	52 32 15.81	1.34063	–19.66	0.27	9.5	6	0.7	···	···	–38 ± 61
12013242	14 16 55.22	52 31 38.98	1.28679	–21.31	0.45	10.1	25	1.2	···	···	–73 ± 22
12015177	14 18 55.51	52 37 18.84	0.98609	–20.23	0.48	9.6	11	1.7	···	···	–101 ± 18
12015226	14 18 53.61	52 35 48.28	0.91600	–19.30	0.29	9.1	4	0.7	···	···	16 ± 18
12015295	14 18 55.92	52 37 07.05	0.49157	–19.52	0.81	10.4	1	1.2	···	···	···
12015313	14 18 50.39	52 36 21.36	0.68009	–20.72	1.21	11.2	···	0	···	···	···
12015320	14 18 51.69	52 36 00.43	0.98573	–22.09	1.05	11.3	40	2.6	···	···	···
12015563	14 18 34.29	52 36 49.30	1.28239	–21.30	0.59	10.3	···	0	7	22	–98 ± 42
12015643	14 18 49.35	52 36 08.38	0.24718	–17.97	0.51	9.3	0	1.6	···	···	···
12015680	14 18 42.71	52 36 35.96	0.75867	–20.47	0.55	10.3	21	2.9	68	279	148 ± 61
12015682	14 18 49.05	52 36 29.65	1.28371	–21.52	0.62	11.2	27	1.4	···	···	–99 ± 93

Table 3.1 (cont'd)

ID	RA[b] (J2000)	Dec[c] (J2000)	z_{sys}	M_B	$U-B$	M_* (log $M_\odot$)	SFR[d] ($M_\odot$ yr^{-1})	A_{UV}[e]	A_{74}[f] (kpc^2)	πR_P^2[g] (kpc^2)	$V_1 \pm \delta V_1$[h] (km s^{-1})
12015775	14 18 18.64	52 36 47.89	1.22428	–19.36	0.22	9.6	4	0.7	4	19	–105 ± 43
12015792[i]	14 18 19.81	52 35 15.88	1.23068	–21.23	0.95	11.0	12	2.2	0	0	–27 ± 85
12015858	14 18 26.49	52 36 08.41	1.23068	–19.87	0.21	9.5	8	0.8	53	202	–54 ± 60
12015908	14 18 08.59	52 36 10.08	0.99924	–20.25	0.64	10.0	21	3	27	82	45 ± 23
12015914	14 18 22.10	52 35 27.04	1.10461	–19.82	0.33	10.1	8	1.1	3	10	51 ± 21
12015933	14 18 25.38	52 37 11.55	1.28514	–20.34	0.66	9.7	···	0	13	57	–22 ± 81
12016019	14 18 07.96	52 36 43.93	1.08467	–20.71	0.62	10.0	18	1.9	44	182	48 ± 14
12016050	14 18 08.67	52 35 13.82	0.97971	–19.71	0.44	9.5	15	2.6	11	48	–15 ± 22
12016054	14 18 06.66	52 35 06.05	0.68377	–20.73	1.08	11.2	16	4.1	43	134	72 ± 185
12016075	14 18 05.98	52 34 08.42	1.11739	–19.67	0.54	9.4	5	1.2	9	41	13 ± 49
12016337	14 18 03.71	52 34 23.42	0.72026	–20.27	1.01	10.9	9	3.3	144	617	···
12016903	14 17 12.78	52 34 28.40	1.15998	–21.46	0.50	10.2	25	1	46	202	2 ± 30
12017063	14 16 57.61	52 34 28.14	0.73912	–19.79	0.51	10.1	5	1.2	···	···	–70 ± 30

Table 3.1 (cont'd)

ID	RA[b] (J2000)	Dec[c] (J2000)	z_{sys}	M_B	$U-B$	M_* (log $M_\odot$)	SFR[d] ($M_\odot$ yr^{-1})	A_{UV}[e]	A_{74}[f] (kpc^2)	πR_P^2[g] (kpc^2)	$V_1 \pm \delta V_1$[h] (km s^{-1})
12019542	14 18 49.94	52 40 22.15	1.27848	–21.68	0.70	10.4	40	2.3	88	243	–183 ± 60
12019674	14 18 56.19	52 38 43.89	0.98491	–21.48	0.96	11.1	15	2.2	135	443	130 ± 86
12019697	14 18 49.69	52 37 42.18	0.26481	–17.25	0.54	9.0	0	1.8	27	111	···
12019709	14 18 47.13	52 37 52.21	0.75792	–19.90	0.48	9.7	···	0	10	23	–77 ± 151
12019916	14 18 36.51	52 40 20.89	0.72849	–20.26	0.83	10.7	11	3.3	48	156	49 ± 32
12019923	14 18 35.21	52 39 42.89	0.72674	–20.19	0.76	10.4	5	1.6	47	160	56 ± 37
12019962	14 18 36.59	52 37 43.63	0.64444	–19.22	0.45	9.7	1	0.8	32	144	104 ± 31
12019973	14 18 28.61	52 40 53.43	0.81886	–19.80	0.53	10.1	10	2.3	41	123	–58 ± 27
12019995	14 18 47.09	52 37 54.47	0.24888	–19.06	0.52	9.8	···	0	42	150	···
12019996	14 18 36.64	52 37 54.62	1.28128	–21.71	0.63	10.6	43	1.8	164	499	117 ± 24
12020031	14 18 41.23	52 39 34.32	0.82072	–22.00	0.97	11.2	36	2.4	427	1391	64 ± 108
12020064	14 18 46.56	52 38 13.78	1.31479	–21.12	0.59	10.3	26	2	58	138	–62 ± 56
12020075	14 18 48.94	52 37 30.01	0.80829	–20.52	0.64	10.6	12	1.9	77	279	–52 ± 17

Table 3.1 (cont'd)

ID	RA[b] (J2000)	Dec[c] (J2000)	z_{sys}	M_B	$U-B$	M_* (log $M_\odot$)	SFR[d] ($M_\odot$ yr^{-1})	A_{UV}[e]	A_{74}[f] (kpc^2)	πR_P^2[g] (kpc^2)	$V_1 \pm \delta V_1$[h] (km s^{-1})
12024014	14 18 50.28	52 42 05.78	1.29775	–20.51	0.49	9.9	···	0	6	17	···
12024045	14 18 51.65	52 40 56.08	0.24698	–18.91	0.61	9.9	5	4.5	61	424	···
12024133	14 18 51.82	52 41 11.85	1.12415	–21.14	0.81	10.5	36	3	49	202	–57 ± 43
12024181	14 18 49.60	52 42 36.79	1.08692	–21.00	0.80	10.5	35	3.3	96	479	–57 ± 32
12024409	14 18 33.91	52 41 28.32	1.03579	–20.59	0.84	9.9	11	1.7	48	138	–104 ± 42
12024524	14 18 33.28	52 41 10.89	0.90300	–20.93	0.71	10.4	32	2.7	119	393	–31 ± 23
12100420	14 16 57.97	52 31 58.63	1.19952	–20.63	0.60	10.0	9	1	3	10	71 ± 18

[a] " ··· " indicates no data.

[b] Units of right ascension are hours, minutes, and seconds.

[c] Units of declination are degrees, arcminutes, and arcseconds.

[d] Dust-corrected UV star-formation rate estimated from *GALEX* observations.

[e] Dust attenuation estimated from UV colors.

[f] Galaxy "clump area" (Section 3.2.2).

[g] Galaxy Petrosian area.

Table 3.2. Correlations Between V_1 Outflow Velocity and Galaxy Properties

Property	Correlation with V_1[a]
SFR	1.2, –0.17 (47)
sSFR	2.3, –0.33 (47)
$\Sigma_{\rm SFR}(\rm R_P)$	2.4, –0.40 (36)
	3.1, –0.54[b](34)
$\Sigma_{\rm SFR}(\rm A_{74})$	2.4, –0.40 (36)
	3.1, –0.54[b](34)
i	0.9, –0.14 (46)
$\rm R_P$	–1.4, 0.20 (47)
$(\rm A_{74}/\pi)^{1/2}$	–0.9, 0.14 (47)

[a]The first number indicates the number of standard deviations from the null hypothesis that the quantities are uncorrelated, according to the Spearman ρ correlation test. A larger number of standard deviations means a higher likelihood that the data are correlated; negative values refer to inverse correlations. The second number is the correlation coefficient, r_S. The quantity in parentheses indicates the number of objects in the sample.

[b]Correlations calculated omitting two outliers (12015914 and 12100420) whose extremely compact morphologies translated into large size uncertainties.

Table 3.3. Composite Spectra

Composite	Average Value	V_1[a] (km s^{-1})	V_{max}(Mg II)[b] (km s^{-1})	V_{max}(Fe II)[c] (km s^{-1})
EGS	···	–5 ± 6	–730 ± 93	–564 ± 87
SFR – *high*	32 ± 4 $M_\odot$ yr^{-1}	–24 ± 9	–748 ± 94	–514 ± 84
SFR – *low*	7 ± 1 $M_\odot$ yr^{-1}	29 ± 11	–614 ± 83	–453 ± 104
sSFR – *high*	1.9 ± 0.2 × 10^{-9} yr^{-1}	–34 ± 9	–605 ± 80	–556 ± 94
sSFR – *low*	4.1 ± 0.6 × 10^{-10} yr^{-1}	27 ± 11	–834 ± 148	–456 ± 86
$\Sigma_{SFR}(R_P)$ – *high*	0.29 ± 0.05 $M_\odot$ yr^{-1} kpc^{-2}	–25 ± 6	–862 ± 69	–614 ± 97
$\Sigma_{SFR}(R_P)$ – *low*	0.05 ± 0.007 $M_\odot$ yr^{-1} kpc^{-2}	33 ± 13	–668 ± 105	–444 ± 87
$\Sigma_{SFR}(A_{74})$ – *high*	0.93 ± 0.15 $M_\odot$ yr^{-1} kpc^{-2}	–31 ± 7	–855 ± 66	–611 ± 103
$\Sigma_{SFR}(A_{74})$ – *low*	0.18 ± 0.02 $M_\odot$ yr^{-1} kpc^{-2}	44 ± 15	–640 ± 117	–451 ± 86
A_{UV} – *high*	2.7 ± 0.13	–3 ± 10	–732 ± 71	–497 ± 88
A_{UV} – *low*	1.1 ± 0.078	–10 ± 9	–652 ± 89	–522 ± 91
i – *high*	58° ± 1°	28 ± 11	–692 ± 95	–464 ± 77
i – *low*	38° ± 1°	–19 ± 9	–811 ± 140	–557 ± 101

[a]Outflow velocity measured from the simultaneous fit to five resonance Fe II absorption lines, as described in Section 3.3.2 and Martin et al. (2012).

[b]Maximal outflow velocity measured from the 2796 Å Mg II line (Section 3.4.3).

[c]Maximal outflow velocity measured from the 2374 Å Fe II line (Section 3.4.3).

CHAPTER 4

Fine-Structure Fe II* Emission and Mg II Emission in $z \sim 1$ Star-Forming Galaxies

The transport of gas into and out of galaxies has been recorded at a range of redshifts (e.g., Heckman et al., 1990; Steidel et al., 1996b; Franx et al., 1997; Martin, 1999; Pettini et al., 2000, 2001; Shapley et al., 2003; Martin, 2005; Veilleux et al., 2005; Rupke et al., 2005; Tremonti et al., 2007; Weiner et al., 2009; Steidel et al., 2010; Coil et al., 2011). This cycling of baryons is an integral component of galaxy evolution as galactic winds are thought to drive the mass-metallicity relation (Tremonti et al., 2004; Erb et al., 2006b), enrich the intergalactic medium in metals (Bordoloi et al., 2011; Ménard et al., 2011), and regulate both star formation and black hole growth (Tremonti et al., 2007; Gabor et al., 2011).

In the local universe, galactic winds are revealed through Hα and X-ray imaging of high surface brightness gas around the disks of starburst galaxies (e.g., Lehnert & Heckman, 1996). At higher redshifts, however, studies of galactic winds often rely on spectral data tracing foreground gas absorbed against the light of background galaxies or quasars (e.g., Sato et al., 2009; Weiner et al., 2009; Steidel et al., 2010; Rubin et al., 2010b; Coil et al., 2011). While absorption lines unambiguously probe gas between Earth and a more distant light source, emission lines can arise from either foreground or background gas due to scattering. Observations of emission lines associated with galactic winds accordingly

comprise rich datasets complementing absorption-line studies.

One of the first spectroscopic observations of resonant emission associated with outflowing gas was made by Phillips (1993) of a Na I P-Cygni profile in the local starburst galaxy NGC 1808. Resonance emission, also known as scattering, arises after an electronic transition back down to the ground state. Another category of emission is fine-structure emission, where a non-resonance photon is emitted following an electronic transition to an excited ground state. Since the observations of Phillips (1993), many authors have noted resonance and fine-structure emission lines in diverse samples of star-forming galaxies hosting galactic winds at $0.5 < z < 4$ (Shapley et al., 2003; Weiner et al., 2009; Rubin et al., 2010b, 2011; Coil et al., 2011; Kornei et al., 2012; Martin et al., 2012; Jones et al., 2012).

Quantifying the velocities of emission lines relative to a systemic rest frame is not sufficient for determining if emission lines trace galactic winds or star-forming regions (Prochaska et al., 2011). As line emission from an optically thin source will be visible over both its approaching and receding sides (i.e., its blueshifted and redshifted sides), the emission profile can remain centered at roughly 0 km s^{-1} while still tracing a gas flow. Likewise, an emission line arising from a stationary H II region will exhibit a line profile largely at the systemic velocity. Rubin et al. (2011) investigated fine-structure Fe II emission in a starburst galaxy at $z \sim 0.7$ and concluded that since the emission is redward or within 30 km s^{-1} of the systemic velocity, the velocity profile of Fe II fine-structure emission is significantly different from both absorption lines tracing galactic winds and nebular lines associated with H II regions. On the other hand, Coil et al. (2011) reported that these same transitions are consistently *blueshifted* in a sample of post-starburst and active galactic nucleus (AGN) host galaxies at

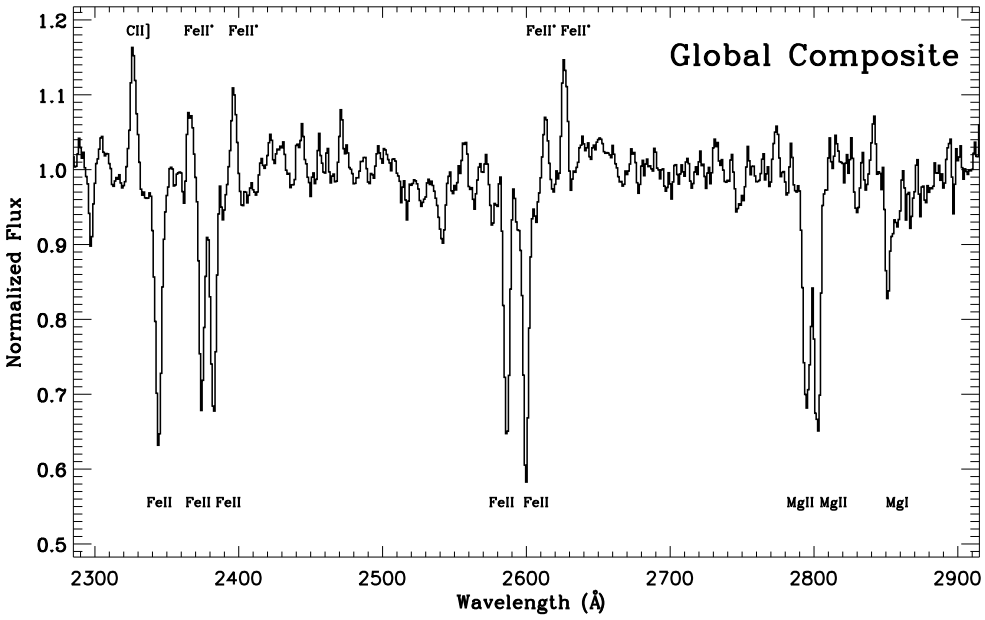

Figure 4.1 Composite spectrum of all of the data in our sample. Prominent interstellar absorption lines (Fe II, Mg II, and Mg I) and emission lines (C II] and fine-structure Fe II*) are labeled; the absorption line at 2297 Å is a stellar C III line.

$0.2 < z < 0.8$. At higher redshift, Erb et al. (2012, in prep.) studied 96 star-forming galaxies at $1 \lesssim z \lesssim 2$ and found that the measured velocities of Fe II fine-structure emission scattered around 0 km s^{-1}. At $z \sim 3$, Shapley et al. (2003) measured an average redshift of 100 ± 35 km s^{-1} for Si II fine-structure emission, although these authors cautioned that the presence of nearby absorption features may be biasing the emission centroids to more redshifted values. The kinematics of fine-structure emission are still an open question and more data are clearly needed.

The prevalence of emission lines has been found to vary widely among different samples; studies at $0.5 < z < 3$ routinely detect fine structure Si II, fine structure Fe II, and resonance Mg II emission lines (e.g., Shapley et al., 2003; Weiner et al., 2009; Rubin et al., 2010b). In a study of 1406 star-forming galaxies at $z \sim 1.4$, Weiner et al. (2009) found that $\sim 4\%$ of objects showed excess Mg II emission; these authors attributed the presence of Mg II emission to low-level AGNs but still observed Mg II emission even when the AGN candidates were removed from the sample. Rubin et al. (2011) detected Mg II emission in a starburst galaxies at $z \sim 0.7$ and measured that the emission was spatially extended to distances of ~ 7 kpc. Local star-forming galaxies, on the other hand, are strikingly bereft of these features (Leitherer et al., 2011). Giavalisco et al. (2011) and Erb et al. (2012, in prep.) suggest that slit losses are responsible for the lack of emission in nearby samples, given that spectroscopic observations in the local universe typically probe only the inner regions of galaxies where emission may not be present.

While previous studies have collectively shown that emission lines are present in galaxies at $z \gtrsim 0.5$ exhibiting galactic winds, a systematic analysis of the prevalence and properties of emission lines as a function of host galaxy stellar

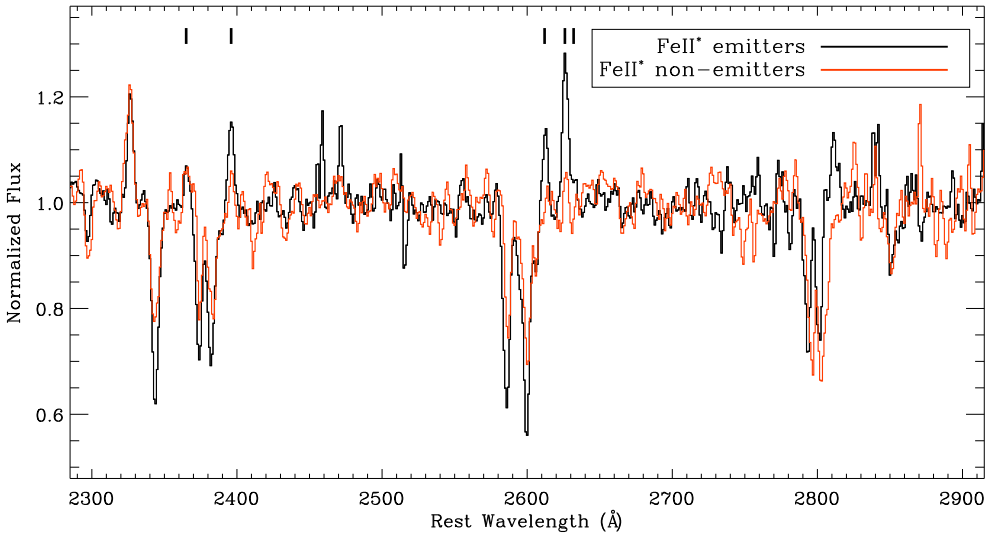

Figure 4.2 A comparison of composite spectra assembled from Fe II* emitters (black) and non-emitters (red), respectively. Short vertical lines delineate the locations of Fe II* emission features at 2365, 2396, 2612, 2626, and 2632 Å; the line at 2326 Å is a blend of C II] and [O III] transitions. On average, Fe II* emitters show deeper Fe II absorption, weaker Mg II absorption, and more blueshifted Mg II absorption than Fe II* non-emitters.

populations, star-formation rate surface density, and outflow characteristics has thus far been absent from the literature. We present here an investigation of the prevalence, strength, and kinematics of ultraviolet Fe II and Mg II emission lines in a sample of 212 galaxies at $0.7 < z < 1.3$ for which stellar populations and outflow properties have been estimated. In Section 4.1, we present the observations and discuss how outflow velocities were measured. Section 4.2 summarizes the Fe II* emission features seen in the data while Section 4.3 is devoted to Mg II observations. A discussion appears in Section 4.4 and conclusions are presented in Section 4.5. Throughout the paper, we assume a standard ΛCDM cosmology with $H_0 = 70$ km s^{-1} Mpc^{-1}, $\Omega_{\rm M} = 0.3$, and $\Omega_\Lambda = 0.7$. All wavelengths are measured in vacuum. At $z = 0.7$ (1.3), an angular size of $1''$ corresponds to 7.1 (8.4) kpc.

4.1 Observations

The 212 objects presented here are drawn from the DEEP2 survey utilizing the DEIMOS spectrograph on Keck II (Newman et al., 2012). While the DEIMOS spectra are generally dominated by nebular emission features, the majority of low- and high-ionization interstellar absorption features tracing outflows are in the rest-frame ultraviolet and are observed at shorter wavelengths than the blue edge of the typical DEIMOS spectra ($\sim$ 6500 Å in the observed frame). In order to probe these outflow features (e.g., Fe II λ2344, Fe II $\lambda\lambda$2374,2382, Fe II $\lambda\lambda$2587,2600, Mg II $\lambda\lambda$2796,2803), we obtained spectroscopic data using the LRIS spectrograph on Keck I. These LRIS data are described in detail in Martin et al. (2012) and we provide here only a summary of the observations.

The LRIS data were collected from 2007–2010 using $1.''2$ slits on multi-object slitmasks targeting 20–28 objects each. We used two set-up configurations, both

with the Atmospheric Dispersion Corrector: the d680 dichroic with the 400 line mm^{-1} grism and the 800 line mm^{-1} grating (145 objects) and the d560 dichroic with the 600 line mm^{-1} grism and the 600 line mm^{-1} grating (67 objects). Integration times varied from 3–9 hours per slitmask, where objects observed with the d560 dichroic had typically shorter exposures (3–5 hours) than objects observed with the d680 dichroic (5–9 hours); the slitmasks used with the d560 dichroic were reserved for brighter objects observed in poorer conditions. The resolutions of the 800, 600 and 400 line mm^{-1} gratings/grisms are $R = 2000$, 1100, and 700, respectively, and the reduction procedure – flat-fielding, cosmic ray rejection, background subtraction, one-dimensional extraction, wavelength and flux calibration, and transformation to the vacuum wavelength frame – was completed using `IRAF` scripts (Martin et al., 2012). The continuum signal-to-noise (S/N) ratios of the LRIS observations over the rest wavelength interval 2400–2500 Å range from $\sim$ 1–25 pixel^{-1} with a median of 6 pixel^{-1}.

The spectra were continuum-normalized and composite spectra were assembled from stacks of mean-combined rest-frame spectra. In assembling the composite spectra, we smoothed the spectra of objects obtained with the 600 line mm^{-1} grism or grating in order to account for the difference in resolution between those obtained with the 600 line mm^{-1} and 400 line mm^{-1} setups. In Figure 4.1, we show the composite spectrum assembled from all of the data in our sample.

72 of the galaxies observed with LRIS fall in the Extended Groth Strip and accordingly have extensive multi-wavelength coverage from the All-Wavelength Extended Groth Strip International Survey (AEGIS; Davis et al., 2007). AEGIS observations cover a broad range in wavelength; we utilized *Chandra* X-ray, *GALEX* FUV and NUV imaging, *HST* ACS F606W (V) and F814W (I) imaging, optical

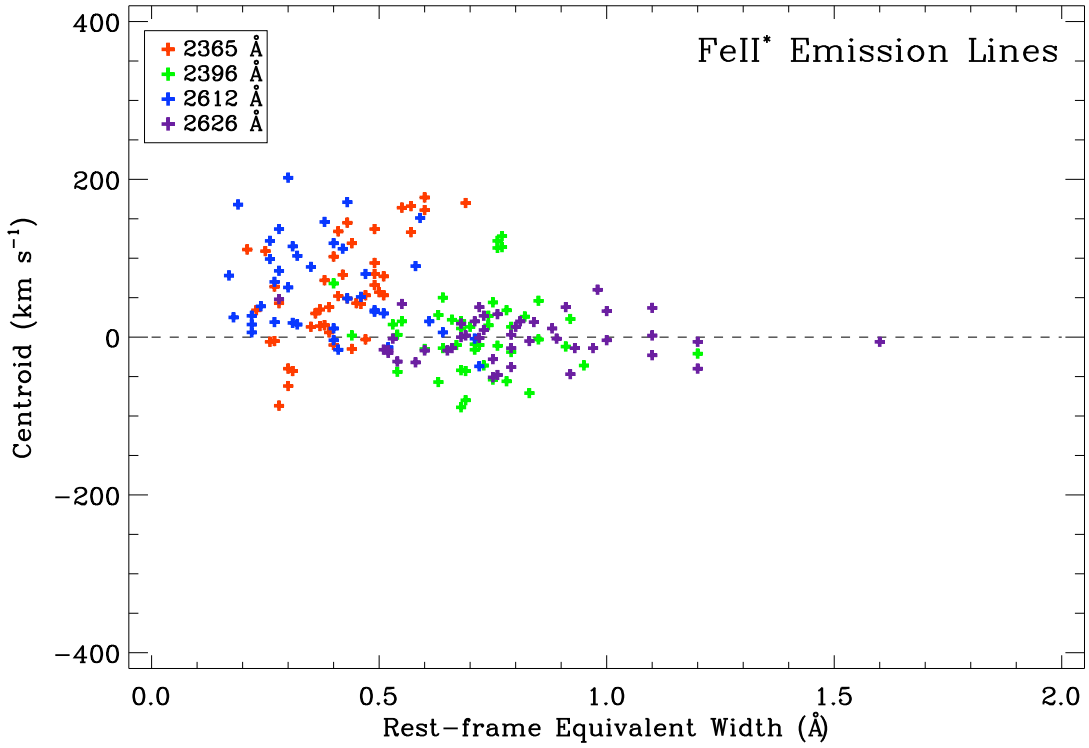

Figure 4.3 Fe II* kinematics versus equivalent width for a set of high S/N composite spectra. As there is substantial overlap among the samples that comprise each composite spectrum, the data points are not independent. Stronger features – 2396 and 2626 Å – show kinematics consistent with 0 km s^{-1} while weaker lines – 2365 and 2612 Å – exhibit systematic redshifts. The 2626 Å feature is isolated from neighboring absorption lines and its centroid is therefore the most robust of the Fe II* features. We accordingly conclude that the kinematics of Fe II* emission are consistent with the systemic velocity.

CFHT and MMT observations, Palomar/WIRC J and K_s imaging, and *Spitzer* IRAC and MIPS pointings in our analyses. We specifically employed *GALEX* observations to estimate dust-corrected star-formation rates and *HST* imaging to estimate disk inclinations and galaxy areas; we refer the reader to Kornei et al. (2012) for a full description of these quantities.

4.1.1 The Determination of Systemic and Outflow Velocities

As the kinematics of galactic winds are only meaningful when compared to a systemic redshift frame, $z_{\rm sys}$, we used nebular emission lines such as [O II] $\lambda\lambda$3726,3729, [O III] $\lambda\lambda$4959,5007, and the Balmer series to define $z_{\rm sys}$ for each galaxy in our sample (Martin et al., 2012). Comparing our measurements of $z_{\rm sys}$ determined from the LRIS data with those given for the DEIMOS data in the DEEP2 catalogs, we find a mean velocity discrepancy of –14 $\pm$ 3 km s^{-1} and a standard deviation of 41 km s^{-1}. We accordingly assume a systemic redshift uncertainty of 41 km s^{-1} for our observations and require that secure detections of galactic winds meet the criterion of velocity offsets having a magnitude of at least 41 km s^{-1}.

We discuss our procedure for determining outflow velocities in Martin et al. (2012) and provide here only a summary of the methodology. We fit a single-component model simultaneously to five resonance Fe II absorption lines tracing cool (T $<$ 10^4 K) gas at 2249.88, 2260.78, 2344.21, 2374.46, and 2586.65 Å in the LRIS spectra[1]. The model fit to the Fe II lines has four free parameters: Doppler shift, optical depth at line center, Doppler width (b, where $b = \sqrt{2}\sigma$

[1]The Fe II features at 2382.76 and 2600.17 Å are purposefully omitted from fitting as these lines are more susceptible to filling from resonance emission; this "emission filling" can shift the measured centroid of absorption lines to bluer wavelengths (e.g., Prochaska et al., 2011; Martin et al., 2012).

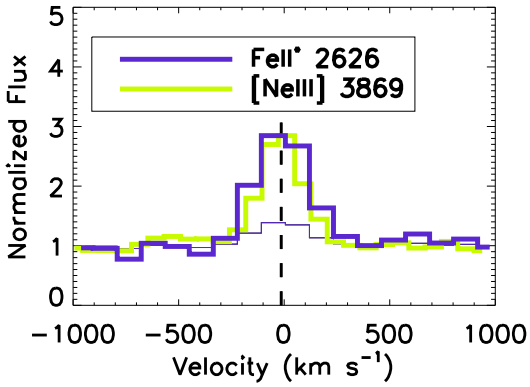

Figure 4.4 A spectral stack of the 12 objects showing $\geq 2\sigma$ detections of Fe II* 2626 Å and $\geq 3\sigma$ detections of the nebular emission line [Ne III] 3869 Å. The kinematics of Fe II* and [Ne III] are similar, with Fe II* showing a velocity offset of –12 ± 14 km s^{-1} from systemic velocity and [Ne III] shifted by –16 ± 4 km s^{-1} (overlapping vertical dashed lines). Given the systematic uncertainty on the systemic redshift determination (Section 4.1.1), we conclude that the centroids of both the Fe II* 2626 Å and [Ne III] 3869 Å emission lines are consistent with 0 km s^{-1}.

= FWHM/$2\sqrt{\ln 2}$), and covering fraction. Due to the low spectral resolution and finite S/N of the observations, the Doppler shift is the primary quantity of interest; the other three parameters of the model will not be discussed in this paper. We measured velocities for 172/212 objects, where 40 objects had no significant absorption lines and therefore could not be modeled, and find velocities ranging from –302 to +401 km s^{-1} with a mean of –30 km s^{-1} and a 1σ dispersion of 89 km s^{-1}. We define here the convention of employing "V_1" to refer to the measured velocity shift of the deepest part of the Fe II absorption line fit, relative to a systemic reference frame typically defined by nebular emission lines. Negative V_1 values refer to blueshifts ("outflows") while positive V_1 values correspond to redshifts ("inflows"). Fe II velocity shifts significant at the 1σ (3σ) level are observed in $\sim$ 55% (22%) of the sample. In this paper, we primarily utilize the V_1 measurements of composite spectra.

4.2 Fine-Structure Fe II* Emission

The Fe II ion has myriad transitions in the rest-frame ultraviolet and several authors have used Fe II resonance absorption lines to trace the bulk motion of outflowing interstellar gas (Rubin et al., 2010b; Coil et al., 2011; Kornei et al., 2012; Martin et al., 2012). The absorption of a resonance photon can result in either the re-emission of another resonance photon to the ground state (scattering) or the emission of a photon to an excited ground state (fluorescence). We observe resonance Fe II absorption in our data, but do not see resonance Fe II emission as Erb et al. (2012, in prep.) do. Here, we focus on the emission features of Fe II resulting from fluorescence, where we denote these fine-structure lines with an asterisk: Fe II*. In this work, we examine four Fe II* lines at 2365.55, 2396.35, 2612.65, and 2626.45 Å. An additional Fe II* line within our data's wavelength

coverage, at 2632.11 Å, is absent in individual observations but plausibly detected in a stack of the strongest Fe II*-emitting galaxies.

4.2.1 Fe II* Emitters and Non-emitters

We measured the equivalent widths of the Fe II* features on a per-object basis. The equivalent width of each line was calculated over a fixed wavelength interval approximately 10 Å wide, where the precise wavelength interval was derived from the 3σ extent of each Fe II* feature measured in a high S/N stack of all the spectral data[2]. We find typical rest-frame Fe II* equivalent widths of several tenths of an angstrom and the number of objects exhibiting $\geq 2\sigma$ detections of each of the four Fe II* lines – 2365, 2396, 2612, and 2626 Å – is 23, 37, 23, and 58, respectively. We observe that the 2626 Å line is the most frequently detected of the four Fe II* lines. Since this feature is in relative isolation from neighboring absorption lines, the kinematics of the 2626 Å line may furthermore be more robust than those of other Fe II* features.

Using individual measurements of Fe II* equivalent widths, we isolated subsamples of objects exhibiting strong or weak Fe II* emission and examine the structural, outflow, and star-forming properties of these galaxies. We focused our selection criteria on the 2396 Å and 2626 Å features given that the largest number of objects had significant detections in these lines. Furthermore, a high S/N spectral stack of all the data showed larger equivalent widths for the 2396 and 2626 Å features (0.72 ± 0.07 and 0.80 ± 0.09 Å, respectively) than for the 2365 and 2612 Å lines (0.42 ± 0.05 and 0.41 ± 0.09 Å, respectively). None of the Fe II* lines are resolved at our spectral resolution.

[2]The exact wavelength intervals we use are: 2360.4–2371.4 Å for Fe II* 2365 Å, 2390.9–2401.1 Å for Fe II* 2396 Å, 2607.8–2617.2 Å for Fe II* 2612 Å, and 2622.2–2630.3 Å for Fe II* 2626 Å, respectively.

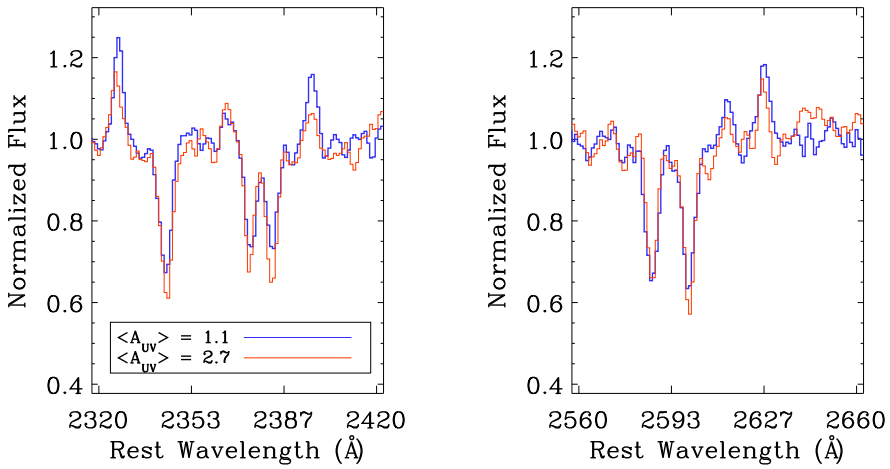

Figure 4.5 A comparison of composite spectra of different attenuation levels. Lower attenuation objects ($\langle A_{UV} \rangle = 1.1$) are shown in blue, while higher attenuation objects ($\langle A_{UV} \rangle = 2.7$) are plotted in red. Fe II* emission lines are weaker in dustier systems, consistent with predictions by Prochaska et al. (2011). We find that objects with larger A_{UV} values show, on average, more blueshifted 2626 Å Fe II* emission (–20 ± 42 km s^{-1} compared with 37 ± 41 km s^{-1}), although the kinematic differences are small and are not statistically significant given the systemic redshift uncertainties of our data. Higher resolution data are needed in order to test the Prochaska et al. (2011) hypothesis that increased dust attenuation produces more blueshifted Fe II* profiles.

We define a subsample of 13 "Fe II* emitters" based on objects having $>$ 4σ equivalent width detections in either the 2396 Å or 2626 Å lines, where this detection threshold was motivated by visual inspection of obects showing obvious Fe II* emission. These 13 objects have continuum S/N ranging from 7.8–25.1 pixel^{-1}. We also collect a subsample of 9 "Fe II* non-emitters" selected to have $< 1\sigma$ equivalent width detections in both the 2396 Å and 2626 Å lines and continuum S/N > 7.8 pixel^{-1}. We imposed a S/N threshold for both the Fe II* emitter and non-emitter samples in order to ensure a fair comparison between samples of comparable S/N. Three of the Fe II* non-emitters have colors typical of "Green Valley" galaxies; our conclusions remain unchanged if these objects are omitted from analyses.

In Figure 4.2, we compare the composite spectra assembled from the Fe II* emitter and non-emitter samples. The 2365, 2396, 2612, and 2626 Å Fe II* lines are clearly detected in the composite of Fe II* emitters, and the 2632 Å Fe II* line is plausibly detected as a "shoulder" on the red side of the 2626 Å feature. The relatively low spectral resolution of our composite spectra (FWHM $\sim$ 435 km s^{-1}) makes it difficult to detect the 2632 Å feature securely given its proximity to the Fe II* line at 2626 Å (645 km s^{-1} to the blue). In a higher resolution (FWHM $\sim$ 190 km s^{-1}) composite spectrum of 96 star-forming galaxies at $1 \lesssim z \lesssim 2$, Erb et al. (2012, in prep.) detect the 2632 Å line at $\sim 4\sigma$ significance and resolve this feature cleanly from the 2626 Å line. The Erb et al. (2012, in prep.) composite spectrum is inclusive of all these authors' data, while the corresponding stack of all of our data does not show any signature of 2632 Å emission; we only observe 2632 Å emission in the stack of objects specifically selected on the basis of Fe II* emission. Convolving the Erb et al. (2012, in prep.) spectrum to our lower spectral resolution yields a blended 2626+2632 Å complex consistent with the profile of our data. This similarity in profile shape

supports our hypothesis that we detect the 2632 Å line blended with the 2626 Å feature. We fit two Gaussian profiles simultaneously to our data's 2626+2632 Å complex and find that the strength of 2632 Å emission is approximately half that of the 2612 Å feature, as predicted by the ratio of these lines' Einstein A coefficients. In the composite spectrum assembled from all of the data in our sample (Figure 4.1), however, we find that the 3σ upper limit on the strength of 2632 Å emission is 0.21 Å, less than 50% of the strength of the 2612 Å feature (0.55 Å). Additional, unaccounted-for absorption near 2632 Å may be responsible for the weaker-than-expected 2632 Å strength.

The composite spectra assembled from the Fe II* emitter and non-emitter samples exhibit different Fe II* strengths, by construction. However, these spectra also show variation in the strength and kinematics of their Fe II and Mg II resonance absorption features. Evidently, the presence or absence of fine-structure Fe II* emission is linked to the strength and velocity of Fe II and Mg II gas traced by resonance absorption lines. Based on inspection of the composite spectra assembled from the Fe II* emitter and non-emitter samples, two trends are visually apparent:

1. Fe II* emitters show stronger Fe II resonance absorption lines and weaker Mg II resonance absorption lines than Fe II* non-emitters.

2. Fe II* emitters show more blueshifted Mg II resonance absorption lines than Fe II* non-emitters.

The composite spectrum of Fe II* emitters exhibits $\sim$ 50% stronger Fe II absorption troughs and $\sim$ 50% weaker Mg II absorption troughs than the composite spectrum of Fe II* non-emitters. The presence of deeper Fe II absorption with increasing Fe II* emission strength is consistent with the physical picture of fine-structure emission arising from excited states populated by resonance ab-

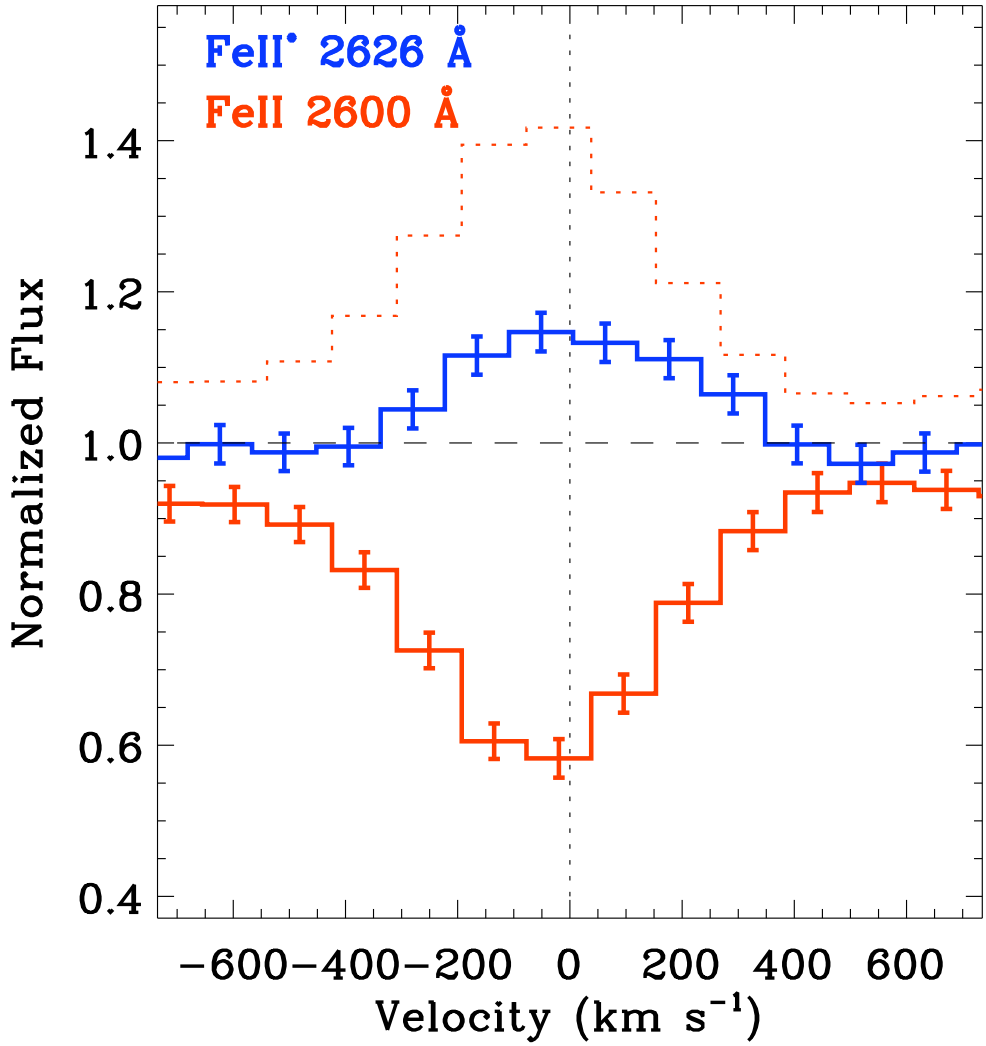

Figure 4.6 Velocity profiles of Fe II 2600 Å absorption (red line) and Fe II* 2626 Å emission (blue line), where the Fe II 2600 Å line is also shown reflected around y = 1 for comparison with the Fe II* 2626 Å emission profile. All of the data in our sample were combined to make these profiles. Fe II absorption is stronger than Fe II* emission, consistent with Erb et al. (2012, in prep.). The blue side of the Fe II feature does not meet the continuum due to the adjacent Fe II absorption feature at 2587 Å.

sorption. In a sample of 96 star-forming galaxies at $1 \lesssim z \lesssim 2$, however, Erb et al. (2012, in prep.) found a trend of *decreasing* Fe II* emission with increasing Fe II absorption. These authors suggest that systems with strong Fe II absorption may be preferentially dusty and therefore show a dearth of emission. Erb et al. (2012, in prep.) also propose that galaxy inclination may modulate the observed ratio of emission and absorption equivalent widths, as an anisotropic (i.e., biconical) outflow viewed edge-on will show more emission than absorption. Furthermore, Erb et al. (2012, in prep.) suggest that slit losses – i.e., the size of the Fe II*-emitting region relative to the area encompassed by the spectroscopic slit – may reduce the observed strength of Fe II* emission if the emission arises from spatially-extended gas. In $z \sim 3$ Lyman Break Galaxies, Shapley et al. (2003) found that fine-structure Si II* emission lines were too strong to be produced in H II regions yet much weaker than the Si II absorption lines. These authors hypothesized that the narrowness of the spectroscopic slit (1.″4) might be including only a small portion of the region in which Si II* emission was arising. The weaker Mg II absorption observed for Fe II* emitters relative to Fe II* non-emitters is in the opposite sense to the trend seen for Fe II absorption. As Fe II* emitters are lower mass and bluer in color than Fe II* non-emitters, these objects may have less systemic Mg II absorption in their interstellar media than the Fe II* non-emitter sample.

The centroids of both features of the Mg II doublet are blueshifted in the Fe II* emitter composite relative to the Fe II* non-emitter composite. While emission filling may be responsible for shifting the centroids of Mg II, we also observe that the overall profiles of the Mg II doublets are offset between the Fe II* emitter and non-emitter composite spectra. In particular, the different velocities seen in the wings of the features – where emission filling is negligible – indicate the discrepancy in gas kinematics between the Fe II* emitter and non-

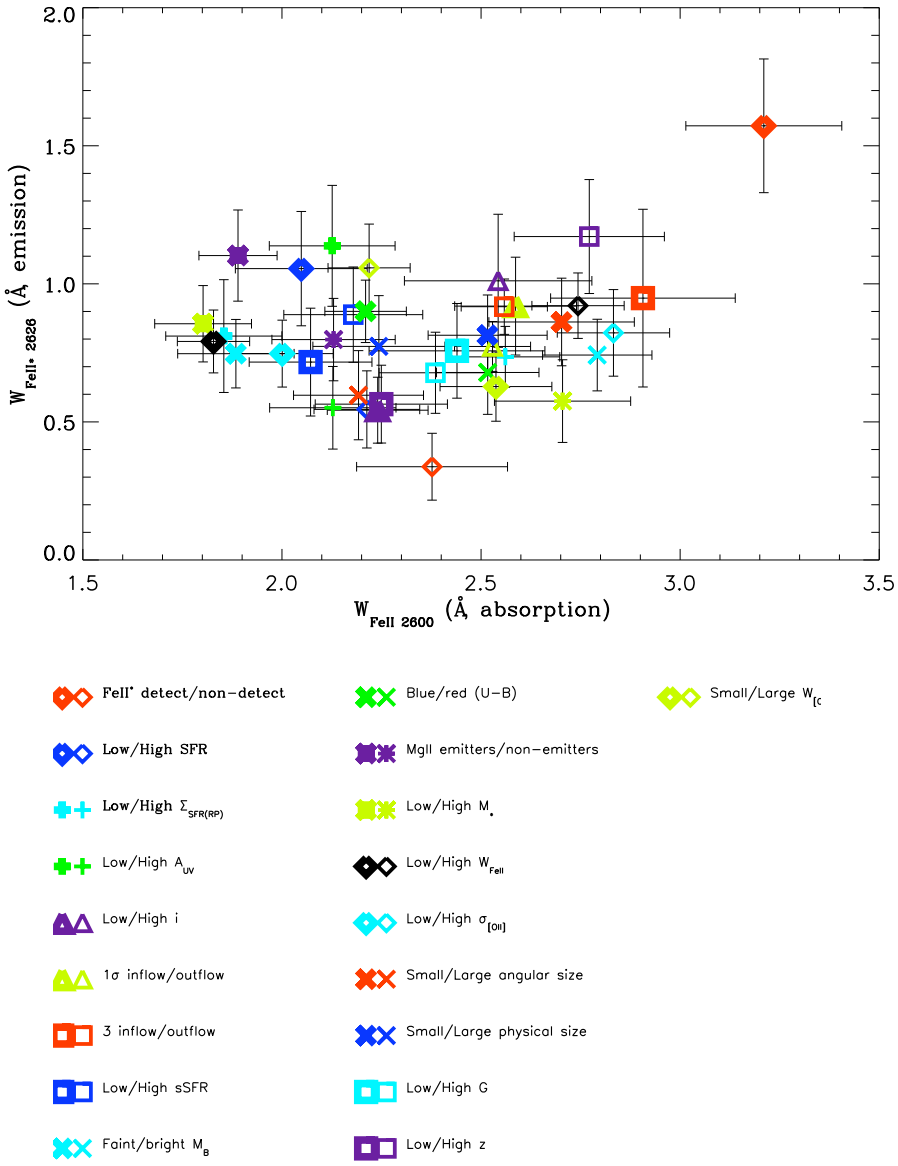

Figure 4.7 Comparison of Fe II absorption equivalent widths and Fe II* emission equivalent widths, for the ensemble of composite spectra. Different composite spectra are plotted as indicated in the legend below. Data with Fe II 2600 Å equivalent widths $\gtrsim$ 2.3 Å show a trend of increasing Fe II* emission strength with increasing Fe II absorption strength, although this trend is not present for composite spectra with weaker Fe II absorption.

emitter populations. The Fe II* emitter spectrum shows evidence for outflows in Mg II, although the Fe II absorption lines are not as strongly blueshifted – we find evidence that some of the Fe II resonance absorption lines are blueshifted, although the difference in absorption line kinematics between the Fe II* emitter and non-emitter composite spectra is not statistically significant. As discussed in Kornei et al. (2012), Mg II is optically thick at lower column densities than Fe II due to its larger oscillator strength. Mg II is therefore a better probe of rarefied gas, which may have a high-velocity component.

4.2.2 Fe II* Kinematics

Strongly blueshifted or redshifted Fe II* emission is consistent with moving gas, although work by Prochaska et al. (2011) has shown that emission profiles centered at roughly 0 km s^{-1} can still arise in the presence of gas flows. Measuring kinematics indicative of stationary gas is therefore not sufficient to robustly determine if the gas is indeed truly at rest with respect to stars. We measured the centroids of the Fe II* lines in the Fe II* emitter composite spectrum using Gaussian fits from the `IDL` routine `gaussfit`. We find that the lines have centroids of –40 ± 111, –36 ± 28, 7 ± 33, and –6 ± 21 km s^{-1}, respectively, where errors were estimated from Monte Carlo simulations. The large uncertainty on the centroid of the 2365 Å line is due to its weak strength. We conclude that the Fe II* centroids are consistent with no offset from the systemic velocity, given both the measured uncertainties on the velocities and the systematic uncertainty on the systemic redshift determination (Section 4.1).

We also measured the centroids of the Fe II* lines in other composite spectra assembled on the basis of morphological and stellar population parameters (Figure 4.3). In the ensemble of composite spectra, we find that the strongest

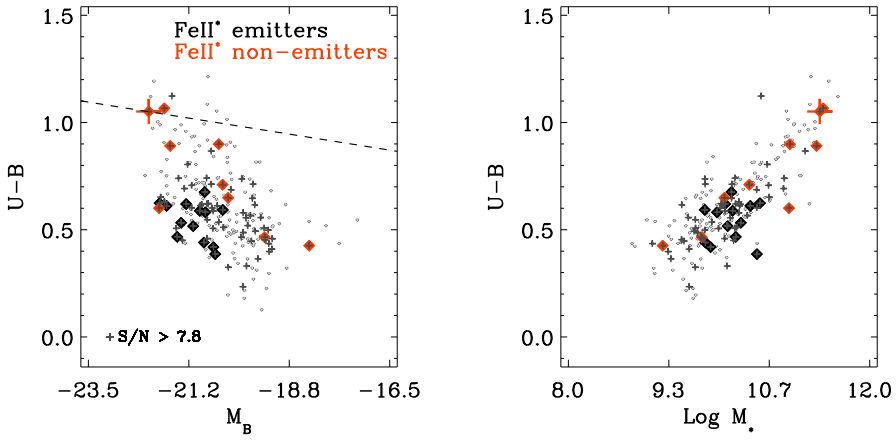

Figure 4.8 *Left:* Color-magnitude diagram of the full sample, where objects with continuum S/N $>$ 7.8 are indicated with black crosses. Within this subsample of objects with higher S/N, Fe II* emitters are shown in black (13 objects) and Fe II* non-emitters are shown in red (9 objects). Object 12015320, a Fe II* non-emitter, is differentiated with a red cross since it is likely an AGN based on its broad Ne V emission and X-ray flux. Fe II* emitters appear to be preferentially bright, blue galaxies, although Figure 4.9 shows no statistically significant trend between Fe II* strength and either luminosity or color, based on a binary division of the data. *Right:* Color vs. stellar mass plot, where the symbols are the same as in the left panel. Fe II* emitters have lower stellar masses on average than the sample as a whole.

Fe II* lines (2396 and 2626 Å) have centroids consistent with 0 km s^{-1} while the weaker Fe II* lines (2365 and 2612 Å) are predominantly redshifted. Since all the Fe II* emission lines trace the same underlying population of gas, we conclude that the kinematics of Fe II* emission are consistent with 0 km s^{-1} based on the measurements of the strongest Fe II* features in composite spectra. Given the relatively low S/N of our data, it is difficult to robustly measure the kinematics of Fe II* in individual objects.

A complementary investigation of Fe II* kinematics is to compare the velocity offsets of a strong Fe II* line and a nebular emission line (Rubin et al., 2011). Nebular emission lines trace star-forming regions and therefore probe largely stationary gas. In Figure 4.4, we show the Fe II* 2626 Å and [Ne III] 3869 Å features of a composite spectrum assembled from the spectra of 12 objects with strong detections of both Fe II* 2626 Å and [Ne III]. The kinematics of these two lines are similar; the Fe II* Å has a centroid of –12 ± 14 km s^{-1} while the [Ne III] line has a centroid of –16 ± 4 km s^{-1}. In light of the uncertainty on our determination of the systemic redshift, we conclude that both Fe II* and [Ne III] have kinematics consistent with being centered at 0 km s^{-1}.

Rubin et al. (2011) measured Fe II* lines in the spectrum of a starburst galaxy at $z \sim 0.69$ and found that Fe II* lines trace gas that is redward or within 30 km s^{-1} of the systemic velocity. These authors note that the kinematics of Fe II* features are inconsistent with the kinematics of both FeII resonance absorption lines (ΔV $\sim$ –200 km s^{-1}, where ΔV is the offset from systemic velocity) and features tracing galactic H II regions ([NeIII], Hδ, Hγ; ΔV $\sim$ 0 km s^{-1}). In contrast with Rubin et al. (2011), Coil et al. (2011) found that Fe II* lines are typically blueshifted in a sample of post-starburst and AGN host galaxies at $0.2 < z < 0.8$. Coil et al. (2011) note that $\sim$ 40% of Fe II* lines are blueshifted at $> 2\sigma$

significance while none are significantly redshifted; the Coil et al. (2011) sample is characterized by a median ΔV of –119 km s^{-1}. These authors propose that Fe II* emission arises in galactic winds as opposed to star-forming regions, since Fe II* emission is observed in post-starburst galaxies not currently experiencing star formation. We note that the composite spectra we use here for measuring Fe II* kinematics have significantly higher S/N (but lower resolution) than the spectra of individual objects employed by both Rubin et al. (2011) and Coil et al. (2011). In composite spectra of star-forming galaxies at $1 < z < 2$, Erb et al. (2012, in prep.) find that Fe II* 2626 Å exhibits blueshifted velocity centroids of about –50 km s^{-1}, although these authors report that individual spectra show Fe II* 2626 Å centroids scattering around 0 km s^{-1}. Erb et al. (2012, in prep.) conclude that Fe II* 2626 Å is on average observed at velocities closer to systemic than the resonance Fe II absorption lines. While the high S/N composite spectra of Erb et al. (2012, in prep.) show Fe II* kinematics near the systemic velocity, as we find in our own sample, high-resolution observations of a large number of individual objects are needed in order to definitively measure the kinematics of fine-structure emission on a per-object basis.

Numerous studies have been devoted to developing models of line emission associated with galactic winds (Steidel et al., 2010; Rubin et al., 2011; Prochaska et al., 2011). In particular, Prochaska et al. (2011) present modeling of Fe II* emission arising from photons scattered in galactic winds. These authors predict Fe II* emission at velocities close to the systemic velocity, since an optically thin galaxy will transmit the Fe II* emission scattered from both the backside and frontside of the wind. However, Prochaska et al. (2011) also note that increased dust opacity may produce more blueshifted Fe II* profiles as the redshifted photons scattering off the backside of the wind will be preferentially suppressed due to their longer path lengths. In Figure 4.5, we compare composite spectra assem-

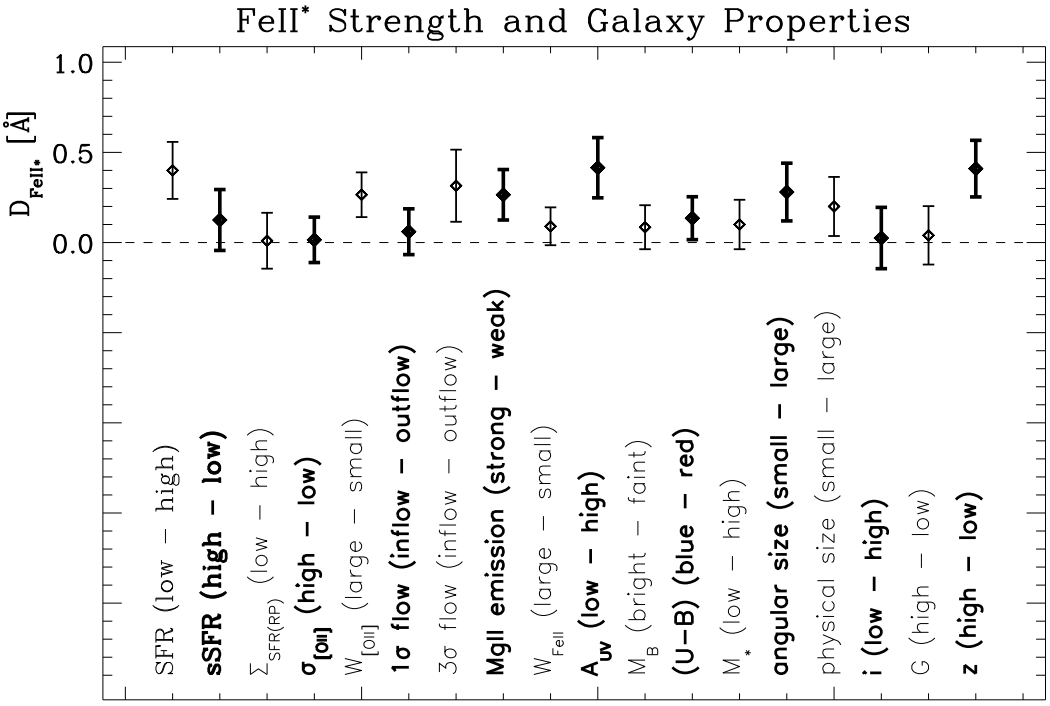

Figure 4.9 Variation of Fe II* emission strength with galaxy properties. D_{FeII^*}, a parameterization of how Fe II* strength changes between two spectra, is shown for pairs of composite spectra assembled according to eighteen different galaxy properties. Lines are alternately bolded for visual clarity. The largest D_{FeII^*} values, significant at $> 2\sigma$, are observed for 3 intrinsic properties: SFR, A_{UV}, and $W_{[OII]}$, as well as z. Stronger Fe II* emission is seen for lower SFR, larger $W_{[OII]}$, lower A_{UV}, and higher z objects. D_{FeII^*} values are significant at $> 1\sigma$ for the following additional parameters: 3σ gas flow, $U - B$ color, the presence of Mg II emission, angular size, and physical size, such that Fe II* emission is more pronounced in systems with 3σ inflows (as opposed to 3σ outflows), bluer $U - B$ colors, stronger Mg II emission, smaller angular sizes, and smaller physical sizes.

bled on the basis of A_{UV}. While we find that objects with larger A_{UV} values show, on average, more blueshifted 2626 Å Fe II* emission (–20 ± 42 km s^{-1} compared with 37 ± 41 km s^{-1}), the kinematic differences are small and are not statistically significant given the systemic redshift uncertainties of our data. Higher resolution data are needed in order to test the Prochaska et al. (2011) hypothesis that increased dust attenuation produces more blueshifted Fe II* profiles. We note that the C II] line at 2326 Å is more blueshifted in objects with larger A_{UV} values, but blending with nearby [O III] transitions renders uncertain the precise rest-frame centroid of this feature.

4.2.3 Fe II* Emission and Resonance Absorption

As Fe II* emission arises from upper states populated by resonance absorption, a strong link between Fe II emission and absorption profiles is expected. In Figure 4.6, we compare the velocity profiles of the Fe II 2600 Å resonance absorption line and the Fe II* 2626 Å fine-structure emission line. We find that both profiles have centroid velocities close to 0 km s^{-1}and that the Fe II absorption is stronger than the Fe II* emission line. These results are consistent with the findings of Erb et al. (2012, in prep.). The fact that Fe II absorption is stronger than Fe II* emission has implications for the derived geometry of galactic winds. For example, an edge-on view of a system with a collimated wind will show emission but no absorption. Likewise, a galaxy viewed face-on will exhibit more absorption than emission. While these inclination effects are important when considering systems on an individual basis, the our finding that Fe II absorption is stronger than Fe II* emission in a composite spectrum assembled from many independent sources provides only an averaged view of what the wind geometry may be.

In Figure 4.7, we show the equivalent width of Fe II* 2626 Å versus the equiv-

alent width of Fe II 2600 Å. We find that these two quantities are positively correlated for the subsample of objects with strong Fe II absorption ($\gtrsim$ 2.3 Å). Erb et al. (2012, in prep.) find that the equivalent width of Fe II* 2626 Å is inversely correlated, however, with the equivalent width of Fe II 2600 Å. These authors propose that the Fe II* emission from dusty, high-mass systems experiences a high optical depth due to a significant interstellar medium. In this physical picture, galaxies with substantial Fe II absorption profiles are also the same systems in which Fe II* emission is extinguished. Support for the hypothesis that massive objects have more optically thick interstellar media was noted by Steidel et al. (2010) in a sample of objects at $z \sim 2$. Steidel et al. (2010) found that systems with larger baryonic masses had more absorption at the systemic velocity. This result corroborates the physical picture of Erb et al. (2012, in prep.) that systems showing stronger interstellar absorption (i.e., more massive galaxies) are the same objects in which Fe II* emission may be the most attenuated. We find, however, that Fe II* equivalent width and Fe II equivalent width are positively correlated, at least over the subsample of objects with strong Fe II absorption. This result is consistent with radiative transfer modeling of a spherically symmetric outflow in the absence of dust (Prochaska et al., 2011). Since all absorbed photons have to be re-emitted from the system (as none are lost due to absorption by dust), conservation of photons implies that the strength of emission equals the strength of absorption. Therefore, in this model from Prochaska et al. (2011), systems showing stronger resonance Fe II absorption will also show correspondingly stronger fine-structure Fe II* emission. In other less simplistic models of outflows (i.e., varying the covering fraction of gas, changing the opening angle of the biconical wind, adding in dust, and including absorption from a stationary interstellar medium), Prochaska et al. (2011) still recover a positive correlation between Fe II absorption strength and Fe II* emission strength. Our

results are accordingly consistent with the findings of Prochaska et al. (2011). As these authors also predict the presence of spatially-extended Mg II line emission in their models, we hypothesize that our sample may exhibit extended emission as well (Martin et al. 2012b, in prep.).

4.2.4 Fe II* Strength and Galaxy Properties

In Figure 4.8, we show a color-magnitude diagram indicating the Fe II* emitters and non-emitters. Objects showing strong Fe II* emission are brighter ($\langle M_B \rangle$ = –21.0 ± 0.1) and bluer ($\langle U - B \rangle = 0.54 \pm 0.02$) than objects of comparable S/N ($\langle M_B \rangle$ = –20.5 ± 0.1; $\langle U - B \rangle = 0.59 \pm 0.02$). While this finding is consistent with the interpretation that Fe II* emitters likely have little dust attenuation (Prochaska et al., 2011, Erb et al. 2012, in prep.), we can use our extensive multi-wavelength dataset to more completely investigate how Fe II* strength depends on galaxy properties.

We measured the equivalent widths of Fe II* features in eighteen pairs of composite spectra assembled based on star-forming, gas flow, Fe II and Mg II, stellar population, size, morphological, and redshift parameters. The star-forming properties include star-formation rate (SFR), specific star-formation rate (sSFR = SFR/stellar mass), star-formation rate surface density assuming a Petrosian area ($\Sigma_{\rm SFR}(\rm R_P)$), [O II] emission linewidth, corrected for instrumental resolution ($\sigma_{[OII]}$), and [O II] emission line equivalent width ($W_{[OII]}$). The gas flow properties are 1σ gas flows and 3σ gas flows. Fe II and Mg II properties include the presence of Mg II emission and Fe II 2344 Å equivalent width (W_{FeII}). Dust attenuation ($\rm A_{UV}$), B-band luminosity (M_B), $U - B$ color, and stellar mass (M_*) are all measured stellar population parameters. Size and morphological properties include angular size, physical size, disk inclination (i), and Gini coefficient

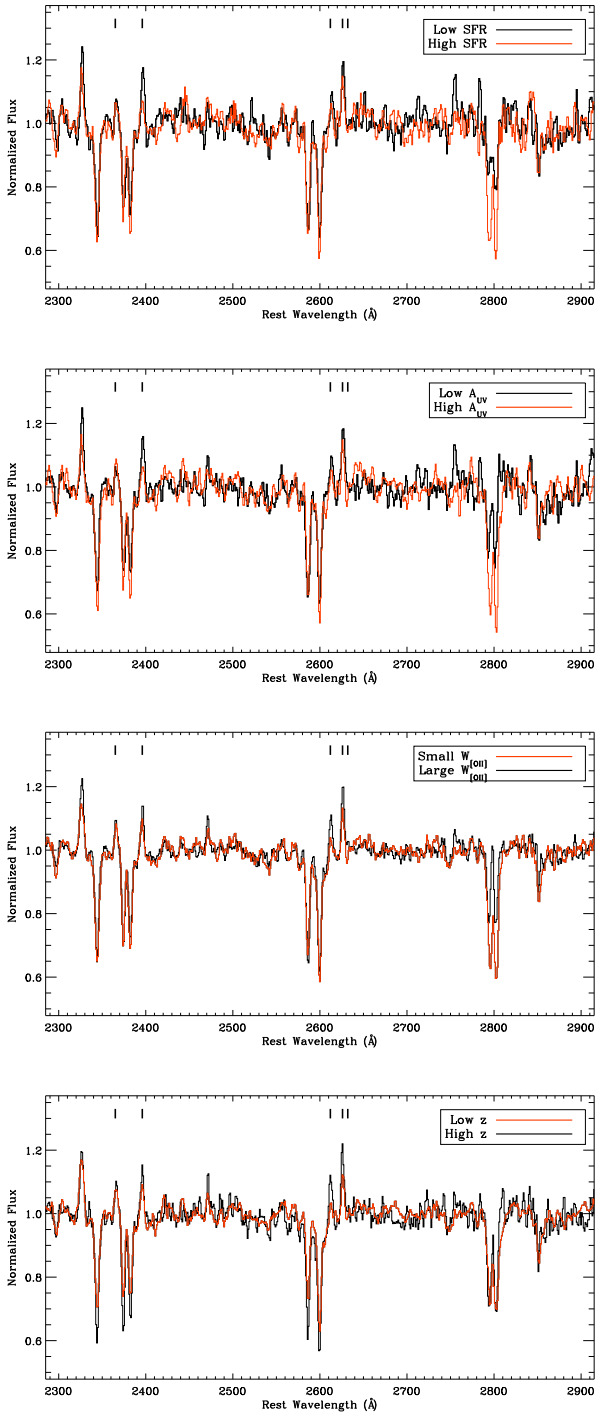

Figure 4.10 Composite spectra of galaxy parameters that strongly modulate Fe II* emission strength. From top to bottom, composite spectra are shown comparing low and high SFR, low and high A_{UV}, small and large $W_{[OII]}$, and low and high z. In each case, the composite spectrum with stronger Fe II* emission is plotted in black.

(*G;* Lotz et al., 2004). Redshift, measured spectroscopically, is an additional parameter.

For each property, we assembled composite spectra based on a binary division of the data according to that parameter. We investigated how the strength of Fe II* varied within each pair of composite spectra based on measurements of the strongest Fe II* features at 2396 Å and 2626 Å. We measured local continua around each Fe II* line and defined the extent of each feature as the region where the flux was greater than the continuum. Fitting a Gaussian profile to each Fe II* line, we estimated the equivalent width by integrating the Gaussian fit and dividing the summed flux by the local continuum. We define the quantity D_{FeII^*} as the average of the equivalent width differences between each pair of composite spectra:

$$D_{FeII^*} = \frac{\Delta EW_{2396} + \Delta EW_{2626}}{2} \tag{4.1}$$

where ΔEW_{2396} is the difference in Fe II* 2396 Å equivalent widths between the composite spectra and ΔEW_{2626} is the analogous difference in the 2626 Å line. In Figure 4.9, we show the values of D_{FeII^*} for the eighteen parameters. We observe D_{FeII^*} ranging from 0.0–0.4 Å. The uncertainty on D_{FeII^*}, δD_{FeII^*}, was estimated through Monte Carlo realizations: for each composite spectrum, we constructed 1000 simulated spectra by perturbing the data by a value drawn from Gaussian distribution of width the data's error. We measured the Fe II* equivalent widths for each ensemble of 1000 simulated spectra and adopted the standard deviation of the equivalent width distribution as the error. Propagating errors through Equation 4.1, we estimated δD_{FeII^*} for each parameter. The average δD_{FeII^*} of the sample is 0.15 Å, with extrema ranging from 0.11–0.20 Å.

D_{FeII^*} is significant at $\geq 2\sigma$ for 4 parameters: SFR, A_{UV}, $W_{[OII]}$, and z.

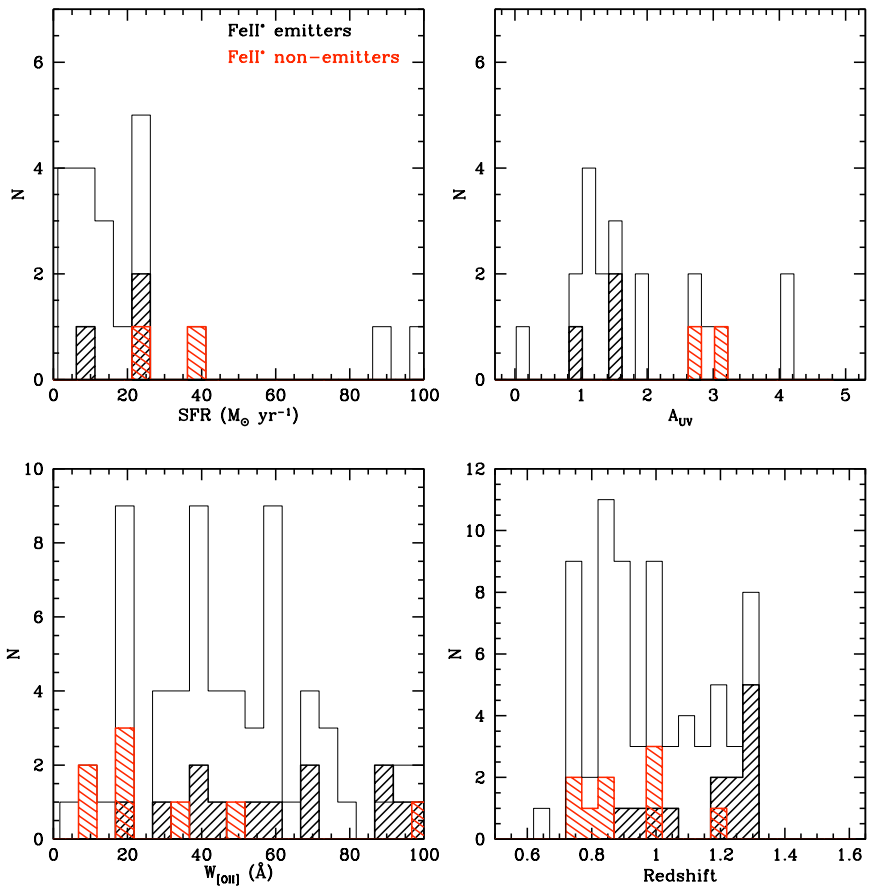

Figure 4.11 Histograms of the four parameters most strongly modifying Fe II* emission strength: SFR, $W_{[OII]}$, A_{UV}, and z. In each panel, the open histogram shows the sample of objects with S/N > 7.8. Fe II* emitters are shown in the black shaded histogram and Fe II* non-emitters are indicated with the red shaded histogram. Fe II* emitters are characterized by lower dust attenuations, smaller SFRs, larger $W_{[OII]}$, and larger redshifts than Fe II* non-emitters.

Stronger Fe II* emission is seen in higher redshift objects, those with lower SFRs, lower A_{UV} values, and larger $W_{[OII]}$ measurements. In Figure 4.10, we show the four pairs of SFR, A_{UV}, $W_{[OII]}$, and z composite spectra. It is important to highlight that the composite spectra assembled on the basis of SFR, A_{UV}, and $W_{[OII]}$ exhibit different properties than the composite spectra made according to z. The stronger Fe II* emission observed in the lower SFR, lower A_{UV}, and larger $W_{[OII]}$ composite spectra is accompanied by weaker Mg II absorption and similar, if not weaker, Fe II absorption. However, the higher z composite shows stronger Fe II* emission and yet comparable Mg II absorption and stronger Fe II absorption than the lower z composite. Therefore, it appears that the division of objects on the basis of redshift yields significantly different spectral trends than the division of the sample according to SFR, A_{UV}, or $W_{[OII]}$. Below, we discuss several complementary analyses of the links between Fe II* emission and SFR, A_{UV}, $W_{[OII]}$, and z.

We utilize our previously-defined samples of Fe II* emitters and non-emitters (Section 4.2) to investigate if and how these objects separate in SFR, A_{UV}, $W_{[OII]}$, and z parameter space (Figure 4.11). Each of these four parameters shows a separation of Fe II* emitters and non-emitters, although the sample size is small in some cases. The larger sample of objects with redshifts permits a Kolmogorov-Smirnov (KS) test of the probability that emitters and non-emitters are drawn from the same parent z population: 0.003. While this result indicates the high significance with which Fe II* emitters and non-emitters separate in z space, such that Fe II* emitters are preferentially found at larger redshifts, z is not an intrinsic property of a galaxy. It is therefore important to examine how SFR, A_{UV}, and $W_{[OII]}$ themselves are correlated with z in order to investigate if the observed trend between Fe II* emission strength and z is a secondary correlation.

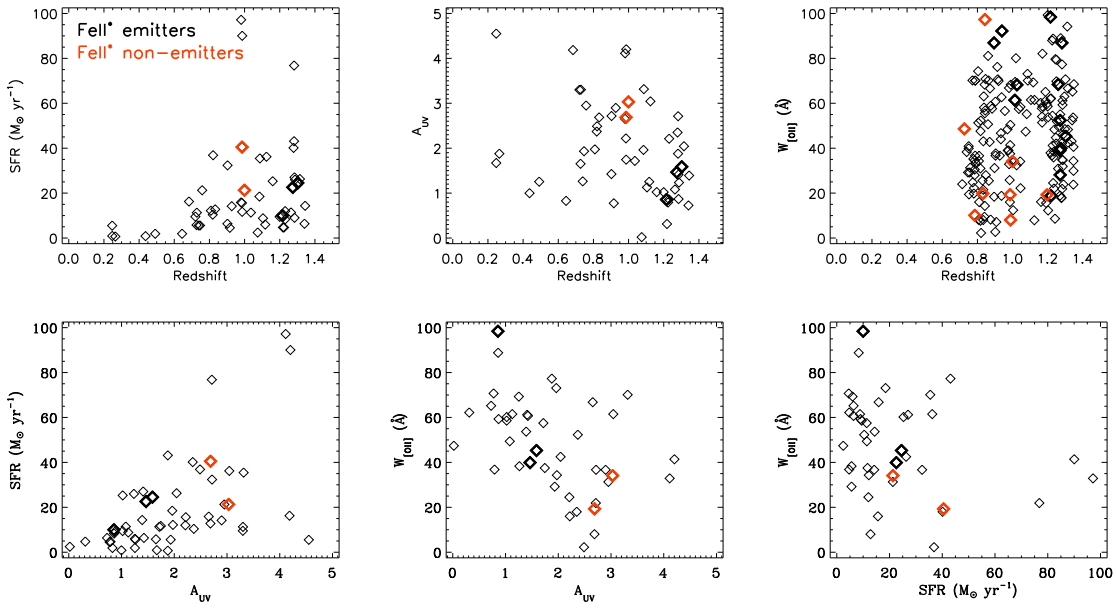

Figure 4.12 *Top panels:* SFR, A_{UV}, and $W_{[OII]}$ (from left to right) versus redshift, where Fe II* emitters are indicated in thick black diamonds and Fe II* non-emitters are shown as thick red diamonds. *Bottom panels:* Correlations among A_{UV}, SFR, and $W_{[OII]}$, using the same notation as above. SFR and A_{UV} are positively correlated, while both $W_{[OII]}$ and A_{UV} and $W_{[OII]}$ and SFR are inversely correlated. These correlations are consistent with A_{UV} being the primary modulator of Fe II* emission, given that Fe II* emitters are characterized by smaller SFRs and larger $W_{[OII]}$ values than Fe II* non-emitters.

In the top panels of Figure 4.12, we plot SFR, A_{UV}, and $W_{[OII]}$ versus redshift. Redshift and SFR are correlated at the 3.1σ level ($r_S = 0.44$), where higher redshift systems have higher SFRs. This positive correlation between redshift and SFR is in the opposite sense of the trends we find with Fe II* emission strength, where both low-SFR and high-redshift systems show stronger Fe II* emission. We also find a correlation at the 2.4σ level ($r_S = -0.33$) between redshift and A_{UV}, such that higher redshift systems are less attenuated. Finally, we find a 2.7σ correlation ($r_S = 0.20$) between redshift and $W_{[OII]}$, in the sense that higher redshift objects have larger $W_{[OII]}$ measurements. Given that intrinsic galaxy properties vary as a function of redshift, we conclude that SFR, A_{UV}, and $W_{[OII]}$ most strongly modulate Fe II* emission strength. The bottom panels of Figure 4.12 show how SFR, A_{UV}, and $W_{[OII]}$ are themselves interrelated: systems with larger SFRs have larger A_{UV} values, objects with stronger $W_{[OII]}$ have lower A_{UV} values, and systems with stronger $W_{[OII]}$ also have larger SFRs. SFR, A_{UV}, and $W_{[OII]}$ are accordingly correlated such that the stronger Fe II* emission in objects with ower SFRs, lower A_{UV} values, and larger $W_{[OII]}$ measurements can be explained as arising primarily due to the effect of a single parameter. In Section 4.4, we propose that the presence or absence of dust may most strongly affect the strength of Fe II* emission.

Other parameters besides SFR, A_{UV}, $W_{[OII]}$, and z also modulate Fe II* emission strength. We find that 3σ gas flow, $U - B$ color, the presence of Mg II emission, angular size, and physical size have D_{FeII^*} values significant at $\geq 1\sigma$, such that stronger Fe II* emission is seen in systems with 3σ inflows (as opposed to 3σ outflows), bluer $U - B$ colors, stronger Mg II emission, smaller angular sizes, and smaller physical sizes. The stronger Fe II* emission observed in systems with smaller angular sizes is consistent with the theory that slit losses may be responsible for the lack of Fe II* emission in galaxies with larger angular sizes.

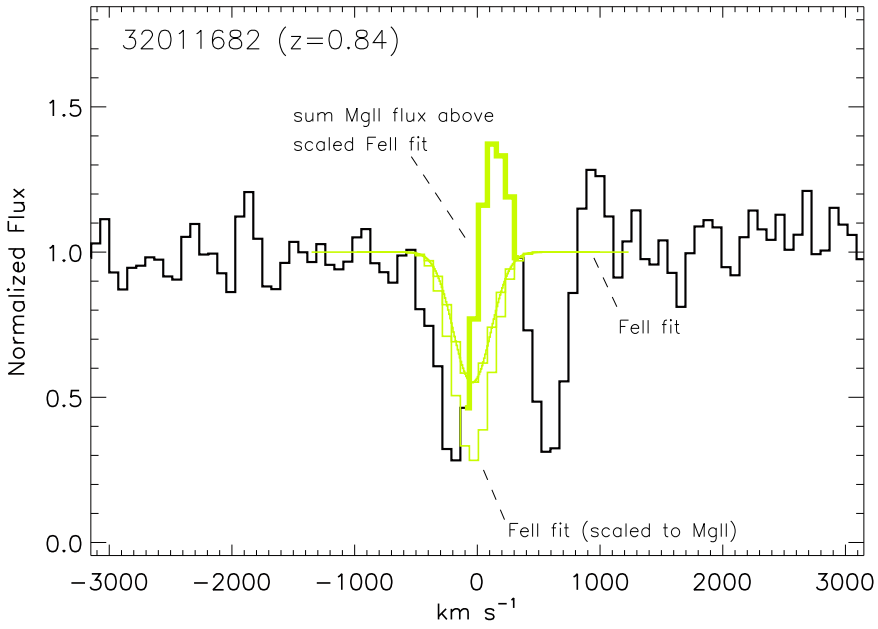

Figure 4.13 Methodology for identifying Mg II emission. We assumed that the Fe II profile, in this case a fit to the 2374 Å feature, represented a fiducial absorption profile largely unaffected by emission filling. We normalized the depth of Fe II profile to that of the Mg II profile and summed the flux in the Mg II feature above the scaled Fe II profile. This summed flux is representative of the emission contribution of Mg II to the overall Mg II profile. We find that 31 objects in the sample show Mg II emission at $\geq 3\sigma$ significance for both the 2796 and 2803 Å Mg II lines.

The fact that we do not observe a correlation between Fe II* emission strength and Fe II equivalent width is striking given that Fe II* emitter and non-emitter composite spectra show differences in Fe II absorption strength (Figure 4.2).

4.3 Mg II Emission

The high cosmic abundance of magnesium (Savage & Sembach, 1996) makes Mg II a useful tracer of interstellar gas in galaxies. Mg II transitions in the rest-frame ultraviolet are commonly used as probes of galactic winds at intermediate redshifts due to their placement above the atmospheric cut-off for samples at $z \gtrsim 0.2$. The Mg II doublet at $\lambda\lambda$ 2796,2803 Å, while primarily seen in absorption, is also observed with a P-Cygni emission profile in objects as varied as Seyfert 1s (Wu et al., 1983), ultraluminous infrared galaxies (ULIRGs; Martin & Bouché, 2009), and high-redshift starbursts (Weiner et al., 2009; Rubin et al., 2011; Giavalisco et al., 2011, Erb et al. 2012, in prep.). The physical origin of Mg II emission has been attributed to both low-level AGN activity and scattering off the backside of the wind (Phillips, 1993; Weiner et al., 2009; Rubin et al., 2011), where the latter process has also been seen in Lyα emission in Lyman Break Galaxies (Pettini et al., 2001; Shapley et al., 2003).

Both features of the Mg II doublet at $\lambda\lambda$ 2796,2803 Å have large oscillator strengths and a high probability of emission due to the lack of excited ground states for fluorescence. We examine here the diversity of Mg II profiles in our sample, focusing specifically on the incidence of Mg II emission. Even in our relatively low resolution data, the Mg II doublet is resolved given its wide velocity separation (770 km s^{-1}). In unsaturated systems, the 2796 Å line of the Mg II doublet should be twice as strong as the one at 2803 Å. However, this 2:1 line ratio is not always seen in our data. Rather, we find that the Mg II features

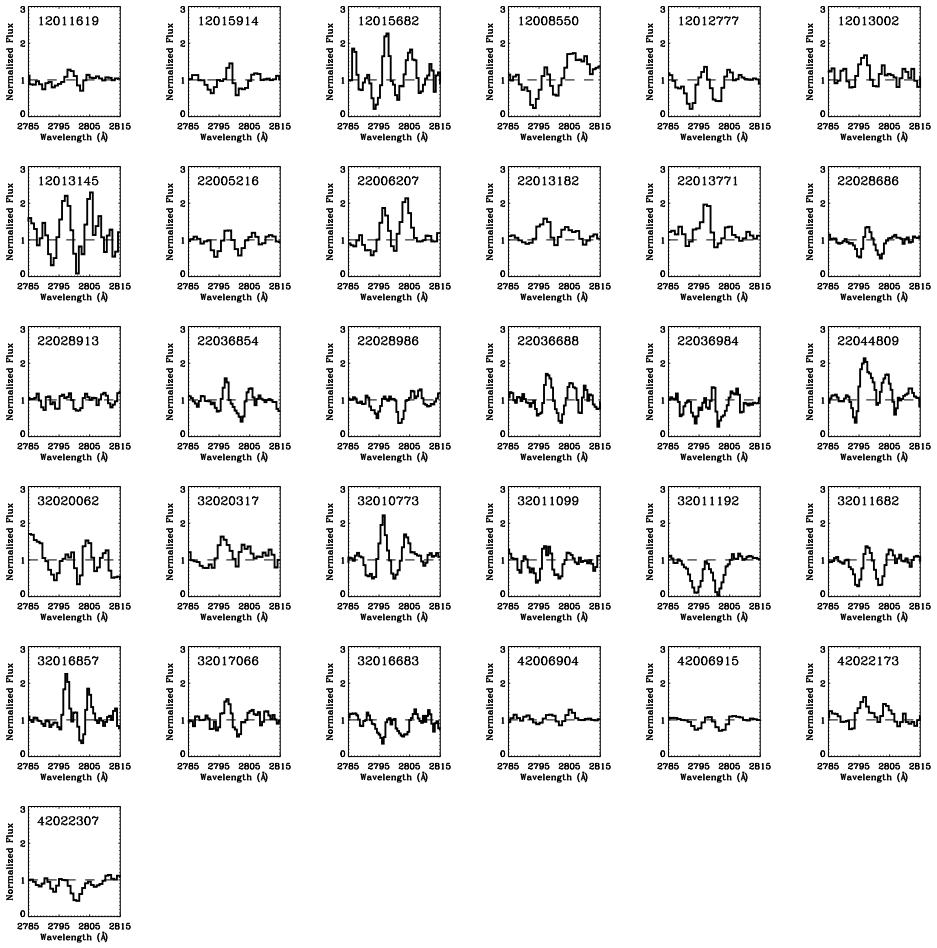

Figure 4.14 Thumbnails of the 31 objects with $\geq 3\sigma$ detections of Mg II emission in both the 2796 and 2803 Å lines. The majority of objects show pronounced Mg II emission above the continuum. Each thumbnail is 30 Å wide.

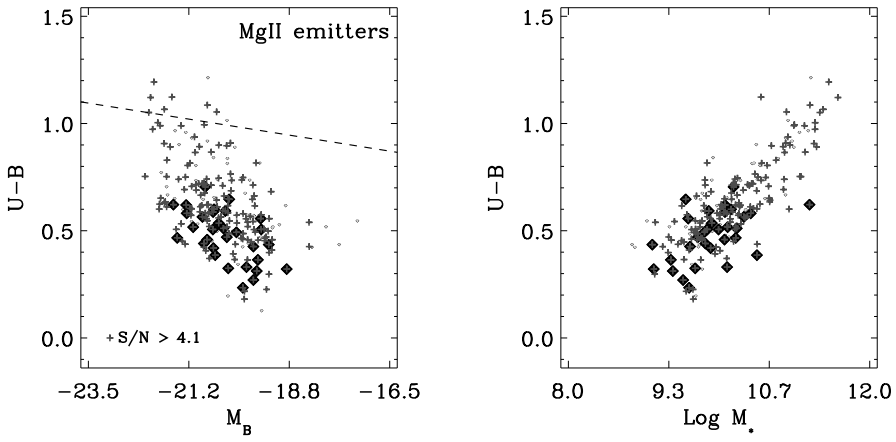

Figure 4.15 *Left:* Color-magnitude diagram with the 31 Mg II emitters shown as filled black diamonds. Gray crosses indicate objects with S/N $>$ 4.1 pixel^{-1}, the minimum S/N of the Mg II emitter sample. Consistent with Weiner et al. (2009), we find that objects showing Mg II in emission are bluer than the general galaxy poulation: the Mg II emitters have an average $U - B$ color of 0.48 $\pm$ 0.02 compared with the global sample average of 0.61 $\pm$ 0.01, where the errors represent the standard deviation of the mean. *Right:* Color vs. stellar mass plot, where the symbols are the same as in the left panel. Mg II emitters have characteristically lower stellar masses than the sample as a whole.

often have roughly equal line strengths, indicative of saturation. In some cases, we even observe systems where the 2803 Å line is stronger than the 2796 Å feature. Emission filling may be responsible for the deviation of these line ratios from their expected values.

4.3.1 Mg II Emitters

Weiner et al. (2009) report Mg II emission in 4% of their sample of $z \sim 1.4$ star-forming galaxies, compared with Rubin et al. (2010b) who find that only 4/468

($< 1\%$) star-forming galaxies at a similar epoch exhibit emission. Both of these authors identified the presence of Mg II emission by comparing the fluxes in two wavelength windows tracing the continuum and the region immediately redwards of the 2796 Å line, respectively (Figure 3 in Weiner et al. 2009). While this technique should robustly identify strong Mg II emitters, it may miss objects with only weak Mg II emission. Weiner et al. (2009) find Mg II emission preferentially in blue, luminous galaxies and propose that the emission may be due to low-level AGN, although these authors fail to find any Ne V emission at 3425 Å characteristic of active galaxies in their co-added spectra. Weiner et al. (2009) still find Mg II emission in a composite spectral stack even after clipping their sample of likely AGN candidates, indicative that Mg II emission is pervasive in star-forming samples. These authors argue that stellar chromospheric Mg II emission is unlikely to account for the observed emission, given that this stellar feature is weaker in hot stars (Snow et al., 1994).

In light of the increased S/N of our data ($\sim$ 11 per resolution element) relative to that of Weiner et al. (2009) ($\sim$ 1 per resolution element) and Rubin et al. (2010b) ($\sim$ 2 per resolution element), we developed a new method to systematically isolate objects with Mg II emission. Instead of relying on flux measurements within prescribed wavelength windows, we employed the fits to the data's resonance Fe II absorption features (Section 4.1.1). Since Fe II, and the Fe II 2374 Å feature in particular, is not as susceptible to emission filling as Mg II, we assumed that the Fe II features served as fiducial profiles largely unaffected by emission filling. In other words, Fe II offers an unbiased view of the intrinsic Mg II absorption profile. In Figure 4.13, we schematically illustrate how we compare the Mg II and Fe II profiles to estimate the contribution of Mg II emission to the overall Mg II profile. For each of the objects with spectral coverage of both Mg II and Fe II, we began by plotting the Fe II and Mg II features in velocity space and

normalizing the Fe II profile (of the 2374 Å line, whenever possible) to the lowest pixel of the Mg II absorption trough. We then estimated the Mg II emission component as being the flux enclosed between the Mg II profile and the normalized Fe II fit. We used the 2374 Å Fe II line when possible due to its strength and minimal susceptibility to emission filling. If the 2374 Å feature was noisy or otherwise compromised (by a sky residual, for example), we employed either the 2344 or the 2587 Å Fe II line. We normalized the depths of the features in order to most fairly compare the enclosed flux.

By calculating the associated error from the error spectra, we assigned an emission significance to each object for both features of the Mg II doublet. This method is sensitive to strong Mg II emitters – such as those found using the technique of Weiner et al. (2009) and Rubin et al. (2010b) – and also objects in which emission may not be visually apparent but the kinematic profile of Fe II differs from that of Mg II. This technique's ability to isolate objects for which the kinematics of Fe II and Mg II differ results in a more complete sample of Mg II emitters than is found using the method employed by Weiner et al. (2009) and Rubin et al. (2010b).

Of the 186 objects in our sample with spectral coverage of Mg II, 49 (26%) show emission at or above the 3σ level in the 2796 Å line while 44 (24%) show emission at the same threshold in the 2803 Å line. 31 objects (17%) exhibit $\geq 3\sigma$ emission in both lines of the Mg II doublet (Figure 4.14). These percentages of Mg II emitters are significantly higher than those found by Weiner et al. (2009) and Rubin et al. (2010b); we attribute this discrepancy to our method's increased sensitivity to objects in which the kinematics of Fe II and Mg II differ. In the left-hand panel of Figure 4.15, we show a color-magnitude diagram and indicate the 31 objects with Mg II emission significances $\geq 3\sigma$ in both lines. Consistent

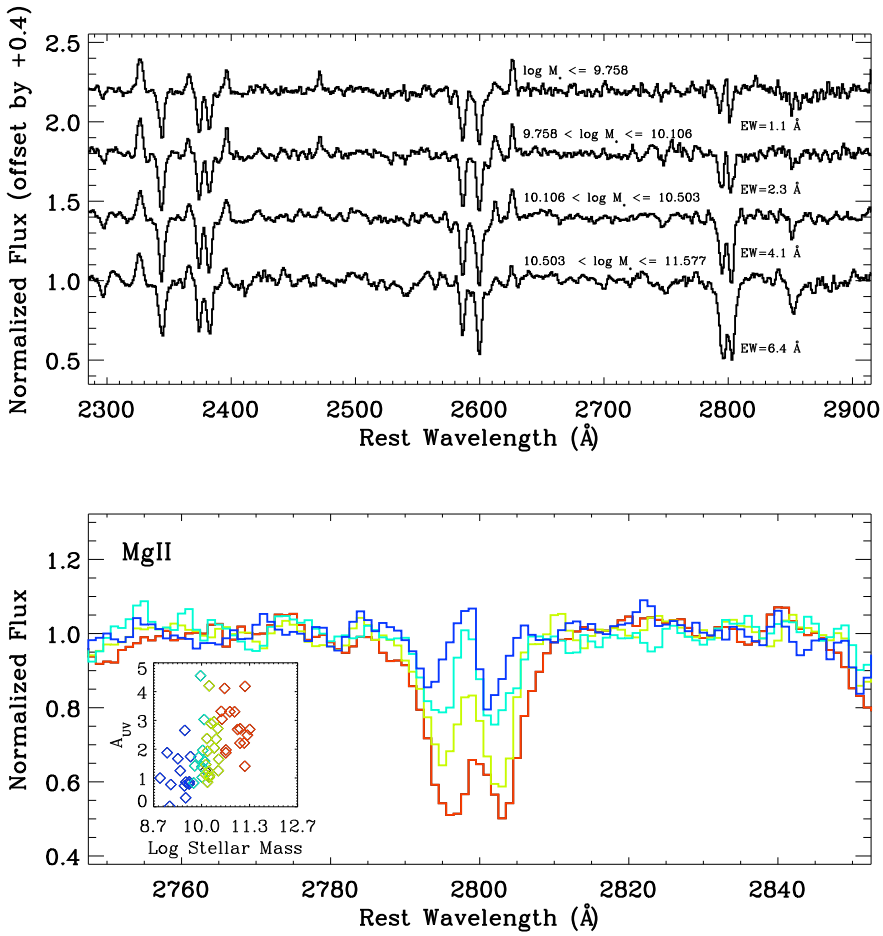

Figure 4.16 *Top:* Composite spectra in four bins of stellar mass, where the strongest variation with stellar mass is seen in Mg II strength and kinematics. Deep Mg II absorption is observed in high stellar mass objects, while less massive objects show weaker Mg II absorption. The equivalent width values listed in the figure are calculated by summing over both the 2796 and 2803 Å lines. *Bottom:* Comparison of the Mg II feature in the four composite spectra. The inset shows A_{UV} versus stellar mass; the most massive galaxies (in red) are characterized by the largest dust attenuations. The shallower Mg II absorption profiles seen in low-mass galaxies may be due to a combination of more emission and less intrinsic absorption. The differences in the red wings of the Mg II doublet are indicative of emission filling, consistent with the picture of low-mass objects exhibiting more emission.

with Weiner et al. (2009), we find that galaxies showing strong Mg II emission are preferentially blue, with an average $U - B$ color of 0.48 ± 0.02 (compared with 0.61 ± 0.01, the average $U - B$ color of the whole sample); the errors on these colors represent the standard deviation of the mean. We also find that objects with strong Mg II emission have lower stellar masses ($\langle M_* \rangle = 8 \times 10^9\ M_\odot$), on average, than the population as a whole ($\langle M_* \rangle = 1 \times 10^{10}\ M_\odot$; right-hand panel, Figure 4.15). Weiner et al. (2009) also propose that objects showing Mg II in emission are typically drawn from a more luminous population. We conducted a KS test comparing the distributions of the B-band absolute luminosities of the 31 objects with Mg II emission significances $\geq 3\sigma$ in both lines and the entire sample of objects. We find a probability of $\sim 70\%$ that the two distributions are drawn from the same parent population, indicating that our data do not suggest an intrinsic luminosity difference between objects showing Mg II in emission and those exhibiting Mg II in absorption.

In the top panel of Figure 4.16, we show four composite spectra of objects divided on the basis of stellar mass. Mg II emission is prominent in the lowest mass composite, consistent with the trend seen in Figure 4.15 of Mg II emitters being preferentially low-mass objects. The highest mass objects, in comparison, show deep Mg II absorption that is nearly 6 times stronger than the absorption profile of the lowest-mass sample. We attribute these differences to low-mass objects experiencing both less intrinsic absorption and also more emission filling; we see evidence for emission filling in the lowest mass composite spectrum in the form of its blueshifted centroid and filled red wing relative to the highest mass composite spectrum. In the bottom panel of Figure 4.16, a zoom-in of the Mg II profile for the four composites are shown, along with an inset plotting A_{UV} versus stellar mass. As the least massive objects show lower dust attenuation than higher mass objects, emission is less likely to escape from high-mass systems. The

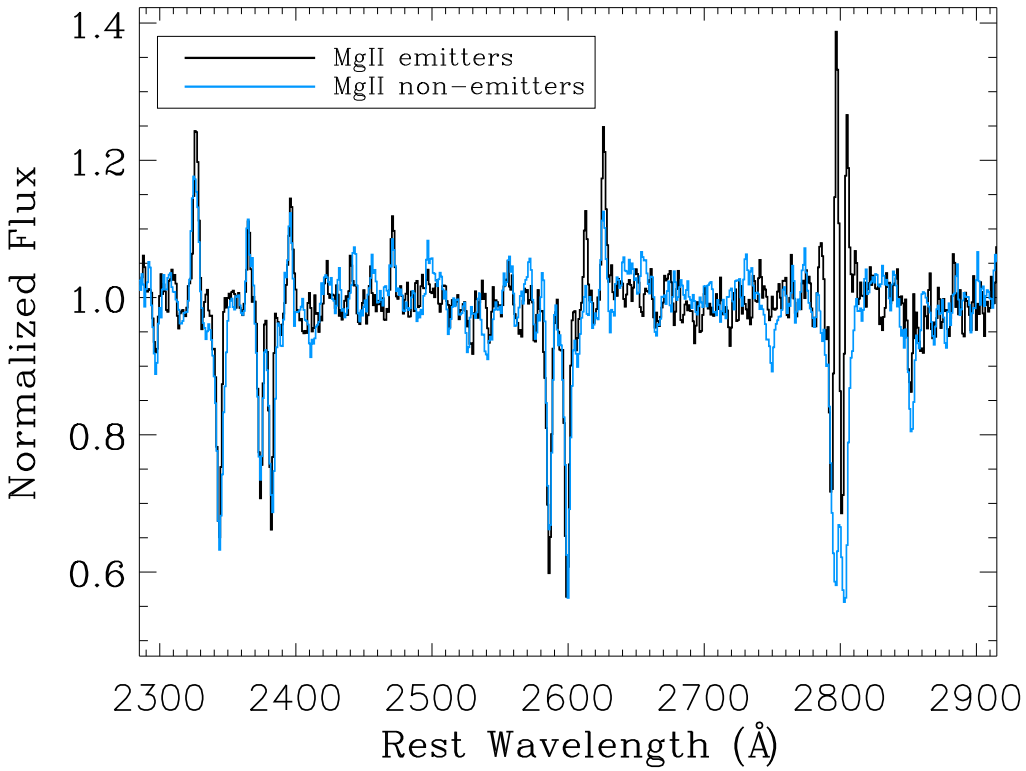

Figure 4.17 Comparison of composite spectra assembled from stacks of the 31 Mg II emitters (black line) and 29 Mg II non-emitters (blue line).

differences in the Mg II doublets – where low-mass objects show more blueshifted absorption centroids – are indicative of emission filling in the lowest mass sample.

We assembled a spectral stack of the 31 objects in our sample exhibiting Mg II emission significances $\geq 3\sigma$ in both lines and find no evidence for Ne V AGN emission at 3425 Å in the 28 objects with spectral coverage of the Ne V region. Based on Chandra X-ray flux catalogs available for the Extended Groth Strip (72/212 objects fall in this field), only one object is likely an AGN due to its X-ray flux and this object does not have spectral coverage of Mg II. We

also assembled a stack of the 29 objects with $< 1\sigma$ detections in both Mg II lines, where we required that each object have a S/N greater than the smallest S/N observed in the Mg II emitter sample (4.1 pixel^{-1}). This methodology of requiring comparable S/N in the Mg II emitter and non-emitter samples ensures that objects do not scatter into the Mg II non-emitter sample purely on the basis of being noisy. In Figure 4.17, we plot these two composite spectra. While Fe II* emission is stronger in the stack of Mg II emitters, the composite spectra are otherwise comparable in terms of Fe II kinematics and strength. 10 objects in the sample of Mg II non-emitters have colors indicative of "Green Valley" galaxies; our conclusions remain unchanged if these objects are removed from the non-emitter sample.

4.3.2 Properties of the Strongest Mg II Emitters

We measured the kinematics of the Mg II emission peaks of the composite spectrum assembled from the 31 objects showing significant Mg II emission. Fitting a Gaussian profile to the 2796 and 2803 Å features separately, we find that the emission peaks are located at 108 ± 26 and 176 ± 17 km s^{-1}, respectively. This result that the emission peaks are redshifted is different from the findings of Coil et al. (2011). These authors reported that 7/11 X-ray AGN and post-starburst galaxies at $0.2 < z < 0.8$ have Mg II velocity centroids consistent with the systemic velocity (less than 3σ deviant) while only 4 objects show blueshifted or redshifted emission.

According to Prochaska et al. (2011), the ratio of absorption to emission equivalent width of Mg II depends both on the geometry of the wind and the amount of dust in the system. These authors use radiative transfer modeling and find that the opening angle of the biconical outflow strongly modulates the

strength of Mg II emission, with more collimated outflows showing less emission. According to these models, the 31 objects in our sample that show significant Mg II emission would be expected to have narrower gas flows. Integral field unit observations of the geometry of emission lines are necessary in order to investigate this hypothesis.

Prochaska et al. (2011) also conclude that the presence of dust affects the incidence of Mg II emission; dustier systems show significantly less emission. The Mg II $\lambda\lambda$ 2796,2803 Å doublet is particularly susceptible to attenuation by dust since resonance photons scatter and experience longer path lengths (and therefore more opportunities for encountering a dust grain) than non-resonance photons. We also find that Mg II emission is stronger in systems with bluer $U-B$ colors, as discussed below.

4.3.3 Mg II Strength and Galaxy Properties

Given the diversity of Mg II profiles in our sample, we now turn to systematically analyzing how galaxy properties are correlated with Mg II emission strength. In Figure 4.15, we showed that individual objects with strong Mg II emission have bluer colors and lower stellar masses than the sample as a whole. Here, we employ composite spectra to investigate how the strength of Mg II emission varies as a function of many different galaxy properties.

We employed a similar technique for measuring Mg II emission strength in the composite spectra that we utilized for the individual spectra (Section 4.3.1). Instead of defining the intrinsic Mg II absorption profiles based on the fits to the Fe II absorption lines as we did in Section 4.3.1, we assumed that the Fe II data themselves were accurate tracers of Mg II absorption. This technique is robust for the composite spectra due to their higher S/N compared with the individual

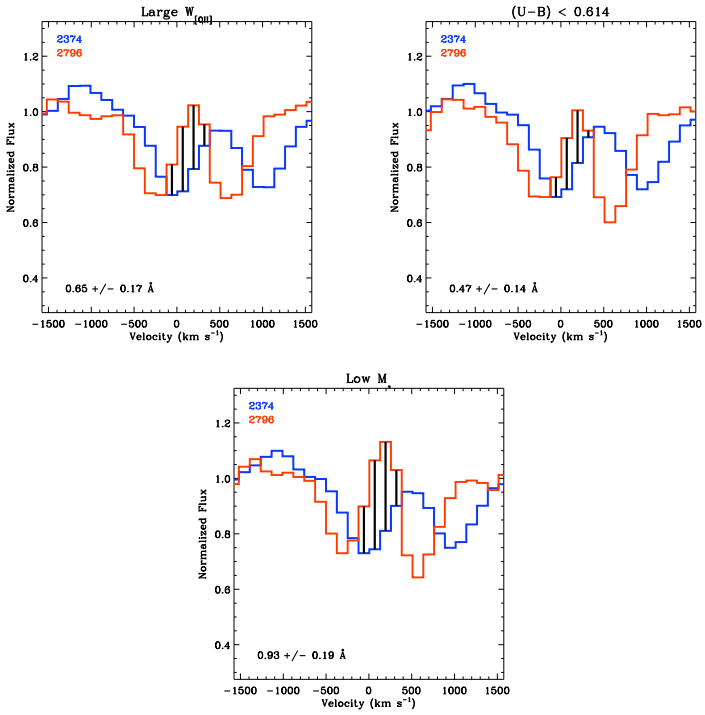

Figure 4.18 Excess Mg II 2796 Å emission relative to the Fe II 2374 Å profile. Three composite spectra – large $W_{[OII]}$, blue $U - B$ color, and low M_* – exhibit Mg II emission at $\geq 3\sigma$ significance. For each composite, the Fe II profile (blue line) is shown overplotted on the Mg II profile (red line) in velocity space and the vertical black lines delineate excess Mg II emission above the Fe II profile. The excess Mg II emission strength, in Å in shown in the lower left of each plot. These results corroborate the findings of Figure 4.15, in which individual objects with Mg II emission were found to be bluer and lower mass than the sample as a whole. The composite spectrum composed of objects with low A_{UV} values also shows strong Mg II emission, although the emission is not detected at 3σ significance due to the relatively few number of objects with A_{UV} measurements.

spectra. Using the eighteen pairs of composite spectra from Section 4.2.4 that parameterize galaxies on the basis of star-forming, gas flow, Fe II and Mg II, stellar population, size, morphological, and redshift properties, in addition to composite spectra assembled according to Fe II* emission strength, we measured the strength of Mg II emission in the 2796 Å line. We find that three composite spectra show Mg II emission at or above the 3σ level: large $W_{[OII]}$, blue $U-B$, and low M_* (Figure 4.18). The composite spectrum composed of objects with low A_{UV} values also shows strong Mg II emission, although the emission is not detected at 3σ significance due to the relatively few number of objects with A_{UV} measurements. These results are consistent with our observation that individual Mg II emitters are preferentially bluer and lower mass than the sample as a whole (Figure 4.15). As we discuss below, we propose that dust is the primary factor modulating Mg II emission strength.

4.4 Discussion

4.4.1 The Absence of Fe II* Emission in Local Samples

While Fe II* emission lines are prevalent in samples at $z \geq 0.5$, including star-forming and post-starburst galaxies, AGNs, and quasars (Wang et al., 2008; Coil et al., 2011; Giavalisco et al., 2011; Rubin et al., 2010a, 2011, Erb et al. 2012, in prep., this work), Fe II* emission is conspicuously absent in local starbursts. Figure 4.19 contrasts a $z \sim 0$ composite starburst spectrum from Leitherer et al. (2011) with the composite spectrum of $z \sim 1$ star-forming galaxies from this work. One immediately notices the lack of Fe II* emission in the local sample. Giavalisco et al. (2011) propose that nearby samples do not exhibit Fe II* emission simply due to slit losses: Fe II* lines arising from spatially-extended winds will

not fall within the spectroscopic slit at $z \sim 0$. Given the small physical-to-angular conversion valid for the local universe – 170 pc/″ at the average redshift of the Leitherer et al. (2011) sample – spectroscopic observations at $z \sim 0$ fail to encompass the halos of galaxies where Giavalisco et al. (2011) propose Fe II* emission originates. In particular, the Leitherer et al. (2011) observations target only small H II regions of size $\sim$ 100 pc. Spectroscopic observations of distant galaxies, in comparison, are inclusive of extended Fe II* emission given physical-to-angular conversions of 8 kpc/″ at $z = 1$ and typical slit widths of $\sim 1''$.

The hypothesis that slit losses are responsible for the lack of Fe II* emission in local samples is supported by theory. Prochaska et al. (2011) present models of galactic winds in which Fe II* line emission is generated by *all* galaxies driving a cool gas outflow. While not all objects in our sample show evidence for outflows, we use spatially-resolved imaging in Kornei et al. (2012) and outflow fraction calculations in Martin et al. (2012) to infer that the prevalence of outflows is likely modulated by galaxy inclination. All star-forming systems may in actuality drive outflows, but only a fraction of objects exhibit outflow signatures depending on the orientation of the outflowing wind with respect to the observer. While work by Prochaska et al. (2011) focuses on Fe II* emission arising in the presence of gas flows, Fe II* lines are generated even in the absence of galactic winds. Prochaska et al. (2011) find that Fe II* emission is spatially extended with non-zero surface brightness at large galactocentric radii; a $1''$ slit covering a galaxy at $z > 0.5$ would include less than 50% of the Fe II* emission. At lower redshifts, even less of the Fe II* emission would fall into the spectroscopic slit.

If the frequency of detecting Fe II* emission depends on the spatial scale probed by spectroscopic observations, as Giavalisco et al. (2011) and Prochaska et al. (2011) suggest, one would expect to see variation in the strength of Fe II*

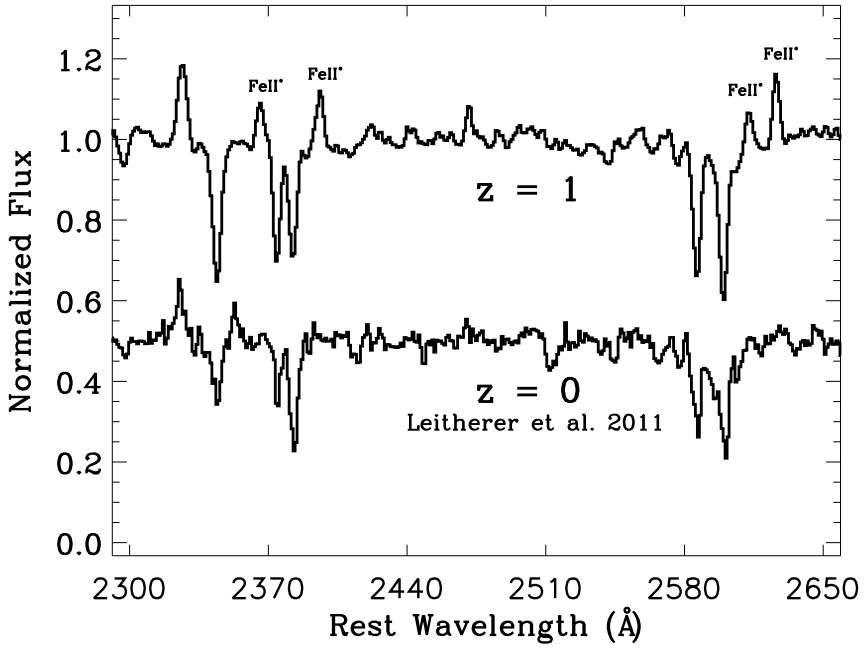

Figure 4.19 Comparison of composite spectra of star-forming galaxies at $z \sim 1$ and $z \sim 0$. Fe II* emission is conspicuous in the $z \sim 1$ sample (data from this work) while the $z \sim 0$ sample (28 local star-forming galaxies observed in 46 unique pointings from Leitherer et al. (2011)) is strikingly bereft of Fe II* emission. Giavalisco et al. (2011) and Erb et al. (2012, in prep.) hypothesize that slit losses may be responsible for the lack of Fe II* emission in nearby samples. As the Leitherer et al. (2011) pointings target very small spatial scales (starburst regions of size $\sim$ 100 pc), spatially-extended Fe II* emission would be missed by these observations. On the other hand, spectroscopic observations of galaxies at $z \sim 1$ typically encompass the entire galaxy given the physical-to-angular conversion of ~ 8 kpc/″.

emission as a function of galaxy angular size. We used Petrosian radii – measured in the V band for objects at $z < 1.10$ and in the I band for objects at $z > 1.10$ – to divide the sample into two groups based on angular size. From composite spectra assembled from each group, we found that smaller objects ($\langle R_P \rangle = 0.''6$, where R_P is the Petrosian radius) showed stronger 2396 and 2626 Å Fe II* emission than larger ($\langle R_P \rangle = 1.''3$) objects (Figure 4.20). While these results are consistent with Fe II* emission arising from spatially-extended winds, we caution that solely dividing galaxies on the basis of angular size is a blunt tool for analysis given the diversity of galaxies populating each angular size bin[3].

4.4.2 Fe II* and Mg II Emission are Modulated by Dust

The strongest Fe II* emission in our study is observed in systems with lower SFRs, lower A_{UV} levels, and larger $W_{[OII]}$ measurements. Several authors have proposed different explanations for the changing strength of Fe II* emission in star-forming galaxies, including slit losses (Giavalisco et al., 2011, Erb et al. 2012, in prep.), dust attenuation (Prochaska et al., 2011), and viewing angle effects of observing a non-spherical wind (Erb et al. 2012, in prep.).

Our observations are most consistent with Fe II* emission strength being primarily modulated by the presence of dust, since A_{UV} and other properties closely linked to A_{UV} are correlated with the strength of Fe II* emission. Figure 4.12 shows that systems with lower SFRs and larger $W_{[OII]}$ measurements – those properties found to modulate Fe II* emission – have typically lower A_{UV} levels. The simple picture of emission photons being absorbed by dust is consistent with our data. In Figure 4.20, we show that dividing objects on the basis of angular

[3]Angular size is correlated with redshift at the 2.7σ level, and redshift is in turn correlated with SFR, A_{UV}, and $W_{[OII]}$ (Figure 4.12). In the absence of a larger sample, it is difficult to isolate objects that vary in angular size but do not vary significantly in other galaxy properties.

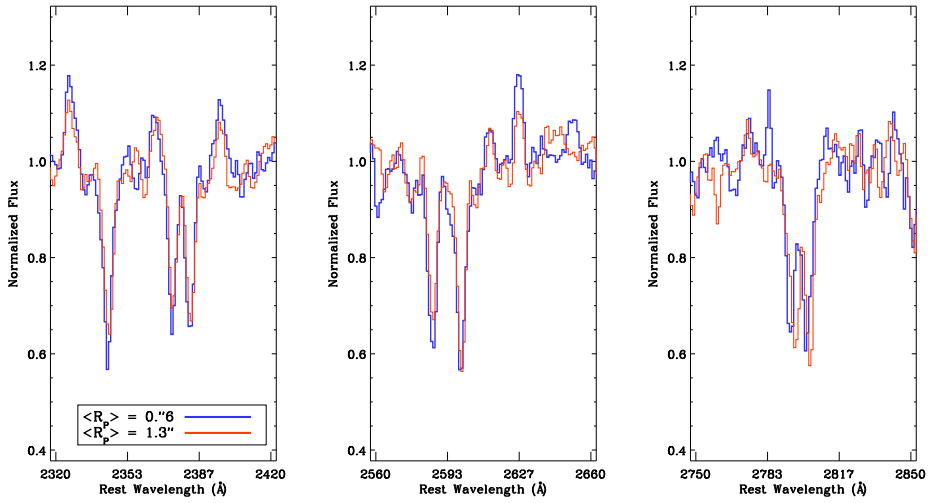

Figure 4.20 Composite spectra assembled on the basis of angular Petrosian radius. The stack of smaller objects ($\langle R_P \rangle = 0.''6$) is shown in blue while the composite spectrum comprised of larger objects ($\langle R_P \rangle = 1.3''$) is shown in red. Smaller objects show stronger 2396 and 2626 Å Fe II* emission than larger objects, consistent with the theory of Fe II* emission slit losses presented by Giavalisco et al. (2011) and Erb et al. (2012, in prep.). Smaller objects also exhibit more blueshifted Mg II centroids, although the overall strengths of Mg II absorption in the two composite spectra are comparable.

size (i.e., simulating the effects of slit losses) yields a qualitative difference in Fe II* strength, but one that is weaker than the difference in Fe II* emission observed when the data are divided according to A_{UV} (Figure 4.9). A non-spherical galactic wind will also introduce variations in Fe II* emission strength purely dependent on the viewing geometry of the observer with respect to the wind. For a biconical wind arising perpendicular to a galaxy disk, observations of the system face-on will yield strong absorption signatures and weak emission measurements while a galaxy viewed edge-on will predominantly show emission. When we divided our sample on the basis of disk inclination, we find no significant change in Fe II* emission strength. While we caution that the sample of objects with inclination estimates is small, this result does not suggest that the viewing angle effects of observing a non-spherical wind strongly affect the measured Fe II* emission strength. The conclusion that Fe II* emission is modulated by dust is the simplest inference, given the uncertainties in estimating differential slit losses and disk inclinations in our dataset.

We find that Mg II emission is most prevalent in systems with larger $W_{[OII]}$ measurements, bluer $U - B$ colors, and lower stellar masses. These correlations are also consistent with Mg II emission being primarily modulated by dust. High levels of dust would attenuate [O II] emission and redden systems with intrinsically blue $U - B$ colors. Since low-mass objects are less attenuated than high-mass objects (Hopkins et al., 2001), the stronger Mg II emission seen in systems with lower stellar masses can be plausibly explained by lower dust levels in these objects.

These properties of Mg II emitters – stronger [OII] emission, bluer colors, and lower stellar masses – are accordingly consistent with objects having low dust attenuation. Composite spectra assembled on the basis of A_{UV} also show

pronounced differences in Mg II strength, with lower A_{UV} systems showing weaker Mg II absorption (Figure 4.10). The uncertainties on the Mg II strengths in the A_{UV} composites are large given the relatively few number of objects with A_{UV} measurements, however, so A_{UV} was not flagged as a parameter controlling Mg II strength in Section 4.3.3. We conclude that dust is the primary property modulating Mg II emission.

4.5 Summary and Conclusions

We have investigated the properties and prevalence of fine-structure Fe II* emission and resonance Mg II emission in a sample of 212 star-forming galaxies at $z \sim 1$. Using rest-frame ultraviolet spectroscopy and a rich ancillary dataset comprised of *GALEX*, *HST*, and *Spitzer* imaging, we studied how the strength of both Fe II* and Mg II vary as a function of star-forming, gas flow, Fe II and Mg II, stellar population, size, morphological, and redshift properties. We provide below a numbered list of our main conclusions:

1. Fe II* emission is prevalent at $z \sim 1$ in composite spectra assembled from a range of galaxy properties, although Fe II* emission is not observed in local studies probing star-forming regions.

2. The kinematics of the strongest Fe II* emission lines are consistent with the systemic velocity.

3. Fe II* emission is most strongly correlated with SFR, A_{UV}, and $W_{[OII]}$, where lower SFR, lower A_{UV}, and higher $W_{[OII]}$ systems preferentially exhibit Fe II* emission. We propose that Fe II* emission is modulated by the presence of dust.

4. Mg II emission is most strongly correlated with $W_{[OII]}$, stellar mass, and

Table 4.1. Fe II and Fe II* Lines

λ[a] (Å)	J_{lower}[b]	J_{upper}[b]	A_{21}[c] (s^{-1})	Feature Type	Equivalent Width[d] (Å)
2344.21	9/2	7/2	1.7×10^8	resonant abs.	1.94 ± 0.06
2365.55	7/2	7/2	5.9×10^7	fine-structure em.	–0.42 ± 0.05
2380.76	5/2	7/2	3.1×10^7	fine-structure em.	··· [e]
2374.46	9/2	9/2	4.3×10^7	resonant abs.	1.39 ± 0.08
2396.35	7/2	9/2	2.6×10^8	fine-structure em.	–0.72 ± 0.07
2382.77	9/2	11/2	3.1×10^8	resonant abs.	1.53[e]± 0.06
2586.65	9/2	7/2	9.0×10^7	resonant abs.	1.72 ± 0.06
2612.65	7/2	7/2	1.2×10^8	fine-structure em.	–0.41 ± 0.09
2632.11	5/2	7/2	6.3×10^7	fine-structure em.	–0.21[f]
2600.17	9/2	9/2	2.4×10^8	resonant abs.	2.35 ± 0.09
2626.45	7/2	9/2	3.5×10^7	fine-structure em.	–0.80 ± 0.09

[a]Vacuum wavelengths from Ralchenko et al. (2005).

[b]Orbital angular momenta.

[c]Einstein A coefficients.

[d]Equivalent width of feature measured in the global composite spectrum (Figure 4.1). Negative equivalent widths correspond to features in emission.

[e]Fe II* 2380.76 Å is blended with Fe II 2382.77 Å.

[f]3σ upper limit.

color, where objects with higher $W_{[OII]}$, bluer $U - B$ colors, and lower stellar masses are more likely to show Mg II emission. Like Fe II* emission, Mg II emission is dependent on the level of dust attenuation; low-A_{UV} objects show weaker Mg II absorption than high-A_{UV} systems.

Galactic winds are a critical component of the regulation of star formation and prescriptions of galaxy evolution are dependent on detailed modeling of outflows. Probing the spatial and morphological properties of galactic winds in emission – information that is lacking from long-slit spectroscopic observations – will be possible with new instrumentation such as the Keck Cosmic Web Imager and the Multi Unit Spectroscopic Explorer on the VLT. Upcoming observations with these instruments will be important for understanding the enrichment of the circumgalactic medium and the connections between galaxies and their environments.

CHAPTER 5

Conclusions and Future Work

5.1 Summary & Conclusions

In this dissertation, I have explored the environment and regulation of star formation using samples of galaxies at $z \sim 1$ and $z \sim 3$. Chapter 2 focused on a population of 321 Lyman break galaxies at $z \sim 3$ for which rest-frame ultraviolet spectroscopy and multiwavelength imaging were available. I measured the spectroscopic strength of the H I Lyα line for each galaxy and studied how Lyα line strength varied as a function of stellar populations (star-formation rate, E(B–V), stellar mass, and dust attenuation). I found that objects with the strongest Lyα emission were preferentially older, less dust attenuated, and forming stars at a lower rate than galaxies with weaker (or absent) Lyα emission. This result is consistent with the physical picture of older galaxies having experienced galactic winds from massive stars and supernovae that cleared their halos of dust and enabled Lyα photons to escape unimpeded.

Within the same sample of Lyman break galaxies, I also investigated the spatial distribution of neutral, ionized, and dust species in the interstellar medium. I used resonant Lyα photons and non-resonant continuum photons as two complementary probes of the interstellar medium, based on the knowledge that Lyα resonantly scatters off of neutral hydrogen, does not interact with ionized hydrogen, and is absorbed by dust while continuum emission does not interact

with either neutral or ionized hydrogen and is absorbed by dust. Comparing the strengths of Lyα and continuum emission provides information that models of the spatial distribution of neutral, ionized, and dust species can be tuned to match. I find that Lyα photons are generally more attenuated than continuum photons, consistent with an interstellar medium in which neutral, ionized, and dust species are evenly distributed. This result constrains the structure of the interstellar medium at $z \sim 3$, an epoch for which it is difficult to attain direct imaging of galaxies.

Chapter 3 of this dissertation presented a study of 72 star-forming galaxies in the Extended Groth Strip (EGS) at $z \sim 1$. These objects are part of a larger sample of 212 objects for which rest-frame ultraviolet spectroscopy was obtained using LRIS on Keck I. With *GALEX*, *Hubble Space Telescope*, and *Spitzer* imaging available for the EGS enabling estimates of dust-corrected star-formation rates, star-formation rate surface densities, galaxy areas, and disk inclinations, I investigated the properties and prevalence of galactic winds at $z \sim 1$. These winds, arising from the combined energy and momentum of massive stars and supernovae, are a critical component of galaxy evolution as they disperse, heat, and accelerate the reservoirs of cool gas necessary for star formation. From observations of resonance lines of Fe II and Mg II absorbed against the light of host galaxies, I measured the spectral shifts of Fe II and Mg II relative to the systemic frame defined by nebular emission lines. I found that gas flows significant at the 1σ level are found in 40% of the sample. The velocity of the gas flows traced by Fe II and Mg II are most strongly correlated with star-formation rate surface density, consistent with recent modeling of galactic winds. Furthermore, Mg II absorption traces gas at systematically larger velocities than Fe II absorption; the Mg II features have larger oscillator strengths than the Fe II lines so this observation may simply be due to Mg II tracing a more tenuous population of

high-velocity ions. Using spatially-resolved *Hubble Space Telescope* imaging, I found that outflows are more prevalent in face-on systems, supporting the hypothesis that winds are biconical in geometry and arise perpendicular to galactic disks. This result supports other observations at similar redshifts that winds emerge in distinct geometries (Bordoloi et al., 2011), although higher redshift observations ($1.5 < z < 3.6$) suggest that winds are not collimated (Law et al., 2012b). Understanding what causes this transition in wind geometry is an open question that future observations will help to constrain.

While absorption lines are an important probe of gas flows, observations of resonant and fine-structure emission lines associated with galactic winds enable a complementary investigation of outflowing gas. The scattering of emission lines ensures that lines can be observed at spatial positions other than their point of origin; this property complicates interpretation of observations but also enables detailed study of the morphology and structure of the circumgalactic medium. In Chapter 4, I present measurements of emission lines from Fe II* transitions in a sample of 212 star-forming galaxies at $z \sim 1$. The Fe II* lines correspond to fine-structure transitions, in which electrons fall to excited ground states. These Fe II* lines are seen in four strong transitions at 2365, 2396, 2612, and 2626 Å in our data; I find that Fe II* emission is most pronounced in systems with low star-formation rates, low dust attenuations, and large [OII] emission equivalent widths. These trends are consistent with Fe II* emission being strongly attenuated by dust and therefore most prevalent in systems with low levels of dust. The kinematics of Fe II* emission are consistent with 0 km s^{-1}, although it is difficult to unequivocally state that the emission therefore arises from stationary H II regions. Since emission may be seen from both the backside (i.e., receding) and frontside (i.e., approaching) of the wind, modeling suggests that emission tracing gas flows may nonetheless appear centered at roughly the systemic velocity.

5.2 Future Work

Precision studies of the environment and regulation of star formation will be greatly aided by upcoming new instruments and telescopes. While current studies of Lyα-emitters rely on stellar population modeling of stacks of data, the James Webb Space Telescope will enable detailed studies of individual Lyα-emitters at high redshift. Long integration times and the low background of space will ensure that stellar population modeling can be done on a per-object basis. Investigations of the Lyα escape fraction will continue to yield information about the structure of the interstellar medium at epochs where spatially-resolved imaging becomes ever more difficult.

The anticipated Keck Cosmic Web Imager on the Keck telescopes will provide detailed observations of the tenuous emission from galactic winds and will enable studies of the morphology and density structure of emission tracing gas flows. The ongoing CANDELS project using the *Hubble Space Telescope* is obtaining diffraction-limited imaging in the rest-frame optical; these data are critical for investigating accurate sizes of galaxies, disk inclinations, and the outflow geometry of galactic winds.

While new telescopes and instrumentation enable ever deeper observations, larger surveys, and increased redshift space available for study, local studies of star-forming regions afford a unique perspective on the stellar environment. New observations of super star clusters – local analogs to high-redshift starbursts – reveal a detailed look at star-formation feedback occurring on the scales of parsecs. Nearby sources provide an important local laboratory for investigating theories of high-redshift star formation.

Advances in models and simulations are also critical to furthering our under-

standing of the environment of star formation. Simulations of the propagation of Lyα photons through an interstellar medium can be matched to observations in order to infer the distribution of neutral, ionized, and dust species. Models of galactic winds are also key components in the study of gas regulation. Theoretical work, with predictions that can readily be tested with data of achievable signal-to-noise and spectral resolution, will provide important benchmarks against which future observations can be compared. Studying star formation across different epochs is critical to tracing the build-up of matter in the Universe and better understanding the evolution of galaxies across cosmic time.

Bibliography

Adelberger, K. L., Shapley, A. E., Steidel, C. C., Pettini, M., Erb, D. K., & Reddy, N. A. 2005a, ApJ, 629, 636

Adelberger, K. L., Steidel, C. C., Giavalisco, M., Dickinson, M., Pettini, M., & Kellogg, M. 1998, ApJ, 505, 18

Adelberger, K. L., Steidel, C. C., Pettini, M., Shapley, A. E., Reddy, N. A., & Erb, D. K. 2005b, ApJ, 619, 697

Adelberger, K. L., Steidel, C. C., Shapley, A. E., & Pettini, M. 2003, ApJ, 584, 45

Ando, M., Ohta, K., Iwata, I., Akiyama, M., Aoki, K., & Tamura, N. 2006, ApJL, 645, L9

Ando, M., Ohta, K., Iwata, I., Watanabe, C., Tamura, N., Akiyama, M., & Aoki, K. 2004, ApJ, 610, 635

Atek, H., Kunth, D., Schaerer, D., Hayes, M., Deharveng, J. M., Östlin, G., & Mas-Hesse, J. M. 2009, A&A, 506, L1

Bell, E. F., McIntosh, D. H., Katz, N., & Weinberg, M. D. 2003, ApJS, 149, 289

Bertin, E., & Arnouts, S. 1996, A&AS, 117, 393

Blanc, G. A., Adams, J. J., Gebhardt, K., Hill, G. J., Drory, N., Hao, L., Bender, R., Ciardullo, R., Finkelstein, S. L., Fry, A. B., Gawiser, E., Gronwall, C., Hopp, U., Jeong, D., Kelzenberg, R., Komatsu, E., MacQueen, P., Murphy, J. D., Roth, M. M., Schneider, D. P., & Tufts, J. 2011, ApJ, 736, 31

Bordoloi, R., Lilly, S. J., Knobel, C., Bolzonella, M., Kampczyk, P., Carollo, C. M., Iovino, A., Zucca, E., Contini, T., Kneib, J.-P., Le Fevre, O., Mainieri, V., Renzini, A., Scodeggio, M., Zamorani, G., Balestra, I., Bardelli, S., Bongiorno, A., Caputi, K., Cucciati, O., de la Torre, S., de Ravel, L., Garilli, B., Kovač, K., Lamareille, F., Le Borgne, J.-F., Le Brun, V., Maier, C., Mignoli, M., Pello, R., Peng, Y., Perez Montero, E., Presotto, V., Scarlata, C., Silverman, J., Tanaka, M., Tasca, L., Tresse, L., Vergani, D., Barnes, L., Cappi, A., Cimatti, A., Coppa, G., Diener, C., Franzetti, P., Koekemoer, A., López-Sanjuan, C., McCracken, H. J., Moresco, M., Nair, P., Oesch, P., Pozzetti, L., & Welikala, N. 2011, ApJ, 743, 10

Bouwens, R. J., Illingworth, G. D., Franx, M., Chary, R., Meurer, G. R., Conselice, C. J., Ford, H., Giavalisco, M., & van Dokkum, P. 2009, ApJ, 705, 936

Bouwens, R. J., Illingworth, G. D., Franx, M., & Ford, H. 2008, ApJ, 686, 230

Brocklehurst, M. 1971, MNRAS, 153, 471

Bruzual, G., & Charlot, S. 2003a, MNRAS, 344, 1000

—. 2003b, MNRAS, 344, 1000

Bundy, K., Ellis, R. S., Conselice, C. J., Taylor, J. E., Cooper, M. C., Willmer, C. N. A., Weiner, B. J., Coil, A. L., Noeske, K. G., & Eisenhardt, P. R. M. 2006, ApJ, 651, 120

Calzetti, D., Armus, L., Bohlin, R. C., Kinney, A. L., Koornneef, J., & Storchi-Bergmann, T. 2000, ApJ, 533, 682

Cecil, G., Bland-Hawthorn, J., Veilleux, S., & Filippenko, A. V. 2001, ApJ, 555, 338

Chabrier, G. 2003, PASP, 115, 763

Chapman, S. C., Blain, A. W., Smail, I., & Ivison, R. J. 2005, ApJ, 622, 772

Chapman, S. C., & Casey, C. M. 2009, MNRAS, 398, 1615

Chary, R., & Elbaz, D. 2001, ApJ, 556, 562

Chen, Y.-M., Tremonti, C. A., Heckman, T. M., Kauffmann, G., Weiner, B. J., Brinchmann, J., & Wang, J. 2010, AJ, 140, 445

Coil, A. L., Weiner, B. J., Holz, D. E., Cooper, M. C., Yan, R., & Aird, J. 2011, ApJ, 743, 46

Cole, S., Lacey, C. G., Baugh, C. M., & Frenk, C. S. 2000, MNRAS, 319, 168

Conroy, C., Shapley, A. E., Tinker, J. L., Santos, M. R., & Lemson, G. 2008, ApJ, 679, 1192

Cowie, L. L., & Hu, E. M. 1998, AJ, 115, 1319

Croton, D. J., Springel, V., White, S. D. M., De Lucia, G., Frenk, C. S., Gao, L., Jenkins, A., Kauffmann, G., Navarro, J. F., & Yoshida, N. 2006, MNRAS, 365, 11

Daddi, E., Dickinson, M., Morrison, G., Chary, R., Cimatti, A., Elbaz, D., Frayer, D., Renzini, A., Pope, A., Alexander, D. M., Bauer, F. E., Giavalisco, M., Huynh, M., Kurk, J., & Mignoli, M. 2007, ApJ, 670, 156

Dalla Vecchia, C., & Schaye, J. 2012, MNRAS, submitted (astro-ph/1203.5667)

Davis, M., Guhathakurta, P., Konidaris, N. P., Newman, J. A., Ashby, M. L. N., Biggs, A. D., Barmby, P., Bundy, K., Chapman, S. C., Coil, A. L., Conselice, C. J., Cooper, M. C., Croton, D. J., Eisenhardt, P. R. M., Ellis, R. S., Faber,

S. M., Fang, T., Fazio, G. G., Georgakakis, A., Gerke, B. F., Goss, W. M., Gwyn, S., Harker, J., Hopkins, A. M., Huang, J., Ivison, R. J., Kassin, S. A., Kirby, E. N., Koekemoer, A. M., Koo, D. C., Laird, E. S., Le Floc'h, E., Lin, L., Lotz, J. M., Marshall, P. J., Martin, D. C., Metevier, A. J., Moustakas, L. A., Nandra, K., Noeske, K. G., Papovich, C., Phillips, A. C., Rich, R. M., Rieke, G. H., Rigopoulou, D., Salim, S., Schiminovich, D., Simard, L., Smail, I., Small, T. A., Weiner, B. J., Willmer, C. N. A., Willner, S. P., Wilson, G., Wright, E. L., & Yan, R. 2007, ApJL, 660, L1

Dayal, P., Ferrara, A., Saro, A., Salvaterra, R., Borgani, S., & Tornatore, L. 2009, MNRAS, 1479

de Vaucouleurs, G. 1948, Annales d'Astrophysique, 11, 247

De Young, D. S., & Heckman, T. M. 1994, ApJ, 431, 598

Deharveng, J.-M., Small, T., Barlow, T. A., Péroux, C., Milliard, B., Friedman, P. G., Martin, D. C., Morrissey, P., Schiminovich, D., Forster, K., Seibert, M., Wyder, T. K., Bianchi, L., Donas, J., Heckman, T. M., Lee, Y.-W., Madore, B. F., Neff, S. G., Rich, R. M., Szalay, A. S., Welsh, B. Y., & Yi, S. K. 2008, ApJ, 680, 1072

Dickey, J. M., & Garwood, R. W. 1989, ApJ, 341, 201

Dickinson, M., Giavalisco, M., & The Goods Team. 2003, in The Mass of Galaxies at Low and High Redshift, 324

Diehl, R., Halloin, H., Kretschmer, K., Lichti, G. G., Schönfelder, V., Strong, A. W., von Kienlin, A., Wang, W., Jean, P., Knödlseder, J., Roques, J.-P., Weidenspointner, G., Schanne, S., Hartmann, D. H., Winkler, C., & Wunderer, C. 2006, Nature, 439, 45

Dove, J. B., Shull, J. M., & Ferrara, A. 2000, ApJ, 531, 846

Elbaz, D., Daddi, E., Le Borgne, D., Dickinson, M., Alexander, D. M., Chary, R.-R., Starck, J.-L., Brandt, W. N., Kitzbichler, M., MacDonald, E., Nonino, M., Popesso, P., Stern, D., & Vanzella, E. 2007, A&A, 468, 33

Erb, D. K., Shapley, A. E., Pettini, M., Steidel, C. C., Reddy, N. A., & Adelberger, K. L. 2006a, ApJ, 644, 813

—. 2006b, ApJ, 644, 813

Erb, D. K., Steidel, C. C., Shapley, A. E., Pettini, M., Reddy, N. A., & Adelberger, K. L. 2006c, ApJ, 646, 107

Fazio, G. G., Hora, J. L., Allen, L. E., Ashby, M. L. N., Barmby, P., Deutsch, L. K., Huang, J.-S., Kleiner, S., Marengo, M., Megeath, S. T., Melnick, G. J., Pahre, M. A., Patten, B. M., Polizotti, J., Smith, H. A., Taylor, R. S., Wang, Z., Willner, S. P., Hoffmann, W. F., Pipher, J. L., Forrest, W. J., McMurty, C. W., McCreight, C. R., McKelvey, M. E., McMurray, R. E., Koch, D. G., Moseley, S. H., Arendt, R. G., Mentzell, J. E., Marx, C. T., Losch, P., Mayman, P., Eichhorn, W., Krebs, D., Jhabvala, M., Gezari, D. Y., Fixsen, D. J., Flores, J., Shakoorzadeh, K., Jungo, R., Hakun, C., Workman, L., Karpati, G., Kichak, R., Whitley, R., Mann, S., Tollestrup, E. V., Eisenhardt, P., Stern, D., Gorjian, V., Bhattacharya, B., Carey, S., Nelson, B. O., Glaccum, W. J., Lacy, M., Lowrance, P. J., Laine, S., Reach, W. T., Stauffer, J. A., Surace, J. A., Wilson, G., Wright, E. L., Hoffman, A., Domingo, G., & Cohen, M. 2004, ApJS, 154, 10

Feigelson, E. D., & Nelson, P. I. 1985, ApJ, 293, 192

Ferrara, A., & Ricotti, M. 2006, MNRAS, 373, 571

Ferrarese, L., & Merritt, D. 2000, ApJL, 539, L9

Finkelstein, S. L., Rhoads, J. E., Malhotra, S., & Grogin, N. 2009, ApJ, 691, 465

Ford, H. C., Clampin, M., Hartig, G. F., Illingworth, G. D., Sirianni, M., Mart el, A. R., Meurer, G. R., McCann, W. J., Sullivan, P. C., Bartko, F., Benitez, N., Blake slee, J., Bouwens, R., Broadhurst, T., Brown, R. A., Burrows, C. J., Campbell, D., Cheng , E. S., Feldman, P. D., Franx, M., Golimowski, D. A., Gronwall, C., Kimble, R. A., Kris t, J. E., Lesser, M. P., Magee, D., Miley, G., Postman, M., Rafal, M. D., Rosati, P. an d Sparks, W. B., Tran, H. D., Tsvetanov, Z. I., Volmer, P., White, R. L., & Woodruff, R. A. 2003, in Presented at the Society of Photo-Optical Instrumentation Engineers (SPIE) Conference, Vol. 4854, Society of Photo-Optical Instrumentation Engineers (SPIE) Conference Series, ed. J. C. Blades & O. H. W. Siegmund, 81–94

Förster Schreiber, N. M., Genzel, R., Bouché, N., Cresci, G., Davies, R., Buschkamp, P., Shapiro, K., Tacconi, L. J., Hicks, E. K. S., Genel, S., Shapley, A. E. andErb, D. K., Steidel, C. C., Lutz, D., Eisenhauer, F., Gillessen, S., Sternberg, A., Renzini, A., Cimatti, A., Daddi, E., Kurk, J., Lilly, S., Kong, X., Lehnert, M. D., Nesvadba, N., Verma, A., McCracken, H., Arimoto, N., Mignoli, M., & Onodera, M. 2009, ApJ, 706, 1364

Förster Schreiber, N. M., Genzel, R., Lehnert, M. D., Bouché, N., Verma, A., Erb, D. K., Shapley, A. E., Steidel, C. C., Davies, R., Lutz, D., Nesvadba, N., Tacconi, L. J., Eisenhauer, F., Abuter, R., Gilbert, A., Gillessen, S., & Sternberg, A. 2006, ApJ, 645, 1062

Franx, M., Illingworth, G. D., Kelson, D. D., van Dokkum, P. G., & Tran, K. 1997, ApJL, 486, L75+

Fujita, A., Martin, C. L., Mac Low, M., New, K. C. B., & Weaver, R. 2009, ApJ, 698, 693

Gabor, J. M., Davé, R., Oppenheimer, B. D., & Finlator, K. 2011, MNRAS, 417, 2676

Gawiser, E., Francke, H., Lai, K., Schawinski, K., Gronwall, C., Ciardullo, R., Quadri, R., Orsi, A., Barrientos, L. F., Blanc, G. A., Fazio, G., Feldmeier, J. J., Huang, J.-s., Infante, L., Lira, P., Padilla, N., Taylor, E. N., Treister, E., Urry, C. M., van Dokkum, P. G., & Virani, S. N. 2007, ApJ, 671, 278

Gawiser, E., van Dokkum, P. G., Gronwall, C., Ciardullo, R., Blanc, G. A., Castander, F. J., Feldmeier, J., Francke, H., Franx, M., Haberzettl, L., Herrera, D., Hickey, T., Infante, L., Lira, P., Maza, J., Quadri, R., Richardson, A., Schawinski, K., Schirmer, M., Taylor, E. N., Treister, E., Urry, C. M., & Virani, S. N. 2006, ApJL, 642, L13

Genzel, R., Newman, S., Jones, T., Förster Schreiber, N. M., Shapiro, K., Genel, S., Lilly, S. J., Renzini, A., Tacconi, L. J., Bouché, N., Burkert, A., Cresci, G., Buschkamp, P., Carollo, C. M., Ceverino, D., Davies, R., Dekel, A., Eisenhauer, F., Hicks, E., Kurk, J., Lutz, D., Mancini, C., Naab, T., Peng, Y., Sternberg, A., Vergani, D., & Zamorani, G. 2011, ApJ, 733, 101

Giavalisco, M., & Dickinson, M. 2001, ApJ, 550, 177

Giavalisco, M., Ferguson, H. C., Koekemoer, A. M., Dickinson, M., Alexander, D. M., Bauer, F. E., Bergeron, J., Biagetti, C., Brandt, W. N., Casertano, S., Cesarsky, C., Chatzichristou, E., Conselice, C., Cristiani, S., Da Costa, L., Dahlen, T., de Mello, D., Eisenhardt, P., Erben, T., Fall, S. M., Fassnacht, C., Fosbury, R., Fruchter, A., Gardner, J. P., Grogin, N., Hook, R. N., Hornschemeier, A. E., Idzi, R., Jogee, S., Kretchmer, C., Laidler, V., Lee, K. S.,

Livio, M., Lucas, R., Madau, P., Mobasher, B., Moustakas, L. A., Nonino, M., Padovani, P., Papovich, C., Park, Y., Ravindranath, S., Renzini, A., Richardson, M., Riess, A., Rosati, P., Schirmer, M., Schreier, E., Somerville, R. S., Spinrad, H., Stern, D., Stiavelli, M., Strolger, L., Urry, C. M., Vandame, B., Williams, R., & Wolf, C. 2004, ApJL, 600, L93

Giavalisco, M., Steidel, C. C., & Macchetto, F. D. 1996, ApJ, 470, 189

Giavalisco, M., Vanzella, E., Salimbeni, S., Tripp, T. M., Dickinson, M., Cassata, P., Renzini, A., Guo, Y., Ferguson, H. C., Nonino, M., Cimatti, A., Kurk, J., Mignoli, M., Tang, Y., & . 2011, ApJ, 743, 95

Gnedin, N. Y., Kravtsov, A. V., & Chen, H.-W. 2008, ApJ, 672, 765

Granato, G. L., Lacey, C. G., Silva, L., Bressan, A., Baugh, C. M., Cole, S., & Frenk, C. S. 2000, ApJ, 542, 710

Gronwall, C., Ciardullo, R., Hickey, T., Gawiser, E., Feldmeier, J. J., van Dokkum, P. G., Urry, C. M., Herrera, D., Lehmer, B. D., Infante, L., Orsi, A., Marchesini, D., Blanc, G. A., Francke, H., Lira, P., & Treister, E. 2007, ApJ, 667, 79

Hainline, K. N., Shapley, A. E., Kornei, K. A., Pettini, M., Buckley-Geer, E., Allam, S. S., & Tucker, D. L. 2009, ApJ, 701, 52

Hansen, M., & Oh, S. P. 2006, MNRAS, 367, 979

Hayashino, T., Matsuda, Y., Tamura, H., Yamauchi, R., Yamada, T., Ajiki, M., Fujita, S. S., Murayama, T., Nagao, T., Ohta, K., Okamura, S., Ouchi, M., Shimasaku, K., Shioya, Y., & Taniguchi, Y. 2004, AJ, 128, 2073

Heckman, T. M. 2002, in ASP Conf. Ser. 254: Extragalactic Gas at Low Redshift, 292

Heckman, T. M., Armus, L., & Miley, G. K. 1990, ApJS, 74, 833

Heckman, T. M., Borthakur, S., Overzier, R., Kauffmann, G., Basu-Zych, A., Leitherer, C., Sembach, K., Martin, D. C., Rich, R. M., Schiminovich, D., & Seibert, M. 2011, ApJ, 730, 5

Heckman, T. M., Lehnert, M. D., Strickland, D. K., & Armus, L. 2000, ApJS, 129, 493

Heckman, T. M., & Leitherer, C. 1997, AJ, 114, 69

Heckman, T. M., Sembach, K. R., Meurer, G. R., Leitherer, C., Calzetti, D., & Martin, C. L. 2001a, ApJ, 558, 56

Heckman, T. M., Sembach, K. R., Meurer, G. R., Strickland, D. K., Martin, C. L., Calzetti, D., & Leitherer, C. 2001b, ApJ, 554, 1021

Hopkins, A. M., Connolly, A. J., Haarsma, D. B., & Cram, L. E. 2001, AJ, 122, 288

Hu, E. M., & McMahon, R. G. 1996, Nature, 382, 231

Isobe, T., & Feigelson, E. D. 1990, in Bulletin of the American Astronomical Society, Vol. 22, Bulletin of the American Astronomical Society, 917–918

Isobe, T., Feigelson, E. D., & Nelson, P. I. 1986, ApJ, 306, 490

Iye, M., Ota, K., Kashikawa, N., Furusawa, H., Hashimoto, T., Hattori, T., Matsuda, Y., Morokuma, T., Ouchi, M., & Shimasaku, K. 2006, Nature, 443, 186

Jones, T., Stark, D. P., & Ellis, R. S. 2012, ApJ, 751, 51

Kennicutt, Jr., R. C. 1998, ARAA, 36, 189

Kobayashi, M. A. R., Totani, T., & Nagashima, M. 2010, ApJ, 708, 1119

Kornei, K. A., Shapley, A. E., Martin, C. L., Coil, A. L., Lotz, J. M., Schiminovich, D., Bundy, K., & Noeske, K. G. 2012, ArXiv e-prints

Kroupa, P. 2001, MNRAS, 322, 231

Krug, H. B., Rupke, D. S. N., & Veilleux, S. 2010, ApJ, 708, 1145

Kulas, K. R., Shapley, A. E., Kollmeier, J. A., Zheng, Z., Steidel, C. C., & Hainline, K. N. 2012, ApJ, 745, 33

Lai, K., Huang, J.-S., Fazio, G., Gawiser, E., Ciardullo, R., Damen, M., Franx, M., Gronwall, C., Labbe, I., Magdis, G., & van Dokkum, P. 2008, ApJ, 674, 70

Laird, E. S., Nandra, K., Georgakakis, A., Aird, J. A., Barmby, P., Conselice, C. J., Coil, A. L., Davis, M., Faber, S. M., Fazio, G. G., Guhathakurta, P., Koo, D. C., Sarajedini, V., & Willmer, C. N. A. 2009, ApJS, 180, 102

Lavalley, M. P., Isobe, T., & Feigelson, E. D. 1992, in Bulletin of the American Astronomical Society, Vol. 24, Bulletin of the American Astronomical Society, 839–840

Law, D. R., Steidel, C. C., Erb, D. K., Larkin, J. E., Pettini, M., Shapley, A. E., & Wright, S. A. 2009, ApJ, 697, 2057

Law, D. R., Steidel, C. C., Erb, D. K., Pettini, M., Reddy, N. A., Shapley, A. E., Adelberger, K. L., & Simenc, D. J. 2007, ApJ, 656, 1

Law, D. R., Steidel, C. C., Shapley, A. E., Nagy, S. R., Reddy, N. A., & Erb, D. K. 2012a, ApJ, 745, 85

—. 2012b, ApJ, submitted (astro-ph/1206.6889)

Le Tiran, L., Lehnert, M. D., van Driel, W., Nesvadba, N. P. H., & Di Matteo, P. 2011, A&A, 534, L4

Lee, K.-S., Giavalisco, M., Gnedin, O. Y., Somerville, R. S., Ferguson, H. C., Dickinson, M., & Ouchi, M. 2006, ApJ, 642, 63

Lehnert, M. D., & Heckman, T. M. 1996, ApJ, 462, 651

Leitherer, C., & Heckman, T. M. 1995, ApJS, 96, 9

Leitherer, C., Schaerer, D., Goldader, J. D., Delgado, R. M. G., Robert, C., Kune, D. F., de Mello, D. F., Devost, D., & Heckman, T. M. 1999, ApJS, 123, 3

Leitherer, C., Tremonti, C. A., Heckman, T. M., & Calzetti, D. 2011, AJ, 141, 37

Lequeux, J., Kunth, D., Mas-Hesse, J. M., & Sargent, W. L. W. 1995, A&A, 301, 18

Lilly, S. J., Le Fevre, O., Hammer, F., & Crampton, D. 1996, ApJL, 460, L1

Lotz, J. M., Davis, M., Faber, S. M., Guhathakurta, P., Gwyn, S., Huang, J., Koo, D. C., Le Floc'h, E., Lin, L., Newman, J., Noeske, K., Papovich, C., Willmer, C. N. A., Coil, A., Conselice, C. J., Cooper, M., Hopkins, A. M., Metevier, A., Primack, J., Rieke, G., & Weiner, B. J. 2008, ApJ, 672, 177

Lotz, J. M., Primack, J., & Madau, P. 2004, AJ, 128, 163

Madau, P. 1995, ApJ, 441, 18

Madau, P., Ferguson, H. C., Dickinson, M. E., Giavalisco, M., Steidel, C. C., & Fruchter, A. 1996, MNRAS, 283, 1388

Maiolino, R., Nagao, T., Grazian, A., Cocchia, F., Marconi, A., Mannucci, F., Cimatti, A., Pipino, A., Ballero, S., Calura, F., Chiappini, C., Fontana, A., Granato, G. L., Matteucci, F., Pastorini, G., Pentericci, L., Risaliti, G., Salvati, M., & Silva, L. 2008, A&A, 488, 463

Malhotra, S., & Rhoads, J. E. 2002, ApJL, 565, L71

Maraston, C. 2005, MNRAS, 362, 799

Markwardt, C. B. 2009, in Astronomical Society of the Pacific Conference Series, Vol. 411, Astronomical Data Analysis Software and Systems XVIII, ed. D. A. Bohlender, D. Durand, & P. Dowler, 251

Martin, C. L. 1999, ApJ, 513, 156

—. 2005, ApJ, 621, 227

Martin, C. L., & Bouché, N. 2009, ApJ, 703, 1394

Martin, C. L., Shapley, A. E., Coil, A. L., Kornei, K. A., Bundy, K., Weiner, B. J., Noeske, K. G., & Schiminovich, D. 2012, ApJ, submitted (astro-ph/1206.5552)

Martin, D. C., Fanson, J., Schiminovich, D., Morrissey, P., Friedman, P. G., Barlow, T. A., Conrow, T., Grange, R., Jelinsky, P. N., Milliard, B., Siegmund, O. H. W., Bianchi, L., Byun, Y., Donas, J., Forster, K., Heckman, T. M., Lee, Y., Madore, B. F., Malina, R. F., Neff, S. G., Rich, R. M., Small, T., Surber, F., Szalay, A. S., Welsh, B., & Wyder, T. K. 2005, ApJL, 619, L1

Mas-Hesse, J. M., Kunth, D., Tenorio-Tagle, G., Leitherer, C., Terlevich, R. J., & Terlevich, E. 2003, ApJ, 598, 858

Matsuda, Y., Yamada, T., Hayashino, T., Tamura, H., Yamauchi, R., Ajiki, M., Fujita, S. S., Murayama, T., Nagao, T., Ohta, K., Okamura, S., Ouchi, M., Shimasaku, K., Shioya, Y., & Taniguchi, Y. 2004, AJ, 128, 569

McCarthy, J. K., Cohen, J. G., Butcher, B., Cromer, J., Croner, E., Douglas, W. R., Goeden, R. M., Grewal, T., Lu, B., Petrie, H. L., Weng, T., Weber, B., Koch, D. G., & Rodgers, J. M. 1998, in Proc. SPIE Vol. 3355, p. 81-92, Optical Astronomical Instrumentation, Sandro D'Odorico; Ed., Vol. 3355, 81–92

McLure, R. J., Cirasuolo, M., Dunlop, J. S., Foucaud, S., & Almaini, O. 2009, MNRAS, 528

Ménard, B., Wild, V., Nestor, D., Quider, A., Zibetti, S., Rao, S., & Turnshek, D. 2011, MNRAS, 417, 801

Meurer, G. R., Heckman, T. M., & Calzetti, D. 1999, ApJ, 521, 64

Murray, N., Martin, C. L., Quataert, E., & Thompson, T. A. 2007, ApJ, 660, 211

Murray, N., Ménard, B., & Thompson, T. A. 2011, ApJ, 735, 66

Murray, N., Quataert, E., & Thompson, T. A. 2005, ApJ, 618, 569

Neufeld, D. A. 1990, ApJ, 350, 216

—. 1991, ApJL, 370, L85

Neugebauer, G., Habing, H. J., van Duinen, R., Aumann, H. H., Baud, B., Beichman, C. A., Beintema, D. A., Boggess, N., Clegg, P. E., de Jong, T.,

Emerson, J. P., Gautier, T. N., Gillett, F. C., Harris, S., Hauser, M. G., Houck, J. R., Jennings, R. E., Low, F. J., Marsden, P. L., Miley, G., Olnon, F. M., Pottasch, S. R., Raimond, E., Rowan-Robinson, M., Soifer, B. T., Walker, R. G., Wesselius, P. R., & Young, E. 1984, ApJL, 278, L1

Newman, J. A., Cooper, M. C., Davis, M., Faber, S. M., Coil, A. L., Guhathakurta, P., Koo, D. C., Phillips, A. C., Conroy, C., Dutton, A. A., Finkbeiner, D. P., Gerke, B. F., Rosario, D. J., Weiner, B. J., Willmer, C. N. A., Yan, R., Harker, J. J., Kassin, S. A., Konidaris, N. P., Lai, K., Madgwick, D. S., Noeske, K. G., Wirth, G. D., Connolly, A. J., Kaiser, N., Kirby, E. N., Lemaux, B. C., Lin, L., Lotz, J. M., Luppino, G. A., Marinoni, C., Matthews, D. J., Metevier, A., & Schiavon, R. P. 2012, ApJ, submitted (astro-ph/1203.3192)

Nilsson, K. K., Møller, P., Möller, O., Fynbo, J. P. U., Michałowski, M. J., Watson, D., Ledoux, C., Rosati, P., Pedersen, K., & Grove, L. F. 2007, A&A, 471, 71

Nilsson, K. K., Möller-Nilsson, O., Møller, P., Fynbo, J. P. U., & Shapley, A. E. 2009a, MNRAS, 400, 232

Nilsson, K. K., Tapken, C., Møller, P., Freudling, W., Fynbo, J. P. U., Meisenheimer, K., Laursen, P., & Östlin, G. 2009b, A&A, 498, 13

Noeske, K. G., Weiner, B. J., Faber, S. M., Papovich, C., Koo, D. C., Somerville, R. S., Bundy, K., Conselice, C. J., Newman, J. A., Schiminovich, D., Le Floc'h, E., Coil, A. L., Rieke, G. H., Lotz, J. M., Primack, J. R., Barmby, P., Cooper, M. C., Davis, M., Ellis, R. S., Fazio, G. G., Guhathakurta, P., Huang, J., Kassin, S. A., Martin, D. C., Phillips, A. C., Rich, R. M., Small, T. A., Willmer, C. N. A., & Wilson, G. 2007, ApJL, 660, L43

Oke, J. B., Cohen, J. G., Carr, M., Cromer, J., Dingizian, A., Harris, F. H., Labrecque, S., Lucinio, R., Schaal, W., Epps, H., & Miller, J. 1995, PASP, 107, 375

Oppenheimer, B. D., & Davé, R. 2006, MNRAS, 373, 1265

Osterbrock, D. E. 1989, Astrophysics of gaseous nebulae and active galactic nuclei, ed. Osterbrock, D. E.

Ouchi, M., Shimasaku, K., Akiyama, M., Simpson, C., Saito, T., Ueda, Y., Furusawa, H., Sekiguchi, K., Yamada, T., Kodama, T., Kashikawa, N., Okamura, S., Iye, M., Takata, T., Yoshida, M., & Yoshida, M. 2008, ApJS, 176, 301

Ouchi, M., Shimasaku, K., Okamura, S., Furusawa, H., Kashikawa, N., Ota, K., Doi, M., Hamabe, M., Kimura, M., Komiyama, Y., Miyazaki, M., Miyazaki, S., Nakata, F., Sekiguchi, M., Yagi, M., & Yasuda, N. 2004, ApJ, 611, 685

Papovich, C., Dickinson, M., & Ferguson, H. C. 2001, ApJ, 559, 620

Peng, C. Y., Ho, L. C., Impey, C. D., & Rix, H.-W. 2002, AJ, 124, 266

—. 2010, AJ, 139, 2097

Pentericci, L., Grazian, A., Fontana, A., Castellano, M., Giallongo, E., Salimbeni, S., & Santini, P. 2009, A&A, 494, 553

Pentericci, L., Grazian, A., Fontana, A., Salimbeni, S., Santini, P., de Santis, C., Gallozzi, S., & Giallongo, E. 2007, A&A, 471, 433

Pettini, M., Kellogg, M., Steidel, C. C., Dickinson, M., Adelberger, K. L., & Giavalisco, M. 1998, ApJ, 508, 539

Pettini, M., Rix, S. A., Steidel, C. C., Adelberger K. L., Hunt, M. P., & Shapley, A. E. 2002, ApJ, 569, 742

Pettini, M., Shapley, A. E., Steidel, C. C., Cuby, J., Dickinson, M., Moorwood, A. F. M., Adelberger, K. L., & Giavalisco, M. 2001, ApJ, 554, 981

Pettini, M., Steidel, C. C., Adelberger, K. L., Dickinson, M., & Giavalisco, M. 2000, ApJ, 528, 96

Phillips, A. C. 1993, AJ, 105, 486

Press, W. H., Teukolsky, S. A., Vetterling, W. T., & Flannery, B. P. 1992, Numerical Recipes in FORTRAN: the Art of Scientific Computing (Cambridge: University Press, 2nd ed.)

Prévot, M. L., Lequeux, J., Prévot, L., Maurice, E., & Rocca-Volmerange, B. 1984, A&A, 132, 389

Prochaska, J. X., Kasen, D., & Rubin, K. 2011, ApJ, 734, 24

Quider, A. M., Pettini, M., Shapley, A. E., & Steidel, C. C. 2009, MNRAS, 1081

Ralchenko, Y., Fuhr, J. R., Jou, F.-C., Kramida, A. E., Martin, W. C., Podobedova, L. I., Reader, J., Saloman, E. B., Sansonetti, J. E., & Wiese, W. L. 2005, in American Institute of Physics Conference Series, Vol. 771, Atomic and Molecular Data and their Applications, ed. T. Kato, D. Kato, & H. Funaba, 276–285

Reddy, N. A., & Steidel, C. C. 2009, ApJ, 692, 778

Reddy, N. A., Steidel, C. C., Erb, D. K., Shapley, A. E., & Pettini, M. 2006a, ApJ, 653, 1004

Reddy, N. A., Steidel, C. C., Fadda, D., Yan, L., Pettini, M., Shapley, A. E., Erb, D. K., & Adelberger, K. L. 2006b, ApJ, 644, 792

Reddy, N. A., Steidel, C. C., Pettini, M., Adelberger, K. L., Shapley, A. E., Erb, D. K., & Dickinson, M. 2008, ApJS, 175, 48

Renzini, A. 2006, ARAA, 44, 141

Rhoads, J. E., Malhotra, S., Dey, A., Stern, D., Spinrad, H., & Jannuzi, B. T. 2000, ApJL, 545, L85

Robertson, B., Hernquist, L., Cox, T. J., Di Matteo, T., Hopkins, P. F., Martini, P., & Springel, V. 2006, ApJ, 641, 90

Rubin, K. H. R., Prochaska, J. X., Koo, D. C., & Phillips, A. C. 2012, ApJL, 747, L26

Rubin, K. H. R., Prochaska, J. X., Koo, D. C., Phillips, A. C., & Weiner, B. J. 2010a, ApJ, 712, 574

Rubin, K. H. R., Prochaska, J. X., Ménard, B., Murray, N., Kasen, D., Koo, D. C., & Phillips, A. C. 2011, ApJ, 728, 55

Rubin, K. H. R., Weiner, B. J., Koo, D. C., Martin, C. L., Prochaska, J. X., Coil, A. L., & Newman, J. A. 2010b, ApJ, 719, 1503

Rupke, D. S., Veilleux, S., & Sanders, D. B. 2002, ApJ, 570, 588

—. 2005, ApJS, 160, 115

Salim, S., Rich, R. M., Charlot, S., Brinchmann, J., Johnson, B. D., Schiminovich, D., Seibert, M., Mallery, R., Heckman, T. M., Forster, K., Friedman, P. G., Martin, D. C., Morrissey, P., Neff, S. G., Small, T., Wyder, T. K., Bianchi, L., Donas, J., Lee, Y., Madore, B. F., Milliard, B., Szalay, A. S., Welsh, B. Y., & Yi, S. K. 2007, ApJS, 173, 267

Salpeter, E. E. 1955, ApJ, 121, 161

Sanders, D. B., & Mirabel, I. F. 1996, ARAA, 34, 749

Sato, T., Martin, C. L., Noeske, K. G., Koo, D. C., & Lotz, J. M. 2009, ApJ, 696, 214

Savage, B. D., & Sembach, K. R. 1996, ARAA, 34, 279

Scannapieco, E., Silk, J., & Bouwens, R. 2005, ApJL, 635, L13

Schiminovich, D., Wyder, T. K., Martin, D. C., Johnson, B. D., Salim, S., Seibert, M., Treyer, M. A., Budavári, T., Hoopes, C., Zamojski, M., Barlow, T. A., Forster, K. G., Friedman, P. G., Morrissey, P., Neff, S. G., Small, T. A., Bianchi, L., Donas, J., Heckman, T. M., Lee, Y., Madore, B. F., Milliard, B., Rich, R. M., Szalay, A. S., Welsh, B. Y., & Yi, S. 2007, ApJS, 173, 315

Schwartz, C. M., & Martin, C. L. 2004, ApJ, 610, 201

Seibert, M., Martin, D. C., Heckman, T. M., Buat, V., Hoopes, C., Barlow, T., Bianchi, L., Byun, Y., Donas, J., Forster, K., Friedman, P. G., Jelinsky, P., Lee, Y., Madore, B. F., Malina, R., Milliard, B., Morrissey, P., Neff, S., Rich, R. M., Schiminovich, D., Morrissey, P., Neff, S., Rich, R. M., Schiminovich, D., & Wyder, T. K. 2005, ApJL, 619, L55

Shapley, A. E., Steidel, C. C., Adelberger, K. L., Dickinson, M., Giavalisco, M., & Pettini, M. 2001, ApJ, 562, 95

Shapley, A. E., Steidel, C. C., Erb, D. K., Reddy, N. A., Adelberger, K. L., Pettini, M., Barmby, P., & Huang, J. 2005, ApJ, 626, 698

Shapley, A. E., Steidel, C. C., Pettini, M., & Adelberger, K. L. 2003, ApJ, 588, 65

Shapley, A. E., Steidel, C. C., Pettini, M., Adelberger, K. L., & Erb, D. K. 2006, ApJ, 651, 688

Sharma, M., & Nath, B. B. 2012, ApJ, 750, 55

Shopbell, P. L., & Bland-Hawthorn, J. 1998, ApJ, 493, 129

Siana, B., Smail, I., Swinbank, A. M., Richard, J., Teplitz, H. I., Coppin, K. E. K., Ellis, R. S., Stark, D. P., Kneib, J.-P., & Edge, A. C. 2009, ApJ, 698, 1273

Siana, B., Teplitz, H. I., Chary, R.-R., Colbert, J., & Frayer, D. T. 2008, ApJ, 689, 59

Snow, T. P., Lamers, H. J. G. L. M., Lindholm, D. M., & Odell, A. P. 1994, ApJS, 95, 163

Socrates, A., Davis, S. W., & Ramirez-Ruiz, E. 2008, ApJ, 687, 202

Stanway, E. R., Bunker, A. J., Glazebrook, K., Abraham, R. G., Rhoads, J., Malhotra, S., Crampton, D., Colless, M., & Chiu, K. 2007, MNRAS, 376, 727

Steidel, C. C., Adelberger, K. L., Giavalisco, M., Dickinson, M., & Pettini, M. 1999, ApJ, 519, 1

Steidel, C. C., Adelberger, K. L., Shapley, A. E., Pettini, M., Dickinson, M., & Giavalisco, M. 2000, ApJ, 532, 170

—. 2003, ApJ, 592, 728

Steidel, C. C., Erb, D. K., Shapley, A. E., Pettini, M., Reddy, N., Bogosavljević, M., Rudie, G. C., & Rakic, O. 2010, ApJ, 717, 289

Steidel, C. C., Giavalisco, M., Dickinson, M., & Adelberger, K. L. 1996a, AJ, 112, 352

Steidel, C. C., Giavalisco, M., Pettini, M., Dickinson, M., & Adelberger, K. L. 1996b, ApJL, 462, L17+

Steidel, C. C., Pettini, M., & Adelberger, K. L. 2001, ApJ, 546, 665

Steidel, C. C., Shapley, A. E., Pettini, M., Adelberger, K. L., Erb, D. K., Reddy, N. A., & Hunt, M. P. 2004, ApJ, 604, 534

Strickland, D. K., & Heckman, T. M. 2009, ApJ, 697, 2030

Strickland, D. K., Heckman, T. M., Colbert, E. J. M., Hoopes, C. G., & Weaver, K. A. 2004, ApJ, 606, 829

Swinbank, A. M., Smail, I., Chapman, S. C., Borys, C., Alexander, D. M., Blain, A. W., Conselice, C. J., Hainline, L. J., & Ivison, R. J. 2010, MNRAS, 405, 234

Talia, M., Mignoli, M., Cimatti, A., Kurk, J., Berta, S., Bolzonella, M., Cassata, P., Daddi, E., Dickinson, M., Franceschini, A., Halliday, C., Pozzetti, L., Renzini, A., Rodighiero, G., Rosati, P., & Zamorani, G. 2012, A&A, 539, A61

Tapken, C., Appenzeller, I., Noll, S., Richling, S., Heidt, J., Meinköhn, E., & Mehlert, D. 2007, A&A, 467, 63

Teplitz, H. I., McLean, I. S., Becklin, E. E., Figer, D. F., Gilbert, A. M., Graham, J. R., Larkin, J. E., Levenson, N. A., & Wilcox, M. K. 2000, ApJL, 533, L65

Tremonti, C. A., Heckman, T. M., Kauffmann, G., Brinchmann, J., Charlot, S., White, S. D. M., Seibert, M., Peng, E. W., Schlegel, D. J., Uomoto, A., Fukugita, M., & Brinkmann, J. 2004, ApJ, 613, 898

Tremonti, C. A., Moustakas, J., & Diamond-Stanic, A. M. 2007, ApJL, 663, L77

Tully, R. B., & Fisher, J. R. 1977, A&A, 54, 661

Vanzella, E., Giavalisco, M., Dickinson, M., Cristiani, S., Nonino, M., Kuntschner, H., Popesso, P., Rosati, P., Renzini, A., Stern, D., Cesarsky, C., Ferguson, H. C., & Fosbury, R. A. E. 2009, ApJ, 695, 1163

Veilleux, S., Cecil, G., & Bland-Hawthorn, J. 2005, ARAA, 43, 769

Verhamme, A., Schaerer, D., Atek, H., & Tapken, C. 2008, A&A, 491, 89

Verma, A., Lehnert, M. D., Förster Schreiber, N. M., Bremer, M. N., & Douglas, L. 2007, MNRAS, 377, 1024

Wang, T., Dai, H., & Zhou, H. 2008, ApJ, 674, 668

Weiner, B. J., Coil, A. L., Prochaska, J. X., Newman, J. A., Cooper, M. C., Bundy, K., Conselice, C. J., Dutton, A. A., Faber, S. M., Koo, D. C., Lotz, J. M., Rieke, G. H., & Rubin, K. H. R. 2009, ApJ, 692, 187

Willmer, C. N. A., Faber, S. M., Koo, D. C., Weiner, B. J., Newman, J. A., Coil, A. L., Connolly, A. J., Conroy, C., Cooper, M. C., Davis, M., Finkbeiner, D. P., Gerke, B. F., Guhathakurta, P., Harker, J., Kaiser, N., Kassin, S., Konidaris, N. P., Lin, L., Luppino, G., Madgwick, D. S., Noeske, K. G., Phillips, A. C., & Yan, R. 2006, ApJ, 647, 853

Wilson, J. C., Eikenberry, S. S., Henderson, C. P., Hayward, T. L., Carson, J. C., Pirger, B., Barry, D. J., Brandl, B. R., Houck, J. R., Fitzgerald, G. J., & Stolberg, T. M. 2003, in Instrument Design and Performance for Optical/Infrared Ground-based Telescopes. Edited by Iye, Masanori; Moorwood, Alan F. M. Proceedings of the SPIE, Volume 4841, 451–458

Witt, A. N., & Gordon, K. D. 2000, ApJ, 528, 799

Wu, C., Boggess, A., & Gull, T. R. 1983, ApJ, 266, 28

York, D. G., Adelman, J., Anderson, Jr., J. E., Anderson, S. F., Annis, J., Bahcall, N. A., Bakken, J. A., Barkhouser, R., Bastian, S., Berman, E., Boroski, W. N., Bracker, S., Briegel, C., Briggs, J. W., Brinkmann, J., Brunner, R., Burles, S., Carey, L., Carr, M. A., Castander, F. J., Chen, B., Colestock, P. L., Connolly, A. J., Crocker, J. H., Csabai, I., Czarapata, P. C., Davis, J. E., Doi, M., Dombeck, T., Eisenstein, D., Ellman, N., Elms, B. R., Evans, M. L., Fan, X., Federwitz, G. R., Fiscelli, L., Friedman, S., Frieman, J. A., Fukugita, M., Gillespie, B., Gunn, J. E., Gurbani, V. K., de Haas, E., Haldeman, M., Harris, F. H., Hayes, J., Heckman, T. M., Hennessy, G. S., Hindsley, R. B., Holm, S., Holmgren, D. J., Huang, C.-h., Hull, C., Husby, D., Ichikawa, S.-I., Ichikawa, T., Ivezić, Ž., Kent, S., Kim, R. S. J., Kinney, E., Klaene, M., Kleinman, A. N., Kleinman, S., Knapp, G. R., Korienek, J., Kron, R. G., Kunszt, P. Z., Lamb, D. Q., Lee, B., Leger, R. F., Limmongkol, S., Lindenmeyer, C., Long, D. C., Loomis, C., Loveday, J., Lucinio, R., Lupton, R. H., MacKinnon, B., Mannery, E. J., Mantsch, P. M., Margon, B., McGehee, P., McKay, T. A., Meiksin, A., Merelli, A., Monet, D. G., Munn, J. A., Narayanan, V. K., Nash, T., Neilsen, E., Neswold, R., Newberg, H. J., Nichol, R. C., Nicinski, T., Nonino, M., Okada, N., Okamura, S., Ostriker, J. P., Owen, R., Pauls, A. G., Peoples, J., Peterson, R. L., Petravick, D., Pier, J. R., Pope, A., Pordes, R., Prosapio, A., Rechenmacher, R., Quinn, T. R., Richards, G. T., Richmond, M. W., Rivetta, C. H., Rockosi, C. M., Ruthmansdorfer, K., Sandford, D., Schlegel, D. J., Schneider, D. P., Sekiguchi, M., Sergey, G., Shimasaku, K., Siegmund, W. A., Smee, S., Smith, J. A., Snedden, S., Stone, R., Stoughton, C., Strauss, M. A., Stubbs, C., SubbaRao, M., Szalay, A. S., Szapudi, I., Szokoly, G. P., Thakar, A. R., Tremonti, C., Tucker, D. L., Uomoto, A., Vanden Berk, D., Vogeley,

M. S., Waddell, P., Wang, S.-i., Watanabe, M., Weinberg, D. H., Yanny, B., & Yasuda, N. 2000, AJ, 120, 1579